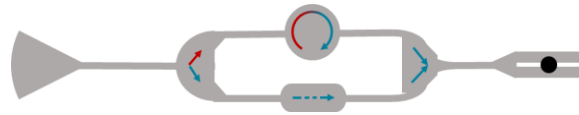


Harvesting solar energy on a silicon photonic chip



Yannick D'Mello



McGill

Department of Electrical & Computer Engineering
McGill University
Montreal, Canada

April, 2023

Thesis submitted to McGill University in partial fulfilment of the requirements for the degree of
Doctor of Philosophy.

© 2022 Yannick D'Mello.

Abstract

An hour of sunlight can satisfy global power consumption for a year, yet solar energy contributes to only 2% of electricity generation. This gap is due to the high price per watt of capture, conversion, and retention. Solar panels capture only direct sunlight, and it depends on weather conditions. The fraction of the solar spectrum that is converted into electricity is limited by the absorption spectrum of silicon (Si). This electricity is retained in batteries whose capacity is further limited by the fermionic nature of electrons. These limitations on the electrical process of harvesting solar energy motivate us to consider an optical process.

In this thesis, we show that sunlight can be captured into optical modes, retained via the bosonic nature of photons, and transferred to electron kinetic energy. Hence, rather than transferring energy from sunlight to bound electrons and then storing electrical energy, our scheme captures and stores optical energy and then transfers it to free electrons. It employs complementary metal oxide-semiconductor technology to ensure inexpensive mass-manufacturability and leverages the maturity of the Si photonic (SiP) platform to design wavelength-dependent but scale-invariant optical devices. We present this scheme as a SiP circuit consisting of 6 devices which perform the following functions: (i) capture ambient light into confined modes, (ii) split the modes based on polarization, (iii) rotate one polarization, (iv) match the phases, (v) combine them into a single mode, and (vi) transfer the energy to free electrons.

(i) To capture ambient sunlight, we analyze the harvesting mechanisms of naturally occurring, biosilica frustules in diatoms. We find that sub-wavelength structures in the frustule together enhance optical capture, redistribution, and retention in the cell by 9.83%. This shows how the silica cladding of a SiP chip can enhance free-space coupling to on-chip devices. (ii) To split the fundamental transverse electric (TE_0) and transverse magnetic (TM_0) modes, we demonstrate an on-chip polarization beam splitter. Our design offers a high fabrication tolerance in a compact form factor resulting in an insertion loss of 2 dB and extinction ratio of 11.45 dB over a wavelength range of 1500-1600 nm. (iii) To rotate the TE_0 mode towards TM_0 , we demonstrate an on-chip electromagnetic coil which uses 14 mA of current to generate an alternating magnetic flux density up to 1.16 mT inside a strip waveguide. We calculate a Faraday rotation of 34.65 p-deg at 1550 nm over an interaction length of 1097.4 μm . We also identify ways to increase the rotation by orders of magnitude. (iv) To phase-match both branches, we design a dual polarization phase shifter to

induce the Pockels effect in an electro-optic polymer. Simulations show a phase shift of 67.5 mrad/V over an interaction length of 8 mm. (v) The two branches are then combined (demonstrated but not included). (vi) To convert light into electricity, we design an exposed slot waveguide to maximize the overlap between a TM_0 supermode and co-propagating free electrons. We optimize the coupling efficiency over the interaction length to achieve an electron energy gain of 28.27 keV from an optical pulse energy of 0.22 nJ. Increasing the kinetic energy of the electron is equivalent to increasing the electric current, or generating electricity. Overall, our results reveal the potential of an optical process to harvest solar energy as either a substitute or a complement to the current electrical process.

Our novel device designs already offer direct applications to a variety of fields including telecommunications, sensing, and quantum information science. Their separate applications incentivize further development, which is supported by the modularized design of our circuit. In this context, the thesis provides a starting point on the roadmap towards harvesting solar energy on a SiP chip.

Résumé

Une heure d'ensoleillement peut satisfaire la consommation électrique mondiale pendant un an, mais l'énergie solaire ne contribue que 2 % de la production d'électricité. Cet écart est dû au prix élevé du watt de captage, de conversion et de rétention. La fraction du spectre solaire qui est convertie en électricité est limitée par le spectre d'absorption du silicium (Si). Cette électricité est retenue dans des batteries dont la capacité est limitée par la nature fermionique des électrons. Ces limitations du processus électrique de récupération de l'énergie solaire nous incitent à envisager un processus optique.

Dans cette thèse, nous montrons que la lumière solaire peut être capturée dans des modes optiques, retenue par des photons et transférée à des électrons. Notre schéma capture et stocke l'énergie optique puis la transfère aux électrons libres. Il utilise une technologie complémentaire d'oxyde métallique-semi-conducteur pour assurer une fabrication de masse peu coûteuse et tire parti de la maturité de la plate-forme photonique Si (SiP) pour concevoir des dispositifs optiques. Nous présentons ce schéma sous la forme d'un circuit SiP composé de 6 dispositifs qui remplissent les fonctions suivantes : (i) capturer la lumière ambiante en modes confinés, (ii) diviser les modes en fonction de la polarisation, (iii) faire pivoter une polarisation, (iv) faire correspondre les phases, (v) les combiner en un seul mode, et (vi) transférer l'énergie aux électrons libres.

(i) Pour capter la lumière solaire ambiante, nous analysons les mécanismes de récolte des frustules de biosilice dans les diatomées. Nous constatons que les structures de sous-longueur d'onde dans le frustule améliorent ensemble la capture optique, la redistribution et la rétention dans la cellule de 9,83 %. Cela montre comment le revêtement en silice d'une puce SiP peut améliorer le couplage en espace libre avec les dispositifs sur puce. (ii) Pour diviser les modes électriques transversal fondamental (TE₀) et magnétique transversal (TM₀), nous démontrons un séparateur de polarisation sur puce. Notre conception offre un facteur de forme compact résultant en une perte d'insertion de 2 dB et un rapport d'extinction de 11,45 dB sur des longueurs d'onde de 1500-1600 nm. (iii) Pour faire pivoter le mode TE₀ vers TM₀, nous démontrons une bobine électromagnétique sur puce qui utilise 14 mA de courant pour générer une densité de flux magnétique alternatif jusqu'à 1,16 mT à l'intérieur d'un guide d'ondes à bande. Nous calculons une rotation de Faraday de 34,65 p-deg à 1550 nm sur une longueur d'interaction de 1097,4 μm . Nous identifions également

des moyens d'augmenter la rotation par ordres de magnitude. (iv) Pour mettre en phase les deux branches, nous concevons un déphaseur à double polarisation. Les simulations montrent un déphasage de 67,5 mrad/V sur une longueur d'interaction de 8 mm. (v) Les deux branches sont ensuite combinées (démontré mais non incluse). (vi) Pour convertir la lumière en électricité, nous concevons un guide d'ondes à fentes exposées pour maximiser le chevauchement entre un supermode TM₀ et des électrons libres co-propagateurs. Nous optimisons l'efficacité de couplage sur la longueur d'interaction pour obtenir un gain d'énergie électronique de 28,27 keV à partir d'une énergie d'impulsion optique de 0,22 nJ. Augmenter l'énergie cinétique de l'électron équivaut à augmenter le courant électrique ou à générer de l'électricité. Dans l'ensemble, nos résultats révèlent le potentiel d'un processus optique pour récolter l'énergie solaire en tant que substitut ou complément au processus électrique actuel.

Nos nouvelles conceptions d'appareils offrent déjà des applications directes dans divers domaines. Leurs applications séparées incitent à un développement ultérieur, qui est soutenu par la conception modulaire de notre circuit. Dans ce contexte, la thèse fournit un point de départ sur la feuille de route vers la récupération de l'énergie solaire sur une puce SiP..

Acknowledgements

All of the research work during my doctoral residency, including this thesis, was enabled by my supervisor, Prof. David V. Plant, to whom I am extremely grateful. His reliable support and patient guidance cultivates a culture of perseverance and accountability, which empowers his students to carve their own path by following their curiosity and interests. With Dave in my corner, I was able to draw on the insightful and enlightening counseling of my committee members, Prof. Mark Andrews and Prof. Andrew Kirk, who have shaped much of this thesis by helping me focus my creative energies. My growth process was fueled by James Skoric, Santiago Bernal, late Dr. Dan Petrescu, and Siddiqui Hakim who, as colleagues and close friends, have used their front row seats to provide me with necessary, difficult, and hilarious feedback. It was bolstered by Dr. Eslam El-fiky, Dr. Orad Reshef, Dr. Michel Lortie, Dr. Philip Roche, Prof. Ido Kaminer, Raphael Dahan, and Prof. Nicolas Abadia who fueled my breakthroughs and accommodated my dark days. It was enhanced by Dr. David Patel, Olivier Carpentier, Dr. Oscar Wang, Adam Helmy, Essam Berika, Dr. Mohammad Saber, Dr. Luhua Xu, Ezz Aboulez, Nathan Clairmonte, Schicheng Xu, Dr. Deng Mao, Amar Kumar, Maria Schiavone, Dr. Maxime Jacques, Dr. Zhenping Xing, Angus McLean, Dr. Alireza Samani, Dr. Mohamed Osman, Dr. Rui Li, Jinsong Zhang, Matthew Haines, and many others in the community of McGill University who work together in overcoming the struggles and needs of graduate students. My work was heavily supported by Maru Basanez, Kay Johnson, Brent Snow, and Melanie Gorman without whom our laboratories might fall apart. The courage to attempt a Ph.D. was instilled by my previous mentors Prof. Tom Smy, Prof. Jacques Albert, Prof. Steven McGarry, Anne Toscano, Andrew Parks, David Markin, Penka Matanska, Dr. Miriam Däubler, Dr. Victor Sanchez, Prof. Roberto Morandotti, and my teachers at St. Vincent's school who pulled me up enough to start climbing on my own.

McGill University is a wonderfully diverse ecosystem that acts as a career launchpad. By tapping into it, I had the opportunity to dive into both research and entrepreneurship, which inculcated complementary and highly transferable skills. I am particularly indebted to my co-founders, team members, and collaborators at Stocate, NiPAMS, and Patterns for their unwavering belief and relentless support, which gave me the confidence to figure out my own leadership style. Through these ventures, I have had the opportunity to supervise the Capstone theses of more than

120 undergraduate students who continue to awe and inspire me with their faith, tolerance, and enthusiasm.

On a personal note, I am indebted to my parents Yvette and Brian D’Mello for raising me to question everything and then navigating those increasingly difficult questions during my free-thinking phases. In the solitary, intellectual journey of a graduate student, resilience must be derived from good mental and physical health. My deep dives into research were possible because of a regular physical training regimen which maintained my focus, calm, and a steady endorphin flow. This discipline was inculcated by my coaches Sensei Kailas Lohar, Sensei Tham Chand, Zoltan Csepregi, Bill Meyer, Sensei Jason Bassels, and my parents who pushed me to exceed my capabilities and rarely let me give up when I failed. My progress was enhanced by caffeine and other substances, meditation and dancing, and award money, which I will continue to enjoy.

It is often said that the supporters of graduate students need their own support groups. I would like to express my deep appreciation for my close friends, counselors, and guides –Angela, Andrei, Juan, Krystina, Kathleen(s), Naomi, Evgenia, Zoe, Lauren(s), Jalomi, Louis, Catherine, Dion, Diego, Nioushah, Kenneth, and many others including my counselors and therapists – who talked me off cliffs (or balconies), pricked my isolation bubbles, accommodated my binge work sessions, held me to my beliefs, and eased the psychosomatic illnesses associated with stress, anxiety, depression, insecurity, burnout, and grief. Dissimilarly, I am learning to be grateful for the situations caused by the COVID-19 pandemic because they pushed me to find my self-love, self-worth, and priorities. Last and certainly not least, I would like to thank my extended family, both friends and relatives, of whom there are too many to name.

Associated Publications

This thesis is based on my original contributions to scientific evidence. It spans 5 journal articles [1-5] and 5 conference proceedings [6-10], which were not used to obtain any other degree. My contributions and those of my co-authors are stated for each relevant publication. The terminology is used with the following implications:

- “Conceiving the idea” implies producing the objective, outline, and expected results.
- “Designing” implies using research-based evidence to develop technical solutions, producing a proof of concept, and validating the accuracy of the results.
- “Running” implies debugging, testing, optimizing, and producing measurement results.

My main research contributions have been documented in 7 journal articles [1-5, 11, 12], 7 conference proceedings [6-10, 13, 14], 2 patents [15, 16] and 2 federal research grants [17, 18] among other publications, reports, proposals, and awards. For brevity, only first (or co-first) authored works are included in the following lists, in the order of their appearance in the thesis.

Journal Articles Related to this Thesis

[1] **Yannick D'Mello**, Orad Reshef, Santiago Bernal, Eslam El-fiky, Yun Wang, Maxime Jacques, and David V. Plant, "Integration of periodic, sub-wavelength structures in silicon-on-insulator photonic device design," *IET Optoelectronics*, vol. 14, no. 3, pp. 125-135, 2020.

I conceived the idea, designed the simulation study, and wrote the paper. The co-authors contributed by discussing the designs, running simulations, and revising the manuscript.

[2] **Yannick D'Mello**, Santiago Bernal, Dan Petrescu, Mark Andrews, and David V. Plant, "Solar Energy Harvesting Mechanisms of the Frustules of *Nitzschia Filiformis* Diatoms," *Optical Materials Express*, vol. 12, no. 12, pp. 4665-4681, 2022.

- Also featured in news articles: [19-24]

I conceived the idea, designed and ran the simulation and experimental study, and wrote the paper. The coauthors contributed by discussing the idea and design, running the simulations and experiments, and revising the manuscript.

[3] **Yannick D'Mello**, Eslam El-Fiky, James Skoric, Amar Kumar, Michael Hui, Yun Wang, Laurent Guenin, David Patel, and David V. Plant, "Compact, Angled Polarization Splitter: Characterization of Broadband Performance and Fabrication Tolerance," *IEEE Photonics Journal*, vol. 10, no. 6, pp. 1-12, 2018.

I conceived the idea, designed and ran the simulation and experimental study, and wrote the paper. The coauthors contributed by discussing the idea and design, running the simulations and experiments, and revising the manuscript.

[4] **Yannick D'Mello**, Santiago Bernal, Adam Helmy, Essam Berikaa, Olivier Carpentier, Imtiaz Alamgir, Md Samiul Alam, Eslam El-Fiky, and David V. Plant, "Standalone, CMOS-based Faraday rotation in a silicon photonic waveguide," *Optics Express*, vol. 30, no. 14, pp. 24602-24610, 2022.

I conceived the idea, designed and ran the simulation and experimental study, and wrote the paper. The coauthors contributed by running simulations and experiments, and revising the manuscript.

[5] **Yannick D'Mello**, Raphael Dahan, Santiago Bernal, Xihang Shi, Ido Kaminer, and David V. Plant, "Efficient coupling between free electrons and the supermode of a silicon slot-waveguide," submitted to *Optics Express*, 2023.

I conceived the idea, designed and ran the simulation study, and wrote the paper. The coauthors contributed by discussing the idea and design, running simulations, and revising the manuscript.

Conference Proceedings Related to this Thesis

[6] **Yannick D'Mello**, Dan Petrescu, James Skoric, Melissa Campbell, Mark Andrews, David V. Plant, "Characterization of the Photonic Response in *Nitzschia Filiformis* Phytoplankton," in *Conference on Lasers and Electro-Optics*, San Jose, California, 2018/05/13 2018: Optical Society of America, in OSA Technical Digest (online), p. JTh2A.96.

I conceived the idea, designed and ran the simulation and experimental study, and wrote the paper. The coauthors contributed by discussing the idea and design, running experiments, and revising the manuscript.

[7] **Yannick D'Mello**, Santiago Bernal, James Skoric, Dan Petrescu, Mark Andrews, David V. Plant, "Photonic Crystal Behavior of *Nitzschia Filiformis* Phytoplankton for Chlorophyll A Photosynthesis," in *Conference on Lasers and Electro-Optics*, San Jose, California, 2019/05/05 2019: Optical Society of America, in OSA Technical Digest, p. JW2A.121.

I conceived the idea, designed and ran the simulation and experimental study, and wrote the paper. The coauthors contributed by discussing the design, running simulations and experiments, and revising the manuscript.

[8] **Yannick D’Mello**, James Skoric, Eslam Elfiky, Michael Hui, David Patel, Yun Wang, and David V. Plant, "Numerical Analysis and Optimization of a Multi-Mode Interference Based Polarization Beam Splitter," in *COMSOL Conference Boston*, Boston, 2017: COMSOL.

I conceived the idea, designed and ran the simulation study, and wrote the paper. The coauthors contributed by discussing the design, running simulations, and revising the manuscript.

[9] **Yannick D’Mello**, Eslam El-Fiky, James Skoric, Yun Wang, Amar Kumar, David Patel, and David V. Plant, "Extremely Compact and Broadband Polarization Beam Splitter Enabled by Customized Port Angles," in *Frontiers in Optics / Laser Science*, OSA Technical Digest (Optical Society of America, 2018), paper JW4A.10.

I conceived the idea, designed and ran the simulation and experimental study, and wrote the paper. The coauthors contributed by discussing the idea, running simulations and experiments, and revising the manuscript.

[10] **Yannick D’Mello**, Michael Hui, James Skoric, Matthew Haines, Andrew Kirk, Mark Andrews, and David V. Plant, "Silicon-Organic-Hybrid Independent Simultaneous Dual-Polarization Modulator: Device Theory and Design," in *COMSOL Conference Boston*, Boston, 2017: COMSOL.

I conceived the idea, designed the simulation study, and wrote the paper. The coauthors contributed by running simulations and revising the manuscript.

Journal Articles Unrelated to this Thesis

[11] **Yannick D’Mello**, James Skoric, Shicheng Xu, Megan Akhras, Philip J. R. Roche, Michel A. Lortie, Stéphane Gagnon, and David V. Plant, "Autocorrelated Differential Algorithm for Real-Time Seismocardiography Analysis," *IEEE Sensors Journal*, vol. 19, no. 13, pp. 5127-5140, 2019.

[12] **Yannick D’Mello**, James Skoric, Shicheng Xu, Philip J. R. Roche, Michel Lortie, Stephane Gagnon, and David V. Plant, "Real-Time Cardiac Beat Detection and Heart Rate Monitoring from Combined Seismocardiography and Gyrocardiography," *Sensors*, vol. 19, no. 16, p. 3472, 2019.

Conference Proceedings Unrelated to this Thesis

[13] **Yannick D’Mello**, James Skoric, Lea Moukarzel, Siddiqui Hakim, and David V. Plant, "Wearable Fiber Optic Sensors for Biomechanical Sensing via Joint Angle Detection," in *2019 41st Annual International Conference of the IEEE Engineering in Medicine and Biology Society (EMBC)*, pp. 32221-32225, 23-27 July 2019.

[14] **Yannick D'Mello**, James Skoric, Siddiqui Hakim, Ezz Aboulezz, Nathan Clairmonte, Michel Lortie, and David V. Plant, "Identification of the Vibrations Corresponding with Heart Sounds using Vibrational Cardiography," in *42nd Annual International Conference of the IEEE Engineering in Medicine & Biology Society (EMBC)*, pp. 17-20, 20-24 July 2020.

Patents Unrelated to this Thesis

[15] **Yannick D'Mello**, Philip J. R. Roche, and Michel Lortie, "Method and Apparatus for Deriving Biometric Information using Multiple-Axis Seismocardiography," Patent Appl. CA2018051006, 2018.

[16] **Yannick D'Mello**, James Skoric, David V. Plant, and Michel Lortie, "Systems, Methods, and Devices for Non-Invasive and Continuous Hemodynamic Measurement," Patent Appl. 63/033,103, 2021.

Research Grants Unrelated to this Thesis

[17] David V. Plant*, **Yannick D'Mello***, and James Skoric, "Non-invasive Physiological Activity Monitoring System (NiPAMS)," Collaborative Research and Development grant, National Science and Engineering Research Council (NSERC), 2019. Monetary value: \$856,300 CAD. Duration: 4 years.

[18] David V. Plant*, **Yannick D'Mello***, James Skoric, and Siddiqui Hakim, "Non-invasive, Wearable Physiological Activity Monitors," Research Tools and Instruments grant, National Science and Engineering Research Council (NSERC), 2019. Monetary value: \$146,829 CAD. Duration: 2 years.

Along with the listed research contributions, I co-authored other journal articles, conference proceedings, technical reports, essays, and talks for these and other projects. The publications are listed [here](#) and the projects are described [here](#). They may be made available upon reasonable request.

Table of Contents

Abstract	i
Résumé.....	iii
Acknowledgements	v
Associated Publications	vii
Journal Articles Related to this Thesis.....	vii
Conference Proceedings Related to this Thesis	viii
Journal Articles Unrelated to this Thesis	ix
Conference Proceedings Unrelated to this Thesis.....	ix
Patents Unrelated to this Thesis	x
Research Grants Unrelated to this Thesis	x
Table of Contents	xi
List of Figures	xiv
List of Tables.....	xxiii
List of Acronyms and Abbreviations	xxiv
1. Introduction	1
1.1. Motivation.....	1
1.2. Thesis Organization	4
1.3. Original Contributions	5
2. Background	9
2.1. Predominance of SiP.....	9
2.2. Introduction to Sub-wavelength Structuring.....	13
2.3. Implications of Photonic Band Structure	16
2.4. Single-Mode Devices	22
2.5. Multi-mode Devices.....	30

2.6. Extension: Optimized Devices	35
2.7. Conclusion.....	38
3. Solar Energy Harvesting in Diatom Frustules	39
3.1. Introduction.....	39
3.2. Methods.....	43
3.3. Results.....	45
3.4. Discussion	54
3.5. Conclusion.....	57
4. Passive Polarization Splitter.....	58
4.1. Introduction.....	58
4.2. Design Methodology.....	60
4.3. Parameter Space Characterization.....	64
4.4. Fabrication and Experimental Results	66
4.5. Discussion	71
4.6. Conclusion.....	72
5. Active Polarization Rotation and Phase Delay	74
5.1. SiP Faraday rotator.....	74
5.2. EOP Dual-Polarization Modulator	83
5.3. Conclusion.....	93
6. Coupling to Free Electrons.....	95
6.1. Introduction.....	95
6.2. Device Design	97
6.3. Discussion	101
6.4. Conclusion.....	105
7. Conclusion.....	106

7.1. Overview	106
7.2. Summary of Original Contributions.....	107
7.3. Outlook.....	109
References	115
Appendix A. Supplementary Information for Chapter 3.....	150
A.1. Optical Confinement in Biosilica.....	150
A.2. Variations in the Photonic Band Structure of the Central Lattice	150
A.3. Resonances of the PhC.....	153
A.4. Analysis of Scanning, Near-field Optical Microscopy (SNOM) Images	154
A.5. Solar Energy Harvesting Mechanisms of the Frustule	156
Appendix B. Supplementary Information for Section 5.1	161
B.1. Polarization Mode Conversion in the Waveguide	161
B.2. Generation of an Electro-Magnetic Field	162
B.3. Resistive Heating in the Coil	163
B.4. Inductance of the Coil.....	163
B.5. Characterization of Design Variations.....	164
B.6. Vertical Axis Coils.....	169
B.7. Additional Methods	169
Appendix C. Supplementary Information for Chapter 6.....	172
C.1. Experimental Setup.....	172
C.2. Circuit Layout	173
C.3. Optical Pulse Parameters	174
C.5. Interaction Length.....	178
C.7. Methods.....	185

List of Figures

Figure 1.1. Schematic of a circuit design to: (1) capture and retain light, (2) split polarizations, (3) rotate one polarization, (4) phase match both branches, (5) combine both branches, and (6) transfer the energy to free electrons. Red and blue arrows indicate the fundamental transverse electric (TE_0) and transverse magnetic (TM_0) modes, respectively. The yellow sun on the left represents the optical input of solar energy and the moving black dot on the right represents the electrical output of traveling electrons. This also serves as a graphical abstract of the thesis. 3

Figure 2.1. Wavelength compression in a material. (a) Two waves of the same frequency in a low (blue) and high (red) refractive index material, and at an angle of θ with respect to each other. The wavefronts (dashed, grey) indicate that the waves are phase-matched at this angle. (b) Electric field distributions of the fundamental (top) and first order (bottom) modes in a grating [72]. 17

Figure 2.2. Band diagram of an SOI grating for the in-plane polarization with a pitch of 500 nm, DC of 0.5, and thickness of 220 nm. The propagation (blue), reflection (red) and diffraction (green) regimes are also shown..... 19

Figure 2.3. Cross-sectional profiles of the magnitude of the electric field component of the fundamental (a) TE and (b) TM modes confined to a Si waveguide with a thickness of 220 nm and a width of 500 nm surrounded by SiO_2 cladding..... 23

Figure 2.4. Band diagram of a corrugated waveguide (red, and middle inset) and grating (green, and bottom inset) with a pitch of 210 nm and DC of 0.5. The light lines of the cladding (black) and core (blue) are also shown. 24

Figure 2.5. Band diagram of a SOI grating for TE (solid red) and TM (dashed blue) light with a pitch of 400 nm and DC of 0.5. The insets show a (top) profile view and (bottom) top-down view of its implementation in a GC..... 25

Figure 2.6. (a) Band diagram of a SOI Bragg grating for TE (solid red) and TM (dashed blue) modes with a pitch of 300 nm, DC of 0.5, width of 500 nm, and 125 nm corrugations [40]. The insets show its implementation in (top) a Bragg grating that (bottom) reflects 1550 nm light. (b) Simulated degradation of its optical response (dashed and dotted lines) due to increased lithographic smoothing [40]..... 26

Figure 2.7. Band diagram of a SOI square lattice with a pitch of 360 nm and increasing hole diameters of 70 nm (solid), 90 nm (dashed), 110 nm (dotted). The insets show its implementation in (top) a PhC cavity waveguide supporting (bottom) 1550 nm pulse propagation. 27

Figure 2.8. Band diagram of a SOI SWG for TE (solid red) and TM (dashed blue) polarizations with a pitch of 200 nm and DC of 0.5. The insets show its implementation as (top) a SWG edge coupler [62] supporting (bottom) 1550 nm pulse propagation. 28

Figure 2.9. Band diagram for a SOI SWG for TE (solid red) and TM (dashed blue) polarizations with a pitch of 250 nm and DC of 0.5 [71]. The insets show its implementation in (top) a tilted SWG waveguide supporting (bottom) 1550 nm pulse propagation..... 30

Figure 2.10. Band diagram of a SOI SWG for TE (solid red) and TM (dashed blue) polarizations with a pitch of 190 nm and DC of 0.5. The inset shows its implementation in a MMI-based 2×2 intensity splitter [120]..... 32

Figure 2.11. Integration of a SWG in the design of a 1×2 MMI variable intensity splitter [41].
..... 32

Figure 2.12. Integration of a SWG in the design of a PBS based on the 2×2 MMI [65] shown in Figure 2.10..... 33

Figure 2.13. Band diagram of a SOI SWG for TE (solid red) and TM (dashed blue) polarizations with a pitch of 220 nm and DC of 0.5. The inset shows its integration in the design of a PBS with a 7° tilt [121]..... 34

Figure 2.14. Band diagram of a PhC for TE (solid red) and TM (dashed blue) polarizations with a 390 nm pitch hosting a triangular lattice of holes of radius of 117 nm. The inset shows its integration in the design of a MMI-based PBS [124]. 35

Figure 2.15. (a) Band diagram of a biosilica frustule with square (purple) and triangular (green) lattice configurations with pitches of 330 nm and 300 nm respectively, for water holes of 80 nm diameter. (b) The absorption spectrum of chlorophyll A with peaks at 449 nm and 660 nm [137].
..... 36

Figure 2.16. Schematics of reverse engineered PBS devices with relatively small footprints of (left) 2.8×2.8 μm [141], and (right) 2.4×2.4 μm [143]. 37

Figure 3.1. Architecture of the frustule. (a) SEM of a frustule. (b) Exploded 3D CAD model of the frustule. (c) SEM of a side. (d) Central region of the valve. (e) Schematic of the cross-section. (f) Tail. 46

Figure 3.2. Ensemble averaged photonic band structure of the central lattice. (a) Central region of the valve with a (b) zoom-in of the lattice showing (green) longitudinal and (yellow) lateral spacing. (c) Measured hole diameters, (d) longitudinal and lateral spacing, and (e) angles between holes. (f) Photonic band diagrams and (g) corresponding DOS of each triad of holes with an ensemble average showing the effective optical response. In (f), the shaded gray area indicates the light cone and inset shows the adjacent guided modes. 47

Figure 3.3. Microscope images of the interior of a valve. (a) SEM, (b) AFM with (c) a zoomed-in region, (d) DFM, (e) SNOM at a wavelength of 660 nm with (f) a zoomed-in region. The SNOM and AFM images were obtained concurrently for (b) and (e) as well as (c) and (f). 49

Figure 3.4. Optical response of the region around the raphe. (a) The array of inner protrusions underneath the raphe. (b) Accumulation of yellow light at these protrusions (corresponding to the red box in Figure 3.3(d)). (c) 1D photonic band diagram of this region. 50

Figure 3.5. Optical response of the tail. (a) The tapered, curvature of the tail with insets at the red slices showing the evolution of an incident plane wave as it butt-couples to the frustule. (b) Mode profile of the butt-coupled, confined light propagating longitudinally along the frustule. (c) Transmission spectrum at each of the red slices in (a). 51

Figure 3.6. Optical response of the girdle. (a) The array of holes along the girdle. (b) Diffraction of light by the holes during longitudinal propagation after (left) 27 fs and (right) 40 fs. (c) 1D photonic band diagram of the array of holes. 52

Figure 3.7. Optical response of the frustule. (a) Racetrack hosting lateral circulation around the cross-section shown in Figure 3.1(e). (b) Entire frustule with the blue arrows indicating the various directions of light propagation including lateral circulation, diffraction by the DPhC of the central lattice, diffraction by the row of holes in the girdle, resonance at the raphe, and butt-coupling into the tail. (c) Field distribution of butt-coupling at the tail of the frustule. 53

Figure 4.1. (a) PBS device geometry with the addition of an optional waveguide bend. Interference pattern simulation results for (b) TE and (c) TM fundamental modes. Output waveguides are placed at the self-imaging length of the MMI feature to collect TE polarized light at the bottom in (b) and TM polarized light at the top in (c). 62

Figure 4.2. TM port optimization for (a) TM transmission and (b) TE crosstalk as functions of the position and width of the periscope. The black dots represent the two parameter sets that were

chosen for fabrication. Periscope offset and width parameters chosen for fabrication were: [54 μm , 6.5 μm] and [55.7 μm , 5.5 μm]. 65

Figure 4.3. TE port optimization for (a) TE transmission and (b) TM crosstalk as functions of MMI length and TE Port offset. The four black dots represent the four parameter sets investigated experimentally. MMI length and TE Port offset parameters chosen for fabrication were: [67.25 μm , 0.875 μm], [67.5 μm , 0.875 μm], [67.5 μm , 0.9 μm], [67.25 μm , 0.9 μm]. 65

Figure 4.4. Optical microscope image of the on-chip fabricated PBS connected to input and output grating couplers for testing. Black spots are due to the microscope lens and do not appear on the chip..... 66

Figure 4.5. TE (blue) and TM (green) transmission spectra for all 72 measurements at the (a) TE and (b) TM ports. The darker lines show the mean of all spectra. The white background indicates wavelengths within the C-band range. The IL does not exceed 1 dB in any case, and positive IL values are attributed to device variability or errors in measurement..... 67

Figure 4.6. Extinction ratios of all PBS devices categorized by parameter. The plots show the average ER for all devices with a specific (a) Input Angle, (b) TM Offset and Periscope Width, (c) TE Offset, (d) Bend Radius, and (e) MMI Length. (f) The Best and Worst Performance are also shown. Blue lines correspond to ER at the TE port (TM crosstalk subtracted from TE transmission) and green lines correspond to ER at the TM port. The white background indicates wavelengths within the C-band range. The thick lines represent the average over all 72 variations. 68

Figure 4.7. Characterization of PBS response in the C-band (1530-1565 nm) by varying the input parameters (a) TM periscope offset, (b)TM periscope width, (c) MMI length, (d) TE port vertical offset, (e) input waveguide angle, and (f) bend radius. Each circle represents the worst-case insertion loss for a specific polarization at a specific port. Hence worst-case TE transmission at the TE port for each device is shown in blue, TM transmission at the TM port in yellow, TE crosstalk at the TM port in green, and TM crosstalk at the TE port in violet..... 69

Figure 4.8. Transmission spectrum measurements for the optimal design at the (a) TE and (b) TM ports corresponding to the results in Table 4.2..... 71

Figure 5.1. Design of an electromagnetic coil surrounding a strip waveguide on 3 sides. The Si waveguide (red) is surrounded by the coil made of Al (grey), n-Si (maroon) and TaN (blue) with a core made of Al and TiN (green). The SiO₂ cladding is not shown. (a) Schematic of the front view of a single winding. An input electric current (white arrows) enters from behind and circulates

clockwise through the layers: Al→TaN→Al→TaN→Al→TaN→n-Si→TaN→Al→TaN→n-Si. It then exits the front of the winding from the n-Si layer and enters the next winding through a TaN via (not shown). (b) Side, (c) bottom, and (d) perspective views of the simulated coil with 5 windings and a w_{gap} of 1 μm . Axes units are in μm 76

Figure 5.2. Electrical response of the coil. (a) Simulation of current density through the model coil at an input current of 14 mA. (b) Experimentally measured resistance per unit coil length of 11 device variations (dots) fitted to the simulation result (solid, black line). The labelling convention uses the device number and coil length, as given in Table B.2. The variations include both coil widths and all 3 coil lengths. Axes units are in μm for the device model. (c) Simulation of temperature distribution in the coil at an input current of 14 mA. (d) Temperature in the waveguide across the device length caused by resistive heating in the coil. 78

Figure 5.3. Simulated B field around the coil. (a) Front view, (b) side view, and (c) top view for the coil with a gap width of 1 μm . (e) Front view, (f) side view, and (g) bottom view of the BY component of the same design. In each plot, the positions of its orthogonal cross-sections are visible. Axes units are μm . (d) Both B and BY magnitudes along the waveguide centerline for increasing input currents and a w_{gap} of 1 μm . The interaction length is marked by vertical, black, dashed lines. The black, solid line in the center indicates the location of the image in (a) and (e). Inset: Distribution of BY at the negative peak at a propagation length of 30 μm (indicated by the black, dotted line) with the same colour scale as (e). Axes units are in μm for the device model. (h) BY_{dy} integrated over the propagation length for both gap widths of 0.5 μm and 1 μm , as well as for 160 nm above the coil (equivalent to the distance between the Al strip and the waveguide centerline). Inset: Difference in BY_{dy} between w_{gap} for the positive and negative phases of the integrated BY field. 80

Figure 5.4. Faraday rotation in the device. (a) Rotation of the TM_0 mode at a wavelength of 1310 nm in a strip waveguide along the propagation length for increasing input currents. The beginning and end of the interaction region are marked as black, dashed lines for reference. (b) Spectral dependence of the total accumulated rotation of each mode and each waveguide type for the longest device length of 1097.4 μm at an input current of 14 mA. 82

Figure 5.5. Electric polarization of an EOP under an applied electric field. The thick lines represent the electrodes, the black arrows show the induced electric moment, and the green arrow indicates the oscillation of the electric field of polarized light propagating down the Z axis. In (a),

the molecular electric moments oriented along the positive X axis will interact directly with TE polarized light (E-field parallel to X axis) since they are parallel, whereas in (b), the induced moment only weakly interacts with TM polarized light (E-field parallel to Y axis). Hence, orthogonal polarizations of the optical signal propagating through a thermally poled EOP will experience significantly different refractive indices..... 85

Figure 5.6. Three-dimensional view of proposed configuration for dual polarization modulation. The signal electrodes are represented in red and ground electrode in black. As both ground electrodes are electrically equivalent, they are considered to be a single electrode so as to reduce fabrication complexity. The EOP core is shown in blue, and surrounded by concentric glass cladding..... 86

Figure 5.7. Applied electric field distribution along a cross-section of the EOPM with both electrodes active and (inset) corresponding electrode map using the format depicted in Figure 5.5. 88

Figure 5.8. Fundamental mode profiles for CL1/PMMA (left) and DR1/PMMA (right). 90

Figure 5.9. Phase shift in propagating X-polarized light (E_x) as a function of waveguide length when only the X-axis electrode is active, and corresponding static phase shift induced in orthogonally polarized (E_y) light..... 91

Figure 5.10. Phase change as a function of applied voltage along the X-axis. 92

Figure 5.11. Phase change as a function of waveguide length when both electrodes are active. 92

Figure 6.1. On-chip layout of the device which hosts an optical supermode to overlap with a free-electron beam. (a) Top view of the device layout consisting of an input grating coupler (GC) connected to a 90:10 splitter that sends 10% to a Bragg grating (BG) for alignment feedback and 90% to a slot waveguide via a mode evolution region (MER). An additional GC is placed at a fixed offset from the input GC for stronger feedback during coarse alignment. (b) Top-down view of the slot waveguide accommodating an eBeam that converges in the slot (the MER is not shown). (c) Top-down view of the MER with the simulated electric field distribution, $E_{0,z}$, showing how the input TM_0 mode is converted to the supermode of the slot waveguide. (d) Front view of the slot waveguide at the point of entry or exit of the eBeam. (e) Front view of the slot waveguide with the simulated electric field distribution, $E_{0,z}$, of the converted supermode..... 98

Figure 6.2. Optimization of coupling strength per photon for the given slot waveguide dimensions. (a) Maximum achievable interaction length, L_{eff} , within the range of available eBeam diameters, d_e , and heights, h_e . (b) Coupling constant per photon, g_{Qu} , over the same parameters. A red dot indicates the maximum g_{Qu} . The blank regions indicate inadmissible parameters for which the eBeam was blocked by the sidewalls or BOX. The discontinuity in both plots is caused by switching the electron sources between thermionic and photoemission modes in the UTEM as explained in Appendix C. (c) Distribution of the longitudinal electric field component, E_z , of a supermode hosted by the slot waveguide. The solid and dotted red circles indicate the spot size at the focal point and at the ends of the slot, respectively. Dimensions of the slot waveguide are $t_{Si} = 220 \text{ nm}$, $w_{Si} = 300 \text{ nm}$, and $w_{gap} = 200 \text{ nm}$, which results in a $g_{Qu} = 0.4266$ for a supermode at $\lambda = 1550 \text{ nm}$ matching $\epsilon_e = 196 \text{ keV}$ 100

Figure 7.1: (a) 3D schematic of the fabricated ring resonator synchrotron, and (b) top-down view of a fabricated layout with four waveguides of different widths to extract wavelengths of light generated in the ring (fabricated in the SiEPIC5 tapeout). (c) Layout of a ring with four electrodes and a concentric, dual layer, metal coil for B-field generation (fabricated in the SiEPIC6 tapeout). 114

Figure A.1. Mode confinement in the frustule. (a) Fundamental mode inside the valve. (b) Lower order modes inside the girdle. (c) Higher order modes inside the girdle. 150

Figure A.2. Dependence of the photonic band diagram on the lattice parameters. Variations in (a) symmetry (corresponding to angle), (b) refractive index, n , (c) thickness, t , (d) spacing, a , (e) diameter, d , and (f) polarization. 151

Figure A.3. Effect of resonances on the optical response. (a) Collapsed or open pseudogaps and band crossings with (b) their corresponding DOS. (c,d) Transient response of a resonance (represented by the resonant cavity) showing how (c) an optical pulse undergoes (d) decay due to the retention of light inside the cavity..... 154

Figure A.4. Model of the optical response of the frustule. (a) Photonic circuit of the frustule showing (yellow arrows) incident PAR, (black arrows) light exchanged between different regions and (green arrows) absorption by the chloroplasts. (b) Electrical equivalent circuit with the chloroplasts, frustule, and PAR represented as a load resistor, capacitor, and variable power supply, respectively. (c) Contribution of the frustule to the absorption by the chloroplasts depending on the amount and distribution of irradiation on the cell. The slope represents the

difference in the exposed surface area. The contribution of the frustule is depicted as orange vertical arrows in specific cases. The maximum absorption α_{\max} was reached under an irradiance of $750 \mu\text{mol photons m}^{-2} \text{s}^{-1}$ 157

Figure B.1. Schematic of Faraday rotation illustrating non-reciprocal polarization rotation (violet). (a) clockwise rotation of the plane of polarization of light when propagating (green) in the direction of the magnetic field (red) and (b) counter-clockwise rotation when propagating in the opposite direction. 162

Figure B.2. Top-down photographs of (a) the fabricated SiP chip with 15 variations of the device design as described in Table S2, (b, d) zoom-in of the devices, (c) the coils after breakdown. The different colours are due to the combination of microscope and illumination which was optimized for each image. 166

Figure B.3. Distribution of the electric field magnitudes at a wavelength of 1550 nm. TE_0 mode in the (a) strip and (b) slot waveguide, and TM_0 modes in the (c) strip and (d) slot waveguide. 167

Figure B.4. Characterisation of different modes under study at different wavelengths. (a) Effective index of the TE_0 and TM_0 modes in strip and slot waveguides (solid and dashed lines, left axis) and the half-beat length between the fundamental modes of the slot and strip waveguides (dotted lines, right axis). The half-pitch length of the coil is also shown for reference. (b) Verdet constant for the same two fundamental modes of each waveguide type. 167

Figure C.1. Supermode characteristics for each variation of the waveguide cross-section. (a)-(j) Variation of supermode 2 properties with slot parameters at wavelengths of (a)-(e) 1310 nm and (f)-(j) 1550 nm. (k)-(t) Variation of supermode 3 properties with slot parameters at wavelengths of (k)-(o) 1310 nm and (p)-(t) 1550 nm. In each set, the first two columns show vp and vg along with horizontal, black, dashed lines indicating the limits of ve . The third column of each set shows the maximum E_z field at the center of the waveguide. 177

Figure C.2. Coupling results at $\lambda = 1310 \text{ nm}$ for (a-g, top) supermode 2 and (i-o, bottom) supermode 3 hosted by a waveguide with thickness of 220 nm and varying wall and gap widths. Optimal eBeam parameters are shown as (a,i) initial KE, KE_i , (b,j) diameter, de , and (c,k) height, he . They overlap over (d,l) the effective interaction length, L_{eff} , to maximize (e,m) the coupling per photon, gQ_u , to produce the calculated (f,n) energy gain, $\Delta\epsilon_e$, and (g,o) acceleration gradient, G 184

Figure C.3. Coupling results at $\lambda = 1310$ nm for (a-g, top) supermode 2 and (i-o, bottom) supermode 3 hosted by a waveguide with thickness of 220 nm and varying wall and gap widths. Optimal eBeam parameters are shown as (a,i) initial KE, KE_i , (b,j) diameter, d_e , and (c,k) height, h_e . They overlap over (d,l) the effective interaction length, L_{eff} , to maximize (e,m) the coupling per photon, g_{Qu} , to produce the calculated (f,n) energy gain, $\Delta\epsilon_e$, and (g,o) acceleration gradient, G 184

List of Tables

Table 4.1. Parameter values used for the experimental device performance characterization.	66
Table 4.2. Parameter values corresponding to optimal design, based on the characterization parameters in Table 4.1.	70
Table 4.3. Comparison of PBS designs including this work. The minimum overall extinction ratio is given with its corresponding bandwidth. The fabrication steps refer to the number of etch, deposition, or metallization (m) steps expected to fabricate the device on-chip.	71
Table 5.1. Characteristics of DR1/PMMA and CLD1/PMMA using [270, 272-274].	87
Table 5.2. Waveguide parameters for DR1/PMMA and CLD1/PMMA EOP cores with a borosilicate glass cladding, at a propagating wavelength of 1550nm [273, 274].	89
Table 6.1. Comparative analysis of device designs enabling electron-photon coupling. Brackets indicate values which we calculated because they were not reported. Wg: waveguide, *: designed but not demonstrated, \perp : perpendicular incidence, \parallel : parallel incidence.	103
Table B.1. Inductance of the six fabricated SiP coils as per design variations.	164
Table B.2. Parameters of the design variations that were fabricated on-chip.	165
Table B.3. Rotation of the polarization state for the evaluated devices. The first column indicates the device number (#) corresponding to Table B.2, which also implies the type of waveguide used. Values are shaded from white to green to reflect the smallest to largest angles of rotation.	168

List of Acronyms and Abbreviations

Note: the green text color of acronyms is intended to help a reader navigate the thesis.

Acronym	Term
1D	One Dimensional
2D	Two Dimensional
3D	Three Dimensional
AC	Alternating Current
AFM	Atomic Force Microscopy
BG	Bragg Grating
BOX	Buried Oxide
BW	BandWidth
CAD	Computer Aided Design
CMOS	Complementary Metal-Oxide-Semiconductor
DC	Directional Coupler / Duty Cycle
DFM	Dark field microscopy
DLA	Dielectric Laser Accelerator
DOS	Density Of States
DPhC	Disordered Photonic Crystal
DUVL	Deep Ultra-Violet Lithography
EAP	Electro-Active Polymer
eBeam	Electron Beam
EBL	Electron-Beam Lithography
EDX	Electron Diffraction Spectroscopy
EJ	Exa-Joules
EOP	Electro-Optic Polymer
ER	Extinction Ratio
ES	Electrostatic
EWBE	Electromagnetics Waves, Beam Envelope
EWFD	Electromagnetics Waves, Frequency Domain
FDTD	Finite Difference Time Domain
FEL	Free Electron Laser
FEM	Finite Element Method
GC	Grating Coupler
IL	Insertion Loss
Laser	Light amplification by stimulated emission of radiation
LDOS	Localized Density Of States
LN	Lithium Niobate
MER	Mode Evolution Region
MMI	Multi-Mode Interferometer
MO	Magneto-Optic
MZI	Mach Zehnder Interferometer
MZM	Mach Zehnder Modulator
<i>Nf</i>	<i>Nitzschia filiformis</i>
NiPAMS	Non-invasive physiological activity monitoring system

Acronym	Term
NR	Non-Reciprocal
NRPS	Non-Reciprocal Phase Shift
PAR	Photosynthetic Active Radiation
PBS	Polarization Beam Splitter
PhC	Photonic Crystal
PINEM	Photon Induced Near-field Electron Microscopy
PMC	Polarization Mode Conversion
PMMA	Polymethylmethacrylate
QPM	Quasi Phase Matching
SEM	Scanning Electron Microscopy
Si	Silicon
SiEPIC	Si Electronic-Photonic Integrated Circuit
SiN	Silicon Nitride
SiO ₂	Silicon dioxide
SiP	Silicon Photonics
SNOM	Scanning, Near-field Optical Microscopy
SOI	Silicon-On-Insulator
SWG	Sub-Wavelength Grating
TE	Transverse Electric
TM	Transverse Magnetic
UTEM	Ultrafast Transmission Electron Microscope
UVL	Ultraviolet Lithography

1. Introduction

“Each generation must, in relative opacity, discover its mission, fulfill it, or betray it.”

– Frantz Fanon

Electricity, healthcare, and food are necessities in modern society. However, our current system cannot sustainably provide: (i) renewable energy, (ii) autonomous health monitoring, and (iii) essential goods and services, to every person. During my time in the Plant group at McGill University, I have had the opportunity to initiate and lead three ventures which address these limitations. The first one is reported in this thesis [1-10], which investigates optical methods to potentially overcome the electrical limitations of harvesting solar energy. The other two are reported elsewhere as NiPAMS [11, 12, 14-16, 25-29] and Stocate [30], respectively.

In this chapter, the premise and overview of the thesis is introduced. The motivation behind pursuing this line of questioning is presented in section 1.1. The organization of the remainder of the thesis is outlined in section 1.2. Finally, a summary of the original contributions of this thesis to scientific knowledge is listed in section 1.3.

1.1. Motivation

In 2021, the global energy consumption was 595.15 exajoules (EJ) of which only 13.5% was obtained from renewable sources [31]. In comparison, the amount of solar energy reaching the surface of the Earth is 3.4 million EJ per year (of which 1% is absorbed by photosynthesis) [32]. Solar energy has the potential to satisfy global consumption many times over. However, the technology still faces limitations which increase the price per watt of capture, conversion, and retention. The most common form of solar energy generation is via photovoltaic panels which use a silicon (Si) absorption layer. In this thesis, we address the following three general limitations of such panels.

First, solar panels capture direct sunlight. They must be configured so that the orientation of the panel is aligned with the position of the sun, depending on the time of day. Panels require the surface to be regularly cleaned so that light is not scattered from dust particles [33]. Additionally, the amount of sunlight that is directly incident on the panel depends on weather conditions, including cloud cover. In this context, it is worth exploring natural or alternative methods to harvest ambient sunlight. Since photosynthesis already absorbs 8 times as much energy as global consumption [34], we look to nature for a solution. The most prolific photosynthetic organisms

are unicellular diatoms which grow a biosilica shell whose sub-wavelength architecture is speculated to aid photosynthesis in the cell [35]. In chapter 3, we analyze the frustules of the diatom species *Nitzschia filiformis* (*Nf*) to identify mechanisms that are applicable to harvesting solar energy on-chip.

Second, in solar panels, only a limited spectrum of the captured light is converted into electricity. When light enters the Si lattice, it is absorbed by electrons which transition from the valence to the conduction band to produce electric current. The electronic bandgap of Si determines its absorption bandwidth and consequently, the spectral window of light that can be absorbed [36]. To overcome this limitation, ongoing research examines perovskites, quantum dots, photosynthesis [37], and other methods of solid-state energy conversion. However, bound electrons are subject to material constraints which limit the absorption bandwidth. Therefore, in this thesis, we explore the interaction between confined light and free electrons. In chapter 6, we report a device design that optimizes their quantum coupling efficiency.

Third, once converted to electricity, the moving electrons cannot be retained in the same space or state because they repel each other and are fermions. Instead, the energy must be converted to other forms, such as chemical (e.g., batteries) or potential energy (e.g., water reservoirs). Inefficiencies in the energy conversion and storage process reduce the value of renewable energy sources [38]. Additionally, life cycle analyses of commercial batteries do not find them to be sustainable yet [39]. In this context, it is worth exploring methods to retain the original optical energy so that it can then be converted when needed. Such a system would help smoothen the intermittent supply of solar energy as well as be able to leverage ongoing advances in conversion methods. Additionally, high density energy storage is possible due to the bosonic nature of photons. It would only be limited by the energy capacity or damage threshold of the material. In chapters 2 and 3, we analyze resonant systems that are capable of slowing down or circulating light include rings and photonic crystals (*PhCs*) [1, 2], which could potentially be developed for energy storage.

In this context, harvesting solar energy appears to be limited by electrical material constraints at multiple stages of the process, but the photonic analogs of these stages do not appear to face the same limitations. This raises the question of whether it is possible to circumvent the limitations of the electrical process by instead employing an optical process. In our view, such a process would comprise the following stages: (i) capture ambient light into confined modes, (ii) split the modes

based on their polarization, (iii) rotate one polarization to match the other, (iv) match the phases between both branches, (v) combine them, and (vi) transfer the optical energy to the kinetic energy of free electrons. These stages form the opto-electronic circuit shown in Figure 1.1, which implicitly depicts our approach to harvest solar energy via an all-optical process.

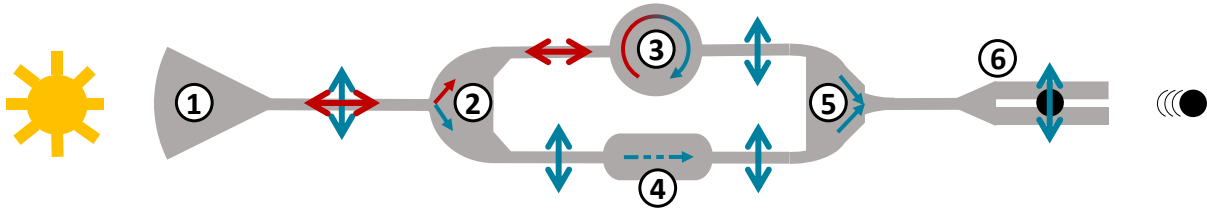


Figure 1.1. Schematic of a circuit design to: (1) capture and retain light, (2) split polarizations, (3) rotate one polarization, (4) phase match both branches, (5) combine both branches, and (6) transfer the energy to free electrons. Red and blue arrows indicate the fundamental transverse electric (TE_0) and transverse magnetic (TM_0) modes, respectively. The yellow sun on the left represents the optical input of solar energy and the moving black dot on the right represents the electrical output of traveling electrons. This also serves as a graphical abstract of the thesis.

In this thesis, we present a device design for each of the circuit components (1-6) in Figure 1.1 along with recommendations on how to improve or test the designs so that they can be connected into the proposed circuit. For each design, we select its operating wavelengths according to the needs of the study since the scale-invariance of electromagnetics (described in section 2.1.2) allows for our methods to still inform the development of future devices even if their operating wavelengths are different. Opto-electronic devices are commonly fabricated on Si photonic (SiP) chips [40], which consist of a Si core with SiO_2 cladding and Complementary Metal-Oxide-Semiconductor (CMOS)-based materials for additional functionality. Our scheme in Figure 1.1 is therefore targeted as a Si electronic-photonic integrated circuit (SiEPIC) to point to its potential commercial viability. Si-based microtechnology already produces key, opto-electronic components for telecommunications, solar energy generation, microscopy, sensing, and medicine. Its maturity, scalability, and the abundance of Si, ensure its technological sustainability. However, the performance of these devices is often constrained by material properties and architecture. Although the field of SiP has experienced an explosive growth in recent decades, progress is limited by fabrication constraints combined with underutilized material properties due to a lack of understanding concerning the light-matter interactions that govern the performance of SiP devices. In this thesis, we develop design processes which are rooted in the fundamental physical phenomena that dictate the functionality and performance of these devices. This creates the

opportunity to redesign devices using recent advances in lithography techniques, metamaterials, and quantum opto-electronics, which can leverage and expand upon the versatility of SiP. It provides the basis for a new avenue of investigation into fabrication-tolerant, on-chip systems which efficiently harvest sunlight.

1.2. Thesis Organization

This thesis is organized according to the path of light flowing through the components in Figure 1.1. Following this chapter, a background of SiP device designs is presented in Chapter 2. This overview places an emphasis on sub-wavelength structures and their ability to engineer the propagation, dispersion, and diffraction of light. It lays the groundwork for the device designs that follow.

The sub-wavelength architecture of Nf frustules is analyzed in Chapter 3. We demonstrate a combination of experimental and numerical techniques to investigate the optical behaviour of the frustule and therefore infer its contributions to solar energy harvesting in the cell. The overall contribution to photosynthesis was modeled by drawing an analogy between the frustule and a SiO₂-based photonic circuit. We therefore show how ambient light is captured into optical modes in the frustule.

A SiP polarization beam splitter (PBS) is demonstrated in Chapter 4. This device splits the fundamental transverse electric (TE₀) and transverse magnetic (TM₀) modes into two separate branches. We show how the design geometry employs large feature sizes and a genus 0 topology to ensure fabrication tolerance over multiple variations.

These two fundamental modes are then converted into the same mode in Chapter 5. This includes two device designs which can separately rotate the polarization and shift the phase of either fundamental mode, thereby matching the two modes so that they can be subsequently merged. Although neither design is ready for use in a circuit yet, we identify methods to improve the designs as well as suggest alternatives for the sake of developing a minimum viable product.

Once merged, the mode is coupled with free electrons in Chapter 6. We characterize the performance for different modes hosted by the desired waveguide at both of the commonly used center wavelengths of 1310 nm and 1550 nm corresponding to the lowest dispersion and loss, respectively, in telecommunications systems. The design overlaps an optical mode with free electrons to transfer optical energy to the kinetic energy of the electrons.

Finally, the thesis is concluded in Chapter 7. The key accomplishments are summarized along with recommendations for next steps and future work.

1.3. Original Contributions

To our knowledge, this thesis proposes the first ever SiP circuit which could be used to harvest solar energy. Its components are based on our original research into unique device functionalities. The following list summarizes the original contributions to scientific evidence that are reported in the thesis:

- To set the groundwork, we first review how periodic, sub-wavelength structures are used for passive wave manipulation in SOI device design [1]. In order of dimensionality, we analyze 1D and then 2D devices for propagation, reflection, and diffraction depending on the pitch. The optical response is evaluated for both orthogonal polarizations at the telecom wavelengths of 1310 nm and 1550 nm. Our analysis identifies common design elements between the devices reported in the literature based on the sub-wavelength spatial arrangement of the Si core. From these elements, we extract a straightforward method for engineering the dispersion of a device using photonic band diagrams. This method consists of a toolkit of techniques to engineer the dispersion of light, which addresses a gap in the literature concerning the design process of integrating sub-wavelength features in conventional SiP device geometries. Addressing this gap was a prerequisite for other aspects of the research reported in this thesis [2, 4, 5, 7, 41]. Furthermore, we show how this method can be used to interpret the functionality of a device as well as reverse engineer device geometries which were designed using optimization methods such as inverse design, evolution, or machine learning. Notable benefits include a fine control of dispersion, wavelength and polarization selectivity, and broadband performance.
- To investigate sunlight harvesting in naturally occurring photonic structures, we analyze the optical behaviour of *Nf* diatom frustules [2, 6, 7]. For the optical analysis, we developed a comprehensive toolkit comprising 4 microscopy techniques with complementary simulations [6] which was informed by the previously described process for connecting photonic band diagrams to sub-wavelength features [1]. We showed how the varying PhC lattice configurations exhibited by the valve affected its optical response [7]. Based on these results, we identify and analyze a number of localized

optical functionalities across the frustule and map them to the overall optical response, resulting in one of the first comprehensive analyses of a whole frustule. To determine the combined effect of the different optical processes at work, we develop the first model of a frustule by treating it as an ellipsoidal optical cavity embedded with these functionalities. Our model shows how the individual optical functionalities might combine to yield three solar energy harvesting mechanisms of capture, redistribution, and retention, which enhance photosynthesis in the cell.

- To split the captured, confined modes based on their polarization, we demonstrate a SiP PBS [3, 8, 9]. In simulations, we optimize its performance for the telecommunications C-band (wavelength range from 1530 nm to 1565 nm) [8]. The device employs an angled input waveguide connected to a multi-mode interferometer (MMI) to extract the images corresponding to the TE and TM polarizations from a single, compact geometry. We demonstrate a novel method to reduce the size of a MMI-based PBS while maintaining its bandwidth and tolerance by modifying the geometry accordingly. The geometry is constrained a topology of genus 0, which implies that the device consists of a single Si block without any holes or subwavelength gratings (SWG). We show that this constraint improves the robustness of the device because it is less susceptible to performance variability caused by fabrication errors and thermal or mechanical stress. We also show that an angled input enables the collection of TM light above the MMI, thereby eliminating the need to cascade successive MMIs as in previous designs. Our design process results in a relatively compact device of length 67.5 μm and width 4 μm , while maintaining a relatively feature sizes comparable to the waveguide width and a consistent performance over 72 parameter variations. We measure an average insertion loss of 2 dB with extinction ratios of at least 13.96 dB and 11.45 dB for the TE and TM polarizations respectively, over a 100 nm wavelength range from 1500 nm to 1600 nm.
- To dynamically rotate the polarized modes, we demonstrate a SiP horizontal coil and simulate its performance for nonreciprocal (NR) polarization mode conversion (PMC) [4]. We demonstrate the first standalone SiP coil which uses an input electrical current to generate a magnetic field inside a Si waveguide along its direction of propagation. To our knowledge, this is the first demonstration of an on-chip, horizontal-axis electromagnet which was fabricated using exclusively the CMOS process flow for the

purpose of standalone NR PMC in Si waveguides. The coil accommodated an electric current up to 14 mA. We simulate NR PMC, which indicates that an alternating magnetic flux density up to 1.16 mT inside a strip waveguide induces a rotation of 50.71 pico-degrees for the fundamental transverse-magnetic mode at a wavelength of 1352 nm. Our analysis further reveals methods to increase the rotation by orders of magnitude. The key advantages of this design are that it required no post-processing and was capable of standalone operation, which make it highly feasible to both manufacture and deploy, respectively, which are crucial to its commercial viability. In this sense, we demonstrate the potential of manufacturing processes and contribute to the development of a commercially viable, on-chip optical isolator.

- To delay the phase of the modes, we present the preliminary design of a dual-polarization modulator using an EOP cladding [10]. In this study, we propose a novel device that can modulate the phase of two orthogonal polarizations separately and simultaneously. Our design exploits the controllable birefringent response in the Pockels effect of specific thermally poled EOPs. We evaluate the performance for a polymethylmethacrylate (PMMA) matrix with DR1 or CLD1 chromophores in a guest-host structure. EOP modulators offer potential improvements in energy consumption and speed due to the utilization of the Pockels effect, and our approach extends this functionality to applications in polarization-division multiplexing.
- To investigate the coupling between light and electrons, we design a novel device whose supermode can overlap with traveling free electrons [5]. The efficiency of this interaction relies on the coupling strength per photon along the interaction length. We therefore design a silicon photonic slot waveguide to host the supermode and a mode evolution region (MER) to convert the TM_0 mode from an input grating coupler (GC) into the desired supermode. We show that by maximizing the coupling per photon to 0.4266, it is possible to achieve an energy gain of 28.27 keV from an optical pulse energy of only 0.22 nJ and duration 1 ps. The acceleration gradient is 1.05 GeV/m, which is lower than the maximum imposed by the damage threshold of Si waveguides. Our scheme shows how the coupling efficiency and energy gain can be maximized without maximizing the acceleration gradient. It highlights the potential of silicon

photonics technology in hosting electron-photon interactions with direct applications in free-electron acceleration, radiation sources, and quantum information science.

In summary, this thesis contributes original analyses, designs, and demonstrations of devices. In doing so, it identifies novel approaches to control light-matter interactions using the properties of the host materials.

2. Background

“Everything should be made as simple as possible, but no simpler.”

– Albert Einstein

As introduced in Chapter 1, this thesis describes devices and designs that are targeted for development using the SiP platform. Therefore, in this chapter, the basics of SiP are introduced. Reasons for the predominance of SiP, its optical properties and building blocks are described in section 2.1. This leads into an introduction to the development of SiP devices in section 2.2. The impact of the sub-wavelength structure of Si on the optical response of the device is analyzed in section 2.3. This builds the foundation for a review of case studies on single-mode device in section 2.4 and multi-mode devices in section 2.5. This analysis is then extended to inversely designed devices in section 2.6, for which the optical response must be investigated rather than designed.

2.1. Predominance of SiP

Computers and smartphones are essential tools in modern life. They perform logical processes and provide access to even more complex processes via internet-based software services such as information exchange, media sharing, networking, data analysis, cloud computing, and multiplayer gaming. A high demand for these services has fueled consistent progress in the speed, size, and efficiency of the infrastructure supporting telecommunication networks. In the past, as the performance of the individual components was expanded and optimized, the capacity of the underlying electronics reached its fundamental limits [42]. This motivated a technological transition to photonic circuits for signal processing and transmission, which were nonetheless controlled by the same electronics which operated the logic and memory. Nowadays, telecommunications infrastructure is comprised of an interconnected network of fiber optic cables that carry light encoded with data by opto-electronic transceivers. Using optical carrier frequencies allows for a higher bandwidth, lower latency, and lower loss. In Canada alone, the photonics industry employs at least 25,000 with an annual revenue of \$4.6 billion [43] and has motivated developments in medicine, sensing, energy, and communications.

Telecommunications is the largest industry that employs photonic systems. Its hardware development is the core value proposition of businesses such as Ciena, Cisco, Ericsson, Lumentum, Sanmina, Nokia, Intel, and IBM, while the software and middleware is developed by businesses such as Google, Meta, Amazon, Microsoft, Apple, and Stocate. As evidenced by the

rise of some of the largest companies to date, this infrastructure boosts technological progress by facilitating an ever-increasing degree of connectivity between access points. The recent COVID-19 pandemic has spurred digital transformations in almost every industry, further pushing the growth of internet traffic, and consequently, the development from standalone computers toward distributed processing. Modern computers and smartphones are therefore being developed as access points for Software-as-a-Service (SaaS) functions to leverage cloud computing. In fact, 77% of internet traffic currently exists within datacenters, and 74% of this load is SaaS-based [44]. Additionally, with the emergence of novel, interactive SaaS functions that enable artificial intelligence, augmented reality, cloud computing, and quantum communications, the demand imposed on datacenters is projected to continue rising. This explosive growth of internet traffic fuels the development of opto-electronic transceivers, which consist of on-chip, opto-electronic circuits.

On-chip, opto-electronic circuits and components are typically manufactured using Silicon Photonic (SiP) technology. This is because SiP leverages low-cost and high yield lithography techniques from the Complementary Metal-Oxide-Semiconductor (CMOS) industry [42]. In doing so, it enables the development of key components in sensing and signal processing systems including receivers, modulators, isolators, splitters, and emitters. This widespread accessibility facilitates rapid, iterative designs with a straightforward process of deployment from the lab to the field. As a result, a significant percentage of the optical components in data centres are SiP-based. Its strong foothold in the telecommunications industry has supported the development of SiP for a variety of applications. However, due to its maturity, SiP devices are often optimized by simply tuning their parameters when in fact, their performance and functionality can be constrained by the physical properties of the host materials. This presents an opportunity for significant advances in SiP design by targeting the underlying physical mechanisms of operation. Hence, this thesis develops design processes for SiP devices which leverage the maturity of available fabrication resources in Canada [45]. By applying recent scientific advances to cutting-edge technology, the SiP platform could usher in a new realm of technological innovation.

This is particularly facilitated by a smooth development pipeline from ideation to simulation to fabrication to testing to commercialization. SiP has grown to provide an innovation platform that can integrate recent technological advances to explore new applications and avenues of inquiry, especially with proper design thinking. For instance, research and development in SiP devices has

already pushed commercial device designs toward their physical limitations. This creates opportunities to realize fundamentally novel designs that still leverage commercial fabrication processes. Note that the operating principle is based on interactions between electrons and light which are mediated by the properties of the host materials. Hence, designing such novel devices must be done from the ground up, that is, starting from the fundamental physical phenomena that can be supported by the host materials. The research presented in this thesis is therefore focused on developing design processes which challenge commonly accepted limitations in SiP by addressing the underlying physical phenomena.

2.1.1. Chip Architecture

A SiP chip is fabricated on a Si wafer. Passive SiP devices confine light using structures patterned from the Si crystal grown on a silicon dioxide (SiO_2) buried oxide (BOX) layer. To actively control the device, SiP chip architecture hosts multiple metallization (e.g., Al with TaN vias), doping (e.g., B for holes, P for electrons), and heating (e.g., TiN) layers, along with complementary materials that are either available through the CMOS process (e.g., Ge, Si_3N_4) or through post-processing (e.g., electro-optic polymers (EOPs), electro-active polymers (EAPs)). Using this additional infrastructure, a passive optical device can be subjected to electric currents, voltages, magnetic fields, and can be doped to modify its electro-optical properties. In this sense, active forces offer the ability to modulate the interaction with light through the optical properties of waveguiding materials. This opto-electronic device architecture can then be covered by a SiO_2 cladding layer.

2.1.2. Optical Response

The field of optics is based on interpreting Maxwell's equations for different situations. These four equations are scale invariant, which implies that any specific optical behaviour can be induced at any wavelength across the electromagnetic spectrum by proportionately scaling the device dimensions and choosing appropriate material properties. This often represents the crossover between physics and engineering in the field. At the macroscopic scale, light is treated as a ray; at the sub-wavelength scale, it is treated as a wave; and at the quantum scale, it is treated as photons. As an electromagnetic wave, it is described by its amplitude, phase, and frequency. Such a wave travels through a material by interacting with its bound electrons. A strong interaction can cause absorption or conversion of the optical energy and therefore lead to propagation loss. In SiP circuits, light is confined by the Si core surrounded by SiO_2 cladding. Although the absorption of

Si and SiO₂ is negligible, the waveguides still incur propagation loss due to scattering from the sidewalls. This is compensated by a compact form factor which is enabled by strong confinement due to the high refractive index contrast between Si and SiO₂. Additionally, the low dispersion of Si allows pulse shape retention over an appreciable propagation length.

We can control the way light propagates through these materials by modifying their shape. Moreover, recent advances in fabrication techniques have enabled feature sizes at the sub-wavelength scale. This is equivalent to spatially rearranging the refractive index and therefore, modifying the dispersion of the material itself. These new techniques in dispersion engineering have informed novel SiP device designs with improved loss, bandwidth, tolerance, and efficiency [1] as reported in the subsequent sections. In fact, the ability to engineer optical propagation and dispersion is relatively mature in the SiP platform, and this provides a basis for using SiP-hosted light to probe the external environment and thereby induce physical phenomena beyond the chip. In this context, the weak nonlinear optical response of Si makes it a perfect probe or sensor. However, the lack of interaction between Si and confined light also presents a drawback. It does not allow for device designs to employ any light-matter interactions associated with nonlinear optical phenomena, which limits the functionality of SiP.

The refractive index of a material is a combination of its dielectric permittivity and magnetic susceptibility. Although the dielectric permittivity of Si has been actively exploited in SiP devices, its magnetic susceptibility remains largely under-developed due to the low magnetic susceptibility of Si and the power consumption required to generate an appreciable magnetic field on-chip. Additionally, Si has a low Verdet constant, which makes it difficult to induce Faraday rotation in a waveguide as investigated in section 5.1. Hence, it is worthwhile to investigate other types of modifications that can enhance the interaction between a Si waveguide and light. One alternative is to modulate the light in the cladding, which is possible with polymer cladding materials. For example, using EOPs to modulate the refractive index or by changing the lattice structure to mechanically modulate Si using vibrational waves. We investigate the combination of Si with a CMOS-compatible EOPs [10] in section 5.2. It is complemented by a pilot study in which we modulated the amplitude using total internal reflection in EAPs [13].

2.1.3. Device Basics

The simplest case of a SiP device is a waveguide which confines optical waves in a rectangular Si strip surrounded by SiO₂ cladding. By modifying the geometry of the Si core, a range of passive

functionalities in SiP can be achieved as explained in section 2.4. For example, increasing the width of the waveguide causes it to act as an MMI, which is further explained in section 2.5 and utilized in chapter 4. Furthermore, incorporating a gap down the middle of the waveguide creates a slot which compresses the mode field, and this effect is utilized in chapter 6. The dispersive properties of the device can also be modified by incorporating periodic, sub-wavelength patterns in its geometry as explained in section 2.2, and this periodicity can be perturbed to tune the optical response further, as mentioned in section 2.6 and analyzed in chapter 3. Regarding active devices, the doping concentration of Si changes its refractive index [46]. This motivated the concept of a depletion region (as in a semiconductor diode) to be implemented in waveguides. By applying an electric voltage laterally across the waveguide, it can be depleted of charge carriers which consequently modulate the phase of light passing through it. This plasma dispersion effect is the basis of Mach-Zehnder Modulators (MZM), in which the phase modulation invokes constructive and destructive interference at the output, thereby resulting in amplitude modulation. This alludes to the potential for exploiting the architecture of SiP to modulate light through diverse means.

For enhanced light-matter interactions, optical cavities can be employed. Such cavities exploit the wave nature of light to induce constructive interference within a finite space, and therefore give rise to optical resonance. Cavities may take the form of rings, Bragg gratings, or PhCs. These cavities facilitate stronger interactions which are useful in modulators or other active device designs. Generally, the optical field interacts with the host material via an applied force field which can be mechanical, thermal, electric, or magnetic.

2.2. Introduction to Sub-wavelength Structuring

Modern technology relies on the internet for data exchange, research, media, and correspondence. As more nodes come online for longer each day, an increased usage of telecommunication networks has placed commensurate demands on the infrastructure supporting online activities. This demand has motivated a shift to higher frequencies in the electromagnetic spectrum. In pursuit of lower latency, reduced propagation loss, energy efficiency, and higher bitrates, transmission lines in the global network have been upgraded to optical fibres [47]. At nearly every scale, from intercontinental submarine cables to intra-datacentre links, communication signals are transmitted at the infrared wavelengths of 1310 nm (O-band) and 1550 nm (C-band) corresponding to the minimum dispersion and loss wavelengths in silica optical fibres [48]. At the transceiver nodes, signal processing is carried out by opto-electronic circuits that interface with electronics hardware.

Recent advances in microfabrication and full-wave simulation techniques have boosted on-chip opto-electronic device design using suitable materials. III-V semiconductors including Indium Phosphide (**InP**), Aluminium Gallium Arsenide (**AlGaAs**), and Gallium Nitride (**GaN**), as well as Silicon Nitride (**Si₃N₄**), are heavily used in lasers, detectors, and gain media although device fabrication is limited by price, scalability, and compatibility. They are complemented by the Silicon-on-Insulator (**SOI**) platform, which uses Si as the waveguiding core surrounded by a SiO₂ cladding. SOI fabrication leverages mature techniques from the CMOS industry [42] to provide low-loss, cost-effective, mass manufacturable chip production. Its CMOS compatibility makes it highly valuable to opto-electronic telecommunications infrastructure [49, 50]. This immediate application has boosted transceiver development toward increasingly complex device designs at sub-micron resolutions with high scalability [42]. Nowadays, hybrid photonic components comprising integrated circuits from both platforms are routinely incorporated into opto-electronic products by companies such as Intel, IBM, Ciena, Ericsson, Cisco, and Elenion. These components enable the generation, manipulation, and detection of light with improvements in speed, size, bandwidth, and power consumption.

Si opto-electronic integrated circuits are manufactured using deep ultraviolet lithography (**DUVL**). The technique enables complex chip architectures that require metallization, doping, heating, multi-etching, and parallel exposure for simultaneous chip fabrication. However, the lithography resolution is low [51] and the lead time takes several months. These limitations present an opportunity for a quicker method of optical device development, the results of which could inform the large scale, complex device designs in DUVL that include opto-electronic control infrastructure. In the research and development phase, electron beam lithography (**EBL**) is often used due to its relatively short lead time and high lithography resolution [45, 52]. These advantages of EBL have lowered the barrier to entry for passive photonic device development in SOI. Moreover, its high resolution has facilitated novel methods of photonic band engineering using sub-wavelength features. A limitation of EBL is the scalability of chip fabrication via serial exposure, which restricts its application to development environments. In the future, extreme UVL [53] might offer another option to this predicament.

SiP technology exploits the high refractive index contrast and mature fabrication processes of the SOI platform at telecommunication wavelengths. Although the absorption of bulk Si is negligible in this range [54], SOI waveguides still exhibit propagation losses in wafer-level

photonic circuitry [55]. Attenuation is mainly caused by scattering due to fabrication imperfections such as lithographic smoothing, sidewall roughness, and mask misalignment [40]. It is compensated to some extent by the high index contrast between Si and SiO₂, which enables smaller devices and waveguide bends, and subsequently denser circuitry [49]. However, their size is still limited because increasing the overlap between confined light and the Si sidewalls contributes further to scattering as seen in Bragg gratings [40], slot waveguides [56], and directional couplers [57]. In this sense, device performance is dependent on lithography resolution. This suggests that designs incorporating sub-wavelength features would be extremely lossy due to the number of small etch boundaries that interact with light. On the contrary, SWGs only weakly interact with confined light [58] and their loss profile is comparable to bulk designs. Such structures have been integrated in waveguides [56], surface [59-61] and edge [62, 63] fibre-chip couplers, directional couplers [64], and polarization [65, 66] and power splitters [41].

Sub-wavelength features that have been incorporated in different devices exhibit similar geometries [67-70]. These similarities allude to a set of guidelines for sub-wavelength engineering in SiP. The transition from bulk Si to sub-wavelength structures is reinforced by fundamental concepts in photonic band engineering. Hence in this work, we present an analysis of state-of-the-art sub-wavelength-based device designs from the perspective of their photonic band structure. In Section 2, we explain concepts in band engineering that are necessary to understand the influence of sub-wavelength features on optical behaviour such as coupling, changing momentum, and pulse distortion. In Section 3, these concepts are applied to single-mode waveguides that employ diffraction, reflection, and propagation as device functionalities. These include diffraction from surface grating couplers and zero-index metamaterials; reflection, resonance, and slow light propagation due to periodic corrugations and holes; and finally, propagation in the sub-wavelength regime directed by the anisotropic propagation constants of SWGs [71]. We extend this analysis in Section 4 to multimode waveguides that have been applied to power and polarization splitters. In Section 5, we investigate instances of sub-wavelength, pseudo-periodic features that appear in designs generated by agnostic optimization techniques such as natural evolution, inverse design, and machine learning. These techniques produce devices with excellent performance, but with complex operating principles that cannot yet be explained, which reinforces the importance of band engineering in SiP design. Finally, we present our concluding remarks in Section 6. Although

the scope of this review is limited to the SOI platform, the designs can be transposed other platforms by simply modifying the materials and dimensions appropriately [72].

2.3. Implications of Photonic Band Structure

The colour of light is determined by the energy of its constituent waves or photons. Both the frequency and wavelength of a wave quantify its energy. In vacuum, the frequency f is inversely proportional to wavelength λ_0 with the proportionality constant being the speed of light c . Inside a material, this relationship is scaled by the refractive index,

$$f = \frac{c}{\lambda_0} = \frac{c}{n(f) \cdot \lambda} = \frac{n(f) \cdot v_p}{\lambda_0} \quad (2.1)$$

Here v_p is the phase velocity and λ is the wavelength of light inside a material. The spectrally dependent refractive index $n(f)$ specifies the relative velocity of a wavefront at a given frequency. The direction of propagation of a wavefront is described by the direction of its wave vector \vec{k} , which is inversely proportional to the wavelength λ . The propagation speed of the wavefront inside a pulse is given by its phase velocity v_p whereas the pulse energy envelope travels at its group velocity v_g . The group index n_g scales the group velocity to the speed of light in vacuum. The spectral dependence of either index is the basis of dispersion.

Dispersion is a measure of the spread of a pulse in time and space during propagation. The dispersion relation of a material describes its optical properties and consequently, its spectrally selective interactions with light. This implies that frequency and wavelength are coupled when accounting for dispersion. In conventional materials, $n(f) > 1$ meaning the waves travel slower and with compressed wavelengths. For a heterogeneous mixture of materials, its optical response depends on the spatial distribution of each refractive index. Interestingly, an ordered, periodic distribution of refractive indices has an unconventional optical response for certain frequencies. The nature of this interaction is controlled by the relationship between the optical periodicity of the material and the effective wave vector of the wave [72].

2.3.1. Periodicity and Wave Vector

A wave can be described by its spatial and temporal frequency. Its temporal frequency f is proportional to the angular frequency ω and its spatial frequency is the wavenumber k that is inversely proportional to λ . The direction of the wave vector \vec{k} provides a valuable degree of freedom in modifying the effective wavenumber with respect to a surface or interface. By

controlling the angle of incidence of the wavefront, the projection of its wave vector onto the surface can be appropriately selected [73]. This directionality allows each frequency to be associated with a range of wavenumbers. For example, the refractive indices of Si and SiO₂ are 3.48 and 1.44 respectively, at a frequency f of 193.41 THz [74]. As per equation (2.1), a wavelength λ_0 of 1550 nm in vacuum or free space would be compressed to a λ of 1076.4 nm in glass and to 445.4 nm in bulk Si. This means that 193.41 THz light propagating through the SOI cladding layer can only be phase-matched with the same frequency in Si if the two waves propagate at an angle of 65.56° with respect to each other. This is depicted in Figure 2.1(a) where the phases of both waves are matched, as represented by their wavefronts. The two lowest order modes, shown in Figure 2.1(b), are typically utilized in SOI designs to maintain high confinement with a small device footprint.

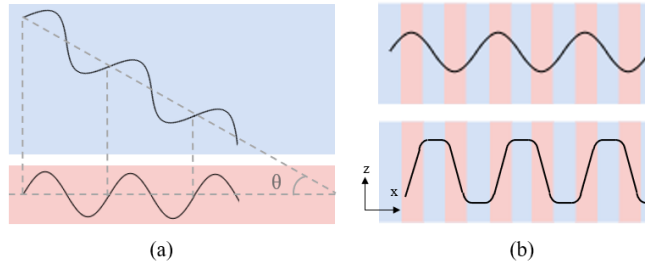


Figure 2.1. Wavelength compression in a material. (a) Two waves of the same frequency in a low (blue) and high (red) refractive index material, and at an angle of θ with respect to each other. The wavefronts (dashed, grey) indicate that the waves are phase-matched at this angle. (b) Electric field distributions of the fundamental (top) and first order (bottom) modes in a grating [72].

The relationship between frequency and wavenumber inside a material is a function of its refractive index tensor and therefore its orientation and geometry. Any geometric modifications are therefore equivalent to a spatial perturbation of the refractive index. At the sub-wavelength scale, these modifications influence the effective index n_{eff} experienced by propagating light. In this manner, the optical properties of a material can be tailored simply by rearranging its spatial distribution within its surrounding environment. Moreover, imposing a periodicity on these modifications produces unconventional optical behaviour for light waves of a comparable effective wavelength. Such a structured material is called a PhC [75, 76]. It is specified as a grating if the periodicity is one-dimensional (1D) as seen in the inset of Figure 2.2. The lattice constant (or pitch) of a periodic index perturbation determines its spectral response. The response can be further tuned via the filling factor (or duty cycle) and scaled by the refractive index. These parameters control

the effective optical periodicity of the material. Its spatial frequency thereby offers an additional degree of freedom in controlling optical interactions, which complements the directionality of the wave vector. Hence, in any optical interaction, the effective wavenumber is intimately coupled with the pitch of a material in determining the nature of the interaction. The periodicity of the index perturbation also causes the lines in its dispersion diagram to split into bands.

2.3.2. Band Diagrams

A sub-wavelength, periodic arrangement of the refractive index gives rise to spectrally selective behaviour that can be modelled from Bloch-Floquet theory [72]. The periodicity in a PhC imposes certain constraints on its interaction with light. The behaviour of light within such a periodically arranged structure may be succinctly described by its photonic band diagram. This diagram describes the nature and probability of optical interactions with the PhC in the parameter space of an optical wave. In other words, every combination of frequency and wave vector that can interact with the PhC is represented as a point on the band diagram. Mathematically, each point represents the properties of a wave that produce a real, continuous, and differentiable solution to the dispersion relation [77]. A set of points forms a curve, or band, which indicates the existence of an optical eigenmode for light to occupy during an interaction. Each band therefore contains all possible (k, ω) combinations of light that exhibit the same electromagnetic field distribution in the PhC specified by the corresponding eigenmode of the band. These modes are referred to as Bloch or Floquet modes since the nature of propagation is determined by the optical periodicity of the PhC similar to regular modes in a bulk material.

An exemplary 1D band diagram of a grating pitch of 500 nm is shown in Figure 2.2. The ratio of the width of the core material a to the pitch Λ is defined as the filling factor or duty cycle (DC). For a DC of 0.5 shown in Figure 2.2, the core and cladding regions contribute equally to the overall optical impedance. Since the pitch and wavenumber are coupled in an optical interaction, the spectral position of the gap in the bands is controlled by the pitch. Similarly, the effect of the DC on the band structure can be inferred as a closing of the band gap toward the lower band for a DC > 0.5 and toward the upper band for a DC < 0.5 . Also shown in Figure 2.2 are regions in the band diagram where light is diffracted, reflected, or propagated depending on the availability and position of bands in its spectral range. Since a SOI device is surrounded by SiO₂ cladding, the light line mapped in this diagram describes the propagation of light in the cladding. The light cone includes all (k, ω) combinations above a light line. The green bands in the light cone represent

modes that can couple to light in the cladding but as a result, typically cannot propagate inside the PhC. The blue bands describe waves propagating as modes in the PhC that experience a higher effective index than the cladding.

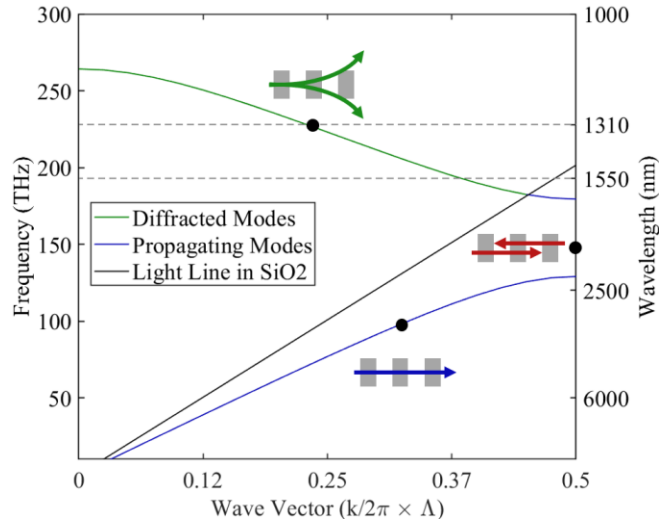


Figure 2.2. Band diagram of an SOI grating for the in-plane polarization with a pitch of 500 nm, DC of 0.5, and thickness of 220 nm. The propagation (blue), reflection (red) and diffraction (green) regimes are also shown.

The relationship between the spatial and temporal frequency of an optical wave inside a PhC is mapped by its band diagram. Optical frequencies in the telecommunication range are plotted on the vertical axis. Wave vectors that can be associated with these frequencies are plotted on the horizontal axis as a function of their spatial frequency in relation to the pitch of the PhC. As explained in section 2.3.1, changing the angle of the wave vector relative to the PhC is equivalent to moving horizontally along the band diagram and selecting a wavenumber. In this context, the phase velocity of a wave is determined simply from its (k, ω) position in the band corresponding to its mode. Its group velocity is the slope of the band at that point.

$$v_p = f\lambda = \frac{\omega}{k}, \quad v_g = \frac{d\omega}{dk} \quad (2.2)$$

The speed of light in the SiO₂ cladding, for example, is given by the slope of the light line in Figure 2.2. The band diagram of a PhC can be used to calculate its coupling efficiency to modes, that is, the probability of light coupling to points on the bands. It therefore indicates the density of optical states accommodated in the PhC as well as the extent and nature of optical interactions. For these reasons, the behaviour of structures presented in this paper will be described in the context of their band diagrams. The band diagrams in this paper were mapped from 3D Finite-

Difference-Time-Domain (FDTD) simulations of infinite, planar, 2D PhCs with a Si core thickness of 220 nm and SiO₂ cladding. Spectrally dispersive refractive indices for both materials were used [78]. The TE and TM polarizations were excited by in-plane electric and magnetic dipoles respectively. Bloch periodic boundary conditions were imposed on the in-plane directions of the unit cell while perfectly matching layers were used as the vertical boundaries. Calculations were performed on the first Brillouin zone with the symmetry points labelled as Γ , X, M, and K depending on the lattice configuration [72]. The intention behind these band diagrams is to provide an intuition for the physical significance of band structure and thereby explain the influence of PhCs on the performance of SOI device designs. There are three distinct regimes of optical interaction that are evident in any band diagram – propagation, reflection, and diffraction.

2.3.3. Propagation

The light line of the cladding imposes an upper bound on the conditions for light confinement. Below the light cone, light waves are confined to the PhC as Bloch modes whose propagation is described by the position and shape of their corresponding bands. A straight band hosts a constant group velocity for optical frequencies that intersect with its region of constant slope. Within this spectral range, a pulse would retain the shape of its energy envelope during propagation. If the intercept of the band is zero, then the phase velocity is equal to the group velocity. An optical pulse within this range would be undistorted because the envelopes and wavefronts of its frequency components would propagate at the same velocity. This region of linear dispersion is the relatively straight section of the lowest band near the Γ point where $k \rightarrow 0$. It is called the sub-wavelength regime [79] because the periodicity of the PhC is smaller than the effective wavelengths interacting with it. As the periodic index perturbations of the PhC are effectively homogenized at this scale, it can be modelled using effective medium theory [80, 81]. The birefringent effective indices n_{\parallel} and n_{\perp} of an infinite, planar SWG can be approximated by Rytov's equations [81],

$$n_{\parallel}^2 = \left(\frac{a}{\Lambda}\right) n_{co}^2 + \left(1 - \frac{a}{\Lambda}\right) n_{cl}^2 \quad , \quad \frac{1}{n_{\perp}^2} = \left(\frac{a}{\Lambda}\right) \frac{1}{n_{co}^2} + \left(1 - \frac{a}{\Lambda}\right) \frac{1}{n_{cl}^2} \quad (2.3)$$

Here n_{co} and n_{cl} are the refractive index of the core and cladding respectively. The components n_{\parallel} and n_{\perp} refer to electric field polarization direction being either parallel (propagating in the X direction in Figure 2.1) or perpendicular (Z or Y direction in Figure 2.1) to the grating lines. A mode in the sub-wavelength regime has a lowered effective index than the core and is therefore higher than the light line of the core. As the index is inversely proportional to velocity, steeper

bands due to a lowered group index indicate faster propagation. Along the propagation direction, the width of a SWG can be narrowed to form a waveguide. Sufficiently narrow SWG waveguide widths support delocalized modes [58] since the wavelength is much larger than the pitch. These Bloch modes have a higher group velocity than equivalent modes in a regular waveguide. Additionally, the spectrally insensitive index asserts a uniform response over a broad bandwidth.

2.3.4. Reflection

Taking dispersion into consideration, no propagation occurs for wavelengths that are even integer multiples of the pitch as per the Bragg condition,

$$\lambda = 2mn_{\text{eff}}\Lambda, \quad m = 0, \pm 1, \pm 2 \dots \quad (2.4)$$

In the Bragg regime, the equivalence of the effective wavelength with the periodicity of a PhC causes forward and backward scattered waves to cancel each other resulting in resonance or reflection. There are no real solutions to the dispersion equation in this range because modes are not supported by the PhC. A corrugated waveguide or SWG in this regime is called a Bragg grating. Such a PhC only supports standing waves with zero group velocity. An exception to this rule is Dirac-cone based metamaterials where two bands intersect and their homogenization yields a linear dispersion with real, finite group velocities [68].

2.3.5. Diffraction

The light cone of the cladding represents the diffraction or radiation regime. Points above the light line represent light waves that interact with but are not confined to a PhC. These lossy modes are responsible for diffraction and coupling between the PhC and the cladding. For example, the second order mode of the grating in Figure 2.2 crosses over the light line resulting in only the larger wavenumbers being confined. In this sense, the grating pitch determines the coupling angle and bandwidth of each diffractive order. The wave vector of light incident on a grating coupler (GC) at an angle θ can be separated into two components – a vertical component k_{\perp} normal to the surface of the GC and a horizontal component k_{\parallel} along the plane of the GC. Light can couple with a GC if the in-plane component k_{\parallel} constructively interferes with the wave vector k_{eff} of confined light in the GC. Mathematically, the difference between the two wave vectors must be an integer multiple of 2π [82],

$$\Lambda k_{\text{eff}} - \Lambda k_{\parallel} = 2\pi m, \quad m = 0, \pm 1, \pm 2 \dots \quad (2.5)$$

Under this condition, the incident and confined wave vectors are phase matched, allowing for energy to be transferred between the two waves as depicted in Figure 2.1(a). The above equation

can also be interpreted as the grating imparting a $2\pi/\Lambda$ change in momentum to an incident wave. In this sense, the periodicity of the grating allows access to wave vectors outside the first Brillouin zone of the lattice by translating them. When the k -vector of a scattered wave is outside this zone, it is mathematically transformed to a vector inside the zone by the addition or subtraction of reciprocal lattice vectors. This can result in a k -vector with a different direction than the original k -vector. This phenomenon of Umklapp scattering [83] explains the unconventional effect of PhCs on the momentum and direction of light without which it would appear that momentum was not conserved. In the reverse direction, confined light propagating as k_{eff} in the plane of a GC is diffracted at angles that permit constructive interference between the waves radiating from the interface discontinuity of each period in the GC. Assuming k_{\parallel} exists in the cladding, the diffraction angle of the m^{th} order is,

$$\sin \theta = \frac{n_{\text{eff}} - \frac{m\lambda}{a}}{n_{\text{cl}}}, \quad m = 0, \pm 1, \pm 2 \dots \quad (2.6)$$

The first order $m = 1$ is typically used due to its practical accessibility and coupling efficiency. Note that the k_{\perp} component is directly incident on the GC at an angle of 0° corresponding to the Γ point on the band diagram. As it does not play a role in coupling, it exerts a force on the grating [84]. The Bloch-Floquet mode in this regime is lossy, which is a necessity for coupling to free space due to reciprocity considerations. In Section 3, these concepts will be further examined in the context of single-mode waveguides and their application to device functionalities.

2.4. Single-Mode Devices

A periodic refractive index distribution gives rise to unconventional optical phenomena such as slow light, resonance, diffraction, and lossless propagation [85-87]. We now evaluate these phenomena from the perspective of their influence on a fundamental building block, that is, a single etch, single-mode waveguide in which propagation can be analysed almost exclusively. By imposing periodic geometric, or equivalently, index perturbations onto single-mode, strip waveguides, we can interrogate the behaviour of confined wave propagation almost independently of interference, phase modulation, or absorption effects. The approach therefore directly informs the design of surface grating couplers and zero index metamaterials in the diffraction regime, Bragg gratings and PhC nanocavity waveguides in the resonance regime, and edge couplers and SWG waveguides in the sub-wavelength regime.

2.4.1. SOI Waveguide with Periodic Corrugations

The SOI platform hosts Si waveguides in an SiO₂ cladding with corresponding refractive indices of $n_{\text{core}} \approx 3.48$ and $n_{\text{clad}} \approx 1.44$ respectively [40], within the telecommunication wavelength range. Since the effective wavelength λ_{eff} for a waveguide mode depends on the index [58], this restricts the cross-sectional dimensions to approximately 500 nm along the axes transverse to the propagation direction. A narrower width would reduce modal confinement and prevent guiding, as well as increase sidewall scattering losses. However, the typical thickness of Si crystal growth on a buried oxide (BOX) layer is only 220 nm [88]. This fails to confine the out-of-plane, TM₀ polarizations which instead propagate through the cladding. Only the in-plane, TE₀ modes are properly confined to the 500 nm width albeit with different effective indices than TM₀. The fundamental mode profiles for TE and TM polarized light in a standard SiP waveguide are shown in Figure 2.3. This effective birefringence in Si waveguides highlights the need for polarization diversity in SiP circuits [89] despite Si being negligibly birefringent.

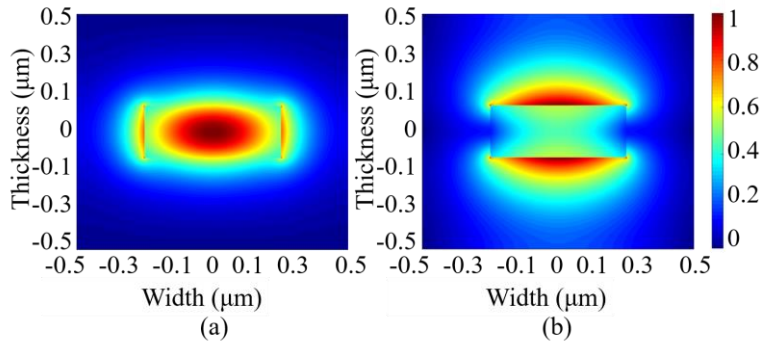


Figure 2.3. Cross-sectional profiles of the magnitude of the electric field component of the fundamental (a) TE and (b) TM modes confined to a Si waveguide with a thickness of 220 nm and a width of 500 nm surrounded by SiO₂ cladding.

As the TM mode profile overlaps much less than TE with the waveguide cross-section, it is less susceptible to geometric perturbations or sub-wavelength features present in the waveguide [58]. Figure 2.4 shows an exemplary 1D band diagram for a Si waveguide with periodic corrugations along its sidewall at different depths and a pitch Λ of 210 nm. The duty cycle was maintained at 0.5, setting the corrugation width equal to the spacing between successive corrugations.

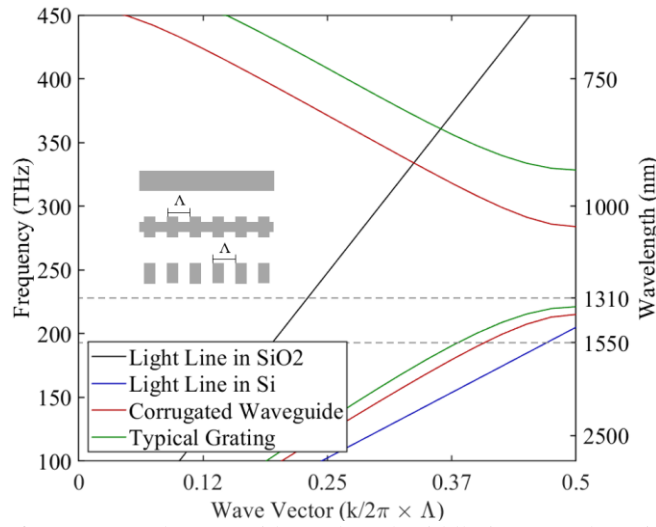


Figure 2.4. Band diagram of a corrugated waveguide (red, and middle inset) and grating (green, and bottom inset) with a pitch of 210 nm and DC of 0.5. The light lines of the cladding (black) and core (blue) are also shown.

As illustrated in the insets of Figure 2.4, a strip waveguide (of width 500 nm) has a corrugation depth of 0 nm. A depth of 125 nm is commonly used as a frequency filter, and a depth of 250 nm completely etches the core, leaving behind periodically spaced pillars. For long wavelengths, the latter two cases permit light propagation as Bloch modes despite being discontinuous with scattering boundaries. A gap between the bands is caused when the periodicity of the index perturbations fulfills the Bragg condition. Since the corrugations reduce the contribution of Si to the lower index segments of the grating, the overall effective index is lowered causing the bands to shift upward indicating higher propagation velocities and longer effective wavelengths. Deepening the corrugations increases the effective index difference between the corrugated and normal segments thereby widening the gap further. As the energy density of the mode corresponding to the second band is concentrated in the corrugated, lower index region [72], as shown in Figure 2.1(b), a deeper corrugation would relatively increase the energy of the system and consequently, its associated phase velocity. In this way, the corrugation depth and fill factor can be used to raise or lower the bands.

2.4.2. Diffraction Coupling

When the pitch of a grating is larger than the effective wavelength of confined light, scattering occurs at the mismatched impedance boundaries. Although scattering at an interface discontinuity is isotropic, the periodicity of the grating exerts restrictions on scattering in the form of angles of constructive and destructive interference. These angular regions map out the diffraction orders of

the grating, which are the higher order modes within the light cone of the band diagram. Normally, only the lower diffraction orders are harnessed in surface fibre-chip GCs. The band structure of a SOI grating pitch of 400 nm is shown in Figure 2.5 where both telecom wavelengths couple to the grating modes at different k -vectors [59] but only the O-band is diffracted.

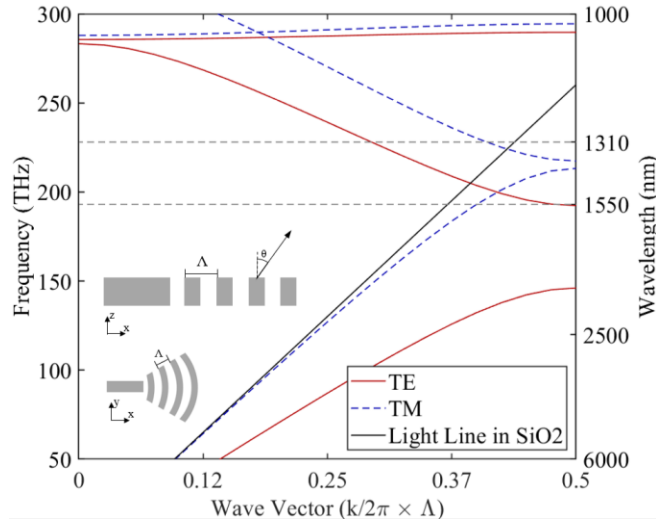


Figure 2.5. Band diagram of a SOI grating for TE (solid red) and TM (dashed blue) light with a pitch of 400 nm and DC of 0.5. The insets show a (top) profile view and (bottom) top-down view of its implementation in a GC.

Grating couplers in the SOI platform normally have a large pitch of around 900 nm to access modes above the light line (upper bands in Figure 2.5) from within the telecom frequency range so that incident light can couple from free space. Due to their large pitch requirement, and consequently large feature sizes, GC resolutions are typically CMOS-compatible. Most designs utilize a lower effective index difference between the alternating sections of the grating to optimize the coupling efficiency and bandwidth by easing the transition to free space. This is achieved by increasing the cladding index through partial etches or sub-wavelength structures that draw on concepts in effective medium theory [80, 81]. Designs using 2D PhCs [90-93] also offer polarization, mode, and frequency selective functionalities.

Recently, the realization of on-chip, zero-index metamaterials [94] has introduced a new regime of radiation that is emitted transverse to the direction of propagation of a waveguide in both the in-plane and out-of-plane directions. Analogous to the electric band structure in graphene, this phenomenon was made possible by a Dirac cone at the Γ ($k=0$) point of a PhC [95]. A Dirac cone is a band-crossing that exhibits linear dispersion (constant group velocity) in both bands for frequencies near the crossing. The position of the bands in the Brillouin zone gives rise to an

infinite phase velocity and wavelength. Using the lattice parameters of the PhC, its spectral position can be aligned to frequencies within the telecom wavelength range. This has recently been realized in CMOS-compatible feature sizes on the SOI platform [96, 97]. Radiation modes can also be excited transverse to the axis of a zero-index metamaterial waveguide resulting in far-field directional couplers [57] and other phenomena [68, 98].

2.4.3. Bragg Reflection

Arguably the most recognizable diffraction element in guided wave optics, Bragg gratings operate as band-stop filters [99-101]. The extent of Bragg reflection can be tuned to either reflect, transmit, or slow down light thereby inducing a resonant effect along the length of the grating. Figure 2.6 shows the band diagram and the transmission and reflection profiles for a Bragg grating of pitch 300 nm that has a 3-dB bandwidth of 20 nm in the O-band [40]. Note that the band gap for TE polarized light is larger due to a higher overlap with the waveguide cross-section, as depicted in Figure 2.3. Such corrugated waveguides are used as frequency filters or contra-directional couplers [102, 103]. The depth of a Bragg filter is determined by the number of grating periods as well as fabrication fidelity. Resonant effects are prevalent after only a few periods. Lithographic smoothing at the corners of each corrugation reduces the step impedance between sections, which manifests as a reduction in the bandwidth and isolation, as can be seen in the dashed and dotted lines of Figure 2.6(b).

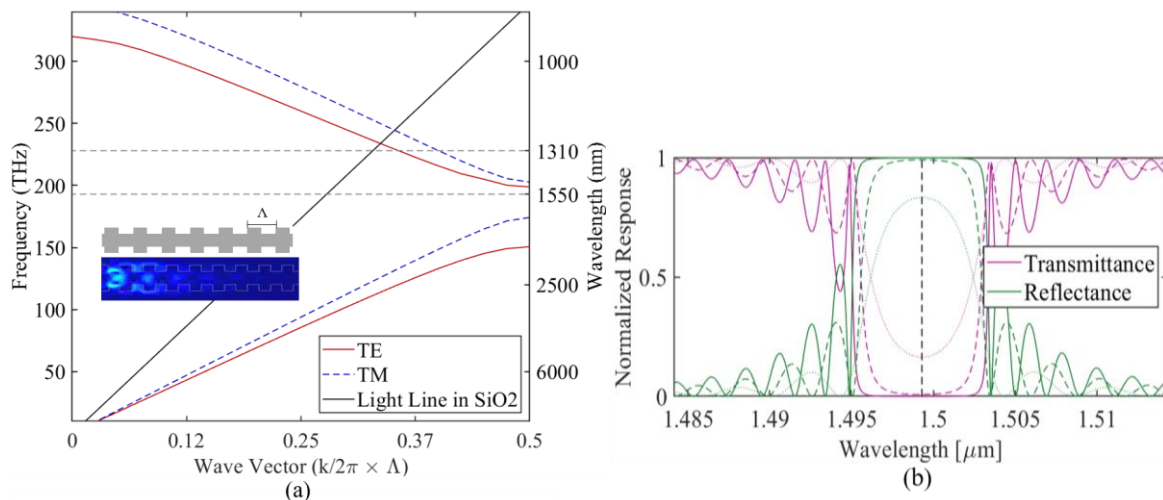


Figure 2.6. (a) Band diagram of a SOI Bragg grating for TE (solid red) and TM (dashed blue) modes with a pitch of 300 nm, DC of 0.5, width of 500 nm, and 125 nm corrugations [40]. The insets show its implementation in (top) a Bragg grating that (bottom) reflects 1550 nm light. (b) Simulated degradation of its optical response (dashed and dotted lines) due to increased lithographic smoothing [40].

In contrast to sidewall corrugations, a periodically varying dielectric permittivity has also been incorporated in waveguides by embedding holes along its axis as seen in Figure 2.7. The holes impose a sinusoidally varying effective index that asserts a stopband similar to the Bragg grating. Such PhC waveguides have been used as resonant or slow light cavities [104, 105] and as optomechanical nanobeam cavities [106, 107] for sensing or modulation [108, 109]. In most resonant cavity designs using corrugated sidewalls or axial holes, back-reflections have been minimized by an apodization of the hole diameters [110]. Such a gradually increasing step index difference provides a smoother transition to the step index profile of the resonant waveguide and consequently better overall performance.

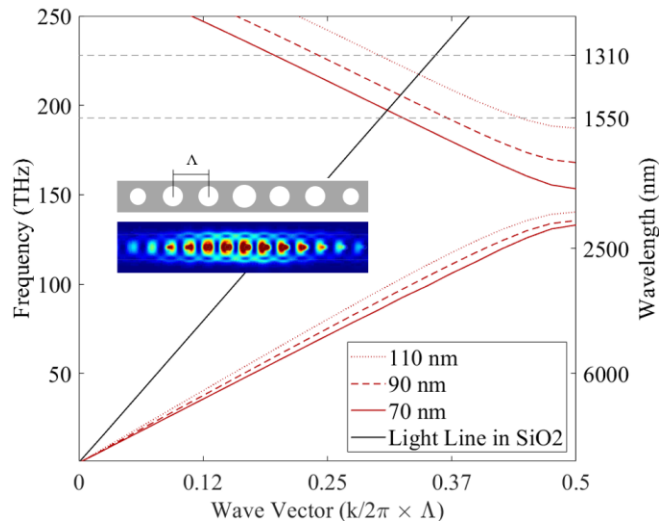


Figure 2.7. Band diagram of a SOI square lattice with a pitch of 360 nm and increasing hole diameters of 70 nm (solid), 90 nm (dashed), 110 nm (dotted). The insets show its implementation in (top) a PhC cavity waveguide supporting (bottom) 1550 nm pulse propagation.

Similar to a PhC waveguide, the bandgap in a 2D PhC slab has also been demonstrated in its capacity for waveguiding by introducing a line defect [105, 111]. Such designs exert a high confinement factor on light propagating through the defect, which allows for extremely dense routing with 90° bends [112]. However, as the defect exists within the bandgap of the 2D PhC, the bandwidth supported by a PhC slab waveguide is much lower than regular waveguides. Alternatively, light can also propagate as Bloch modes confined to a waveguide by implementing gratings designed in the sub-wavelength regime.

2.4.4. Sub-wavelength Propagation

If the pitch of a grating is smaller than the effective wavelength of interacting light, then light may propagate through the PhC as a Bloch mode. Such modes have a low overlap with the sidewalls of the grating, which facilitates relatively low loss, diffraction-less propagation due to negligible scattering from any sidewall roughness [58]. A SWG exhibits anisotropy due to its directional periodicity and can therefore be treated as a uniaxial crystal. The effective index experienced by modes in a SWG-based waveguide depends on the direction of the SWG axis with respect to the polarization direction, as shown in equation (2.3). In the deep sub-wavelength regime, a SWG can be modeled using effective medium theory [80, 81]. The maximum pitch supported for a SOI SWG waveguide propagating the O and C bands has been demonstrated at around 200 nm [62] as shown in Figure 2.8, beyond which the Bragg condition is approached. Individual segments of the grating may be tuned to regulate the mode size or match the effective index in transitioning to a strip waveguide. These parameters have been applied to an edge coupler design with a polarization-independent coupling efficiency of 92% over a 100 nm bandwidth [113]. By reducing the size of individual segments, the effective index was lowered, and the mode size was enlarged to match propagation to a single mode fiber.

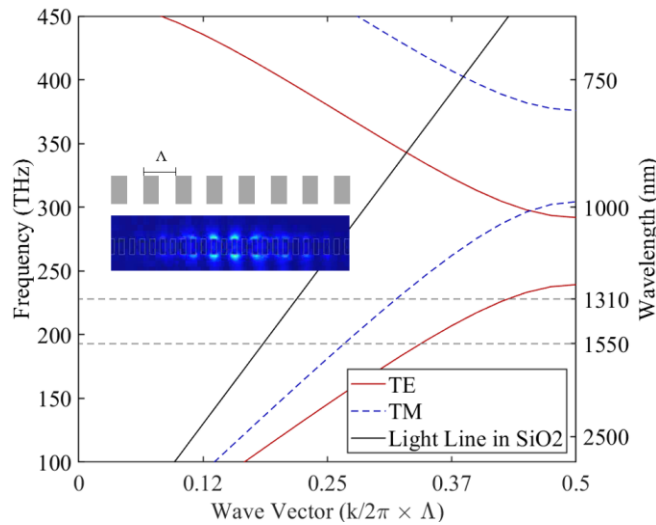


Figure 2.8. Band diagram of a SOI SWG for TE (solid red) and TM (dashed blue) polarizations with a pitch of 200 nm and DC of 0.5. The insets show its implementation as (top) a SWG edge coupler [62] supporting (bottom) 1550 nm pulse propagation.

A valuable property of SWGs is their linear dispersion profile at long wavelengths, which translates to a spectrally independent phase velocity and effective index. This property allows SWGs to be used in highly broadband devices covering both the O and C bands. Furthermore, it

has been recently demonstrated that such waveguides are extremely tolerant to fabrication imperfections and can support efficient light propagation even across missing or deformed gratings [114]. Note that eliminating a SWG section would be akin to doubling the periodicity at a fill factor of 0.25 albeit for barely 1-2 periods. This effect is inconsequential because the strength of PhC behaviour depends on the number of periods contained by the PhC. A DC of 0.5 is typically maintained for single-etch SWG waveguides to maximize their fabrication tolerance, although dispersion can still be fine-tuned by changing their width, pitch, or tilt.

The laminar, periodic structure of a SWG exhibits similar optical behaviour to a homogeneous, uniaxial crystal [71]. Bloch modes propagating through a SWG are subjected to an anisotropic effective index. For comparison, the effective index of a fundamental, TE polarized Bloch-Floquet mode propagating across a SWG (as seen in Figure 2.4 and Figure 2.2) is about 2.66 using equation (2.3), whereas it is 1.88 when traveling along the grating elements [71, 81]. The TM polarization is less influenced by the grating angle because its direction of polarization is always parallel to the interfaces irrespective of its direction of propagation. Indeed, the effective index of the TM mode increases slightly when angled with respect to the grating [71]. Alternatively, it has been shown that the grating angle itself can be tilted in a SWG waveguide thereby modifying the effective index. In such a case, the phase front of the modes is also tilted proportional to the grating [115] and can be determined from their wave vectors using the dispersion equation [71, 77]. This manifestation of tilt in the band diagram of a SWG waveguide requires a treatment of the grating as a periodic, laminar, multilayer stack [72]. The effect can be seen in the 2D band diagram of Figure 2.9 for a SWG with a period of 250 nm [71] where a tilt of 45° was demonstrated.

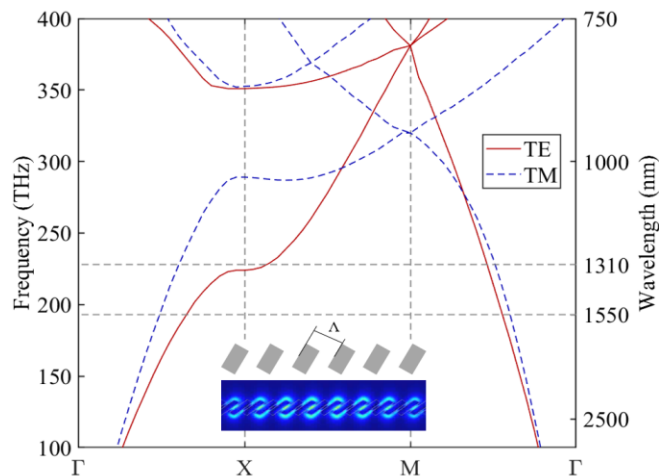


Figure 2.9. Band diagram for a SOI SWG for TE (solid red) and TM (dashed blue) polarizations with a pitch of 250 nm and DC of 0.5 [71]. The insets show its implementation in (top) a tilted SWG waveguide supporting (bottom) 1550 nm pulse propagation.

From this perspective, the SWG waveguide can be interpreted as a 2D lattice with the propagation directed by its tilt angle θ . When the angle is increased and pitch Λ is maintained, the effective grating pitch Λ_{eff} along the direction of propagation is increased to $\Lambda \sec \theta$. Decreasing the effective grating vector consequently reduces the energy $\hbar\omega$ required to support modes. In the context of dispersion, the bands are therefore lowered in frequency. Lowering the bands allows access to modes in the X-M region of the crystal reciprocal lattice that were originally in the sub-wavelength regime for a grating tilt of 0° . Conversely, a propagating mode originally available in the Γ -X region now enters the Bragg regime and is instead guided along the tilt direction in the X-M region. In this manner, the grating tilt offers an additional degree of freedom to engineer the effective index albeit at the cost of higher dispersion. The convenience of using the tilt angle as a parameter for passive wave manipulation is that it does not require smaller feature sizes at larger angles. A rather aggrandized extrapolation of this concept that is still within the realm of single mode waveguiding, is a completely tilted SWG with an angle of 90° but only two periods [108]. Although such a design supports lateral light propagation as a slotted waveguide, it is a different physical phenomenon because of its equivalence to a potential barrier with a thin well in which the pulse is highly confined [116]. The slot offers a strong interaction with its confined mode, which can also be achieved by suspending the SWG albeit for longer wavelengths [117, 118]. Using multiple grating periods allows for homogenization, and across a sufficiently wide cross-section, higher order modes are excited. This has been extensively explored in the context of multi-mode waveguides.

2.5. Multi-mode Devices

The fundamental mode profile of confined light in a single mode waveguide can be expanded to any desired width by adiabatically tapering it. A sufficiently gradual taper does not perturb the effective index along the direction of propagation, and therefore retains its mode profiles. On the other hand, a sharp expansion of the waveguide width induces a strong perturbation of the effective index. In this situation, the fundamental mode leaks energy into higher order modes causing multi-modal propagation. It is analogous to a charged particle traveling across a potential drop. Waveguides that incite and support higher order modes are referred to as MMIs due to their

characteristic interference patterns caused by the superposition of the modes [119]. Antinodes formed at each self-imaging length in the MMI can be extracted as a single mode, and subsequently applied to intensity or polarization splitting. Additionally, the integration of sub-wavelength structures such as SWGs or PhCs in MMI-based device designs has been shown to appreciably improve the insertion loss, extinction ratio, and bandwidth [41, 65, 120].

2.5.1. Intensity Splitters

A drastic change in waveguide width excites higher order modes of which each propagates with its own propagation constant $\beta = 2\pi n_{\text{eff}}/\lambda$. Their mutual interference produces self-images of the input at beat lengths L_π that depend on the propagation constants of the first two modes β_0 and β_1 [119],

$$L_{\text{SI},p} \rightarrow \frac{p}{2}(3L_\pi) = \frac{3p}{2} \left(\frac{\pi}{\beta_0 - \beta_1} \right) \approx \frac{p}{2} \left(\frac{4W_{\text{eff}}^2}{\lambda_0} n_{\text{core}} \right) \quad (2.7)$$

A single image is formed at every even value of p whereas a two-fold image is formed at every odd value. The paraxial approximation for L_π is valid for MMIs with a high refractive index contrast as in the SOI platform. In this case, the effective width W_{eff} can be approximated by the MMI width. As intensity splitters, MMI-based designs have been shown to offer an appreciable bandwidth and fabrication tolerance due to their large cross-section and feature sizes. Additionally, by integrating a SWG into the MMI, its effective index is reduced, thereby shortening the beat length (as calculated from the phase constants) and allowing for smaller designs [120]. As explained in Section 2.4.4, the linear dispersion of the mode in the sub-wavelength regime also enhances the operating bandwidth tremendously [121]. This point is illustrated in the band diagram of Figure 2.10 that shows a constant slope and therefore a constant, reduced effective index across the telecom O and C bands.

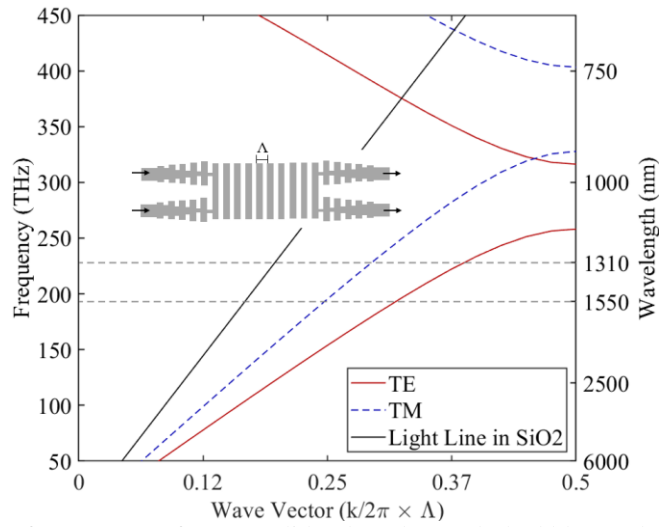


Figure 2.10. Band diagram of a SOI SWG for TE (solid red) and TM (dashed blue) polarizations with a pitch of 190 nm and DC of 0.5. The inset shows its implementation in a MMI-based 2×2 intensity splitter [120].

The 2×2 MMI shown in the inset of Figure 2.10 demonstrates an equal splitting ratio between both ports over a bandwidth of 300 nm [120]. In such a SWG-based MMI, the beat length in equation (2.7) is calculated from the propagation constants of the fundamental and first-order Block-Floquet modes. The choice of a single or two-fold imaging length depends on the design constraints, such as whether filtering or splitting is required. If a higher splitting ratio is required for applications such as monitoring the power through a waveguide, the same concept may be applied to the design of a variable intensity splitter as shown in Figure 2.11. By using a central input and extracting light at the two-fold imaging length, a 1×2 MMI was developed as a power tap for the C-band [122]. In this application, one output could be connected to a photonic integrated circuit with the other to a detector. The splitting ratio was tuned using the device geometry by cutting a corner of the MMI at the side that was designated as the lower power output. Variable splitting ratios were achieved for a 225 nm pitch over a bandwidth of 100 nm [41].

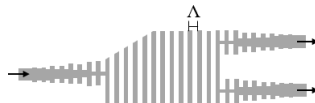


Figure 2.11. Integration of a SWG in the design of a 1×2 MMI variable intensity splitter [41].

The broad bandwidth and customizable splitting ratios offered by SWG MMIs lays the basis for SiP transceiver designs that operate across the entire telecommunications spectrum. Evidence of this claim is in the performance enhancements realized for polarization splitters that utilize a PhC or SWG in an MMI-based design.

2.5.2. Polarization Splitters

An asymmetric waveguide cross-section in the SOI platform causes birefringence due to an inherent effective index difference between the fundamental TE and TM mode profiles as seen in Figure 2.3. However, polarization and mode division multiplexing are often incorporated in SiP circuit design. This introduces the need for polarization diversity in SiP circuits, for which polarization splitters are essential. An intuitive solution is to exploit the effective birefringence in SOI devices for polarization discrimination. Similar to the MMI design in Figure 2.10, a polarization splitter has been demonstrated [65] with a dual polarization input and separate TE and TM outputs. Using the difference in effective indices, and consequently different beat lengths, a self-image of the input was produced at different propagation lengths for each polarization. As can be inferred from the schematic in Figure 2.12, the TE beat length was approximately double that for TM. The integration of a SWG with a pitch of 180 nm into the MMI-based PBS design broadened its bandwidth to 100 nm.

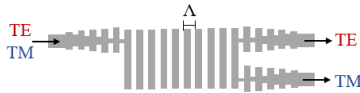


Figure 2.12. Integration of a SWG in the design of a PBS based on the 2×2 MMI [65] shown in Figure 2.10.

As described in Section 3.3 for SWG design, the grating tilt may be used as an additional parameter for controlling the effective index in a PBS [121]. The grating tilt controls the structural anisotropy of the device. In doing so, the effective index of the TE polarization can be increased across the spectrum whereas the effective index for TM light is negligibly affected due to its propagation mainly through the SiO_2 cladding. By fine-tuning the tilt parameters to produce the device shown in Figure 2.13, the TE self-imaging length was reduced so that the overall device length was shortened to less than 100 μm without compromising on bandwidth or extinction ratio.

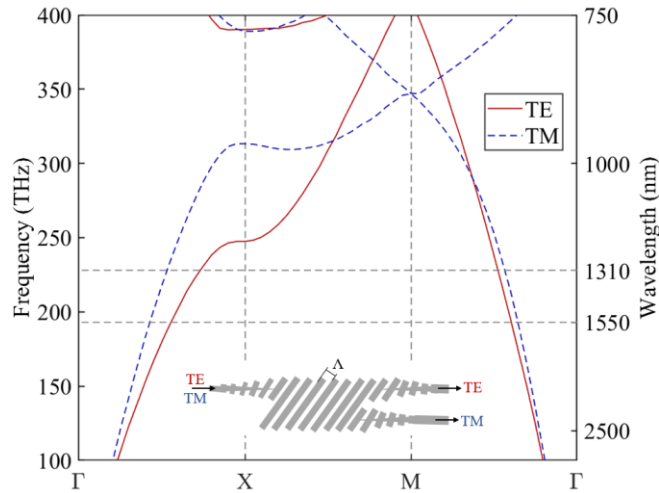


Figure 2.13. Band diagram of a SOI SWG for TE (solid red) and TM (dashed blue) polarizations with a pitch of 220 nm and DC of 0.5. The inset shows its integration in the design of a PBS with a 7° tilt [121].

A tilted SWG PBS supports a TE direct image at the same length as the TM mirrored image due to its anisotropy-induced birefringence. This is due to the ratio of the effective indices for propagation directions parallel and perpendicular to the grating elements [120]. In the context of the band diagram in Figure 2.13, a higher position of the fundamental TM mode at the X point indicates a higher phase velocity and as such, a lower effective index for TM light propagating across the grating, as well as a higher index of the TM mode propagating along the grating at the M point. This higher ratio between the indices results in a longer beat length for TM light, which also explains the reasoning behind the design in Figure 2.12. In this manner, the position of the TE output port can be made to coincide with the location of the TM port along the propagation length. The improved performance suggests that integrating a tilted SWG into an angled MMI PBS design [3] could possibly reduce the form factor further while maintaining the operation bandwidth.

High extinction ratios could also be achieved by filtering the TE polarization at the TM output, as has been shown in [123] and its SiP equivalent [124]. In these designs, a PhC with a triangular lattice was embedded in a conventional MMI as can be seen in the schematic of Figure 2.14. The 2D band structure of the PhC opened a bandgap for TE polarized light that was collected as a back-reflection. TM light, however, propagated unhindered in the sub-wavelength regime and was collected at its mirrored self-imaging length.

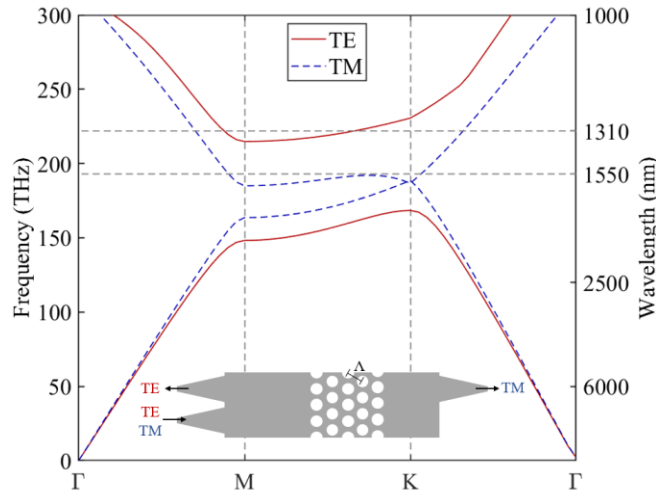


Figure 2.14. Band diagram of a PhC for TE (solid red) and TM (dashed blue) polarizations with a 390 nm pitch hosting a triangular lattice of holes of radius of 117 nm. The inset shows its integration in the design of a MMI-based PBS [124].

Note that the devices described in this paper have been selected for the straightforward design approach they employ. Many other sub-wavelength designs have been proposed for polarization splitting [79] such as contra-directional couplers that filter polarizations [103], directional couplers that separate polarizations [57], and polarization rotators [125, 126]. Furthermore, sub-wavelength structures have been incorporated into a number of SiP device designs including Mach-Zehnder interferometers [127], rings [128], switches [129], detectors [130], demultiplexers [131], and lasers [132, 133]. Interestingly, the successful integration of sub-wavelength structures in nanophotonic device design also extends beyond our level of understanding. At this extreme, devices utilizing dispersion engineering have been realized through natural and artificial means by optimizing the geometry directly. These designs meet their performance targets despite a lack of knowledge surrounding the device physics.

2.6. Extension: Optimized Devices

The application space for sub-wavelength integration in SOI is relatively new with most of the previously mentioned devices having been demonstrated in the last few years. This raises the question of how much further these functionalities can be optimized. We therefore turn our attention to designs generated by state-of-the-art optimization processes.

2.6.1. Evolution: Natural Selection

Photosynthetic organisms absorb solar energy to activate chemical processes that produce oxygen and drive the carbon cycle. Up to 40% of photosynthetic activity is driven by aquatic phytoplankton called diatoms [134]. More than 150,000 species of diatoms have evolved to thrive in most aquatic habitats. Yet despite their ubiquity, diatoms utilize fairly conventional pigments such as chlorophyll A that offer no apparent advantage to the photosynthetic process [135]. Additionally, their limited motility in the turbulent photic zone indicates a lack of directional orientation toward the sun, which puts them at a significant disadvantage. This is why their proliferation in such circumstances suggests the possibility of a physical mechanism that aids the diatom in photosynthesis. Indeed, diatoms grow a biosilica shell that hosts a lattice of periodic perforations resembling a 2D PhC [6, 136], which is speculated to assist in light harvesting. Evidence to corroborate this speculation is mounting, such as recent numerical analyses of the band structure of the shell [7] as replicated in Figure 2.15 for the *Nitzschia Filiformis* species.

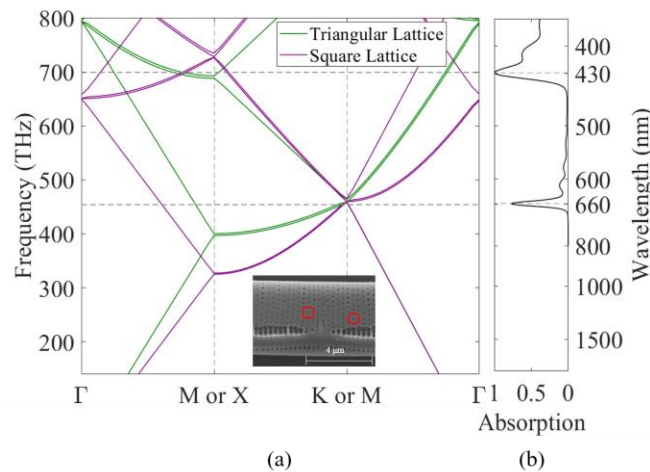


Figure 2.15. (a) Band diagram of a biosilica frustule with square (purple) and triangular (green) lattice configurations with pitches of 330 nm and 300 nm respectively, for water holes of 80 nm diameter. (b) The absorption spectrum of chlorophyll A with peaks at 449 nm and 660 nm [137].

An examination of this band structure reveals promising insights into their light harvesting mechanisms. For example, pseudogaps in the band diagram are seen to coincide with the absorption peaks of chlorophyll A. This high density of optical states suggests a slow light effect to compensate for the limited photosynthetic conversion rate of the chloroplasts during periods of heavy illumination. The PhC topography also exhibits a certain level of disorder, which could be interpreted as fabrication imperfections if every species did not exhibit similar topographical disorder. However, the proliferation of diatoms over several millennia of evolution is testament to

the level of optimization that they have undergone through selective mutations. We therefore speculate that disorder induces a higher fabrication tolerance by effectively smearing the band structure around the absorption peaks to increase the bandwidth of the pseudogap effect. Similar disorder has been observed in designs that demonstrate an improved fabrication tolerance [114, 128, 138] as compared to regular periodic perturbations. This has been further verified by computational optimization techniques for nanophotonic device design.

2.6.2. Computational Optimization

An explosive growth in numerical simulations employing nonlinear and topology optimization algorithms has accelerated design principles in many fields [139, 140] of which nanophotonics is no exception. Advanced pattern recognition algorithms using artificial intelligence have produced designs that contain insights beyond known engineering principles. Many categories of these optimization algorithms have been investigated in the context of SiP design optimization. A gradient-based search tests for convergence, computes a search direction and step length, and then iterates through the parameter space of a device design to improve its performance. A combinatorial search optimizes feasible solutions by eliminating infeasible results. Neural networks on the other hand, use one-time training instances to build and curate a large dataset of examples from which to infer patterns. Although iterative optimization techniques are appreciably more informed than the relatively blind methods of machine learning, both produce informative results. For example, polarization splitters have been realized using inverse design [141, 142] and nonlinear optimization [143] techniques. These methods have produced the MMI-based PBS device designs in Figure 2.16, which are similar to those presented in Section 2.5.2 albeit with the utilization of currently undeveloped mechanisms of dispersion engineering.

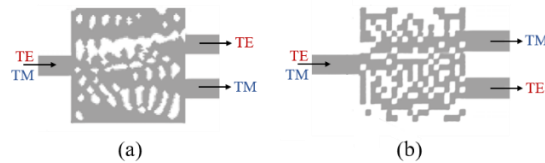


Figure 2.16. Schematics of reverse engineered PBS devices with relatively small footprints of (left) $2.8 \times 2.8 \mu\text{m}$ [141], and (right) $2.4 \times 2.4 \mu\text{m}$ [143].

The performance of such devices, despite their compact form factors, are as yet unachievable through known design principles. While such designs demonstrate the value of optimization techniques in generating hitherto unforeseen results, caution must be taken when a device design

precedes an understanding of the mechanisms at play in its operation. The value of this process could be seen as providing novel and possibly unintuitive directions for future research.

2.7. Conclusion

The benefit of combining sub-wavelength structures with nanophotonic devices for dispersion engineering was developed and evaluated. In doing so, we have provided a framework for SiP dispersion engineering in the SOI platform. These guidelines are based on an intuitive understanding of the unique behaviours of modes that reside in different regions of a band diagram. For example, the diffractive regime is used for external coupling; the reflection regime for filters, resonators, and reflectors; and the propagation regime for broadband responses, polarization discrimination, and index tuning. Based on these tools, known concepts in Bloch-Floquet theory have been integrated in conventional geometries. Tactics such as tuning the index in a tilted SWG [71], broadening the bandwidth of an MMI [41, 120], lowering the insertion loss of an edge coupler [113], increasing the coupling range of a directional coupler [57], or widening the extinction ratio in a PBS [123, 124] have improved and expanded device performance. Furthermore, natural and computational optimization techniques have produced specialized, dispersion engineered optical devices that we have yet to completely understand [6, 7, 141, 143]. Be it natural or human-made, these devices suggest new directions for the iterative scientific process to investigate and subsequently develop. With the aid of biomimetics and reverse engineering, the gap between our understanding and our design achievements leaves much to be explored.

3. Solar Energy Harvesting in Diatom Frustules

“...and it's the phytoplankton that is the basis of all life in the ocean.”

– Sir David Attenborough

In the designs in Chapter 2, light was manipulated by sub-wavelength structures in Si under SiO₂ cladding. However, an appreciable fraction of the light propagates through the SiO₂ cladding. Techniques to manipulate light in the cladding have not been heavily explored mainly due to limitations in the fabrication resolution of SiO₂ structures on-chip. Further patterning of the cladding as well as incorporating disorder into these patterns offers a new avenue for the development of SiP technology. Specifically, this allows us to engineer the dispersion of the devices, and consequently their optical bandwidth as well as tolerance to fabrication variations. This supports the development of devices capable of capturing ambient light rather than only coupling incident light. However, commercial techniques for fabricating on-chip, sub-wavelength features are still nascent. So instead, we look to natural systems.

In this chapter, we investigate the solar energy harvesting mechanisms of frustules belonging to the diatom species *Nitzschia filiformis* (*Nf*). Our methodology combines experimental techniques with numerical modelling as described in section 3.2. These techniques were used to analyze the localized optical behaviour of the frustule and therefore model its optical response in section 3.3. The limitations and implications of the work are discussed in section 3.4. Finally, the findings are summarized in section 3.5.

3.1. Introduction

It has been argued that in the next decade, natural systems alone could mitigate some 37% of the green house gas emissions necessary to limit global warming to 2°C [144]. Photosynthesis is the dominant natural process used to sequester organic and inorganic carbon from CO₂, thereby releasing oxygen that sustains life forms. In accomplishing this, photosynthesis utilizes 8 times as much solar energy as the current overall energy consumption by human society [34]. Studies on primary productivity estimate that almost half of all photosynthetic activity can be attributed to phytoplankton [145], of which the most common types are unicellular micro-organisms known as diatoms [35]. Diatom photosynthesis yields around 25% of atmospheric oxygen [146] and 40% of oceanic carbon fixation [134]. In this context, better understanding of how diatoms couple photons

to drive photosynthetic processes may directly inform and enhance technological developments in solar energy harvesting [147] and carbon sequestration [148].

The proliferation of diatoms is partly due to their capacity for exponential growth, which indicates the potential to achieve reproducible, tailored optical device constructs with yields far beyond current manufacturing technologies [149, 150]. Their ability for niche differentiation has spawned more than 100,000 species which are distributed across almost every type of aquatic habitat [35]. This biodiversity is a result of 150 million years of evolution [151] with cell division occurring daily under favorable conditions [35]. Yet despite such a large genetic diversity, diatoms have similar characteristics. These similarities indicate a convergence of the corresponding evolutionary processes. For example, every species assimilates silicic acid monomers [152] into a hydrated, biosilica cell wall known as a frustule [153], which contains the protoplasm. Commonly, identification of the radial or bilateral symmetries of the frustule leads to non-phylogenetic classifications of diatoms into centric or pennate types, respectively [35]. In certain species of diatoms, the outer cell wall, or frustule, appears to offer mechanical protection [154], chemical buffering [155, 156], and optical manipulation [147].

Diatoms are found in the euphotic zone, that is, the upper layers of water which are shallow enough to allow the penetration of sunlight, but turbulent enough to continually disturb the orientation of suspended diatoms. In such circumstances, the cell cannot easily maintain maximal exposure to incident sunlight as compared to terrestrial plants. The resulting low and intermittent illumination imposes a strong requirement on the cell to harvest sunlight efficiently. Although diatom pigments, antenna complexes, and photosystems exhibit functionality to assist photosynthesis [135, 157], their collective contribution still does not explain the photosynthetic conversion efficiency of diatoms [147]. This suggests that light harvesting mechanisms might also exist that mediate interactions at the interface between the chloroplasts and the optical field. These mechanisms are embedded in the optical properties of the frustule. The frustule is known to facilitate the capture and redistribution of photosynthetic active radiation (PAR) [158-161]. In some pennate and centric diatoms this capability has been attributed to PhC [7, 136, 150, 162-166] and lens [160, 167-171] behavior that appears to be determined by the sub-wavelength architecture of the frustule. However, analysis of the individual optical components does not explain how they are recruited by the frustule as a whole, i.e., at a systems level, to enhance photosynthesis. Therefore, there is a need to identify and analyze the different optical mechanisms at play in the

frustule that collectively govern its overall optical response [147, 161]. We therefore seek to understand how the optical functionalities of the diatom frustule conjoin to harvest PAR for the chloroplasts in the cell.

The frustule is a micron-scale silica structure that is formed by active transport of monosilicic acid into a silica deposition vesicle from which it is eventually extruded. The frustule resembles a decorative pillbox, comprising a top and bottom valve united by one or more girdle bands. The silica is perforated with lattices of nanoscale holes (or areolae) causing a somewhat periodic modulation of the refractive index that results in a PhC response [136] to PAR [7]. As optical device constructs for on-chip optical manipulation, PhCs have been widely designed and fabricated because they provide functional attributes like waveguiding [172], diffractive coupling [173], dispersion engineering [174], lensing [175], and spectral filtering [131, 176]. Unsurprisingly, it has been speculated that the PhC features of diatom frustules might have evolved for cellular PAR manipulation [136, 177]. Interpreting the frustule PhC architecture in a simplified model of square or hexagonal lattices, the patterned shell has been shown to host guided modes [7, 136], resonant bands [164], pseudo-gaps [150], and radiation modes [136]. Valuable as these simplified models are, frustules exhibit nonuniformities in lattice pore size and distribution, and in other morphological features like silica valve thickening and tapering [164, 178-180]. These nonuniformities have been associated with shifts in transmission wavelengths [164] and the presence of quasi-stop bands for blue light absorption [180]. Although nonuniformities and disorder are characteristic of the PhC-like properties of diatom frustules, their effect on the optical response has not been investigated. There is good reason to probe the effect of disorder on PhC properties. For example, when fabricated as optical devices, disordered PhCs (DPhCs) exhibit diffused illumination and enhanced absorption [181, 182], phenomena that might find correspondence with the observed redistribution of light in frustules [158]. In photonic technologies, spatial variations in PhC lattices have been used to guide propagating modes [183]. Indeed, DPhCs have been intentionally introduced in devices to customize performance, broaden resonance bandwidth, or improve tolerance [184]. These are properties that increasingly resemble those of the naturally occurring DPhCs observed in some diatom frustules [174]. Recent advances in metalens design might also explain the wavelength-selective [165, 185, 186] and wide-angle [168] focusing [167, 168, 171, 187] of DPhCs in the valve. The potential benefits to the micro-organism of disorder in the frustule are not known because the optical response of the

frustule itself has not been extensively evaluated. For example, the valves of some centric diatoms have been shown to focus light entering the cell and to back-scatter light escaping the cell [158, 168]. This type of asymmetric optical response suggests that the valves might facilitate transmission to the cell and retention inside it. In the whole frustule, the combination of upper and lower valves might be viewed as a Fabry-Perot cavity [188] whose purpose is to retain light. This view aligns with observations of enhanced absorption of 420 nm light in the region of the quasi-stop band of the frustule of *Melosira varians* [180]. Similarly, the frustule asymmetry in the centric diatom *Coscinodiscus granii* was proposed to not only enhance absorption, but that structures internal to the cell wall behave as diffraction gratings to redistribute incident light more evenly to the organism, particularly the chloroplasts and auxiliary pigments [158]. Despite the increasing sophistication of optical experiments on diatoms, our understanding of the relationship between the complex optical and biological functionalities of the diatom frustule is still evolving [147]. For example, the way that the valves and girdle bands interact in the transport and scattering of light [189] has not yet been explored in much detail to determine how they collaborate as part of the sunlight harvesting mechanism. Moreover, little attention has been paid to the role of disorder in the frustule silica framework and how DPhC features might assist in the coupling and redistribution of light.

In the present work [2], we combine experimental measurements of an entire frustule construct with numerical simulations of its individual optical functionalities to provide a level of integration between frustule form and optical function. Our study focuses on the pennate, biraphid diatom species *Nitzschia filiformis*. This benthic species inhabits sediments in lake beds where the diatom makes use of its motility to position itself at the most beneficial light penetration depth to optimize light exposure [190]. The frustules were studied using our previously developed toolkit comprising 4 microscopy techniques with complementary simulations [6] combined with our process for connecting photonic band diagrams to sub-wavelength features [1]. Our preliminary investigations of *N. filiformis* frustules revealed various PhC lattice configurations inherent in the valve [7]. Here, we use this toolkit to identify and analyze a number of localized optical functionalities across the frustule and map them to the overall optical response. To determine the combined effect of the different optical processes at work, we model the frustule as an optical circuit, treating it as an ellipsoidal optical cavity embedded with these functionalities. Our model establishes how the

individual optical functionalities might combine to yield three solar energy harvesting mechanisms of capture, redistribution, and retention, which enhance photosynthesis in the cell.

3.2. Methods

Diatom cells of the species *N. filiformis* were obtained from the Culture Collection of Algae at the University of Texas at Austin. The exenic samples were cultivated in a modified growth medium under illumination by a diurnal light/dark cycle. The light sources were a 1:1 mix of cool and warm fluorescent lamps which were placed above the samples. Air exchange was achieved by passive diffusion into Erlenmeyer flasks with minimal agitation to prevent breaking the frustules. This arrangement simulates a benthic environment that is characteristically absent of strong currents. Bacterial accumulation was minimized by occasional aseptic transfers once a threshold cell count and average frustule size were obtained. The threshold cell concentration ensured that a sufficient population was available for imaging. Samples of frustules were cleaned and imaged based on previously established protocols [6]. A mixture of oxidizer consisting of 3 parts concentrated sulphuric acid and 1 part 30% hydrogen peroxide (piranha) was used to clean the silica frustules of cellular organic material. The valves and girdle were typically detached by the oxidizing agent.

An FEI Quanta 450 FE-ESEM scanning electron microscope (SEM) was used to obtain 126 images from 3 different cell cultures over a period of 2 years. One of these cultures was grown in-house using the previously described protocols. For imaging, the frustules were drop-casted onto a coverslip and coated with a 5-10 nm layer of Pt. Frustule dimensions were measured from 43 SEM images which detailed 22 valves and 25 girdles. The dimensions and topography of the cleaned frustules were cross-verified with whole diatoms to ensure that the separated frustule components were not damaged by the cleaning process. From the SEM images, the 3D frustule architecture was reconstructed with a computer aided design (CAD) model using Autodesk Inventor, which was used for visualization purposes. Since the occurrence of multiple girdles was indicative of a diatom undergoing cell division, the model comprised of only a single girdle. The surface areas of the valves and girdles were estimated by using rectangular prisms with only 5 and 4 faces, respectively. The elemental composition of the frustule was determined by energy dispersive X-ray analysis (EDX) in the SEM.

The optical response of different regions of the frustule was simulated using the 3D finite difference time domain (FDTD) method in Ansys Lumerical FDTD. The bandwidth of the optical

source was matched to the solar spectrum at sea level. The structure was excited by light sources including plane waves and optical dipoles inside the biosilica. The core material was set as silica with a refractive index of 1.45 [78] to represent the hydrated biosilica material of the frustule. The cladding was set as water at 20°C with a refractive index of 1.33 [78] corresponding to the inner cytoplasm and outer benthic environment of *N. filiformis* [190]. To simulate the response of the girdle, the central region of the frustule was flattened into a planar slab. The in-plane regions of the frustule were emulated using periodic boundary conditions. The external environment was represented by perfectly matched layers at the top and bottom boundaries. For simulations of the entire frustule, the DPhCs and arrays of holes were substituted by birefringent materials using effective medium theory [80, 81, 150] in order to lower the mesh resolution and therefore reduce the computation time.

The positions and diameters of the holes in the central lattice were mapped from the contrast of the SEM images [178]. Their corresponding point pattern was reconstructed as a lattice. The three main lattice parameters were measured by Delaunay triangulation. The distance between each pair of holes was measured as the localized pitch and cut-off at 450 nm to remove extended connections at the edges. The longitudinal pitch was measured along the length of the frustule and the lateral pitch was measured along its width. Their distributions revealed the extent of anisotropy in the lattice. The position of each hole was used to measure the angles between triplets of neighboring holes. To analyze the effect of variations in the lattice, each triad of holes was evaluated as an extended PhC using the supercell approximation [191], which produced one corresponding photonic band structure. Using a similar approach as that previously used to analyze quasi-periodic vibrational signals [11], these photonic band diagrams were then combined into an ensembled average, which revealed the effective photonic band structure of the DPhC.

Scanning, near-field optical microscopy (SNOM) and concurrent atomic force microscopy (AFM) measurements were performed using a WITec Alpha 300S microscope. The SNOM was operated in transmission mode [192], that is, with light coupled to the sample by the aperture in the near-field and collected by the bottom lens in the far-field. In this configuration, light passed from the upper objective through the aperture to the sample and was collected by the lower objective lens. Light was transmitted through an objective lens with NA 0.4 and strength 20x onto an apertured SNOM probe tip. The tip was magnetically attached to a cantilever below the lens and kept at a fixed angle. The inner diameter of the aperture was either 90 nm or 150 nm and its

Al walls were 100 nm thick. This size was large enough to facilitate evanescent coupling into the sample yet small enough to resolve the individual holes of the PhC. At the aperture, an evanescent field interacted with the fine structure of the sample to convert it to a propagating wave [193, 194]. These propagating waves were collected in the far field by a 60x, 0.8 NA lens below the sample and detected by a photomultiplier tube connected to an oscilloscope. Pixels in the image were collected 35 nm apart over a duration of 0.5 s per datapoint. The setpoint, power gain, and current gain for the AFM feedback were set at 2 V, 4%, and 4% respectively. The near-field response was further correlated with the topography of the sample using AFM. The SNOM was operated at two wavelengths – red at 660 nm (or 454 THz) and green at 518.9 nm (or 577 THz) using laser diodes LP660-SF60 and LP520-SF15, respectively, from Thorlabs. Blue wavelengths were not accommodated by the lensing system as explained in Appendix A). Both diodes were operated by a laser mount LDM9LP connected to a controller LDC ITC 4001. There was no analyzer placed before the detector to separate polarizations [192].

Dark field microscopy (DFM) measurements were conducted using a Cytoviva Hyperspectral Imaging system. This configuration used a beam of normal incidence. A Tungsten source illuminated the valve with a white light spectrum within the wavelength range of 400-1000 nm (or 299-749 THz).

The microscopy images represented the highest resolution obtainable with the given instrumentation.

3.3. Results

3.3.1. Architecture

The biosilica frustule consisted of two bilaterally symmetric valves which were separated by one or more girdle bands [35]. It was reconstructed from SEM images as depicted in Figure 3.1. The reconstructed model was verified by images of uncleaned samples and observations of live cultures under an optical microscope. The following reported dimensions refer to the average values of each measurement. Both valves and girdle exhibited a relatively uniform thickness of 400 nm. Only the region around the raphe was thicker than the rest of the frustule. The average height of the valve and girdle were 1.6 μm and 1 μm respectively. The overall height of the frustule depended on the number of girdle bands between the valves. Its length and width were determined by the girdle, which was $110 \pm 10 \mu\text{m}$ and $4 \pm 1 \mu\text{m}$, respectively.

The valves occupied approximately 78% of the exposed surface area of the frustule. They were flat with curved sides and tapered at the ends to connect to the girdle. Each valve hosted a raphe on one side such that the raphes were diagonally opposite to each other as shown in Figure 3.1(e). The raphe consisted of two, 25-nm-wide slits which spanned almost half the length of the valve from the central nodule to the tail as shown in Figure 3.1(d). Although the slits could compromise the structural integrity of the valve, they appeared to be scaffolded by a series of inner protrusions underneath it. The flat region was perforated by a central lattice of holes, which terminated at the raphe and edges. Similarly spaced holes were present alongside the raphe albeit with larger diameters. The girdle also exhibited rows of holes with the same diameter and spacing as the central lattice.

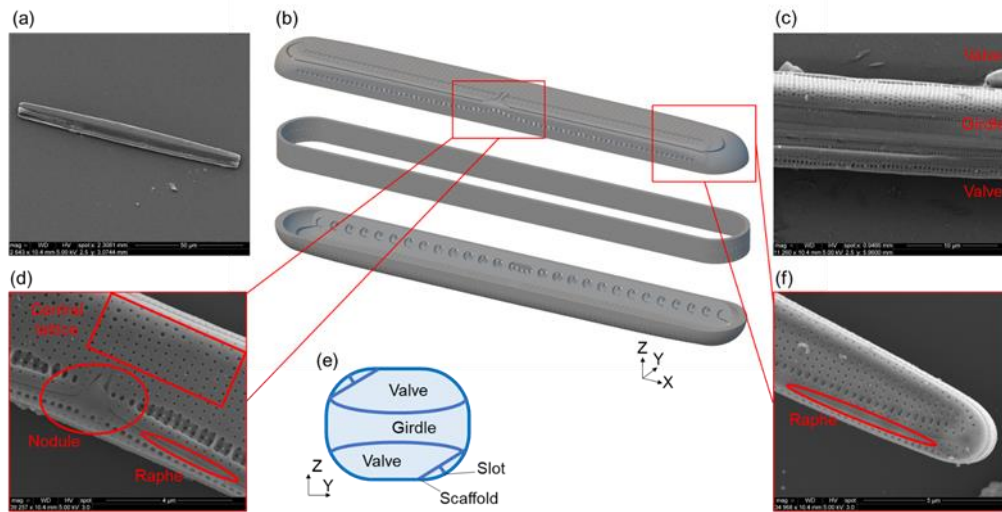


Figure 3.1. Architecture of the frustule. (a) SEM of a frustule. (b) Exploded 3D CAD model of the frustule. (c) SEM of a side. (d) Central region of the valve. (e) Schematic of the cross-section. (f) Tail.

By EDX, the elemental composition of the frustule yielded 39% Si, 52% O, and 9% C, along with traces of Cu and Fe. The dominant phase is silica, while the presence of C can be attributed to organic species incorporated in the porous silica matrix during the frustule production [195]. We approximated the refractive index, n , as that of bulk silica [150] (this is validated in Appendix A). Its absorption was assumed to be low enough to incur negligible loss over the duration of the transient optical response. Due to the low refractive index contrast with the surrounding water and inner cytoplasm, as well as the thinness of the frustule, optical confinement was weak. This condition improved coupling to the cell [158, 163] (see Appendix A for details).

3.3.2. Central Lattice

The central lattice, shown in Figure 3.2(a), spanned most of the surface area of the valve. Its localized parameters were mapped in Figure 3.2(b) to reveal a DPhC with longitudinal periodicity and randomized perturbations. The measurements in Figure 3.2(c,d) confirmed that the diameter and spacing of the holes were distributed about a mean value. Hole diameters were 80 ± 10 nm with a spacing of 300 ± 30 nm corresponding to the width of the striae, that is, the lateral columns of pores of along the valve. Each triad of neighboring holes subtended a slightly different angle as seen in Figure 3.2(e). This gave rise to interspersed square and triangular lattice symmetries resulting in a generally hybrid, ‘oblique’ configuration. Any variations in the PhC proportionally altered its photonic band structure [164], as shown in Figure A.2. The underlying photonic band structure of the DPhC is shown in Figure 3.2(f) as an ensemble average of the photonic band structures obtained from each triad of holes [178] (see Methods). Its corresponding photonic density of states (DOS) is shown in Figure 3.2(g).

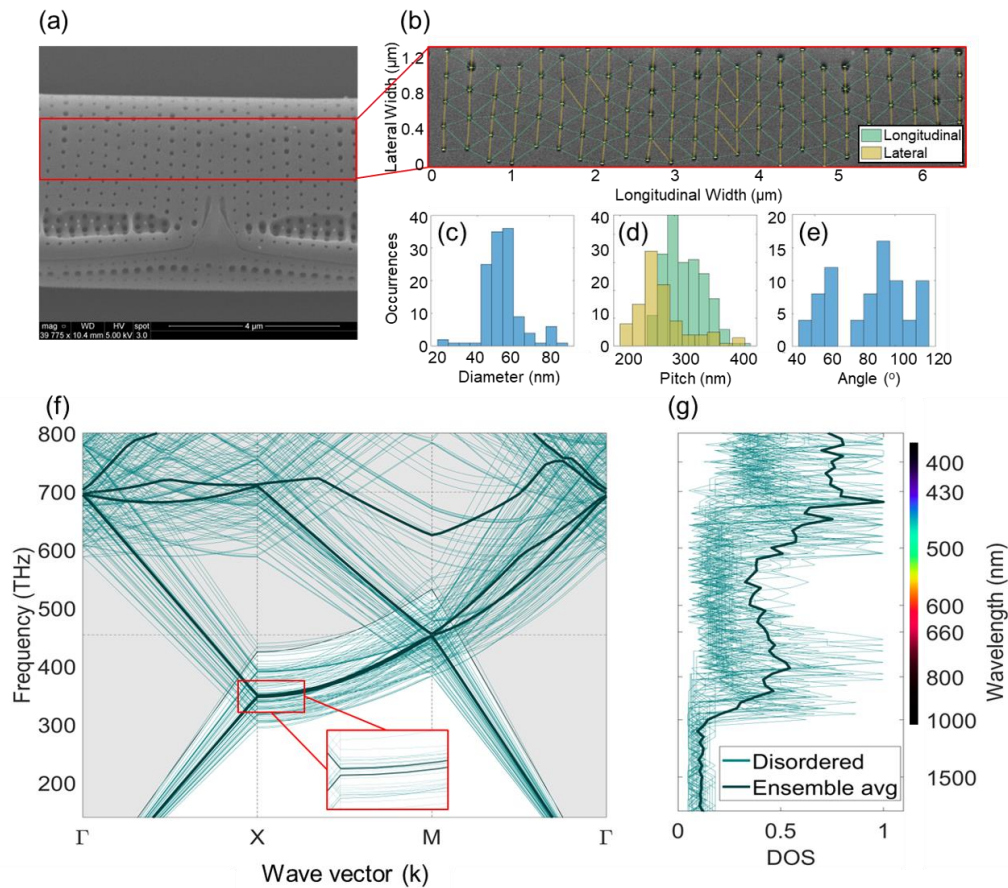


Figure 3.2. Ensemble averaged photonic band structure of the central lattice. (a) Central region of the valve with a (b) zoom-in of the lattice showing (green) longitudinal and (yellow) lateral spacing. (c) Measured hole diameters, (d) longitudinal and lateral spacing, and (e) angles between holes. (f) Photonic band diagrams and (g) corresponding DOS

of each triad of holes with an ensemble average showing the effective optical response. In (f), the shaded gray area indicates the light cone and inset shows the adjacent guided modes.

In this ensemble average, multiple bands are present in the PAR wavelength range of 400-800 nm (or 375-749 THz) [158, 161]. Two guided modes are represented by the adjacent, parallel bands in the light cone between the X-M symmetries and wavelengths of 650-800 nm (or 375-461 THz). The gap between these bands is negligible due to the small hole diameters and low index contrast of the DPhC. This enables evanescent coupling between them, which effectively combines their field distributions and DOS. The physical significance of a combined mode field distribution is a higher probability of overlap with incident light and therefore higher coupling to the structure, which was supported by longer photon lifetimes due to the combined DOS [136] (see Appendix A). The effect is even more prominent in the quadruple degeneracy at the Γ point ($k=0$) around 440 nm (or 681 THz), which results in a heavily smoothed mode field distribution and high DOS. The reduced slopes of the bands at the pseudogap [150] also indicate a lower group velocity and therefore stronger light-matter interaction. Since these bands above the light cone represent radiation modes, their large number indicates that a variety of wavevectors are available for coupling [136].

The consequence of perturbations in the lattice is an effective ‘smearing’ of its corresponding photonic band structure as shown in Figure 3.2(f). As a result, a larger range of wavelengths and wavevectors is accommodated by each band, and the DOS is spread out, especially at the peaks. This broadens the bandwidth and widens the acceptance angles of the modes and resonances in the DPhC. The improvement in its response is also evident from the DOS shown in Figure 3.2(g), which correlates with the absorption spectrum of the chloroplasts [158, 180, 196] better than for the case of a regular PhC [7]. This shows how disorder in the central lattice contributes to the PAR capture mechanism of the frustule, which could enhance photosynthetic conversion in the chloroplasts (this subject is elaborated in Appendix A). Such a response might also provide photoprotection during periods of high illumination by restricting light at the frustule [165, 197-199] so that it does not damage the chloroplasts.

Figure 3.3 shows the concave interior of the valve. The uniform background is due to the cover slip on which it the valve was placed. The localized optical response of the central lattice was examined by SNOM and concurrent AFM as shown in Figure 3.3(b,c) and Figure 3.3(e,f), respectively. At each position, the contact between the probe tip and the sample was verified by

the AFM image and referenced with the topography observed in SEM images. In this way, the AFM and SEM images complemented each other. The blurred regions at the edges of the valve were caused by the limitation of the probe tip in accessing regions of high curvature. The edge of the valve was found to be $1.2\ \mu\text{m}$ higher than at the center. Our analysis and interpretation of the SNOM data are explained in Appendix A. The parallel, bright lines in the central lattice are spaced $300\ \text{nm}$ apart as shown in Figure 3.3(f). These correlate with the guided modes in the band diagram at $660\ \text{nm}$ (or $454\ \text{THz}$). Their lateral orientation confirms that light was diffracted into lateral circulation by the longitudinal periodicity of the lattice. This also explains the brightness at the edges of the valves in the SNOM image in Figure 3.3(f) and the DFM image in Figure 3.3(d).

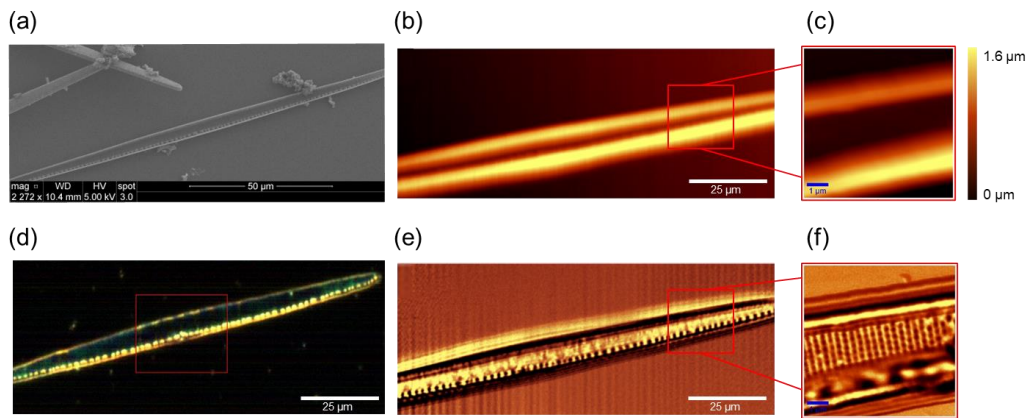


Figure 3.3. Microscope images of the interior of a valve. (a) SEM, (b) AFM with (c) a zoomed-in region, (d) DFM, (e) SNOM at a wavelength of $660\ \text{nm}$ with (f) a zoomed-in region. The SNOM and AFM images were obtained concurrently for (b) and (e) as well as (c) and (f).

In DFM, the light source was blocked so that only scattered light reached the detector. This contrasts with SNOM which only detects transmitted light. DFM therefore imaged the far-field response of the DPhC, whereas SNOM imaged the near-field response. In this sense, the images produced by DFM and SNOM are complementary to each other. The scattered light in the DFM image reveals the wavelength-dependent spatial distribution of the optical response, that is, it shows which wavelengths had interacted with the valve at a given location. As seen in Figure 3.3(d), the central lattice exhibits a green hue, and the valve edges are yellow with traces of red. The green hue indicates that the $400\text{-}600\ \text{nm}$ wavelength range (or $500\text{-}749\ \text{THz}$) from blue to yellow had coupled to radiation modes of the central lattice, which correlates with the band diagrams in Figure 3.2(f). Note that coupling between the radiation modes and free space was bidirectional due to the optical reciprocity of biosilica. So, light that had coupled with the valve

was subsequently radiated after a certain propagation length. This highlights the significance of the valve width, which was sufficiently narrow for laterally propagating light to reach the edges before it could be radiated. This phenomenon therefore contributes to the solar energy harvesting mechanism of retention. In a whole frustule, this light would continue to propagate into an adjoining girdle rather than be scattered from the edge of an isolated valve as in the DFM image. The brownish-yellow color at the edges implies that wavelengths above 560 nm (or 535 THz) either couple into it from free-space or are guided into it from the central lattice. The latter case correlates with the sequence of parallel, bright lines observed in the SNOM images in Figure 3.3. Both cases correlate with the resonance points and guided modes in the band diagrams of Figure 3.2(f). The high intensity observed around the raphe merits a deeper investigation of its optical response.

3.3.3. Raphe

The raphe consists of two longitudinal slits surrounded by a row of holes on either side and scaffolded by protrusions underneath it. Although the spacing between holes is the same as that of the central lattice and girdle, their diameters are about twice as large at 160 ± 15 nm. Since the raphe is known to facilitate locomotion [200], the larger diameter of the holes can be assumed to accommodate the secretion of material for propulsion [35] while the hole periodicity maintains the optical response of the central lattice. The inner protrusions are also periodically spaced. This region exhibits a particularly intense accumulation of yellow light in both DFM and SNOM images, a feature that indicates a high localized DOS (LDOS) [201]. Its behavior can be evaluated using the 1D band diagram shown in Figure 3.4(c), which reveals a resonance at the yellow-red wavelengths. The lack of holes at the nodule and raphe creates defects in the DPhC giving rise to localized states [201].

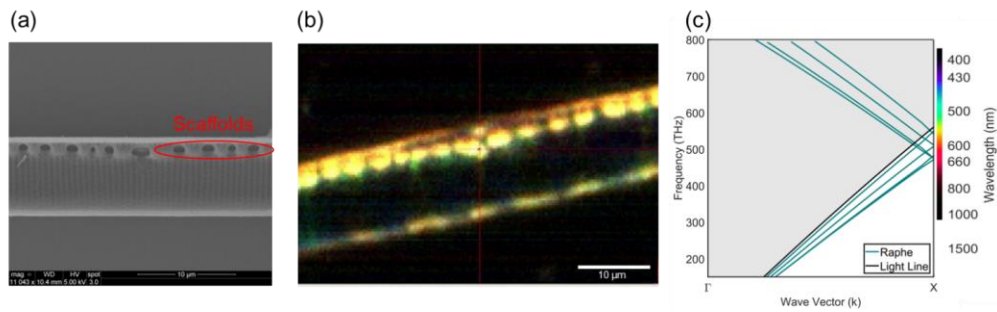


Figure 3.4. Optical response of the region around the raphe. (a) The array of inner protrusions underneath the raphe. (b) Accumulation of yellow light at these protrusions (corresponding to the red box in Figure 3.3(d)). (c) 1D photonic band diagram of this region.

At the raphe, yellow light accumulates at the protrusions along its length. This effect is attributed to the relative thickness of biosilica which increases the LDOS and enables the protrusions to act as temporary reservoirs of light. In this sense, the resonance of the rows of holes surrounding the raphe is supported by the retention of light in the protrusions underneath it. The accumulation of light in this region is therefore amplified by its high LDOS and low confinement, which contribute to retention of light in the frustule for the benefit of photosynthetic absorption in the cell.

3.3.4. Tail

The curvature of the tail resembled a tapered, lensed fiber. It was therefore assumed to enable butt-coupling between the frustule and free-space. Indeed, our simulations showed an insertion loss of 1.4 dB at 450 nm as shown in Figure 3.5(c). The curvature exhibited in the tail region prevents the girdle from operating as a longitudinal racetrack resonator, as observed in some centric diatoms [158, 166]. Once butt-coupled, the light propagates longitudinally, that is, along the length of the frustule. The pennate symmetry of the frustule implies that this light would be coupled out the opposite tail unless it was laterally redirected as it propagated. In fact, the light can be redirected by the longitudinal periodicity of the central lattice (described in section 3.2) and the rows of holes along the girdle (see section 3.5).

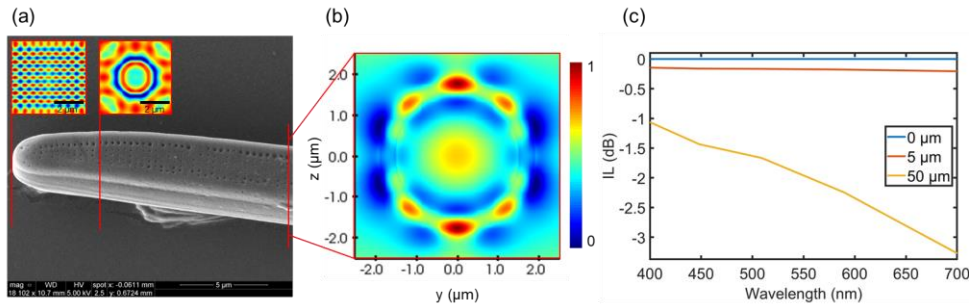


Figure 3.5. Optical response of the tail. (a) The tapered, curvature of the tail with insets at the red slices showing the evolution of an incident plane wave as it butt-couples to the frustule. (b) Mode profile of the butt-coupled, confined light propagating longitudinally along the frustule. (c) Transmission spectrum at each of the red slices in (a).

3.3.5. Girdle Band

As shown in Figure 3.6(a), the girdle band circumscribes and joins the top and bottom valves, and tapers towards the tails. We identified three ways in which light can enter the girdle: by coupling out-of-plane from either free space or the protoplasm, by butt-coupling longitudinally from the tails, or by being guided laterally from the valve edges. Out-of-plane coupling was

assumed to be negligible because the girdle occupies only a fraction of the exposed surface area of the frustule.

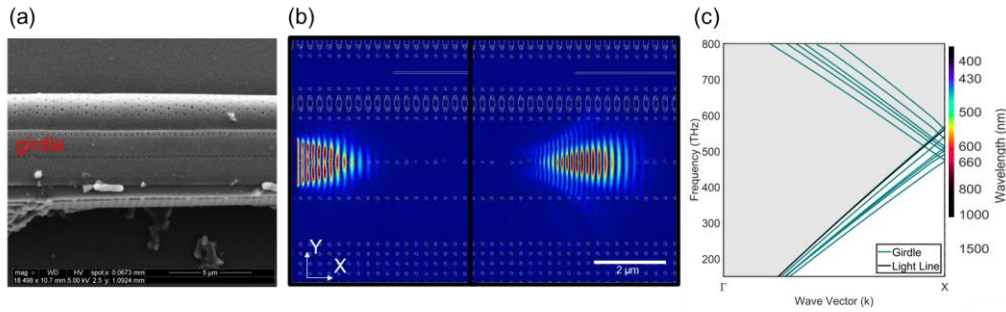


Figure 3.6. Optical response of the girdle. (a) The array of holes along the girdle. (b) Diffraction of light by the holes during longitudinal propagation after (left) 27 fs and (right) 40 fs. (c) 1D photonic band diagram of the array of holes.

The holes in the girdle have a diameter of 78 ± 12 nm and are longitudinally spaced 213 ± 20 nm apart. This spacing matches the periodicity of the central lattice. The holes form a row in each girdle and are spaced approximately 820 nm, corresponding to adjacent girdles. This means that each row functions as an individual grating. Its length and periodicity impose a Bragg effect on longitudinally propagating light. We simulated this behavior as a 1D band diagram in Figure 3.6(c), which reveals a collapsed bandgap within the wavelength range of 550-650 nm (or 461-545 THz). Perturbations in the rows of holes induced sufficient disorder to smear the 1D band diagram (as indicated by the multiple bands), thereby broadening its spectral and directional response [202]. The optical response is shown in Figure 3.6(b) and relates to both remaining methods of light entry into the girdle, that is, longitudinally from the tail and laterally from the valves. Hence, as laterally circulating light reaches the girdle from the central lattice, the rows of holes restrict any longitudinal diffusion so that light is forced to traverse the girdle into the opposing valve. Additionally, as shown in Figure 3.6(b), butt-coupled light from the tails is laterally diffracted by the row of holes. This reduces the amount of light that traverses the girdle longitudinally to the opposite tail. Since the light is incrementally redirected as it propagates down the longitudinal row of holes, this implies that the length of the row is an important factor in increasing the amount of light that is redirected. It is therefore assisted by the elongated, pennate shape of the frustule.

3.3.6. Frustule

The frustule comprises the central lattices, raphes, tails, and girdle. We studied their combined optical behavior to determine the overall response of the frustule. As a whole, the frustule behaves

as an ellipsoidal silica shell in water [203] as shown in Figure 3.7(b). It consists of a cylindrical racetrack (central lattices and girdle, Figure 3.7(a)) which contains two diagonally opposite gratings (raphes) and is capped at both ends by tapered, hemispheric lenses (tails, Figure 3.7(c)).

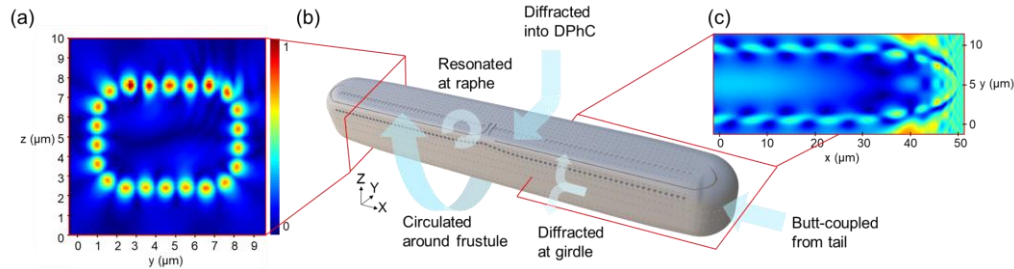


Figure 3.7. Optical response of the frustule. (a) Racetrack hosting lateral circulation around the cross-section shown in Figure 3.1(e). (b) Entire frustule with the blue arrows indicating the various directions of light propagation including lateral circulation, diffraction by the DPhC of the central lattice, diffraction by the row of holes in the girdle, resonance at the raphe, and butt-coupling into the tail. (c) Field distribution of butt-coupling at the tail of the frustule.

The frustule architecture hosts localized optical functionalities which contribute to the solar energy harvesting mechanisms of capture, redistribution, and retention. In our view, incident PAR can be captured by the radiation modes of the central lattice, butt-coupling from the tails as seen in Figure 3.7(c), or at grazing incidence due to the relatively higher refractive index of biosilica. Light entering the frustule can be assumed to be immediately available for absorption by any chloroplast since even unabsorbed light was redistributed across the frustule to regions containing unsaturated chloroplasts. Light is laterally redirected by both the central lattice and rows of holes in the girdle. This light circulates laterally around the cylindrical cross-section of the frustule as seen in Figure 3.7(a). The cross-section therefore can be interpreted as a lateral racetrack resonator with a Q factor of approximately 271 to 822 at wavelengths of 805 nm to 424.8 nm (or 372 THz to 706 THz), respectively. Within the racetrack, we identify additional methods to retain PAR. The DPhC hosts adjacent bands, band crossings, and pseudogaps, which increase the DOS and therefore photon lifetimes in the central lattice. Light from the central lattice is also accumulated by the rows of larger holes around the raphe, which appear to behave as a reservoir for photons. Our results suggest that the individual optical functionalities of the frustule complement each other to harvest PAR.

An analogous photonic circuit diagram of the frustule is shown in Figure A.4 along with a derivation of the modelling approach. We considered the maximum absorption rate of the

chloroplasts to be 3.98×10^{12} photons s^{-1} corresponding to an irradiance of $750 \mu\text{mol photons m}^{-2} \text{ s}^{-1}$ [161]. When the irradiance exceeds this value, we assume that the excess photons would be retained in the frustule. However, when the irradiance is suddenly reduced to $550 \mu\text{mol photons m}^{-2} \text{ s}^{-1}$, then our calculations (as described in Appendix A) indicate that the light retained in the frustule can contribute approximately 9.83% to absorption by the chloroplasts. This would enable photosynthetic activity to continue at reduced light levels. In this manner, our circuit model of the frustule depicts how its retention mechanism can supply photons to the cell during fluctuations in illumination and furthermore, how its harvesting mechanisms can improve the photosynthetic conversion efficiency of the cell during periods of low illumination.

3.4. Discussion

Diatoms exhibit unique light harvesting and energy dissipation mechanisms as compared to other phototrophs. Their proliferation even in harsh, low-light environments, has prompted numerous investigations to determine the solar energy harvesting mechanisms of the cell, including its photo-physiology and optical response. We evaluated the optical behaviour of frustules belonging to the species *N. filiformis*. The architecture exhibited localized optical functionalities including diffraction, resonances, spectral filtering and waveguiding, polarization independence, and wide-angle coupling. The frustule itself acts as an ellipsoidal optical cavity which amplifies these effects. The optical response was strongest within the wavelength range of PAR, which suggests that the frustule could promote absorption of light by the chloroplasts [158, 180, 196]. Biological functionality is co-resident with optical functionality. For example, the holes accommodate the exchange of nutrients with the marine environment [153]. Larger holes around the raphe are also believed to assist locomotion [200].

The thinness and low refractive index of the frustule evokes large mode field distributions with a polarization independent response. This facilitates coupling to the chloroplasts and might even aid fluorescent resonant energy transfer between constituent pigments. Additionally, since both raphes are diametrically opposite each other in the cross-section of the frustule, the space between them is maximized. This space could allow the chloroplasts to cluster around each raphe during periods of darkness, which is supported by in vivo observations of chloroplasts moving within the cell. Our analysis of the DPhC in the central lattice proves that perturbations in the lattice hole periodicity are not only tolerated but may be beneficial (Appendix A). This suggests that disorder might have evolved to enhance the light harvesting efficiency of the frustule. This could likely

happen during the growth process which could be interpreted as a Turing reaction diffusion mechanism during self-organization. However, the processes involved in the structuring and composition modification of the frustule in response to environmental stimuli are yet to be determined [153]. Hence, it remains unproven whether this disorder in the lattice geometry is encoded in the genetic information of the cell, is naturally caused by defects that arise during synthesis, or are an adaptive response to environmental pressures [204]. Additionally, although these perturbations enhance the optical response, such an inference should not be misconstrued. Note that the optical behavior of the sub-wavelength architecture was primarily due to its periodicity, and only enhanced by the perturbations. This is not equivalent to the distortions caused by contamination or metabolic insertion [158], which can be fatal to the cell. We therefore infer that as with most natural systems, diatoms flourish when left to their own (optical) devices and are unlikely to benefit from human interference.

Our results confirm that localized regions of the frustule host specific optical functionalities, which when combined, indicates complementary behavior related to the mechanisms for harvesting PAR. This leads to our hypothesis that the frustule aids photosynthesis in the live cell. It could be validated by *in vivo* measurements of the photosynthetic conversion efficiency of the cell, ideally isolating the response with and without a frustule as well as for each of the three solar energy harvesting mechanisms. To support our hypothesis, we modeled the frustule as a photonic circuit and derived its contribution to photosynthesis for the first time. However, the model faces certain limitations based on its assumptions, which particularly do not account for the spectrally dependent response of the frustule and chloroplasts, the molecular adaptation of photosynthesis under fluctuating illumination, and a characterization of the effect of perturbations to the lattice. These limitations could be addressed by further development of the model in a follow-up study. Such a model could be directly applied to the design process for optical interfaces [174] such as photodiodes, grating couplers, and photovoltaic panels. Additionally, our toolkit for analyzing the optical response of the frustule could be applied to other species of diatoms that exhibit a similar architecture and composition. A large-scale study across different species would refine the model and produce a variety of novel insights by leveraging the architectural diversity of different species. This would pave the way for frustules to be used as passive, biomimetic devices in sensing and communications technologies.

Since diatoms are often found in clusters, it is valuable to consider the implications of our findings in the context of multiple neighboring diatoms. Our simulations indicate that the tapered end of the frustule functions as a butt-coupler. This behavior is similar to lensed fibers, which can be measured by their end-to-end coupling efficiency [205]. Based on the reciprocity of light, we infer that since the tail is capable of coupling light into the frustule, it is equally capable of coupling light out to free space, which could then be coupled into the tail of another frustule. A similar hypothesis may be made for evanescent coupling between adjacent frustules. It suggests that light may be transferred from one frustule to another, which would enable light to be shared between cells in clusters via butt or directional coupling. In fact, the optical interactions between cells could be tested by placing the frustules in the same configuration as fiber-to-fiber coupling experiments. The process might also be assisted by the sticky, excreted biofilm that affixes multiple frustules in close proximity to each other [35]. Such coupling would facilitate the redistribution of excess light across a cluster from areas of high illumination to darker areas. These findings allude to a strong evolutionary advantage of the frustule in maintaining the health of the entire cluster, even when under shadows from cloud cover, vertical mixing, or wave focusing. In this context, diatom frustules could be responsible for an even larger enhancement of photosynthesis than indicated by our single-cell model. An analysis of multiple adjacent diatoms could demonstrate the optical behavior of clusters behaving as a superlattice of frustules [162]. Such results could inform new approaches to developing solar energy farms or decentralized telecommunication networks. For example, silica-based PhCs have already been investigated as low-cost coating films to provide dust protection and light harvesting for photovoltaics [168, 206].

Over millions of years of evolution, successive generations of diatoms seem to have perfected the ability to grow the custom optical tools that are necessary for their survival. A better understanding of their photonic toolbox offers significant implications for biomimetic technological development. Their potential as species-specific devices is further supported by a high adaptability via selective breeding, genetic diversity offering a variety of nanophotonic design constructs, and the compatibility of the biosilica frustule with semiconductor chip fabrication processes allowing them to be directly used as passive optical devices. Since the frustule of each species exhibits a unique combination of optical functionalities, the existence of over 100,000 species has significant implications for new nanophotonic paradigms. For example, the mechanical, biochemical, and optical characteristics of the frustule already allow it to be used as a

meta-surface for biosensing [207], carrier for drug delivery [208], and template for solar energy conversion [147, 159, 209]. Furthermore, their ability to reproduce in exponentially increasing numbers at negligible cost could be leveraged toward mass manufacturing [149]. In this context, diatom frustules could already provide the basis for a nanophotonic, biomimetic platform which combines diatom frustules and silicon photonic chips to realize novel optical functionalities. This could accelerate development in solar cells [209], nano-antennas [177], biofuels [210], and sensing [207]. Since diatoms are light-activated carbon sequestration systems, the cultivation of diatoms alone could support research in carbon sequestration, oceanic health monitoring, biotechnology [37, 149, 210], and solar energy harvesting [37, 147, 211]. Such progress is needed to reduce climate change and accelerate progress toward a sustainable society, which diatom frustules can facilitate at a very high benefit-cost ratio.

3.5. Conclusion

Using a combination of SEM, AFM, SNOM, DFM, CAD modelling, and numerical modelling, we analyzed the optical response of the frustule belonging to the species *Nitzschia filiformis*. Its response was enabled by a higher refractive index of biosilica compared to the surrounding water and cytoplasm. A determining factor was the architecture, which behaved as an ellipsoidal micro-shell with localized, sub-wavelength features including DPhCs, gratings, a racetrack, and lenses. Each feature evoked specific functionalities including coupling, waveguiding, scattering, diffraction, spectral filtering, resonance, and dispersion control. Our analysis of perturbations in these features showed that the frustule can not only tolerate defects but actually exploit them to improve its robustness, bandwidth, and acceptance angles. Together, these functionalities contributed to PAR harvesting mechanisms of capture, redistribution, and retention. Our findings therefore suggest that the frustule could assist the absorption rate of chloroplasts to improve the photosynthetic conversion efficiency of the cell. We developed this hypothesis by modeling the frustule as a photonic circuit. Using it, we estimate that the optical response contributed to 9.83% of photosynthesis in the cell during periods of low, intermittent illumination. Furthermore, these apparently complementary functionalities could justify an evolutionary purpose for the optical response of the frustule. Our analysis of light harvesting mechanisms in the frustule further motivates the cultivation of diatoms for solar energy harvesting, carbon sequestration, and other technological applications.

4. Passive Polarization Splitter

“If you want to find the secrets of the Universe, think in terms of energy, frequency and vibration.”

– Nikola Tesla

Once ambient light is coupled into optical modes as explained in chapters 2 and 3, the modes must then be isolated based on their polarization so that they can be studied in the context of coupling to free electrons.

In this chapter, we propose and experimentally demonstrate a broadband polarization beam splitter on the silicon-on-insulator platform using the concept of multi-mode interference. The need for such devices in SiP is described in section 4.1. It leads into section 4.2 which describes the device design to use an angled, MMI to extract TE₀ and TM₀ polarized light. The effect of key design parameters on the performance is characterized in section 4.3. Based on this characterization, variations of the device were fabricated, and their measurements are presented in section 4.4. The core aspects of the device design are discussed in section 4.5 along with applications and next steps. Finally, the design and demonstration results are summarized in section 4.6.

4.1. Introduction

The development of microfabrication techniques for chip-scale devices has enabled the fabrication of photonic integrated circuits with feature sizes at sub-micron scales. Specifically, SiP technology offers advantages of compactness, low cost, and mass production by virtue of the fact that it uses mature fabrication processes leveraged from the CMOS industry [40, 42]. The degree of light confinement induced by the high refractive index of Si enables compact photonic integrated circuits that are heavily used in fields such as telecommunications and sensing [40]. However, the refractive index contrast between the Si core and SiO₂ cladding results in an effective index difference between the TE, and the less confined TM polarizations for waveguides with an asymmetric cross-sections [212], as is typical of SiP fabrication processes. This manifests as birefringence, which affects devices in the SiP platform. The resultant polarization mode dispersion has the potential to severely degrade the applicability of device designs [213]. This problem necessitates the incorporation of polarization diversity [89] in SiP circuits [214]. It is overcome by using PBSs, which separate incoming polarizations, thereby enabling an independent

treatment of each polarization. An additional advantage is the possibility of doubling system capacity through the simultaneous exploitation of independent polarizations [215].

We present a passive polarization beam splitter that splits input TE_0 and TM_0 modes by exploiting the effective birefringence of 220 nm thick Si in the case of a MMI. The attraction of MMI-based PBS devices such as cascaded [216] or wedge [217] designs is in their resilience to nanofabrication errors, mainly due to large feature sizes [218]. MMI-based designs maintain a high fabrication tolerance due to their larger and relatively simplistic device geometry. This reduces the effect of errors that are introduced by electron beam or ultraviolet lithography techniques for silicon-on-insulator chip design, such as smoothing at sharp edges, sidewall roughness, or inaccurate patterning [219]. However, large feature sizes typically imply a larger device size, and the trade-off is a correspondingly large design footprint (several hundred micrometres in length) [220]. Considering this limitation, there is an interest in reducing the footprint of devices that have relatively simplistic functionality, such as polarization splitting in a PBS. In this regard, increasingly compact and broadband PBS structures have been proposed using SWGs [65, 126, 143], directional couplers (DC) [221, 222], or additional layers [223, 224]. Although these designs offer a significant reduction in size, their applicability is limited because the performance of the fabricated devices is inconsistent due to their small feature sizes, or incompatibility with CMOS fabrication processes. For example, directional coupler based designs [221, 222] have a smaller footprint but the precise gap width implies a high temperature and fabrication sensitivity, which affects repeatability and robustness.

Our work demonstrates a novel idea to reduce the size of a MMI-based PBS by altering the geometry of the design while maintaining a topology of genus zero. A genus zero PBS design indicates that the device consists of a single Si block and does not contain any holes or SWGs. This restriction improves the robustness of the device because it is less susceptible to performance variability caused by fabrication errors and thermal or mechanical stress. This differentiates our MMI-based PBS from MMI based designs incorporating photonic band engineering [65, 143]. Preliminary results have been published in [9]. In this paper, we present the design, simulation, and experimental characterization of the performance of our proposed PBS versus different key parameters. The device has a compact footprint with a width of 4 μm and length of 67.5 μm . An angled input waveguide facilitated the coupling of the TM interference pattern above the MMI. A total of 72 variations for the device geometry were fabricated by sweeping key device parameters

including the input angle, TE port position, TM port position, and bend radius. A representative device was chosen based on its performance in the C-band considering an insertion loss (IL) and extinction ratio (ER) of at least 2.5 dB and 11.45 dB respectively. The incorporation of a waveguide bend at the TE port did not show a significant reduction in the TM crosstalk.

4.2. Design Methodology

The MMI pattern was simulated using the Lumerical FDTD method and cross-verified using the COMSOL Finite Element Method (FEM). The COMSOL simulation was used to further optimize device parameters. The parameter dimensions were optimized for performance, specifically extinction ratio and insertion loss, at a central wavelength of 1550 nm. A self-imposed design constraint on the geometry was to limit the minimum feature size of the device to 500 nm while maintaining its small footprint. This limit was dictated by the width of the input and output waveguides.

4.2.1. Multi-Mode Interferometer

The cross-sectional dimensions of a waveguide constrains the number of modes that it can confine. The input and output Si waveguides had a width of 500 nm and thickness of 220 nm, which allowed for a confinement of only the fundamental TE and TM modes at the central wavelength of 1550 nm. The multi-mode waveguide of width 3 μm confined 16 modes (10 TE modes and 6 TM modes) at a wavelength of 1500 nm, and 14 modes (9 TE modes and 5 TM modes) at a wavelength of 1600 nm as determined from two dimensional (2D) Eigenmode analysis. The interference pattern generated by higher order modes in a multi-mode waveguide was determined using the guided mode propagation analysis technique [119], which predicts the self-imaging length of the MMI to be $3L_\pi$ as shown in equation (2.7). The difference in effective indices between the TE and TM modes in the MMI imposed different self-imaging lengths for each mode, which enable its implementation as a polarization splitter. The self-imaging length was calculated separately for the TE₀ and TM₀ modes to extract their corresponding beat length. All other parameters kept constant, $L_\pi \propto W_e^2$, which implies that a narrower MMI width requires a shorter self-imaging length, and therefore smaller overall size. Hence the width of the MMI was set at 3 μm as represented in Figure 4.1(a). Using Eigenmode analysis, the effective refractive indices of the TE₀ and TM₀ modes were calculated to be 2.839 and 2.0472, respectively. The mirrored single image lengths ($3L_\pi$) for the TE₀ and TM₀ modes in a standard rectangular MMI were therefore calculated to be 75 μm and 53

μm respectively. This suggested a design implementation that extracted the TM_0 mode prior to extracting the TE_0 mode along the direction of propagation. Assuming efficient TM collection, the light propagating beyond the TM port was assumed to contain almost exclusively the TE component. The MMI was therefore tapered beyond the TM port in order to collect all the remaining light at a shorter length than necessitated by the TE self imaging length. The design methodology therefore allowed for a shorter distance of the TE port from the input waveguide, which in turn reduced the overall PBS length from $75 \mu\text{m}$ to $67.5 \mu\text{m}$. Tapering also helped minimize lithography smoothing effects [40, 213], and facilitated better collection by minimizing back-reflections. The fidelity of the interference pattern was maintained by tuning the angle made by the input waveguide with the MMI. The different effective indices for TE and TM polarized light resulted in shifted interference patterns for each polarization as shown in Figure 4.1(b) and (c).

Typical MMI-based PBS designs cascade multiple MMIs to filter out one polarization at its self-imaging length, and subsequently collect the remaining light corresponding to the other polarization at the complementary output. In this design however, both TE and TM fundamental modes were extracted at their self-imaging lengths. The comparably shorter length of the TM interference pattern implied that TM light could not be naturally collected without breaking the continuity of the TE interference pattern. The problem was resolved by extracting TM light above the MMI structure instead of along its expected path of propagation. It was achieved by modifying the directionality of the input light, that is, rotating the input waveguide such that light enters at an angle and therefore propagates at an angle [225]. The rotated input waveguide allowed for the extraction of TM light above the MMI as can be seen in Figure 4.1(c).

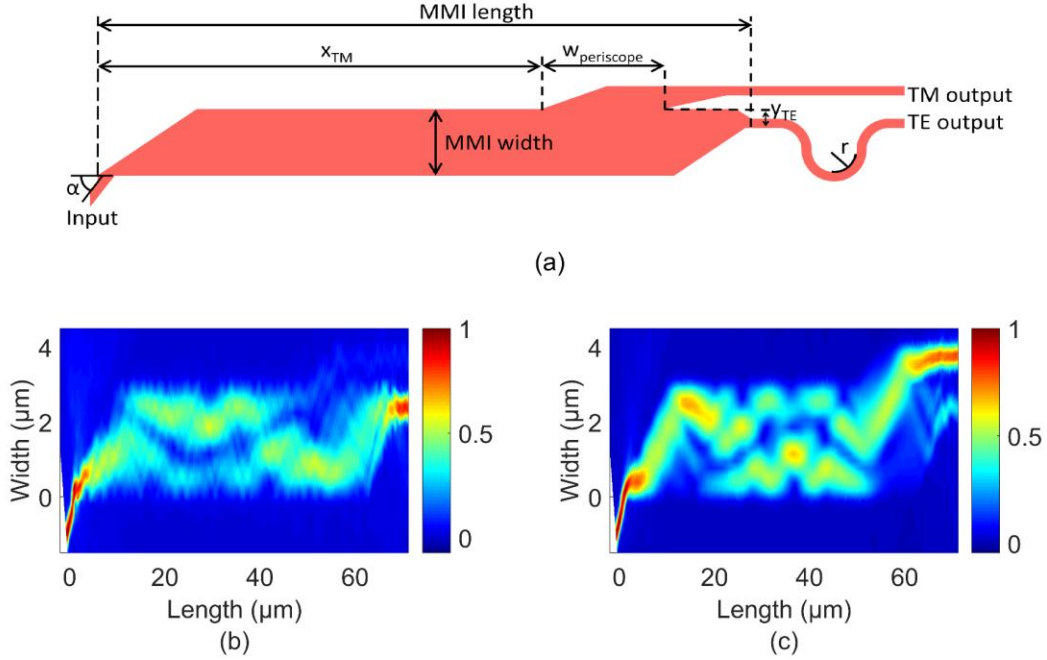


Figure 4.1. (a) PBS device geometry with the addition of an optional waveguide bend. Interference pattern simulation results for (b) TE and (c) TM fundamental modes. Output waveguides are placed at the self-imaging length of the MMI feature to collect TE polarized light at the bottom in (b) and TM polarized light at the top in (c).

4.2.2. Input and Output Waveguides

The PBS ports were tapered out from the MMI to reduce possible back-reflections and therefore ensure optimal transmission into and out of the main MMI block. The mirror point of the TM interference pattern was extended upwards through two techniques. The addition of an extra Si parallelepiped positioned above the MMI at a distance of x_{TM} allowed TM light at the mirror point to diffuse into it due to the gradually varying effective index at that region. Additionally, the propagation of TM light beyond the expected MMI geometry was facilitated by an angled waveguide at the input. The incident angle sufficiently modified the overall propagation direction so that the TM antinode extended into the top block. TM light was therefore selectively collected using this top structure that we will refer to as the periscope. The periscope implementation precluded the need to cascade MMIs as seen in previous PBS designs, because both polarizations were separated in the main MMI itself. The TM waveguide was spaced away from the MMI to minimize coupling between the TE and TM output waveguides. The width of the periscope, $w_{periscope}$, was minimized to reduce TE crosstalk at the TM port. Additionally, the position of the periscope was centered around a region of destructive interference of the TE mode, seen in Figure

4.1, to further minimize crosstalk. Once the TM interference pattern was coupled into the periscope and extracted, the remaining TE light was collected at its self-imaging length. An offset of y_{TE} for the TE output waveguide enabled bi-directional tapering of the MMI towards the waveguide, and therefore significantly better collection.

The inclusion of different waveguide bend radii at the TE output was also considered. This is because the asymmetry of the waveguide cross-section (width of 500 nm and thickness of 220 nm) caused an effective index difference and better confinement for TE than TM. This selective confinement between TE and TM suggested the possibility of incorporating a sufficiently sharp waveguide bend at the TE port to induce the leakage of TM crosstalk, as has previously been implemented in a directional coupler PBS [222]. The experimental characterization was therefore extended to evaluate the benefit of a TE output bend as an optional feature of the design.

4.2.3. Simulation Parameters

The simulation was carried out using FEM available through the Wave Optics module in COMSOL Multiphysics. A matched boundary condition was imposed on the output ports in order to eliminate back reflections. A numerical port was used to solve for the fundamental modes of the given geometry at the input. The waveguide material was Si obtained from the COMSOL material library with a wavelength dependent refractive index following piecewise cubic interpolation of Li 293K [226]. Similarly, the cladding was set to be SiO₂ (Ghosh-0) from the COMSOL material library [227]. Using the numerical port, TE and TM modes were solved separately. This separation allowed for a simpler analysis albeit at the cost of running two separate simulations. A scattering boundary condition was used to eliminate potential reflections caused by decaying waves, and therefore allowed the simulation region to be limited to the device instead of incorporating an extensive cladding region. Additionally, a non-uniform mesh was implemented to obtain higher resolutions where the light was concentrated.

The MMI length was determined to be approximately 75 μm from the self-imaging length formula [119]. However, parameter sweeps in numerical simulations of the MMI for power transmission predicted an optimal length of 67.25 μm . Adjusting the input angle led to an improved contrast in the interference pattern and a clearer separation of TE and TM. The Lumerical FDTD method was used to evaluate the interference pattern when sweeping the input angle. The strength of the interference pattern was measured by the contrast ratio of the pattern calculated using the images shown in Figure 4.1(b) and (c). The angle optimization results were cross-verified with

FEM and produced an input waveguide angle of 29.39° . The bend at the TE port was optimized separately in Lumerical FDTD and resulted in a radius of $3\ \mu\text{m}$.

4.3. Parameter Space Characterization

The device performance was characterized for variations in its geometric parameters to ensure consistency and to probe the design methodology for relatively sensitive parameters. As expected, the response of the MMI was found to be most sensitive to the dimensions and positions of its ports. Hence, the values of the input angle, and output horizontal and vertical positions of the ports were varied. The consequent change in performance was evaluated using the IL, ER, and interference pattern strength as figures of merit [8]. This characterization of the PBS design parameter space informed the choices for parameter values that were consequently fabricated and tested.

Regarding the TM port, its location was optimized using the width of the periscope, $w_{periscope}$, and its horizontal position, x_{TM} . However, since $w_{periscope}$ and x_{TM} are coupled to each other, the problem space was characterized in a two-dimensional sweep of both parameters as shown in Figure 4.2. It was evident that there was no clear optimum for a combination of parameters at the TM port that simultaneously maximized TM transmission (corresponding to IL) while minimizing TE crosstalk (corresponding to ER). The black dots in Figure 4.2 show two parameter sets corresponding to a periscope offset and width of $[54\ \mu\text{m}, 6.5\ \mu\text{m}]$, and $[55.7\ \mu\text{m}, 5.5\ \mu\text{m}]$. As the TM transmission showed a stronger dependence on parameter values, the parameter values chosen for fabrication were determined by prioritizing TM transmission while maintaining low TE crosstalk.

The TE port was characterized over the MMI length (corresponding to the horizontal position of the TE port), and the vertical offset of the TE port from the top. Figure 4.3 shows the surface plot for the two parameters. In this case, preference was given to TE transmission since TM crosstalk was consistently low within the well region of Figure 4.3. Four parameter sets were chosen in and around the well, with the center of the well located at $[67.25\ \mu\text{m}, 0.875\ \mu\text{m}]$.

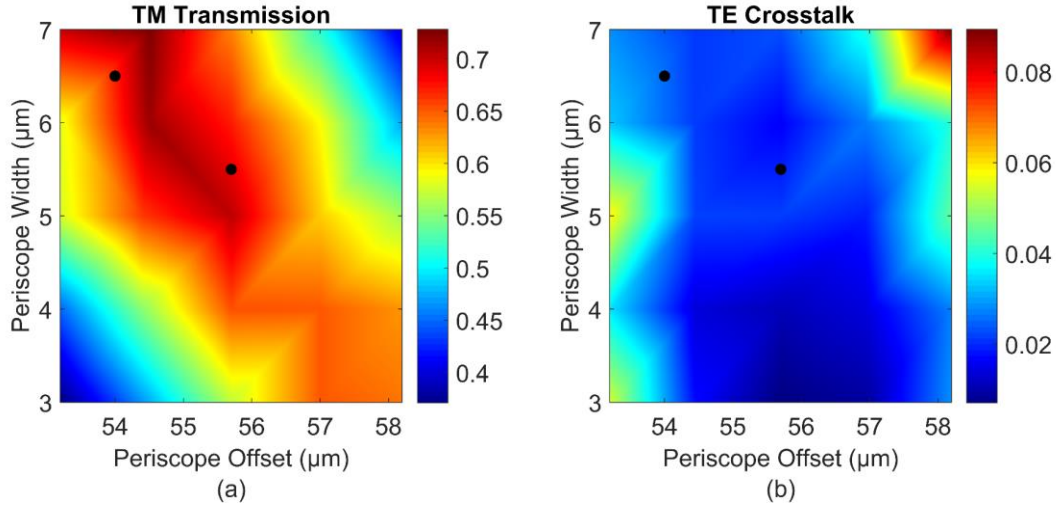


Figure 4.2. TM port optimization for (a) TM transmission and (b) TE crosstalk as functions of the position and width of the periscope. The black dots represent the two parameter sets that were chosen for fabrication. Periscope offset and width parameters chosen for fabrication were: [54 μm , 6.5 μm] and [55.7 μm , 5.5 μm].

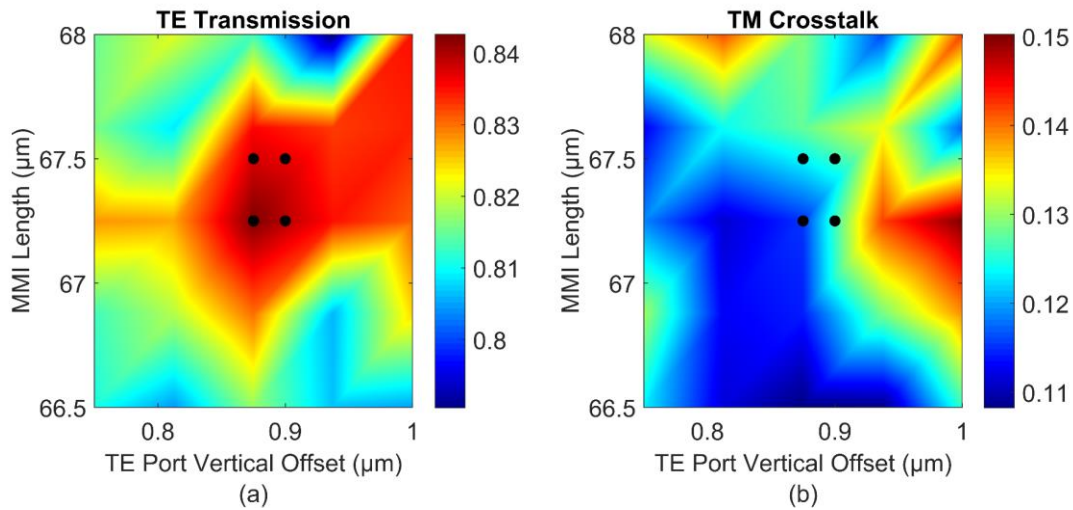


Figure 4.3. TE port optimization for (a) TE transmission and (b) TM crosstalk as functions of MMI length and TE Port offset. The four black dots represent the four parameter sets investigated experimentally. MMI length and TE Port offset parameters chosen for fabrication were: [67.25 μm , 0.875 μm], [67.5 μm , 0.875 μm], [67.5 μm , 0.9 μm], [67.25 μm , 0.9 μm].

The angle of the input waveguide, and the bend radius were each used to optimize the interference pattern strength and extinction ratio at the TE port respectively. Input angle was a critical parameter of this design due to its effect on the interference pattern in the MMI. The parameter values chosen for further experimental analysis are shown in Table 4.1, which comprise 72 variations of the device geometry for specific combinations of parameter values.

Table 4.1. Parameter values used for the experimental device performance characterization.

Parameter	Variable	Values	Units
Periscope offset (TM port offset)	x_{TM}	54, 55.7	μm
Periscope width	$w_{periscope}$	5.5, 6.5	μm
MMI length (TE port position)	l_{MMI}	67.25, 67.5	μm
TE port vertical offset	y_{TE}	875, 900	nm
Input angle	α	27, 29.39, 33	$^{\circ}$
TE output waveguide bend radius	r	0, 3, 5	μm

4.4. Fabrication and Experimental Results

Multiple PBS designs were fabricated using electron beam lithography [52]. Each PBS was connected to single-polarization broadband GCs [228] and measured using a Yenista CT400 detector and tunable laser. The measurements were taken over the 1500 nm to 1600 nm wavelength range with a resolution of 0.1 nm. The insertion loss and crosstalk for each polarization were measured simultaneously and the results were used to calculate extinction ratios. The losses were normalized with back-to-back reference GCs that were placed near the devices on the same chip for each polarization. As the grating couplers offered only a single polarization response, TE and TM responses were measured separately using separate, adjacent copies of the same device. As a result, the PBS was characterized by exciting either the TE_0 or TM_0 modes separately via the choice of grating couplers. Additionally, the waveguide geometry maintained the mode propagation as it only confined the fundamental modes. The testing process was carried out using a custom-built, automated passive optical testing setup for SiP chips.

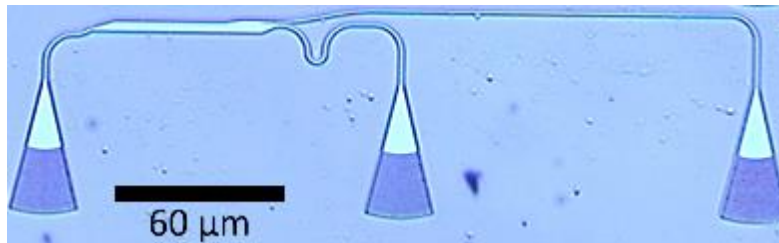


Figure 4.4. Optical microscope image of the on-chip fabricated PBS connected to input and output grating couplers for testing. Black spots are due to the microscope lens and do not appear on the chip.

4.4.1. Analysis

The IL from each device was normalized by subtracting from a reference GC response to obtain a GC-independent insertion loss. Insertion loss results above 0 dB (but below 1 dB) were observed for certain devices and are attributed to fabrication variations between GCs, or systematic errors in the measurement process. These results were retained as the ER values are still relevant to the characterization. The performance of all 72 parameter combinations within a 100 nm bandwidth (BW) from 1500 nm to 1600 nm, are shown in Figure 4.5. These 72 variations consisted of 24 different test cases (two TM port combinations were not considered as seen in Figure 4.2) of the base PBS design that were chosen for experimental characterization. The cases were also tested with the inclusion of a bend of radius 3 μm or 5 μm in the TE output waveguide. The average transmission response is indicated as a darker, solid line.

The transmission at both ports was contained within a relatively tight range of 5 dB. The TE and TM transmission losses were comparable, indicating the ER difference was not due to transmission (as was prioritized in section 3), but instead the ability of the device to filter out crosstalk. The extinction ratio for TE was found to be optimal within the C-band for all variations, since the wavelength-dependent L_π was designed at a central wavelength of 1550 nm. As expected, performance degraded with increasing bandwidth. The TM extinction ratio however, declined with wavelength despite the consistent transmission response. This suggests the possibility of prioritizing the minimization of TE crosstalk at the TM port in future designs.

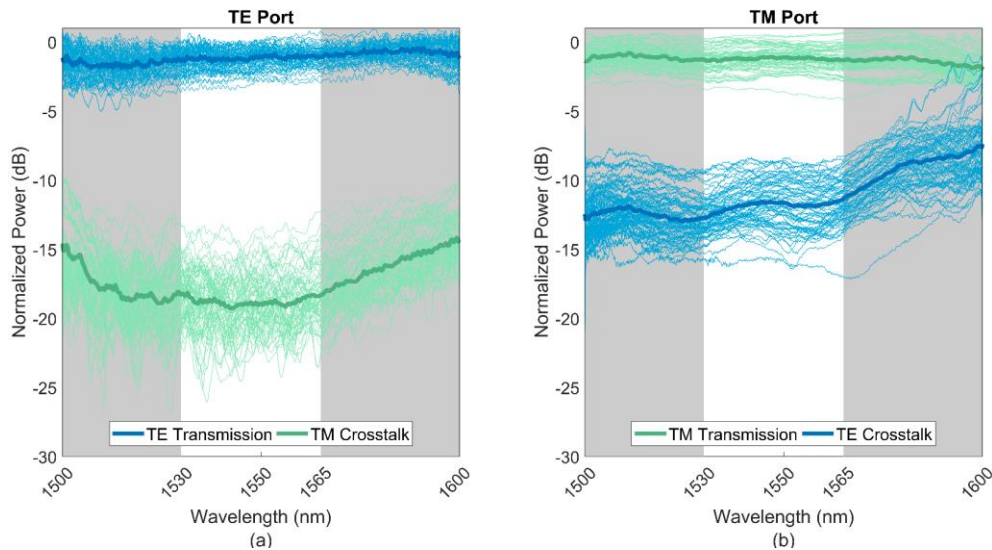


Figure 4.5. TE (blue) and TM (green) transmission spectra for all 72 measurements at the (a) TE and (b) TM ports. The darker lines show the mean of all spectra. The white background indicates wavelengths within the C-band range.

The IL does not exceed 1 dB in any case, and positive IL values are attributed to device variability or errors in measurement.

Figure 4.6 demonstrates the resilience of this design to variability in its key parameters. Since transmission was relatively consistent across the parameter space, the ER at each port was selected as a figure of merit for device performance. In order to compare parameter-dependent performance variability, it was deemed valuable to understand the effect on performance of changing each parameter value separately. Therefore, Figure 4.6 shows the average ER for all devices when the value of any one parameter is held constant. For example, in Figure 4.6(b) for the TM port, it can be seen that the periscope offset and width combination of $54\ \mu\text{m}$ and $6.5\ \mu\text{m}$ results in an improved ER for the PBS, at the expense of reducing the ER at the TE port. These two parameters were paired in the problem space characterization and are hence shown together here. Figure 4.6(f) represents the devices with the best and worst ER in the parameter space, as determined by their average ER in the C-band. Figure 4.6 therefore visualizes slices of the parameter space by showing the dependence of performance on each parameter variation.

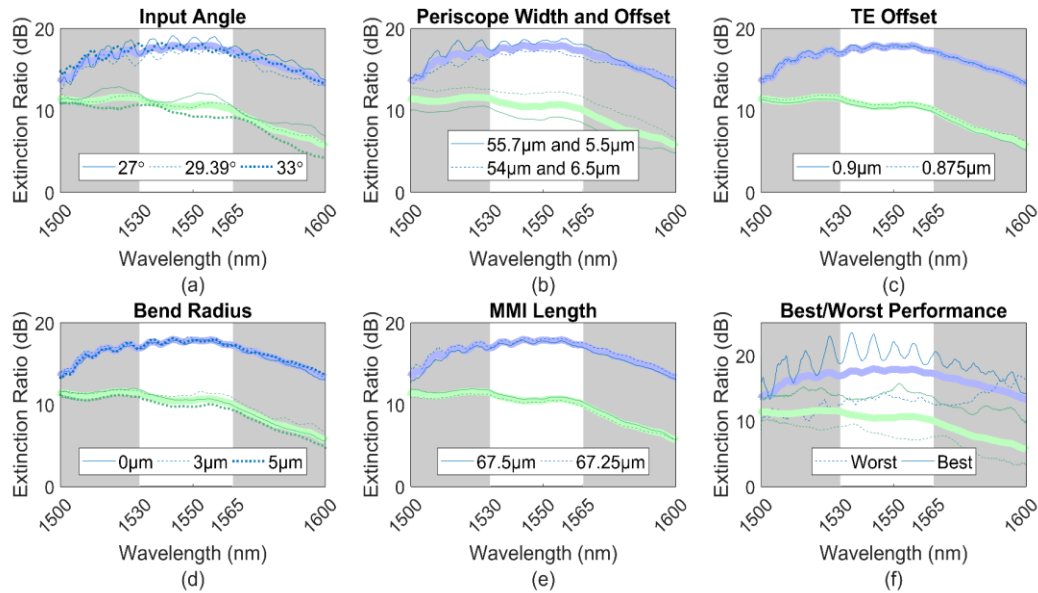


Figure 4.6. Extinction ratios of all PBS devices categorized by parameter. The plots show the average ER for all devices with a specific (a) Input Angle, (b) TM Offset and Periscope Width, (c) TE Offset, (d) Bend Radius, and (e) MMI Length. (f) The Best and Worst Performance are also shown. Blue lines correspond to ER at the TE port (TM crosstalk subtracted from TE transmission) and green lines correspond to ER at the TM port. The white background indicates wavelengths within the C-band range. The thick lines represent the average over all 72 variations.

A higher variation of ER in the C-band was observed at the TE port, with a maximum difference of approximately 12 dB. The maximum variation between devices at the TM port was approximately 7 dB in the C-band range. The largest variation at the TM port occurred in Figure 4.6(b). Hence as expected, the TM transmission was found to be most sensitive to changes in the dimensions of the periscope at the TM port. In order to observe trends within the parameter space, the maximum C-band transmission and crosstalk IL for every device as classified by parameter, are shown in Figure 4.7. In concurrence with Figure 4.5, TE and TM transmission IL do not vary significantly. The clustering of the rings demonstrates a high tolerance to parameter variations and therefore fabrication errors, which is in agreement with the results in Figure 4.5. The periscope offset x_{TM} appeared to demonstrate a lower crosstalk at 54 μm , which again suggests a reduction in this dimension for further optimization. At the TE port, crosstalk was found to be significantly lower for a MMI length of 67.5 μm , which also corresponded with better TE transmission. Characterization of the bend radius further indicated the possibility of extending the device by including a bend for lower crosstalk at the TE port, however this could not be conclusively verified given the distribution of points with lower crosstalk.

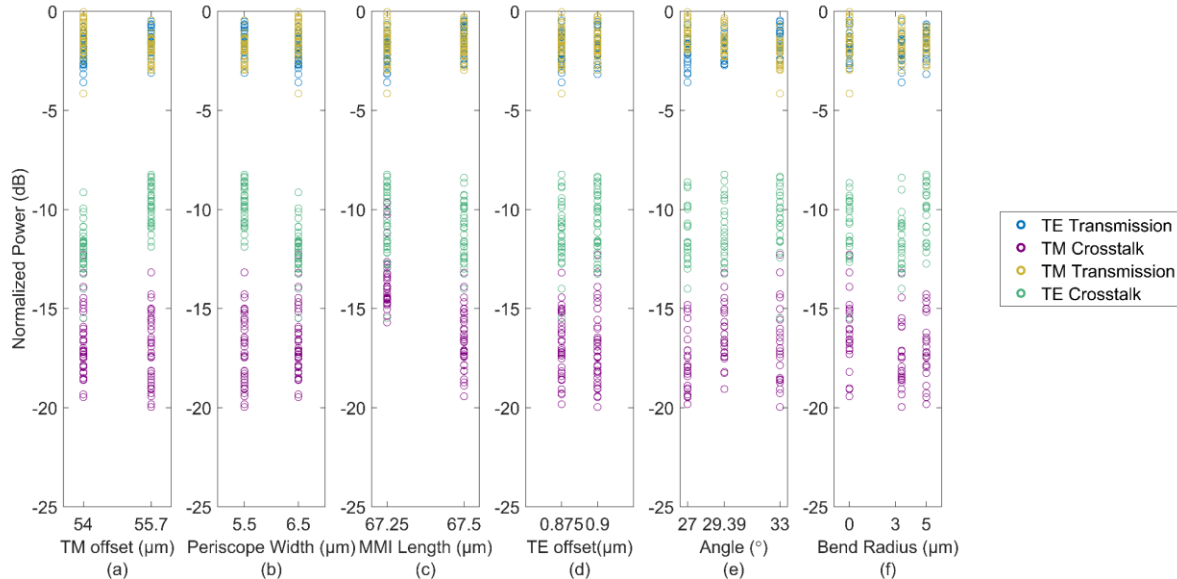


Figure 4.7. Characterization of PBS response in the C-band (1530-1565 nm) by varying the input parameters (a) TM periscope offset, (b) TM periscope width, (c) MMI length, (d) TE port vertical offset, (e) input waveguide angle, and (f) bend radius. Each circle represents the worst-case insertion loss for a specific polarization at a specific port. Hence worst-case TE transmission at the TE port for each device is shown in blue, TM transmission at the TM port in yellow, TE crosstalk at the TM port in green, and TM crosstalk at the TE port in violet.

4.4.2. Optimization

The characterization of the PBS parameter space provided the means for an experimental parameter optimization. As determined by the simulations, it was seen that the cases with the highest transmission did not correspond with those with the lowest crosstalk, hence offering more choices in device design based on required specifications. The best simulation and experimental performance are shown in Figure 4.8 with the optimal values depicted in Table 4.2 along with a comparison of the simulation results.

Table 4.2. Parameter values corresponding to optimal design, based on the characterization parameters in **Table 4.1**.

Parameter	Symbol	Simulation	Experimental	Units
Input Angle	α	29.39	29.39	$^{\circ}$
TM: Periscope offset	x_{TM}	55.7	54	μm
TM: Periscope width	$w_{periscope}$	5.5	6.5	μm
TE: MMI length	l_{MMI}	67.25	67.5	μm
TE port vertical offset	y_{TE}	875	875	nm
TE bend radius	r	0	0	μm

The representative PBS demonstrated a minimum insertion loss of 2.73 dB and 0.59 dB for TE and TM modes, with minimum ERs of 13.96 dB and 11.45 dB at the TE and TM ports respectively, across the entire telecom C-band wavelength range of 1530 nm to 1565 nm. The ER degraded to 11.49 dB and 6.73 dB within the expanded range of 1500 nm to 1600 nm. The experimental characterization showed a higher performance for devices with a longer TE port offset and shorter TM port offset. However, considering the relative insensitivity of the device performance to parameter variations, the difference in performance was within the range of measurement error. For example, the 0.25 μm difference in optimum MMI lengths corresponded to an ER difference of only 1 dB. The waveguide bend was found to have negligible effects on the IL and ER at the TE port. Cascaded bends with TM coupling to dummy ports could be implemented to improve TE extinction ratios. The relatively worse insertion loss for TE transmission in Figure 4.8 indicated possible back-reflections, which were confirmed by the lower quality interference pattern observed in Figure 4.1(b), and the lower transmission for TE than TM. The wavelength-dependent oscillations in Figure 4.8(a) are attributed to the free spectral range of the MMI for the fundamental TM mode.

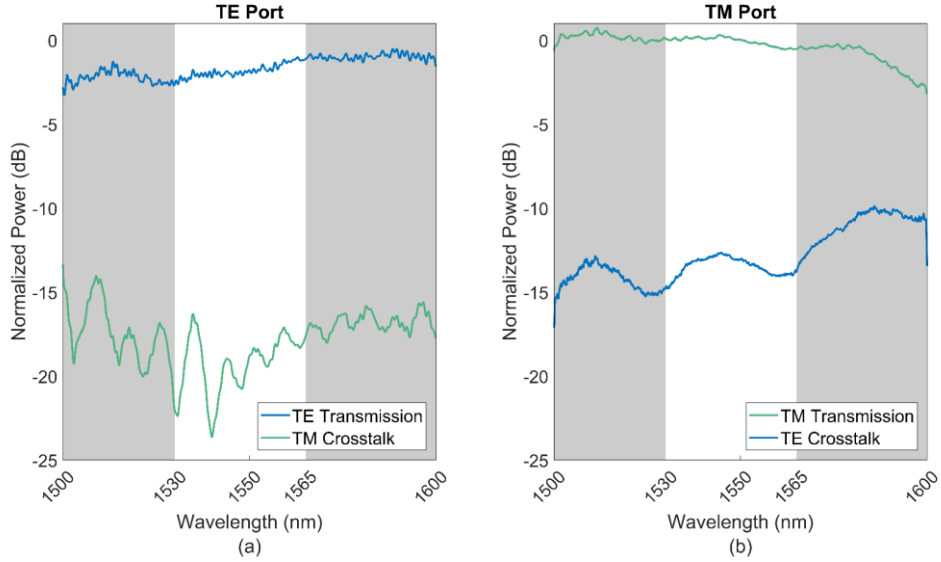


Figure 4.8. Transmission spectrum measurements for the optimal design at the (a) TE and (b) TM ports corresponding to the results in Table 4.2.

4.5. Discussion

A selection of state-of-the-art PBS devices (including our device) are shown in Table 4.3.

Table 4.3. Comparison of PBS designs including this work. The minimum overall extinction ratio is given with its corresponding bandwidth. The fabrication steps refer to the number of etch, deposition, or metallization (m) steps expected to fabricate the device on-chip.

Device	Topology / Parts	Fabrication Steps	Material	Length (μm)	Width (μm)	Feature Size (nm)	ER _{min} (dB)	BW (nm)
Cascaded MMI [216]	1	1	Si	364	10	500	14	55
Wedge MMI [217]	1	1	Si	202	5	500	12	50
2x2 MMI [218]	1	1	Si	132.6	4.2	500	15	26

InP MMI [229] ¹	1	1	InP	950	13	1000	34	35
Pixelated [143]	>25	1	Si, SiO ₂	2.4	2.4	120	10	32
SWG [65]	683	1	Si, SiO ₂	92.7	4	90	11.7	84
Plasmonic DC [224] ¹	2	2 + 1m	Si, Ag	8.1	2.6	150	16.9	35
DC [230]	2	1	Si, SiO ₂	20	6.9	275.5	30	85
Plasmonic MMI [231] ^{1,2}	3	1 + 2m	Si, Ag	5	1.8	30	14	285
3 slot [232] ¹	7	4	a-Si, SiO ₂	33	1.1	300	20.8	100
TM tap [233] ¹	1	2	Si	0.790	0.625	100	20	150
Proposed device	1	1	Si	67.5	4	500	11	75
¹ Simulated device with no experimental results.								
² Device not designed for the C-band.								

The proposed device was designed for reliable performance and low fabrication cost in a wide variety of integrated SiP circuits. With this in mind, the footprint and performance were optimized while maintaining constraints such as a single etch fabrication process, single material core, non-cascaded MMIs, genus zero topology, and minimum feature size larger than 500 nm. These constraints ensured its tolerance to fabrication errors, reliability under thermal or mechanical stress, reproducibility, and consistency in performance over a large spectral range. The proposed device therefore offers a smaller footprint or better fabrication tolerance as compared to most PBS designs and maintains a comparable performance in the C-band.

4.6. Conclusion

We have experimentally demonstrated a novel, compact $4\ \mu\text{m} \times 67.5\ \mu\text{m}$ polarization beam splitter by combining the concepts of an angled MMI, wedges, and tapering. This represents an extremely small form factor for a PBS design with a topology of genus zero, that is, one single block of Si

with no holes or sub-wavelength features. The geometric simplicity facilitates a high fabrication tolerance, and its compact size allows for a broadband response, as was characterized using parameter variations over 72 fabricated test structures. An angled input waveguide combined with the addition of a $1\ \mu\text{m} \times 6.5\ \mu\text{m}$ periscope, facilitated the extraction of the TM interference pattern above the MMI instead of in-line with propagation. The device was measured with and without a waveguide bend at the TE port and did not show a significant improvement in the reduction of the TM crosstalk through the waveguide as a result of this bend. An average insertion loss of approximately 1.6 dB was measured for all variations over a 100 nm wavelength range from 1530 nm to 1665 nm. In the C-band, TE and TM extinction ratios of at least 13.96 dB and 11.45 dB respectively, were observed.

5. Active Polarization Rotation and Phase Delay

“Nothing rests; everything moves; everything vibrates.”

– the Kybalion

Coupled polarized modes were split in Chapter 5 because a specific polarization is typically preferred to maximize coupling with free electrons (see Chapter 6). Hence, it is necessary to be able to rotate and delay the phase of each polarization so that both branches can be matched and then merged into a single mode.

In this chapter, we design two devices to rotate the polarization of a mode using an electrically applied magnetic field [4] in section 5.1, and to modulate the phase using an electric field across an EOP [10] in section 5.2.

5.1. SiP Faraday rotator

5.1.1. Introduction

Optical nonreciprocity enables isolation and circulation, which prevent undesired light routing to mitigate back-reflections and interference between components. However, Lorentz reciprocity cannot be broken in linear waveguides [234], which accommodate a bidirectional flow of light. This presents a crucial limitation for SiP circuits, which leverage the commercially available CMOS process flow to enable low-cost, large-scale deployment. Nevertheless, integrated optical isolators have been demonstrated by inducing NR behaviour via magneto-optic or acousto-optic [235] interactions. Acousto-optic interactions have employed SiN [236] or lithium niobate (LN) [237] racetrack resonators. However, these designs have a narrow bandwidth [238] and require CMOS-incompatible fabrication processes. Alternatively, magneto-optic (MO) interactions evoke NR behaviour via either polarization mode conversion (PMC) [239] or a NR phase shift (NRPS) [240]. Relative to the direction of propagation, a perpendicular magnetic field induces NRPS between counter-propagating modes in a racetrack whereas a parallel magnetic field induces Faraday rotation of the modes in a waveguide which manifests as PMC. Faraday rotation has been the most commonly used approach because of its low insertion loss (IL), high isolation ratio, and broad optical bandwidth. It is limited by birefringence due to the asymmetry of the waveguide cross-section, which can be mitigated by quasi-phase matching (QPM) the modes [241, 242]. The strength of the MO interaction depends on the Verdet constant, V , of the host material. For reference, V is 12-17°/(T-cm) for single crystalline Si [243] or up to 103°/(T-cm) for n-type

Si [244] at a wavelength of 1550 nm. Hence, achieving an appreciable rotation would require either a long interaction length [245, 246] or a strong applied magnetic field for it to be comparable to $-1263^\circ/\text{cm}$ for Ce-doped yttrium iron garnet (Ce:YIG), $100^\circ/\text{cm}$ for YIG on Si [247], or $-5900^\circ/\text{cm}$ for Ce:YIG on SiN [248] at saturation magnetization. These options utilize a garnet layer deposited on the waveguide which induces an MO interaction with the evanescent field of the optical mode [249]. As a result, operation is limited to the TM mode even though photonic circuits typically use the TE mode [250]. It is possible to switch between modes by using a reciprocal PMC [250, 251] albeit with additional complexity and loss. Additionally, garnets offer high yield and throughput but compatibility is restricted due to mismatched lattice constants and thermal expansion coefficients [238] as well as contamination from introducing garnets to the CMOS process. Hence, although standalone, integrated isolators have been demonstrated using a vertical-axis electromagnet above garnet on a waveguide [252-254], these solutions still require post-processing steps in addition to those available to the CMOS fabrication process flow. The main limitation of utilizing garnets is therefore their requirement of post-processing and magnetic biasing [238]. Alternatively, all-passive NR transmission was demonstrated in SiP [255] but required high intensity optical pulses which are not used in optical communication systems. In this context, previously demonstrated on-chip isolators required customized post-processing steps which are incompatible with the process flow of integrated photonics foundries. They essentially face a trade-off between performance and feasibility. This introduces a need to quantify the limitations of CMOS fabrication processes in meeting the requirements for on-chip optical isolator designs and achieving MO interactions using SiP. Addressing it would help determine whether modern fabrication techniques may enable isolator designs which were previously considered infeasible [256]. We therefore demonstrate a standalone device which generates a magnetic field inside Si waveguides using an input electrical current. To our knowledge, this is the first demonstration of an on-chip, horizontal-axis electromagnet which was fabricated using exclusively the CMOS process flow for the purpose of standalone NR PMC in Si waveguides. In this sense, the key advantages of this design are that it required no post-processing and was capable of standalone operation. It is therefore highly feasible to both manufacture and deploy, respectively, which are crucial to its commercial viability.

5.1.2. Device Design

A Si waveguide was surrounded by an electromagnetic coil to emulate a tunnel of electrical current. The coil was situated above the waveguide and surrounded it on three sides rather than being wound around it. This is because the Si crystal was grown directly on the buried oxide (BOX) layer prior to the deposition of additional materials, which implied that the fabrication process did not accommodate metallization below the Si layer. The coil was separated from the waveguide by a gap of 1 μm on the sides and 600 nm above. Its axis was parallel to the waveguide to align the direction the magnetic field with the optical path. The pitch was minimized to 9.3 μm and height was fixed at 2.95 μm within the constraints of the fabrication process [257]. Electrical connections consisted of a phosphorus-doped Si (n-Si) layer, and two aluminium (Al) metallization layers along with their tantalum nitride (TaN) vias. To compensate for the diamagnetic expulsion of the magnetic field by Si and SiO₂, two longitudinal strips each of Al and titanium nitride (TiN) were deposited co-axially inside the coil to emulate a paramagnetic solenoid core. This design was the basis for 15 device variations, which were fabricated on a SiP chip as shown in Figure B.2. These variations reflected the common use cases in SiP circuitry and were characterized in Appendix B. The primary design spanned a length of 1097.4 μm (corresponding to 118 windings) around a Si strip waveguide of 500 nm width and 220 nm thickness. The model of the device was scaled-down to only 5 windings, as shown in Figure 5.1, to minimize the computational demand of the 3D simulation. The total length of this model was 51.5 μm , which consisted of the coil length and an electrical connection shown in Figure 5.1(c). It hosted an interaction length of 47.17 μm , which was 0.667 μm longer than the coil length due to the overlap between windings.

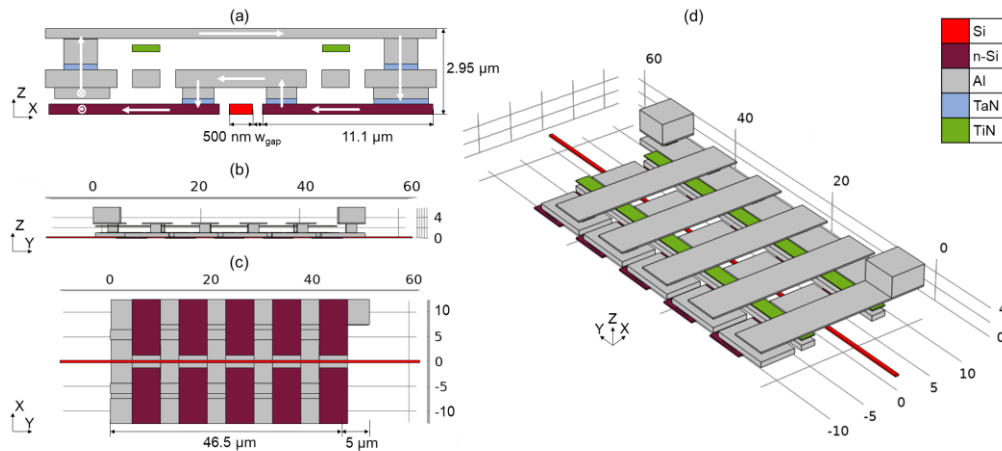


Figure 5.1. Design of an electromagnetic coil surrounding a strip waveguide on 3 sides. The Si waveguide (red) is surrounded by the coil made of Al (grey), n-Si (maroon) and TaN (blue) with a core made of Al and TiN (green). The

SiO₂ cladding is not shown. (a) Schematic of the front view of a single winding. An input electric current (white arrows) enters from behind and circulates clockwise through the layers: Al→TaN→Al→TaN→Al→TaN→n-Si→TaN→Al→TaN→n-Si. It then exits the front of the winding from the n-Si layer and enters the next winding through a TaN via (not shown). (b) Side, (c) bottom, and (d) perspective views of the simulated coil with 5 windings and a w_{gap} of 1 μm . Axes units are in μm .

The coil was designed to maximize the B -field in the waveguide while minimizing its size and response time. To ensure a fast response, the inductance also needed to be minimized. This could be accomplished in three ways based on equation (B.10): (i) by minimizing the inner cross-sectional area A_{coil} , (ii) by increasing the length, l , or (iii) by reducing the number of windings, n . However, increasing l for a constant n or vice versa would increase the pitch and thereby reduce the B field. For the area, the width of the gap between the doped-Si edges of the coil and the sidewalls of the Si waveguide, w_{gap} , was set at either 0.5 μm or 1 μm to characterize the trade-off between inductance and applied B field. A w_{gap} of 1 μm resulted in an area A_{coil} of 37.19 μm^2 which resulted in a transient time of 210 fs based on equation (B.11).

5.1.3. Device Response

5.1.3.1. Electro-thermal Response

An applied DC voltage difference generated an input current up to 14.28 mA with a current density distribution shown in Figure 5.2(a). The average resistance per unit length was measured to be 12.8294 $\Omega/\mu\text{m}$ at room temperature, which is the vertical intercept of Figure 5.2(b). Resistance was proportional to input current due to the corresponding rise in temperature from resistive heating as simulated in Figure 5.2(c). This asymptotic rise imposed an upper limit on the current. It also increased the temperature in the waveguide as seen in Figure 5.2(d).

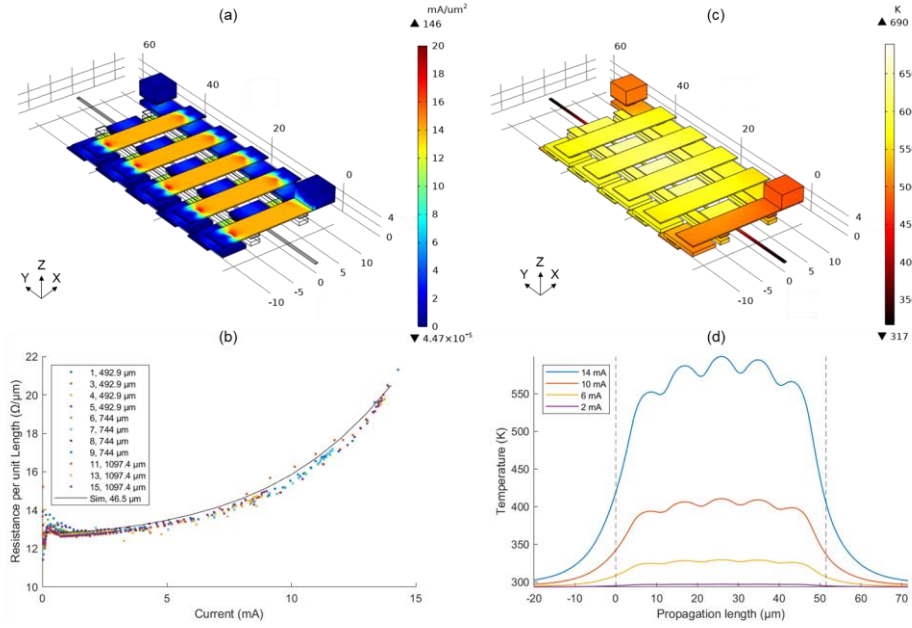


Figure 5.2. Electrical response of the coil. (a) Simulation of current density through the model coil at an input current of 14 mA. (b) Experimentally measured resistance per unit coil length of 11 device variations (dots) fitted to the simulation result (solid, black line). The labelling convention uses the device number and coil length, as given in Table B.2. The variations include both coil widths and all 3 coil lengths. Axes units are in μm for the device model. (c) Simulation of temperature distribution in the coil at an input current of 14 mA. (d) Temperature in the waveguide across the device length caused by resistive heating in the coil.

The current density in the upper Al layer was much higher than that in the lower layers due to the difference in resistivity between Al and n-Si. The contribution of Al and TaN to resistive heating was also negligible. Hence, only the dominant, temperature-dependent resistivity of n-Si was evaluated. Based on the measurements in Figure 5.2, the electrical response of n-Si followed equation (B.8). Its coefficient of resistivity at room temperature, ρ_0 , and temperature coefficient of resistivity, α , were fitted at $1.5152 \times 10^{-5} \Omega\text{-m}$ and 0.0019 K^{-1} , respectively. The initial decline in resistance at low currents was assumed to be caused by either the semiconductor-metal junctions between the n-Si and TaN layers which acted as Schottky barriers, or a loading effect of the measurement equipment. At an input current of 14 mA, the maximum temperature in the waveguide was 600 K. Although this was lower than the melting point of the materials, it may affect dispersion [74] and consequently the Verdet constant of the modes. It could be compensated by externally regulating the temperature of the chip. Additionally, considering its fast response time, larger currents could be admissible by driving the coil with a pulsed signal so that the maximum B field could be increased at a relatively reduced average power. Resistive overheating

would therefore be mitigated by balancing the duty cycle of the pulse with the time required to sufficiently cool the device. However, stabilizing the temperature fluctuations could prove challenging.

The operating voltage reached a maximum of 145 V before breakdown. This limit did not depend on the input current even though the power drawn, $P = V^2/R$ was different for each tested coil length. Hence, it is likely that the breakdown did not occur in the coil itself. Damage was only noticeable at the ends of the coil as seen in Figure B.2(c), which indicated a possible breakdown in its connection. This could be caused by a high voltage difference between two layers. For example, the electrical [258] and thermal [259] conductivity of TaN are both approximately 100 times smaller than Al. Additionally, the dielectric strength of non-conductive layers is also weakened at higher temperatures. Since the Si substrate acts as a floating ground, a breakdown pathway could have been thermally activated in the SiO₂ layer between the metals and the substrate.

5.1.3.2. **Electro-magnetic Response**

The magnetic flux density around the device is shown in Figure 5.3(a)-(g) for an input current of 14 mA. The serpentine architecture of the coil generated an alternating B -field [260] as shown by the distribution of the B_Y component in Figure 5.3(e)-(g). Figure 5.3(e) shows how the positive phase of the B_Y oscillation, $B_Y(+)$, was focused by the current tunnel. In between tunnels, as shown in the inset of Figure 5.3(d), the waveguide was exposed to the core which caused a leakage of the internal B -field. It effectively reversed the direction of B_Y in the waveguide to produce oscillations between -0.58 mT and 1.16 mT. This field reversal could be used to support QPM in the waveguide as indicated in Figure B.4. The MO interaction could therefore be enhanced by shaping the applied B -field oscillations for a suitably dispersion engineered [1] waveguide mode.

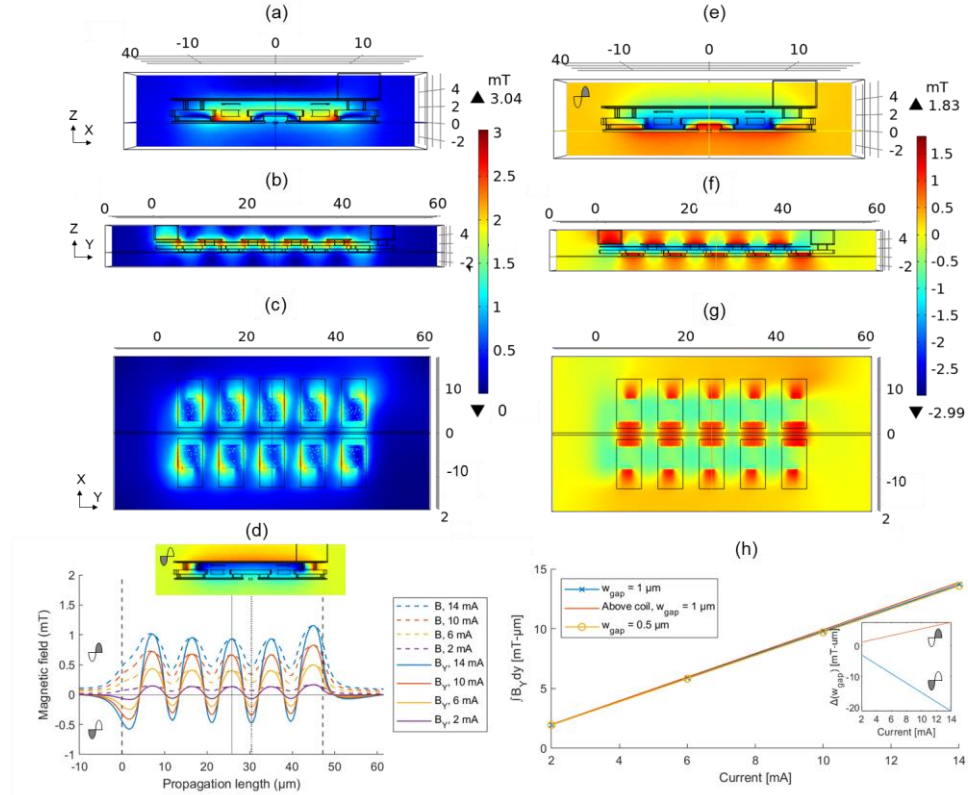


Figure 5.3. Simulated B field around the coil. (a) Front view, (b) side view, and (c) top view for the coil with a gap width of $1\ \mu\text{m}$. (e) Front view, (f) side view, and (g) bottom view of the B_Y component of the same design. In each plot, the positions of its orthogonal cross-sections are visible. Axes units are μm . (d) Both B and B_Y magnitudes along the waveguide centerline for increasing input currents and a w_{gap} of $1\ \mu\text{m}$. The interaction length is marked by vertical, black, dashed lines. The black, solid line in the center indicates the location of the image in (a) and (e). Inset: Distribution of B_Y at the negative peak at a propagation length of $30\ \mu\text{m}$ (indicated by the black, dotted line) with the same colour scale as (e). Axes units are in μm for the device model. (h) $\int B_Y dy$ integrated over the propagation length for both gap widths of $0.5\ \mu\text{m}$ and $1\ \mu\text{m}$, as well as for $160\ \text{nm}$ above the coil (equivalent to the distance between the Al strip and the waveguide centerline). Inset: Difference in $\int B_Y dy$ between w_{gap} for the positive and negative phases of the integrated B_Y field.

In Figure 5.3(h), the B_Y -field was integrated along the interaction length, $\int B_Y dy$ inside the waveguide for both gap widths. For comparison with the upper half of the coil, it was also evaluated above the top Al layer (at the same distance as the waveguide centerline from the bottom Al layer). The field above the coil was found to be equivalent to that in the current tunnel due to the higher current density in the upper region. Counter-intuitively, a larger w_{gap} of $1\ \mu\text{m}$ supported a stronger overall B_Y -field in the waveguide despite the oscillation amplitude being smaller. This was because the walls and upper layer of the coil acted as a secondary current tunnel which focused

the $B_Y(-)$ field along whichever segments of the waveguide were not shielded by the lower windings of the coil. The effect is shown in the inset of Figure 5.3(d). Additionally, since a wider w_{gap} was accommodated by a wider coil (as described in Appendix B), $B_Y(-)$ was less focused. This effect is shown in the inset of Figure 5.3(h) in which the two lines represent $\int B_{Y,w_{\text{gap}}=0.5\mu\text{m}} dy - \int B_{Y,w_{\text{gap}}=1\mu\text{m}} dy$ for the negative and positive phases of B_Y separately. The larger offset of the negative phase indicates that the contribution of $B_Y(+)$ from the tunnel was less dependent on w_{gap} than $B_Y(-)$ from the coil. The negative phase also exhibited a steeper rate of change because the current density was higher in the upper parts of the coil. As a result, the overall B_Y -field was stronger for a w_{gap} of 1 μm . The B_Y strength could therefore be increased by redesigning the coil to supply a higher current density in the lower region and mitigate any leakage. For example, removing the n-Si layer would reduce the resistance by two orders of magnitude.

5.1.3.3. Magneto-optic Response

Each single-mode waveguide was evaluated for both TE_0 and TM_0 modes at center wavelengths of 1310 nm and 1550 nm corresponding to the lowest dispersion and loss wavelengths, respectively, in optical communication systems. The Verdet constant, V , of the modes in each waveguide was determined by their frequency-dependent effective index as shown in Figure B.4. Its dependence on the chromatic dispersion of the modes was found to be strongly related to the waveguide geometry. This relationship explains the difference in V between these waveguides and bulk Si [243]. Modal dispersion also affected the PMC efficiency because of the resulting phase mismatch between modes as seen in Figure 5.4. Propagation loss was neglected since its main source was sidewall roughness, which was assumed negligible at micrometer length scales. A low loss allows the device to be cascaded or incorporated in a racetrack so that rotation could be accumulated by multiple passes through the interaction region. This could be amplified by dispersion engineering the waveguide to increase the optical path length [1] and enhance the interaction [261].

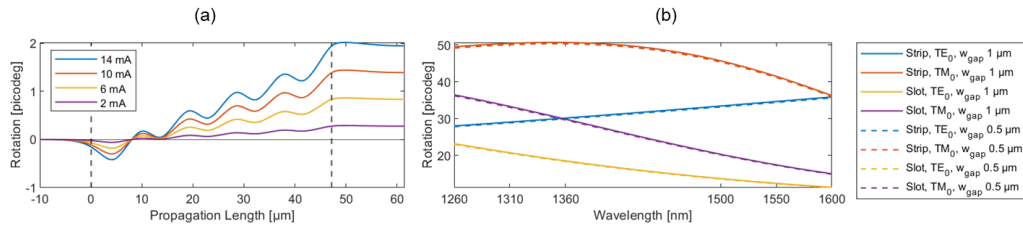


Figure 5.4. Faraday rotation in the device. (a) Rotation of the TM_0 mode at a wavelength of 1310 nm in a strip waveguide along the propagation length for increasing input currents. The beginning and end of the interaction region are marked as black, dashed lines for reference. (b) Spectral dependence of the total accumulated rotation of each mode and each waveguide type for the longest device length of 1097.4 μm at an input current of 14 mA.

The rotation of the TM_0 mode at a wavelength of 1310 nm is shown in Figure 5.4(a) for increasing input currents. Since the angle of rotation was too low to be measured, the effect of mode beating was ignored. This implied the assumption of perfect phase matching between the TE_0 and TM_0 modes. The oscillatory behaviour of the rotation along the interaction length was therefore caused by the alternating B_Y -field in the waveguide. The accumulated rotation of each mode was extrapolated for the fabricated device lengths and are listed in Table B.3. The rotation at the longest interaction length of 1097.4 μm is shown in Figure 5.4(b) for both gap widths and strip and slot waveguide types. These curves resemble V in Figure B.4 since the rotation depended on V when the applied B field and interaction length were fixed. Hence the spectral dependence of rotation was determined by V . The TM_0 mode of the strip waveguide underwent the most rotation of $50.71 \times 10^{-12}^\circ$ at a wavelength of 1352 nm.

5.1.4. Discussion

This standalone device acts as a building block on the roadmap toward utilizing magnetic fields on-chip in commercial applications, which to our knowledge, has not been demonstrated by state-of-the-art integrated MO isolators. The target rotation was 45° since it could be connected in series with a 45° reciprocal PMC [241, 242] to achieve full 90° rotation for NR PMC. The output polarization could be filtered by a polarization beam splitter [3] to measure an intensity and phase modulation in the output polarizations. A change of the input current could then be mapped to a change in the output polarization state using the Poincaré sphere [241]. If the change in intensity is small, it could be detected by a lock-in amplifier, which would require the coil to be driven by an AC signal with a pulse duration larger than its transient time. Forward and backward propagation could be measured by reversing the direction of electric current in the coil, which is equivalent to reversing the propagation direction [250] due to the device symmetry.

In this design, the angle of rotation mainly depended on the input current, interaction length, and dispersion of the fundamental modes. It could be improved by optimizing w_{gap} , removing n-Si from the coil, co-designing the coil and waveguide to ensure QPM, and enhancing the MO interaction. It is possible that resistive heating could be circumvented to some extent by driving

the coil for a shorter duration of time than that required to reach a temperature corresponding to its damage threshold. Essentially, the time required for heating or cooling could be regulated by an alternating current (AC) with an appropriate frequency and duty cycle. An AC driving signal could also be connected to a lock-in amplifier to detect small changes in the optical response. The interaction region could be increased by either cascading the devices, incorporating an optical cavity, or dispersion engineering the waveguide. In an optical cavity such as a racetrack, the optical pulse would undergo multiple passes as determined by its quality factor, Q , and accumulate a rotation of $\theta \times Q$. Alternatively, a spiral waveguide could also facilitate a predefined number of passes through the interaction region [245, 246]. It is also worth considering inducing NRPS instead of NR PMC, since this would lift the degeneracy of counter-propagating resonant modes [247], thereby inducing isolation. The disadvantage would be a narrower optical bandwidth [238] in comparison to interferometer-based designs [262]. Additionally, the resonance would not increase rotation since the MO interaction is independent of the amplitude of the optical pulse.

Additional materials may also be considered to improve the performance. Doping the waveguides could enable their refractive index to be dynamically modulated using the free-carrier plasma dispersion effect. This would allow for the spatiotemporal modulation of MO coupling for slow light, which could improve the interaction or enable explorations in combining the Zeeman and Stark effects [263]. Additionally, combining the coil design with garnet deposition would enable a standalone, MO isolator for commercial applications. Specifically garnet deposited in a slot waveguide [241, 264] could provide a significantly enhanced MO interaction. The lower index of garnet would also amplify the field concentrated in the slot. It could be complemented by CMOS-compatible materials such as SiN, Ge [265], or complementary materials such as graphene [266]. Along with overcoming the limitations described previously, these upgrades are expected to increase the angle of rotation by multiple orders of magnitude. We believe that a combination of these techniques would enable mass manufacturable, integrated optical isolators.

5.2. EOP Dual-Polarization Modulator

5.2.1. Introduction

The implementation of photonics in telecommunication architecture has significantly increased the bandwidth of current data communications, and motivated progress in throughput, latency and efficiency. This is motivated by a push towards increasingly high-speed and high-bandwidth

devices at low costs as a direct response to global demand [40]. In order to cater to this need, smarter signal processing tools are designed to employ multiple degrees of freedom (frequency, polarization/mode, phase, amplitude) within the same signal therefore compounding the data carrying capacity of networks. Regarding the transmission and reception ends, significant emphasis is placed on improving modulation and multiplexing schemes with a view to increasing size, speed, or efficiency within devices [42].

The current industry standards for modulators make use of various optical phenomena to modulate a propagating signal. For example, the Franz-Keldysh effect [267] is used in electro-absorption modulators; the plasma dispersion effect in phase modulators [268]; as well as other effects such as the acousto-optic effect [269] for frequency shifting, or electro-optic effect [270] for phase shifting. LiNbO₃ is a commonly used nonlinear optical material for fiber-based modulators due to its optical transparency in the telecom wavelength range and high bandwidth, obtained through the implementation of the electro-optic effect [271]. However, the integration of LiNbO₃ in CMOS-compatible systems can be challenging. An interesting alternative is found as an application of polymer chemistry. Electro-optic polymers undergo an isochoric change in their electromagnetic properties, such as refractive index, upon application of an electric field. This change is caused by a bulk electro-optic effect from the overall dipole orientation of chromophores within the polymer, known as the Pockels effect [272].

5.2.2. Theory

The Pockels effect is a second-order nonlinear optical effect that is dependent on the polarizability of a material – inherent and induced. It is referred to as a linear electro-optic effect of the first order because the resultant change in refractive index P/E varies linearly with the applied electric field [272],

$$\Delta n \propto \frac{\vec{P}}{E} \propto n_0 + r_{ijk}\vec{E} + \dots \quad (5.1)$$

Here, Δn represents an induced change in refractive index caused by an applied external field \vec{E} on a material with initial refractive index n_0 and a linear electro-optic tensor r_{ijk} that determines its electro-optic responsivity to the applied electric field. Although the optical response time correlates with the mobility of electrons, this response is quick enough (sub-picosecond regime) that the electro-optic coefficient can be considered independent of the magnitude and modulation frequency of the applied field [272].

An applied field implicitly interrogates every nonlinear term associated with a material. However, it is possible to enhance the inherent $\chi^{(2)}$ of an EOP through thermal poling which results in an amplified Pockels effect [270]. Through the process of thermal poling, the dipole orientation of the chromophores within the EOP lose their rigidity when heated to the glass transition temperature so that they can align to an externally applied electric field. Due to the uniaxial orientation of the poled EOP chromophores, the effective nonlinear coefficients are stronger for any propagating light that is polarized such that its oscillating electric field is parallel to the poled dipole orientation. In this manner, a birefringence is induced in the EOP molecules as depicted in Figure 5.5.

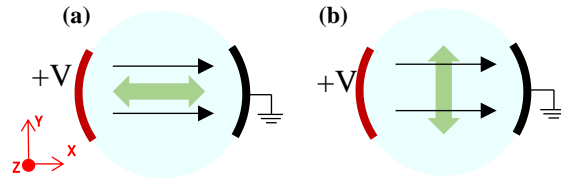


Figure 5.5. Electric polarization of an EOP under an applied electric field. The thick lines represent the electrodes, the black arrows show the induced electric moment, and the green arrow indicates the oscillation of the electric field of polarized light propagating down the Z axis. In (a), the molecular electric moments oriented along the positive X axis will interact directly with TE polarized light (E-field parallel to X axis) since they are parallel, whereas in (b), the induced moment only weakly interacts with TM polarized light (E-field parallel to Y axis). Hence, orthogonal polarizations of the optical signal propagating through a thermally poled EOP will experience significantly different refractive indices.

Poling imposes a cylindrical point group symmetry with the axis parallel to the poling field. This point group symmetry reduces r_{ijk} to r_{mk} thus restricting the tensor to three independent elements, which correspond to the dipole orientation along the X, Y and Z axes [270],

$$r_{ijk} \rightarrow r_{mk} = \begin{bmatrix} 0 & 0 & r_{13} \\ 0 & 0 & r_{13} \\ 0 & 0 & r_{33} \\ 0 & r_{31} & 0 \\ r_{31} & 0 & 0 \\ 0 & 0 & 0 \end{bmatrix} \quad (5.2)$$

As determined by the electro-optic coefficient tensor, the application of an electric field causes a proportional variation in refractive index, which differs for polarizations that are parallel or perpendicular to the \vec{E} vector. For example, poling along the direction of polarization induces a change in refractive index that can be approximated by [270],

$$n_i(E) = n_0 - \frac{1}{2}r_{33}n_0^3E_i \quad (5.3)$$

Where n_0 denotes the original effective refractive index of the EOP waveguide. If, however, the polymer is poled perpendicular to the direction of polarization, the induced change in refractive index will be given by,

$$n_i(E) = n_0 - \frac{1}{2}r_{31}n_0^3E_j \quad \text{or} \quad n_i(E) = n_0 - \frac{1}{2}r_{13}n_0^3E_k \quad (5.4)$$

depending on the direction of the applied electric field. The oriented gas model is chosen to estimate the relationship between the elements of the tensor, and it predicts that $r_{33} = 3r_{13}$. Additionally, the Kleinman symmetry approximation has been used to set $r_{13} \approx r_{31}$ and is partially based on experimental confirmation [273]. These degrees of freedom will be exploited in our design of a dual polarization EOPM.

5.2.3. Device Design

As discussed in the previous section, the orientation of the chromophores with respect to the polarization of incident light determines the refractive index response. In order to interrogate the r_{33} and r_{13} coefficients for polarized light propagating along the Z-axis through a cylindrical waveguide, it must be possible to apply an electric field along either the X or Y axes. This is made possible by using four opposing electrodes as shown in Figure 5.6.

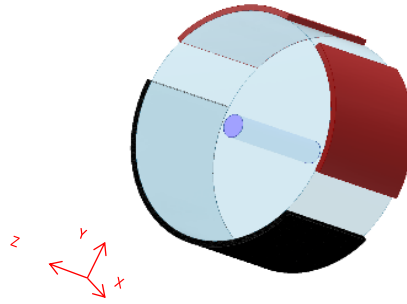


Figure 5.6. Three-dimensional view of proposed configuration for dual polarization modulation. The signal electrodes are represented in red and ground electrode in black. As both ground electrodes are electrically equivalent, they are considered to be a single electrode so as to reduce fabrication complexity. The EOP core is shown in blue, and surrounded by concentric glass cladding.

The dual-polarization electro-optic modulator was designed using two different chromophores. DR1 is used as a reference EOP seeing as its nonlinear properties have been comprehensively explored and are well understood [273]. However, as its r_{33} coefficient is very low, it is no longer used in practical applications. As an alternative, CLD1 has a significantly higher Pockels coefficient [274] making it a suitable candidate for future experimental verification. PMMA was

used as the host matrix in both cases to maintain consistency. The parameters for these two polymers are given in Table 5.1.

Table 5.1. Characteristics of DR1/PMMA and CLD1/PMMA using [270, 272-274].

Parameter		DR1/ PMMA	CLD1/ PMMA
Refractive Index	n_{co}	1.475	1.63
Pockels coeff. [pm/V]			
On-axis	r_{33}	7.6	85
Off-axis	r_{31}	2.9	28.33*
Wt. percent in PMMA	wt%	10	10

*Estimated using $r_{33} = 3r_{31}$ as defined in section 5.2.2.

The percent weight ratio was used to calculate the bulk refractive index of the material [272]. The characterization of DR1/PMMA was extensively performed in [273], which experimentally investigated the $C_{\infty m}$ point group symmetry. This allows the numerical work to be simplified by considering an average of the electro-optic tensor elements r_{42} and r_{51} such that $r_{42}, r_{51} \approx r_{31} \approx 2.9$ pm/V. It has also been assumed that the initial (unpoled) extraordinary and ordinary refractive indices are approximately equal, as represented by n_0 . Hence the change in refractive index along the X- and Y-axis as a result of applying electric fields along the X- and Y-axes respectively, can be reduced to,

$$n_x(E) = n_{0,x} - \frac{1}{2}r_{33}n_{0,x}^3E_x \quad , \quad n_y(E) = n_{0,y} - \frac{1}{2}r_{33}n_{0,y}^3E_y \quad (5.5)$$

In order to produce an intensity variation, the modulator must be placed in a Mach-Zehnder Interferometer configuration in which a π phase shift will be required. As the phase shift is a function of the change in refractive index induced by the applied electric field, the half wave voltage V_π across the electrodes that is required to produce this phase shift is given by,

$$V_\pi = \frac{\lambda d}{n^3 r_{\text{eff}} L \Gamma} \quad (5.6)$$

Here, the central wavelength λ is 1.55 μm , d is the distance between electrodes, L is the interaction length, and Γ is the overlap integral as determined by the vectorial overlap between the signal applied electric field and the confined beam profile. If the applied electric field is parallel to the confined beam at all points, $\Gamma = 1$, and if it is antiparallel, $\Gamma = -1$. In the case of crossed

beams, $\Gamma = 0$ as this is taken into account in the overlap integral for r_{31} . Thus, perpendicular electric field is susceptible to the r_{31} coefficient requiring an expansion of the half-wave voltage equation,

$$V_{\pi} = \left(\frac{1}{r_{33}\Gamma_{\text{on-axis}}} + \frac{1}{r_{31}\Gamma_{\text{off-axis}}} \right) \frac{\lambda d}{n^3 L} \quad (5.7)$$

5.2.4. Simulation Setup

Regarding the propagation of two orthogonal, linear polarizations through the cylindrical EOP core under an externally applied electric field, the overlap criteria must be determined. This implies the determination of the vectorial components of the applied electric field, as well as the beam profile of the fundamental modes propagating through the core.

5.2.4.1. Signal Electric Field

An initial two-dimensional electrostatic and electromagnetic simulation was performed along the cross-section of the proposed structure. This simulation uses the AC/DC > Electrostatic (**ES**) and Optics > Wave Optics > Electromagnetics Waves, Frequency Domain (**EWFD**) modules. The diameter of the cross-section is $20\mu\text{m}$ with a uniform dielectric constant approximation, corresponding to glass. Two signal electrodes are positioned on the left (X-axis) and top (Y-axis), and one uniform ground electrode covers both the right (X-axis) and bottom (Y-axis) with corresponding spacing. The ground electrode therefore complements each signal electrode. Figure 5.7 illustrates the static electric field when the same positive potential is applied to both signal electrodes.

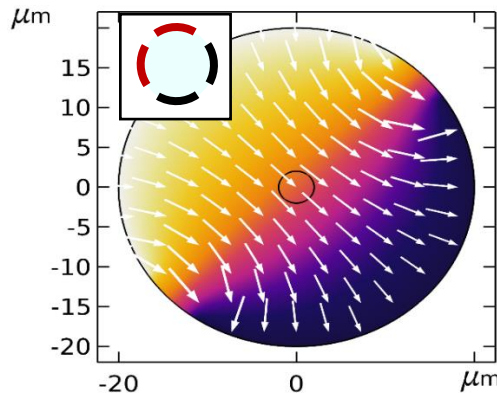


Figure 5.7. Applied electric field distribution along a cross-section of the EOPM with both electrodes active and (inset) corresponding electrode map using the format depicted in Figure 5.5.

The vectorial distribution portrays the directional nature of the electric field along the cross-section of the cylindrical waveguide. As can be seen, a cladding region between electrodes and waveguide core provides a separation between the maximum intensity of the beam profile and the signal field. This separation effectively straightens the electric field through the core, ensuring that it is the intended vectorial sum of both signals. Thus fringe effects between electrodes have been neglected [275]. When a positive voltage is applied to both signal electrodes, the effective angle of the applied external electric field at the core is almost uniformly 45° allowing for an equivalent modulation of both propagating polarizations.

5.2.4.2. Mode Confinement

The parameters used to determine the confinement of both polarizations within the EOP core are given in Table 5.2. These parameters are used to simulate the fundamental mode using COMSOL while neglecting the ordinary and extraordinary refractive index differences as explained in the previous section.

Table 5.2. Waveguide parameters for DR1/PMMA and CLD1/PMMA EOP cores with a borosilicate glass cladding, at a propagating wavelength of 1550nm [273, 274].

Parameter	Value
$n_{\text{DR1/PMMA}}$	1.475
$n_{\text{CLD1/PMMA}}$	1.63
n_{clad}	1.47
r_{core}	2 μm
r_{clad}	20 μm

Analytically, the parameters for DR1/PMMA in Table 2 will only support the fundamental mode in the proposed waveguide since $\frac{2\pi r_{\text{core}}}{\lambda} \sqrt{n_{\text{core}}^2 - n_{\text{clad}}^2} < 2.405$ [212]. Although increasing the core refractive index with the use of CLD1/PMMA permits a higher-order mode as predicted by the dispersion equation [212], the fundamental mode can still be analyzed and compared against DR1/PMMA. Using ‘Mode Analysis’ with EWFD in COMSOL, the parameters in Table 2 were simulated to obtain the beam profiles shown in Figure 5.8.

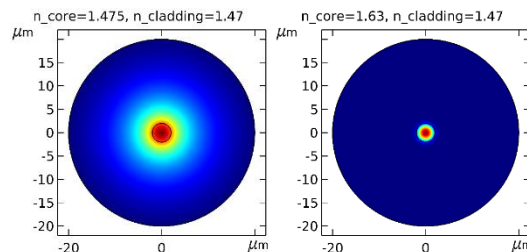


Figure 5.8. Fundamental mode profiles for CL1/PMMA (left) and DR1/PMMA (right).

A vector product of the linearly polarized mode profile, and applied electric field, is used to calculate the effective overlap. This overlap indicates the efficiency of the applied field on phase modulation of light through the polymer. In typical EOP modulators, the optical confinement is considerably greater through the use of high-index polymers [276] or slot waveguides [116], thereby increasing the effective overlap. For the purpose of simplicity, these techniques have not been incorporated and hence much lower efficiencies (and correspondingly higher interaction lengths) are expected. A 3D simulation is carried out to determine the modulation characteristics of this structure.

5.2.4.3. Three-Dimensional Propagation Set-up

The simulation set-up described above was further extended to a three-dimensional cylindrical waveguide. The fiber model is 8mm long and consistent with the parameters in Table 5.1 and Table 5.2. The waveguide length was specifically restricted to 8mm with the interest of conserving simulation time. This is justified by the predictability of the optical response since the magnitude of phase change (with respect to the original wave) is expected to be linearly increasing as the wave propagates through the fiber. As shown in the equation below, the electro-optic phase change is linearly proportional to waveguide interaction length, L [277].

$$|\Delta\varphi| = \frac{rn^3EL}{\lambda_0} \quad (5.8)$$

In preparation for the 3D model construct in COMSOL, the ‘Electromagnetic Waves, Beam Envelope’ (EWBE) module was used instead of the EWFD module. In order to excite 45° (diagonally) polarized light into the fiber, a ‘User Defined’ port was chosen instead of the typical choice of ‘Numeric’ port. This enables the specification of the X and Y components of the port’s $e^{j\beta z}$ fields, thereby allowing the input field into waveguide to be diagonally linearly polarized. Considering the modulation target of a π -phase shift, a ‘Matched Boundary Condition’ was used instead of defining a terminating port; this suggests that the modulator extends beyond the simulated structure, which prevents unintended terminations (i.e., defining a listener port – Port 2) and corresponding back reflections. A scattering boundary condition was also applied to the waveguide structure to indicate that the surrounding environment is air.

Regarding the coupled electrostatic field as calculated within the ES module, a similar configuration is performed for the 3D structure as that used in the 2D simulation. The electrodes

are specified as applied potentials on the top and side. The same technique is used to place a uniform grounding electrode on opposing sides of the electric potential.

The effective index was extracted from the ‘Derived Values > Global Evaluation’ section in the 2D simulation to allow for a comparison against the results obtained in the 3D simulation, which uses a ‘Numeric’ port.

5.2.5. Simulation Results

The 3D device characteristics are predicted for certain key parameters. As phase modulation is the target application of this system, the optical response metric of the device is considered to be the induced phase shift in radians.

An applied signal along one electrode axis is expected to affect the refractive index experienced along that axis itself, and not necessarily the perpendicular axis. However, as shown in the 2D simulation of electric field in Figure 5.7, a minor crosstalk results due to the electrostatic field angles at the core deviating slightly from 45° when both electrode sets are being used. A more severe source of crosstalk due to the static electric field arises from the off-axis electro-optic coefficient that induces a phase shift in the polymer. Crosstalk is expected to accumulate as the optical wave propagates down the interaction length of the electro-optical material. Figure 5.9 illustrates the simulated result when a voltage of 10V is applied along the X-axis and induces approximately $\frac{\pi}{2}$ phase shift along the horizontal axis while imposing an approximately $\frac{\pi}{6}$ phase shift along the vertical axis. The large electro-optic coefficient of CLD-1/PMMA facilitates a much smaller interaction length as compared to DR1 for the same resultant phase shift. As the phase shift measured is a relative quantity that is referenced with the initial phase and a function of the periodic wavelength, the phase shift as well is expected to be periodic over large interaction lengths.

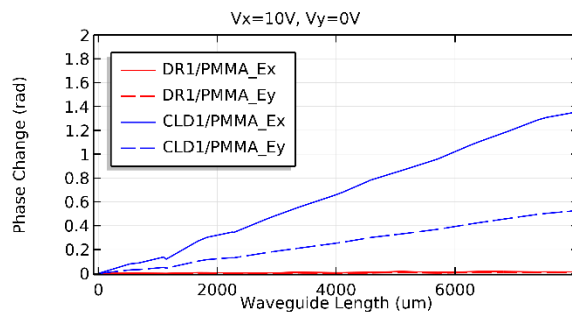


Figure 5.9. Phase shift in propagating X-polarized light (E_x) as a function of waveguide length when only the X-axis electrode is active, and corresponding static phase shift induced in orthogonally polarized (E_y) light.

For a modulator with constrained dimensions, it is expected that CLD1 would require a lower voltage to obtain an equivalent phase shift as DR1 at the same interaction length. Alternatively, increasing the voltage will increase the amount of phase shift experienced by the propagating light, similar to any single polarization modulator. Since the magnitude of phase change is linearly proportional to the applied potential, it can be extracted from Figure 5.10 that a voltage of approximately 20V for a waveguide length of 8mm can achieve a π -phase shift using CLD1/PMMA, considering the simplistic modulator structure designed in section 5.2.3.

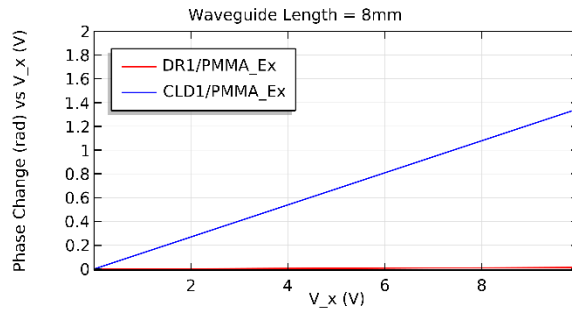


Figure 5.10. Phase change as a function of applied voltage along the X-axis.

Although the static off-axis phase shift induced by an electrode set is relatively strong, the effect of both electrodes being used simultaneously proves the ability to modulate both polarizations within the same structure. From Figure 5.11, it can be seen that the orthogonal electric fields from the dual polarization modulators are affected equally for applied voltages of 10V for X- and Y-axes. As a result, the magnitude of phase shift for both orthogonal fields is nearly identical. It is seen that the calculated phase change for dual polarization modulation is higher than a single axis modulation due to the incumbent phase shift as a result of the magnitude of the diagonal component being stronger than each orthogonal component, as well as the residual phase shift from off-axis components.

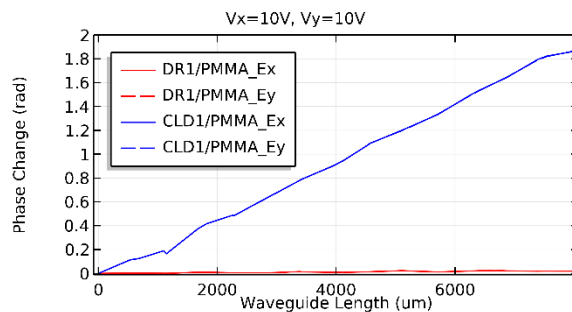


Figure 5.11. Phase change as a function of waveguide length when both electrodes are active.

5.3. Conclusion

First, we demonstrated a standalone, CMOS-based Faraday rotator consisting of a waveguide surrounded by a coil. The electrical response of the coil was demonstrated, and the performance of the device was simulated. The design was characterized over 15 design variations including 4 waveguide types, 2 gap widths, and 3 coil lengths. In this evaluation, the TM_0 mode of the strip waveguide at a wavelength of 1352 nm underwent the most rotation of $50.71 \times 10^{-12}^\circ$. Having been fabricated in the CMOS process flow and capable of standalone operation, it surpasses two key limitations of current on-chip isolator designs regarding manufacturability and deployment, respectively. In this context, the significance of this design is in the commercial viability of the device. Additionally, our investigation provided the basis for a set of clearly identifiable upgrades which will improve the feasibility of inducing NR PMC in the SiP platform before requiring any post-processing, additional materials, or external magnetic biasing. This approach therefore provides a strong, alternative pathway to improve the commercial viability of future isolator designs. Even beyond optical isolation, the realization of a MO interaction using CMOS-compatible fabrication processes can enable a variety of novel design opportunities in SiP.

Next, we report the design and simulation of a dual polarization electro-optic polymer modulator for optical phase modulation applications. The device structure consists of concentric EOP core, glass cladding, and four radially symmetric electrodes, along the axis of propagation for linearly polarized light. Simulation results show an effective phase shift of 1.35 radians for CLD1 and 0.01 radians for DR1 under a 20V applied voltage with an interaction length of 8mm. Additionally, static crosstalk is expected to be approximately a third of the induced phase shift in any scenario. Such a device allows the option of simultaneously modulating two phases within a single structure at an extremely high speed and theoretically low voltage, and thus offers a solution to the speed, size, and efficiency constraint imposed on modulators in contemporary telecommunication architecture. However, the inclusion of polymers in a SiP chip requires post-processing in a wet lab outside the CMOS foundry [10], which increases the complexity of device fabrication. The added complexity renders the fabrication process infeasible for commercial applications that can avail of lower performance analogues in CMOS, which are cheaper to manufacture. Hence, materials that are unavailable in standard CMOS fabrication processes are unlikely to provide a benefit to SiP device design unless they offer sufficiently novel functionality. Although it is worth exploring the off-chip applications of polymer optical devices, this avenue of

exploration would not contribute directly to the goal of harvesting solar energy on a SiP chip. Hence, it is recommended that future iterations of the circuit switch this component to either a passive waveguide loop or a doped waveguide which utilizes the well-established plasma dispersion effect which is typically used in MZMs.

6. Coupling to Free Electrons

"There's plenty of room at the bottom."

– Richard Feynman

Once the polarizations in both branches and their phases are matched, the two modes may be combined using a 1×2 MMI splitter [41]. This single mode may then be coupled with a travelling free electron.

In this chapter, we design a SiP circuit that couples free-space light into the supermode of a slot waveguide which then overlaps with a traveling free electron. The need and value of such a design is argued in section 6.1. The design process is explained in section 6.2, which covers the parameters that were optimized to maximize the coupling strength between the supermode and the electron. The limitations, improvements, and applications of this design are discussed in section 6.3 along with a comparison of previous such device designs. The results of the design process are summarized in section 6.4.

6.1. Introduction

The interactions between electrons and light are indispensable to a range of technologies including radiation therapy [278], imaging the atomic structure of solids via nanoscale microscopy [279], and generating broadband, coherent light for free electron lasers [280]. Although the quantum interactions of free-space light with bound electrons have been studied extensively, the interactions of free electrons with confined light have only recently been made accessible by photon-induced near-field electron microscopy (PINEM) [281, 282]. These interactions are realized by ensuring that the electrons and light are phase-matched in energy–momentum space, which allows for a wide range of phenomena including the Cherenkov and Smith–Purcell effects [283–285]. Using appropriately tailored light fields [286–288], the spatiotemporal and spectral properties of electron wavefunctions can be modulated via PINEM [289] in ways that are instrumental to a plethora of applications in medicine, electron acceleration, and radiation sources. The extent of modulation is determined by the strength of coupling between the electrons and light [281, 282, 287]. This coupling can be maximized using techniques such as shortening the pulse duration [290], amplifying the electric field overlapping with the electron [291], or extending the interaction length [290]. However, such designs are not yet commercially viable, which inhibits follow-on applications. This gap highlights the need for a

scheme which can facilitate electron-photon coupling using an integrated platform. It would benefit investigations in quantum electrodynamics [292] as well as enable applications in electron energy loss spectroscopy [293] and PINEM [281].

A recent class of devices known as dielectric laser accelerators (DLAs) have shown tremendous potential in facilitating such interactions. DLAs can accelerate free electrons within a sub-millimeter interaction length to induce acceleration gradients in the range of GeV/m [294, 295]. Compared to conventional radio-frequency particle accelerators, this represents an improvement of multiple orders of magnitude with respect to both performance and size. Therefore, DLAs herald a new class of devices which allow on-chip access to the interactions between electrons and light. Specifically, they offer the capability to optically supply, absorb, and modulate the kinetic energy of electrons. Using DLAs, these interactions could be pushed into the strong coupling regime [296, 297], resulting in performance improvements that enable quantum entanglement phenomena between free electrons and confined photons [297-301]. In this context, the coupling strength per photon can be considered as a key performance indicator of a DLA because it determines the amount of energy transferred to/from the electron.

For the interaction to be maximized, the electron wavefunction and the light wave must be phase-matched along their overlap region [282]. This can be achieved by overlapping an electron beam (eBeam) and optical pulse at either perpendicular or parallel incidence to each other. In the scenario of perpendicular incidence, the eBeam traverses the alternating near-field of a grating in such a way that electrons are continuously accelerated by the positive phase-fronts of light along their trajectory [302]. Since this approach does not require light to be waveguided (unless imposed by the design [303, 304]), a wide range of optical frequencies can be employed as long as the grating is thinner than its corresponding absorption depth [302]. Nevertheless, the nonzero incident angle of the light causes transverse near-fields which deflect the eBeam and therefore limit the scalability of this approach [305]. Alternatively, the scenario of parallel incidence employs an optical pulse co-propagating with the eBeam, which incurs negligible transverse deflection forces. This allows for longer coupling lengths [298] and cascaded, scalable designs [294, 306]. The coupling strength can be maximized by amplifying the electric field per photon that is available to the electrons using techniques such as compressing the volume of the optical pulse into a waveguide mode [291], reducing the optical pulse duration [295], accessing whispering gallery modes [296], or resonating the field in a racetrack [288, 298, 307]. Such techniques have opened

access to the quantized spectral broadening of the electron wavefunction [290] as well as pushed the interaction into the strong coupling regime [308] albeit with a high propagation loss. These advances and their limitations introduce the need for a scheme that optimizes the coupling efficiency in a commercially viable manner. It must be scalable [309] in order to act as the basis for practical devices that can maximize the kinetic energy gain and acceleration gradient. Such a scheme would support the vision of quantum electro-optic interactions and tabletop electron accelerators including follow-on applications.

In this work, we design a device to maximize the coupling between confined light and free electrons. It is designed as a SiP integrated circuit operating at telecom wavelengths. Commercial SiP technology utilizes the CMOS process flow to enable low-cost, large-scale deployment. Furthermore, by having Si as the core material, the design can benefit from the potential of dielectrics to host extended interactions resulting in a high excitation probability [298], and the high refractive index of Si which increases modal confinement as compared to Si_3N_4 [288, 298, 309]. Our proposed design allows for a modularized system employing well-developed circuit components that can be upgraded in a plug-and-play fashion. The key component is an exposed slot waveguide which hosts a supermode [116] to interact with co-propagating free electrons. Its input is a single-mode waveguide that connects to a sidewall of the slot via a mode evolution region (MER) [310, 311]. Using a single input prevents the potential phase mismatch from two waveguides [291] as well as the imbalanced loss from their corresponding grating couplers (GCs). Additionally, building on the study in [291], we optimize the design parameters and characterize performance at two shorter wavelengths of 1310 nm and 1550 nm for which telecom-based components are readily available and the damage threshold is higher [312, 313]. In doing so, we evaluate the coupling strength per photon over the interaction length and show that this efficiency metric directly maximizes the energy gain. Our scheme can also be used to maximize the acceleration gradient if required by the target application. It therefore offers a core building block on the roadmap towards optically manipulating the kinetic energy of free-electrons in a scalable, commercially-viable manner [314].

6.2. Device Design

The specifications of the target design were constrained to ensure compatibility with an ultrafast transmission electron microscope (UTEM), which was previously used to test similar structures [290, 308]. The steps that were taken to accommodate these compatibility constraints

are described in Appendix C. Using the SiP platform, the device was designed with a Si core material grown on a SiO₂ buried oxide (BOX) layer without any cladding. A layout of the proposed device is shown in Figure 6.1(a). Here, light is coupled into the chip from a surface, vertical GC [315]. The coupled light is asymmetrically split [41, 122] into two branches of which 10% is reflected by a Bragg grating (BG) to provide feedback during the alignment process and 90% is routed to the interaction region. The main component of the circuit is the slot waveguide shown in Figure 6.1(b) and (d), which hosts an optical supermode to overlap with an eBeam at grazing incidence to the chip. It is connected to the circuit by a MER, shown in Figure 6.1(c), which converts the fundamental transverse magnetic (TM₀) mode of from the GC into the required supermode of the slot (Figure 6.1(c) and (e)). At the beginning and end of the interaction length, the cross-sectional geometry of the slot constrains the dimensions of the eBeam, as shown in Figure 6.1(d).

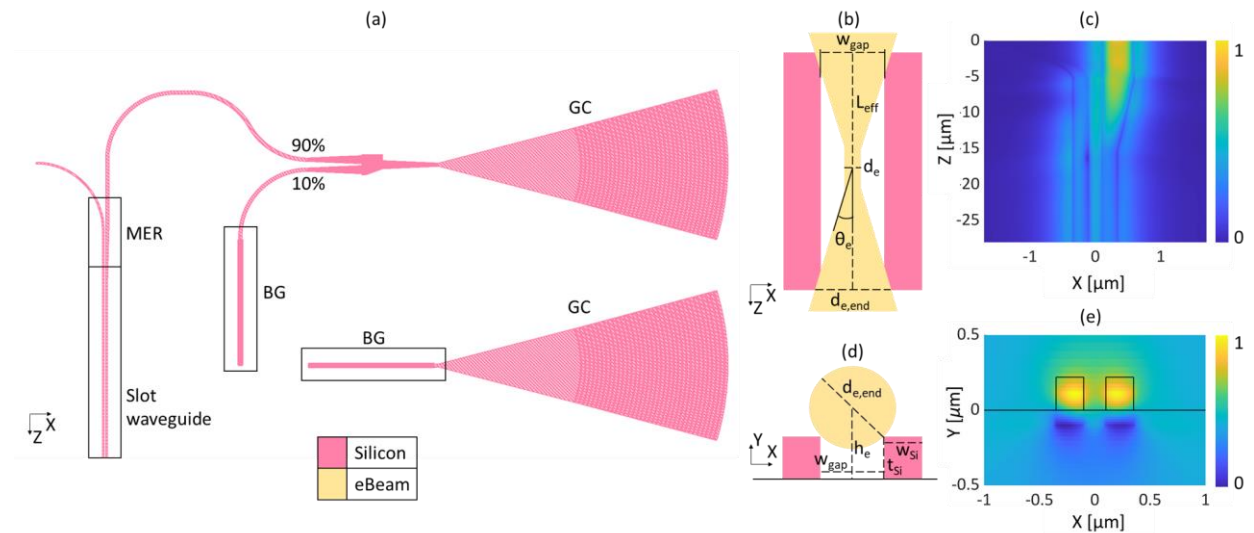


Figure 6.1. On-chip layout of the device which hosts an optical supermode to overlap with a free-electron beam. (a) Top view of the device layout consisting of an input grating coupler (GC) connected to a 90:10 splitter that sends 10% to a Bragg grating (BG) for alignment feedback and 90% to a slot waveguide via a mode evolution region (MER). An additional GC is placed at a fixed offset from the input GC for stronger feedback during coarse alignment. (b) Top-down view of the slot waveguide accommodating an eBeam that converges in the slot (the MER is not shown). (c) Top-down view of the MER with the simulated electric field distribution, $E_{0,z}$, showing how the input TM₀ mode is converted to the supermode of the slot waveguide. (d) Front view of the slot waveguide at the point of entry or exit of the eBeam. (e) Front view of the slot waveguide with the simulated electric field distribution, $E_{0,z}$, of the converted supermode.

We design the slot waveguide to maximize the longitudinal electric field intensity of the optical supermode specifically in the region of overlap with incident free electrons. We target the device operation at wavelengths of 1310 nm and 1550 nm, corresponding to the lowest dispersion and insertion loss, respectively, of optical telecommunication systems. The required circuit components (i.e., GC, splitter, BG) are readily available at these center wavelengths. We neglect any limitations on the coupling bandwidth caused by dispersion effects [298] so the performance is only evaluated at these two wavelengths. The thickness of the Si layer, t_{Si} , was set as 220 nm corresponding to the standard thickness offered in the SOI platform. Within the overlap of the supermode with the eBeam, the coupling strength depends on the amplitude of its longitudinal electric field, E_z , over the effective interaction length, L_{eff} . Using a dielectric like Si as the core ensures a relatively high damage threshold [298, 312, 316]. The high refractive index of Si also strongly confines the supermode and consequently E_z , which is further amplified by compressing the mode volume in the slot [116]. The distribution of E_z for a given supermode is determined by the cross-sectional geometry of the slot represented by the widths of the gap, w_{gap} , between its sidewalls, w_{Si} . These dimensions determine the effective index of the supermode, n_{eff} , and its corresponding phase velocity, v_p , which set the electron velocity, v_e , such that $v_p = v_e$. They also determine the group velocity, v_g , and therefore the time period, Δt , over which the electron passes through the optical pulse of duration, T_{pulse} . We assume that the arrival times of the electron and optical pulse are synchronized such that they coincide in the middle of the interaction length. Therefore L_{eff} is limited by Δt as well as the decline in phase-matching as v_e increases (and decreases) beyond v_p . Under these conditions, we characterize the three lowest order supermodes hosted by the slot waveguide (see Appendix C for details).

To find an optimum overlap between the electron and supermode, we emulate the process of aligning the eBeam to each supermode hosted by a specific waveguide geometry. This is done by varying its parameters to maximize the overlap and then calculating the corresponding coupling strength as shown in Figure 6.2. The eBeam alignment is parametrized by its height from the BOX layer, h_e , and diameter, d_e , which set the divergence angle, θ_e , based on the emittance of the eBeam for a given v_e [289]. Together, these parameters geometrically limit the maximum interaction length, L_{eff} , as shown in Figure 6.2(a). We approximate the spatial probability distribution of the electron wavefunction to be uniform within its spot size since energy can be

exchanged at any (x, y) point in the overlap region. The figure of merit for the interaction is the coupling strength per photon [287, 298], g_{Qu} , as shown in Figure 6.2(b) and derived in Appendix C. The optimal distribution of E_Z to overlap with the electron is shown in Figure 6.2(c). During the interaction, the electron exchanges energy with the optical supermode in steps of $\pm\hbar\omega$, resulting in a quantized broadening of its kinetic energy spectrum [281, 288, 290], $\Delta\varepsilon_e$, and determines the acceleration gradient, G , as derived in Appendix C.

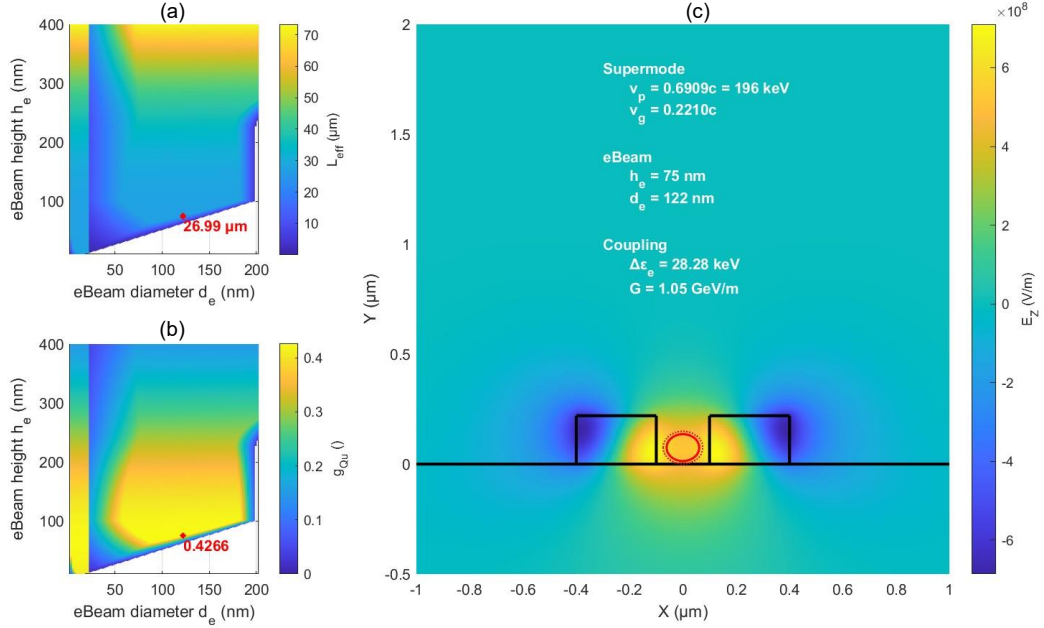


Figure 6.2. Optimization of coupling strength per photon for the given slot waveguide dimensions. (a) Maximum achievable interaction length, L_{eff} , within the range of available eBeam diameters, d_e , and heights, h_e . (b) Coupling constant per photon, g_{Qu} , over the same parameters. A red dot indicates the maximum g_{Qu} . The blank regions indicate inadmissible parameters for which the eBeam was blocked by the sidewalls or BOX. The discontinuity in both plots is caused by switching the electron sources between thermionic and photoemission modes in the UTEM as explained in Appendix C. (c) Distribution of the longitudinal electric field component, E_Z , of a supermode hosted by the slot waveguide. The solid and dotted red circles indicate the spot size at the focal point and at the ends of the slot, respectively. Dimensions of the slot waveguide are $t_{\text{Si}} = 220 \text{ nm}$, $w_{\text{Si}} = 300 \text{ nm}$, and $w_{\text{gap}} = 200 \text{ nm}$, which results in a $g_{\text{Qu}} = 0.4266$ for a supermode at $\lambda = 1550 \text{ nm}$ matching $\varepsilon_e = 196 \text{ keV}$.

The dependence of L_{eff} on the eBeam parameters that are accommodated by the given slot dimensions is shown in the gradient of Figure 6.2(a). Although we constrained $L_{\text{eff}} \leq 500 \mu\text{m}$ to ensure that the device would fit into the sample holder of the UTEM, it was predominantly limited by the phase-mismatch caused by the accelerating and decelerating electrons. The discontinuity in

Figure 6.2(b) at a 20 nm diameter is caused by the different emittance of the eBeam when switching the electron source. The gradient of g_{Qu} reveals its dependence on the alignment of the eBeam, or its misalignment tolerance. As h_e increases, g_{Qu} decays exponentially due to a proportional reduction in E_Z [290]. It increases with a wider d_e because the peaks of the supermode are split such that the E_Z intensity is higher near the sidewalls than in the middle of the slot. This implies that having a tightly focused eBeam is not directly advantageous to the coupling strength (further validated by the characterization results in Appendix C). Counterintuitively, g_{Qu} is not maximized at the longest L_{eff} because of a decrease in the temporal overlap, Δt , beyond the optimum L_{eff} . This is a physical implication of the finite durations of the electron and optical pulse. The interaction is also improved by the slight rotation of the nodes of the supermode, which increases E_Z in the overlap.

Considering the damage threshold of Si and the losses of the GC, splitter, and MER, we calculate an optical pulse energy of 0.22 nJ and duration of 1 ps in the slot (see Appendix C for details). This enables a maximum g_{Qu} of 0.4266 for the design case shown in Figure 6.2, which produces an electron energy gain of 28.27 keV with an acceleration gradient of 1.05 GeV/m. A full characterization of the parameter space is presented in Appendix C.

6.3. Discussion

We evaluated the performance of the design based on its efficiency of inducing a quantum electro-optic interaction between the electron wavefunction and a classical electromagnetic field within the target experimental constraints. We therefore choose g_{Qu} as the figure of merit. The practicality of our design enables it to be employed in a cascaded system by simply tuning the parameters of each device accordingly. In designing the device, we consider the following parameters (correlated quantities are indicated by a double arrow):

- Waveguide: $w_{\text{Si}}, w_{\text{gap}}, t_{\text{Si}}$
 - Optical pulse: T_{pulse}
 - Supermode: $\lambda, n_{\text{eff}} \leftrightarrow v_p, n_g \leftrightarrow v_g, E_Z$
- Electron: $h_e, d_e \leftrightarrow \theta_e, v_e \leftrightarrow \varepsilon_e$
- Coupling: $\Delta t, L_{\text{eff}}, g_{\text{Qu}}, \Delta\varepsilon_e, G$

Our design process revealed a number of constraints, and identified ways of overcoming them, to further improve the coupling efficiency.

The damage threshold of Si limits G and correspondingly, the optical pulse energy and duration in the slot (see Appendix C for calculations). However, although G is limited by the damage threshold of Si, $\Delta\varepsilon_e$ is not. In this context, our scheme shows that the efficiency g_{Qu} can be used to maximize $\Delta\varepsilon_e$ and therefore circumvent the limit on G . Hence, we maximize $\Delta\varepsilon_e$ by maximizing g_{Qu} while still operating within the damage threshold of Si. Additionally, the damage threshold can be included in the design scheme by considering materials with higher thresholds (as indicated by their bandgap [312, 313] [316]), account for the wavelength-dependent damage threshold, and cross-sectional areas (and corresponding MER loss) of every slot waveguide, and characterizing performance over different optical pulse energies and durations. Also, note that the energy in the optical pulse does not directly affect g_{Qu} , but it does increase the spectral broadening caused by the interaction (and therefore G). This affects the maximum interaction length at which phase-matching can be maintained, which in turn affects g_{Qu} .

Another limitation was the dephasing caused by v_e changing beyond v_p . This is unavoidable if the target application requires maximum electron-photon coupling. However, if the goal is to maximize the electron acceleration (and conversely minimize deceleration), then the waveguide design could be modified so that n_{eff} decreases along L_{eff} such that v_p increases along with v_e . This can be achieved by tapering the sidewalls of the slot [291], transitioning to a sub-wavelength grating [1, 56], or cascading multiple such devices [294, 307]. An edge coupler could also be incorporated at the end of the interaction to emit the co-propagating pulse with the electrons so that they continue to exchange energy beyond the chip. However, our simulations show that a lower n_{eff} pushes the mode into the BOX layer thereby reducing its confinement and overlap with the eBeam, which implies that it cannot be reduced below the refractive index of the underlying BOX layer. This limitation can be overcome by suspending the waveguides or using a lift-off technique to separate the Si completely from the substrate. To accommodate a higher range of v_p , t_{Si} could also be reduced to 145 nm. However, note that this weakens the confinement of the mode and consequently E_z in the overlap. A longer L_{eff} would also require Δt to be increased while maintaining that the electron coincides with the peak of the pulse envelope for as long as possible. It can be achieved by either increasing $v_g \rightarrow v_p$ to prevent dephasing or by increasing T_{pulse} at the expense of lowering the optical power [290, 295]. However, since v_g depends on the material properties as well as dimensions, this parameter cannot be regulated as easily as v_p and could be

overcome by dispersion engineering the device [1] or incorporating other materials. Additionally, since g_{Qu} , and consequently $\Delta\varepsilon_e$ and G , are dependent on the energy, duration, and wavelength of the optical pulse, these laser settings may be used to further optimize the interaction as long as the fluence is less than the damage threshold of Si and SiO₂ [291, 312] (as described in Appendix C). Including T_{pulse} as a parameter in the optimization process could also determine whether a longer pulse would improve g_{Qu} or whether a shorter, higher power pulse is more efficient. The limits of T_{pulse} depend on the laser source. Note also that a typical laser or eBeam source emits a finite spectrum rather than a single frequency or energy. So, the accuracy of our predictions can be improved by updating PINEM theory to consider the full interaction between an electron bunch and the range of frequencies in the optical pulse as well as phase-matching along the interaction length. The amount of energy reaching the slot waveguide can also be increased by minimizing the insertion loss of the circuit components, potentially at the expense of their bandwidth, however, this is not currently a limitation since the energy supplied by the laser is mainly limited by the damage threshold of Si. The GC could also be replaced by an edge coupler if permitted by the constraints of the application. Furthermore, the available E_z per photon can be amplified by looping around the ends of each sidewall to form a dual racetrack resonator configuration [307]. Such a configuration can recirculate the remaining optical energy of the pulse after the interaction and therefore harness constructive interference effects [298]. Additionally, the round-trip time of the racetracks can be matched to the repetition rate of a pulsed laser to synchronously pump the system resulting in a resonant amplification of the field strength [317]. If the efficiency is sufficiently high, then the device could even be operated with continuous-wave light [288]. Finally, our system can also potentially be modified by attaching a conductive coating to siphon any excess charge, thereby alleviating a critical bottleneck [288] in reducing the charging caused by the eBeam.

In comparison with previous designs and demonstrations, our proposed design achieves a high coupling efficiency by utilizing a co-propagating optical supermode in a Si slot waveguide at an optimal wavelength. This comparison is shown in Table 6.1.

Table 6.1. Comparative analysis of device designs enabling electron-photon coupling. Brackets indicate values which we calculated because they were not reported. Wg: waveguide, *: designed but not demonstrated, \perp : perpendicular incidence, \parallel : parallel incidence.

Ref., Year	Structure	λ (nm)	Initial ε_e (keV)	$\Delta\varepsilon_e$ (keV)	G (GeV/m)
[318], 2013	\perp SiO ₂ grating	787	27.9	(0.28)	0.025
[319], 2013	\perp SiO ₂ grating	800	60000	(120)	0.3098
[302], 2015	\perp Si/P grating	907	96.3	1.22	0.2
[320], 2015	\parallel Quartz/Cu tube	666205	60	7	0.0025
[307], 2017*	\parallel Si racetrack	2000	30	118.312	0.00113
[321], 2017	\parallel Ge prism	1930	28.4	0.8	0.019
[322], 2018	\perp Si grating	2000	28.1	2.6	0.069
[291], 2018*	\parallel Si slot wg	2000	80	10	0.330
[303], 2020	\perp Si wg	2000	83.4	0.915	0.0305
[290], 2020	\parallel BK7 prism	730	207.2	0.85	(0.00243)
[296], 2020	\parallel SiO ₂ sphere	800	200	0.35	1.4
[306], 2021	\parallel SiO ₂ /Au tube	555170	3000	15	0.0005
[294], 2021*	\perp Quartz prism	1000	300	80	1.6
[288], 2021	\parallel Si ₃ N ₄ ring	1550	115	(200)	(0.0125)
Ours, 2022*	\parallel Si slot wg	1310	69	13.9	1.68
		1550	196	28.27	1.05

The exchange of energy that occurs during the interaction can either accelerate the electron by absorbing energy from the optical mode as in the case of DLAs, or it can increase the energy in the optical mode by decelerating the electron as in the case of stimulated emission in a free electron laser. To produce an overall acceleration of the electron, its broadened energy spectrum must simply be skewed toward energy gain rather than loss. Our utilization of a commercially available SiP chip with a UTEM provides the basis for experiments that modulate the spatiotemporal properties of electrons for optical-electrical energy conversion or quantum information science. For example, the modulated electrons could directly be used in microscopy experiments that require attosecond electron pulses, using the electron coherence to probe the quantum state of matter [323], free-electron quantum-optical detection and free-electron homodyne detection [324], continuous-wave operation of laser-driven microscopes [288, 325], enabling free-electron-bound-electron resonant interactions [326], and other such ideas. As a SiP-based design, it automatically benefits from the low-cost, high yield, and quick turnaround times of SiP technology. Additionally, SiP leverages commercial processes from the CMOS industry to produce highly accessible channels for the fabrication and testing of integrated devices, which has supported its widespread

deployment in a variety of industries including optical communications, sensing, and computing. It has also facilitated an explosive growth in research and development resulting in the functionality of SiP devices being pushed toward their physical limitations. However, since electron-photon interactions are fundamental to the operation of opto-electronic devices, these limitations present an opportunity to investigate the physical mechanisms underlying the device operation. In this context, our work shows how SiP devices can be designed from the ground up to reimagine existing functionalities and explore new ones. For example, it improves upon existing DLA designs and can be used to investigate their quantum nature, which would provide insight into whether the electron energy spectrum exhibits quantized features [327] or whether this effect is eliminated by the limited coherence of the accelerated electrons [290]. It can also improve the prediction accuracy of electron energy gain and loss spectroscopy via electron-photon coincidence detection [308, 328]. Furthermore, the ability to map entanglements onto photon-electron pairs via strong coupling could support a new class of devices which enable electron beams to be used in quantum information science [296, 299, 300, 323, 325]. Our scheme therefore offers a method to efficiently manipulate the coupling between free electrons and light on a SiP chip with the ability to optimize for either the energy gain or the acceleration gradient.

6.4. Conclusion

Our work reveals the potential of combining integrated photonics with electron microscopy. Using a known technology and experimental setup, we designed a device that optimizes electron-photon coupling along its interaction length in a technologically feasible approach. For a 0.22 nJ optical pulse of duration 1 ps in the slot, our design scheme achieves a coupling strength per photon, g_{Qu} , of 0.4266 resulting in a maximum energy gain of 28.27 keV at a wavelength of 1550 nm with a corresponding acceleration gradient of 1.05 GeV/m. Alternatively, the maximum acceleration gradient of 1.68 GeV/m is achieved at a wavelength of 1310 nm for which g_{Qu} is 0.1928, resulting in an energy gain of 13.9 keV. Future work will involve testing on-chip devices and further developing the scheme to incorporate additional design parameters. By maximizing the electron energy gain via the coupling efficiency, our design scheme represents a core building block on the roadmap to realizing a portable, CMOS-based, integrated solution for quantum electro-optic interactions. It enables direct applications in electron acceleration, radiation sources, energy harvesting, and quantum information science. Regarding this thesis, optical energy is efficiently transferred to electrical energy and therefore electric current.

7. Conclusion

“What you leave behind is not what is engraved in stone monuments, but what is woven into the lives of others.”

– Pericles

This thesis presents key components and devices for harvesting solar energy on a SiP chip. An overview of the envisioned process, proposed circuit, and designed components is laid out in section 7.1. It is followed by a summary of the original contributions from this work in section 7.2. Finally, in section 7.3, we look out to the future and describe next steps, broader goals, and future directions of this work.

7.1. Overview

The findings reported in this thesis allow us to reimagine solar energy harvesting as an optical process rather than an electrical one. They offer the basis for a proof-of-concept SiEPIC that can efficiently harvest a specific range of the solar energy spectrum, which is the first step. It provides a platform for developing the optical process of harvesting solar energy, which can overcome inefficiencies in the currently used electrical process. A main outcome of this work was the design and demonstration of novel SiP devices which advanced the robustness, functionality, performance, or efficiency of the state of the art in the field. Mismatches between the operating parameters and constituent materials are addressed, as well as improvements to compatibility and performance. We produced novel SiP device designs by exploiting the properties of CMOS-compatible materials. Our results demonstrate the value of modifying the optical properties of a waveguide by the sub-wavelength spatial arrangement or the application of an electric or magnetic force. They inform the physical analysis as well as performance improvements of opto-electronic device designs for both signal processing and light-matter interactions. The designs are directly applicable to growing markets in telecommunications, sensing, energy conversion, microscopy, nanotechnology, radiation generation, and many other technologies utilizing opto-electronic phenomena. The individual design processes have already informed novel device architectures (which were fabricated via CMOS chip tapeouts offered by CMC) to enhance existing functionalities such as modulation, isolation, and emission. The work has attracted academic collaborations in semiconductor fabrication at Cardiff U. [1], metamaterials at University of Ottawa [1], biochemistry at McGill University [6, 7], and quantum opto-electronics at Technion

University [5], as well as an industrial collaboration with MDA Corporation [11, 12, 14-16, 25-29]. The research findings inform techniques in (bio, pressure) sensing, chemistry (imaging, spectroscopy), medicine (radiotherapy, lab-on-chip), and (quantum, super) computing. Further development of these device designs will push more photonic systems towards commercialization and thereby spawn new research streams and industrial ventures in photonics.

7.2. Summary of Original Contributions

In chapter 2, we reviewed the effects of sub-wavelength periodicity in SiP device structures. Numerical simulations explained the necessity of the photonic band structure in understanding and optimizing dispersion engineered device designs. In doing so, we provide a toolkit for SiP dispersion engineering in the SOI platform. This filled a key gap in the understanding of dispersion engineered SiP devices since the band structure was not commonly used in design optimization due to its complexity, despite it being the only tool that comprehensively described the dispersion of periodic structures. This revealed ways to improve device designs by incorporating sub-wavelength periodicity. For example, the diffractive regime can be used for external coupling; the reflection regime for filters, resonators, and reflectors; and the propagation regime for broadband responses, polarization discrimination, and index tuning. Based on these tools, known concepts in Bloch-Floquet theory have been integrated in conventional geometries. Furthermore, we show that natural and computational optimization techniques have produced specialized, dispersion engineered optical devices that we have yet to completely understand. Be it natural or human-made, these devices suggest new directions for the iterative scientific process to investigate and subsequently develop. With the aid of biomimetics and reverse engineering, the gap between our understanding and our optimized designs leaves much to be explored.

In chapter 3, we turn our attention to fabrication variations in these devices by analyzing the effect of perturbations in the sub-wavelength structure, specifically for the cladding material, SiO₂. Since nanofabrication techniques have not yet been developed to support such resolution, we instead leveraged microscopy techniques to study dispersion engineering in the naturally occurring disordered PhCs of *Nf* diatom frustules. Using a combination of SEM, AFM, SNOM, DFM, CAD modelling, and numerical modelling, we determined that its response was enabled by a higher refractive index of biosilica compared to the surrounding water and cytoplasm. The architecture of the frustule behaved as an ellipsoidal micro-shell with localized, sub-wavelength features including DPhCs, gratings, a racetrack, and lenses. Each feature evoked specific functionalities

including coupling, waveguiding, scattering, diffraction, spectral filtering, resonance, and dispersion control. Our analysis of perturbations in these features showed that the frustule can not only tolerate defects but actually exploit them to improve its robustness, bandwidth, and acceptance angles. Together, these functionalities contributed to PAR harvesting mechanisms of capture, redistribution, and retention. Our findings therefore suggest that the frustule could assist the absorption rate of chloroplasts to improve the photosynthetic conversion efficiency of the cell. We developed this hypothesis by modeling the frustule as a photonic circuit. Using it, we estimate that the optical response contributed to 9.83% of photosynthesis in the cell during periods of low, intermittent illumination. Furthermore, these apparently complementary functionalities could justify an evolutionary purpose for the optical response of the frustule. Our analysis of light harvesting mechanisms in the frustule further motivates the cultivation of diatoms for solar energy harvesting, carbon sequestration, and other technological applications. Our work provides novel insights into optical manipulation techniques, as derived from nature, which could be used toward SiP device designs.

In chapter 4, we demonstrate a polarization splitter employing effective index modulation based on its geometric shape. This informed our design of an anisotropic, planar waveguide geometry to split orthogonal polarizations. By introducing variations in the design, we found that the stable influence of the shape ensured stable performance over a wide range of conditions. Key performance indicators were an insertion loss of 2 dB and an extinction ratio of at least 11.45 dB within a wavelength range of 1500-1600 nm.

In chapter 5, we study the effect of electrically applied magnetic and electric fields on a waveguide. First, we demonstrate a standalone, CMOS-based Faraday rotator consisting of a waveguide surrounded by a coil. The electrical response of the coil is demonstrated, and the performance of the device is simulated. The design was characterized over 15 design variations including 4 waveguide types, 2 gap widths, and 3 coil lengths. In this evaluation, the TM_0 mode of the strip waveguide at a wavelength of 1352 nm underwent the most rotation of $50.71 \times 10^{-12} \text{ }^\circ$. Having been fabricated in the CMOS process flow and capable of standalone operation, it overcomes two key limitations of current on-chip isolator designs regarding manufacturability and deployment, respectively. In this context, the significance of this design is in the commercial viability of the device. Additionally, our investigation provided the basis for a set of clearly identifiable upgrades which will improve the feasibility of inducing NR PMC in the SiP platform

before requiring any post-processing, additional materials, or external magnetic biasing. This approach therefore provides a strong, alternative pathway to improve the commercial viability of future isolator designs. Even beyond optical isolation, the realization of a MO interaction using CMOS-compatible fabrication processes can enable a variety of novel design opportunities in SiP. Next, we report the concept, design and simulation of a polarization-selective phase modulator using EOPs. The device structure consists of concentric EOP core, glass cladding, and four radially symmetric electrodes, along the axis of propagation for linearly polarized light. Simulation results show an effective phase shift of 1.35 radians for CLD1 and 0.01 radians for DR1 under a 20 V applied voltage with an interaction length of 8 mm. Additionally, static crosstalk is expected to be approximately a third of the induced phase shift in any scenario. Such a device could allow the option of simultaneously modulating two phases within a single structure at an extremely high speed and theoretically low voltage, thus offering an alternative solution to the speed, size, and efficiency constraint imposed on modulators in SiP.

In chapter 6, we design exposed Si waveguides to host specifically tailored optical modes which were then used to manipulate the energy spectrum of travelling free electrons inside a UTEM [5]. Our work shows the potential of combining integrated photonics with electron microscopy to enable direct applications in free-electron acceleration, radiation sources, energy harvesting, and quantum information science. Using a known technology and experimental setup, we designed a device that maximizes electron-photon coupling along its interaction length in a practical manner. For a 1 MW optical pulse incident on the chip, our design produces its highest energy gain of 212.85 keV at a wavelength of 1550 nm and its highest acceleration gradient of 38.11 GeV/m at a wavelength of 1310 nm. Our design scheme therefore sets a roadmap to coupling free electrons and light with the ability to optimize for the acceleration gradient or energy gain in a commercially viable manner, which can therefore support future experiments in the field.

7.3. Outlook

In the overlap between engineering and science, this thesis barely scratches the surface. Insightful SiP device design requires a fundamental understanding of the coupling between the electronic, photonic, phononic, and potentially magnetic or plasmonic band structures of the host (meta-)materials at the sub-wavelength scale. To leverage the coupling between these material properties, there is a clear need for deeper analyses concerning the properties of materials in relation to their molecular structures. This would inform device designs employing applied

mechanical (vibrational), electric, magnetic, and thermal fields. It could break new ground in our understanding of, and ability to predict, the phenomena involving light-matter interactions. As a small contribution, this thesis adds detail to the analysis of the photonic band structure and develops relations to electronic, magnetic, and mechanical behaviour. Techniques that combine these realms could significantly expand the versatility of SiP and open new avenues of research and application. Our work therefore invites deeper investigations into light-matter interactions on the SiP platform.

As depicted in Figure 1.1, we present our scheme as a SiP circuit consisting of 6 devices which: (i) capture ambient light into confined modes, (ii) split the modes based on polarization, (iii) rotate one polarization, (iv) match the phases, (v) combine them into a single mode, and (vi) convert the energy to free electrons. Our approach allows for a modularized design consisting of well-developed circuit components that are easily upgraded in a plug-and-play fashion. Nevertheless, the proposed SiEPIC also allows integration into a monolithic system, which could be achieved by combining the design processes between neighbouring devices. Their operating wavelength range could further be extended across the solar spectrum by drawing on concepts in plasmonics [329, 330], quantum electro-optics [5, 292], photoelectric effects [331], superconductivity [330, 332-335], biomimetics [2, 37], inverse design [336], and explainable artificial intelligence [337]. This could significantly improve existing designs and inspire a variety of novel device functionalities. Nevertheless, each of the devices in our circuit already offer direct applications in: (i) solar energy harvesting, biomimetics, sustainable manufacturing, biosensing, metamaterials, (ii) polarization discrimination, SiP transceivers, (iii) polarization rotation, optical isolation, on-chip electro-magnetic-optics, (iv) dual polarization phase modulation, polymer electro-optics, (vi) electron acceleration, radiation sources, and quantum information science. These applications provide immediate incentives to fuel the roadmap towards harvesting solar energy on a SiP chip.

7.3.1. Nanophotonic Biomimetic Platform

Our work on solar energy capture could directly inform sustainable, energy efficient designs of optical transceiver interfaces such as photodiodes, grating couplers, and solar cells. For example, our analysis of Nf frustules revealed a significant benefit of DPhCs in optimizing the bandwidth and tolerance of the optical response. We therefore propose that an entire SiEPIC transceiver may be developed in a compact form factor by using DPhCs. Furthermore, the resonances could reduce

the energy consumption of active devices in the circuit. The performance could further be tuned to minimize insertion loss, maximize bandwidth, or increase fabrication tolerance. This research direction could further be extended to grow specific species of diatoms so that the frustules may be used directly in SiP chips as a replacement for the cladding. In this sense, biomimetic techniques or devices could be directly applied to SiP chips. This would inform passive, biomimetic device design principles for sensing and communications technology.

7.3.2. Characterization of an Angled MMI

In the development of a PBS in chapter 4, we did not reach a fundamentally optimized device for polarization splitting. Particularly, the size-bandwidth trade-off for the MMI was not characterized and the reasoning behind the benefit of an angled input was not determined. We therefore propose further investigation into the design process for an angled, MMI-based PBS for which a draft paper has already been written. This draft may be made available to whoever is interested in continuing the work.

7.3.3. Magnetic Non-reciprocity in a Ring Resonator

Instead of the relatively high resistance incurred by a horizontal-axis coil in section 5.1, vertical coils were also fabricated. These coils comprised of both metallisation layers spiralling inward and outward, and suspended over a Si ring. However, the high inductance degraded the response time. An alternative to a spiral design could be to fabricate an electrical pathway which conducts current radially outward across the ring in the shape of a dome. It would consist of connections at the center of the ring and at its circumference. This allows the magnetic field to be applied in the same direction to almost every part of the ring. It could induce an NRPS in the ring.

Extending the concept of counter-propagating waves in NRPS, we speculate that non-reciprocity could also be explored by treating the phenomena of constructive and destructive interference as analogies for electrons and holes in a semiconductor and combining this with the treatment of photons as quasiparticles. It could also be explored whether the field of a radio frequency wave, or electrons or plasmons could be destructively interfered with the backward wave using techniques similar to those described the following sections. The insights from such studies might help manipulate the material properties of a waveguide to build an optical isolator or Peltier heater.

7.3.4. Stimulating the Indirect Electronic Bandgap of Si

The generation of light is a crucial missing functionality in SiP. Its realization would complete the suite of components necessary for an on-chip optical link comprising of generation, modulation, and detection [4]. Yet despite significant research efforts and commercial interest, an on-chip, CMOS-compatible, standalone SiP laser emitting in the telecommunication wavelength range has not been achieved. This is because the indirect electronic bandgap of Si prevents optical emission, and therefore lasing. A change in electron momentum is required to complete the indirect bandgap in Si, which implies that excited electrons can be stimulated to emit light only if they simultaneously encounter a phonon to compress the lattice in specific directions. It could be attempted by generating vibrational waves that appropriately distort the Si lattice to induce emission from excited electrons. Based on the indirect band gap of Si, we may consider exploring the generation and propagation of phonons with the goal of effectively modulating the electronic band structure. Such a test could be carried out by using EAPs [13] as the optical cladding along with an electrode on top. It is also worth investigating whether the application of a magnetic field on the bulk Si can contribute to the momentum of an electron. Another similar avenue of exploration could be to induce this change in momentum by running a current through the section of the device in the same direction as the phonons that are required for electrons to cross the indirect bandgap. Once emission is realized, it could be stimulated using the resonant amplification of a BG or ring to therefore form a laser.

7.3.5. Electron-Light Coupling

SiP opto-electronic engineering is typically explored in the context of using electrons to manipulate light on-chip. Instead, we use modulation techniques in a reverse scenario, which involves a quantum electro-optic effect that has been largely unexplored using SiP. Current electron accelerators have a footprint of multiple kilometers whereas the proposed device is about 10 m including the UTEM setup.

As an alternative to accessing the indirect bandgap of Si as explained in section 7.3.4, such a device could also be used to harness the radiation from traveling free electrons. As these electrons are brought near a grating on-chip, they emit radiation in a frequency spectrum corresponding to the speed of the electron and the pitch of the grating in the form of SPR or Cerenkov radiation. It is possible that C-band light could be extracted from free electrons by tuning the parameters. The extracted light could be amplified in a ring as explored in section 7.3.8.

7.3.6. Non-reciprocal Intensity Modulation using an Electric-Current

Our research in DLA design provides an understanding of the coupling between free electrons and confined light. This leads to questions concerning the extent of interaction between bound electrons and confined light. Such an interaction could be accessed by reducing the phase velocity of the light (e.g., BG, PhC) or increasing the drift velocity of the electron (e.g., using a metal or graphene strip overlaid on the waveguide). By appropriately tuning the velocities along the propagation length, it could be possible to use the electrons to amplify the light or to absorb energy from it, thereby producing an amplifier or modulator, respectively. Drawing from section 7.3.3, would also be interesting to study non-reciprocity in such a device since the flow of electric current is unidirectional. This would draw on the behavioural similarities between electrons and photons [332, 338]. It could also provide insight into potentially efficient light-matter interactions to develop a novel class of low-energy SiP intensity modulators.

7.3.7. Free Electron Laser on-Chip

We extend the possibilities of light generation in SiP that are explored in sections 7.3.4 and 7.3.5. Recent progress in the applications of photonic technology have demonstrated three key abilities: to accelerate electrons using co-propagating optical pulses, to generate Cerenkov radiation from free electrons traveling along sub-wavelength gratings, and coherent coupling between synchrotron radiation and accelerated electrons to produce lasing at broadband, tunable frequencies. This presents the opportunity to design a SiP system that could use optical pulses to accelerate free electrons, which would generate coherent radiation that could be coupled into a SiP chip. If the process was conducted in an optical cavity such as a racetrack resonator or photonic crystal, it could amplify the stimulated emission of these accelerated electrons, thus producing a SiP free electron laser (FEL).

The research presented in this thesis could be used to develop a SiP FEL with active isolation, if such a device is possible. Essentially, they provide the basis for the design of an on-chip light source using the radiation emitted from travelling charges by drawing from the concept of Synchrotron radiation [339]. The propagation, dispersion, and free-space coupling to the device would be engineered using techniques developed in chapter 2 and 3. Polarization diversity would be implemented by the device geometry using techniques developed in chapter 4. The phase, polarization, and amplitude could be modulated using techniques developed in chapter 5 and 6. It could be isolated from external signals by the device in section 5.2.

In a synchrotron, radiation is typically generated by charged particles circling in a varying B-field and switching E-field [280, 340]. Its development has evolved into a toroidal cavity with circulating electrons [341]. We propose to implement this concept in SiP as a micro-synchrotron design. The design could utilize the coils demonstrated in section 5.1. Preliminary schematics and designs were fabricated by utilizing a Si microring surrounded by electrodes and a metal coil for field generation as seen in Figure 7.1. In future designs, electron scattering can be reduced while still being penetrable by a B-field [342]. This could be achieved by doping the ring with Boron and cooling it to 0.34K for superconductivity [333] or by depositing Graphene [335] or Si nanowires [334] for ballistic conduction.

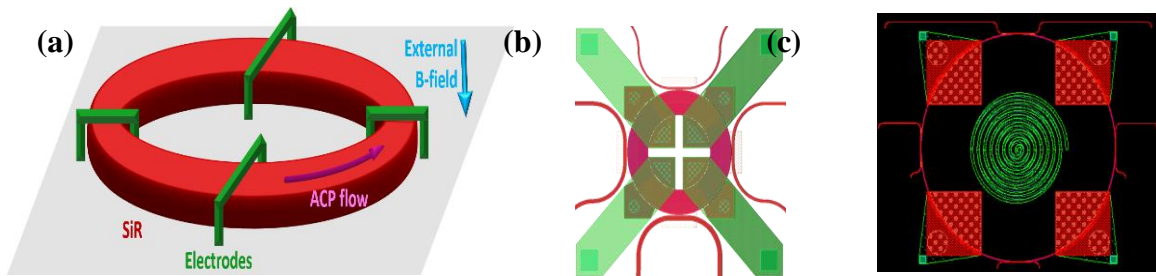


Figure 7.1: (a) 3D schematic of the fabricated ring resonator synchrotron, and (b) top-down view of a fabricated layout with four waveguides of different widths to extract wavelengths of light generated in the ring (fabricated in the SiEPIC5 tapeout). (c) Layout of a ring with four electrodes and a concentric, dual layer, metal coil for B-field generation (fabricated in the SiEPIC6 tapeout).

Based on the FEL concept [343], we speculate that resonance in the ring would interact with the electron flow to stimulate emission at the same frequency. The emitted light would be confined in the ring, which would emulate an optical cavity thereby inducing amplification. It could also be amplified by the fact that light generation via synchrotron radiation induces the radiation of coherent photons resulting in a cascading effect. The realization of a FEL in SiP would offer a tunable source with a broadband response [344]. It would represent the first synchrotron-based controllable light source in SiP and furthermore, suggests the possibility of harnessing electron-light interactions to build an on-chip supercontinuum source. The realization of such a device would be a milestone in the field of nanophotonics and fill an important gap in nanophotonic systems.

"The usefulness of synchrotron light is limited only by our imagination"

– Sir Gustav Nossal

Note to reader: If you are pursuing any of these topics, I would love to collaborate!

References

- [1] Y. D'Mello *et al.*, "Integration of periodic, sub-wavelength structures in silicon-on-insulator photonic device design," *IET Optoelectronics*, vol. 14, no. 3, pp. 125-135, 2020, doi: <https://doi.org/10.1049/iet-opt.2019.0077>.
- [2] Y. D'Mello, S. Bernal, D. Petrescu, J. Skoric, M. Andrews, and D. V. Plant, "Solar energy harvesting mechanisms of the frustules of *Nitzschia filiformis* diatoms," *Opt. Mater. Express*, vol. 12, no. 12, pp. 4665-4681, 2022/12/01 2022, doi: 10.1364/OME.473109.
- [3] Y. D'Mello *et al.*, "Compact, Angled Polarization Splitter: Characterization of Broadband Performance and Fabrication Tolerance," *IEEE Photonics Journal*, vol. 10, no. 6, pp. 1-12, 2018, doi: 10.1109/JPHOT.2018.2878905.
- [4] Y. D'Mello *et al.*, "Standalone, CMOS-based Faraday rotation in a silicon photonic waveguide," *Optics Express*, vol. 30, no. 14, pp. 24602-24610, 2022/07/04 2022, doi: 10.1364/OE.453840.
- [5] Y. D'Mello, R. Dahan, S. Bernal, I. Kaminer, and D. V. Plant, "Strong Coupling of Free Electrons with the Supermode of a Silicon Slot-Waveguide," 2022.
- [6] Y. D'Mello, D. Petrescu, J. Skoric, M. Campbell, M. Andrews, and D. Plant, "Characterization of the Photonic Response in *Nitzschia Filiformis* Phytoplankton," in *Conference on Lasers and Electro-Optics*, San Jose, California, 2018/05/13 2018: Optical Society of America, in OSA Technical Digest, p. JTh2A.96. [Online]. Available: http://www.osapublishing.org/abstract.cfm?URI=CLEO_QELS-2018-JTh2A.96. [Online]. Available: http://www.osapublishing.org/abstract.cfm?URI=CLEO_QELS-2018-JTh2A.96
- [7] Y. D'Mello, S. Bernal, J. Skoric, D. Petrescu, M. Andrews, and D. V. Plant, "Photonic Crystal Behavior of *Nitzschia Filiformis* Phytoplankton for Chlorophyll A Photosynthesis," in *Conference on Lasers and Electro-Optics*, San Jose, California, 2019/05/05 2019: Optical Society of America, in OSA Technical Digest, p. JW2A.121, doi: 10.1364/CLEO_AT.2019.JW2A.121. [Online]. Available: http://www.osapublishing.org/abstract.cfm?URI=CLEO_AT-2019-JW2A.121

- [8] Y. D'Mello *et al.*, "Numerical Analysis and Optimization of a Multi-Mode Interference Based Polarization Beam Splitter," in *Comsol Conference Boston*, Boston, 2017: COMSOL.
- [9] Y. D'Mello *et al.*, "Extremely Compact and Broadband Polarization Beam Splitter Enabled by Customized Port Angles," in *Frontiers in Optics / Laser Science*, Washington, DC, 2018/09/16 2018: Optical Society of America, in OSA Technical Digest, p. JW4A.10. [Online]. Available: <http://www.osapublishing.org/abstract.cfm?URI=LS-2018-JW4A.10>. [Online]. Available: <http://www.osapublishing.org/abstract.cfm?URI=LS-2018-JW4A.10>
- [10] Y. D'Mello *et al.*, "Silicon-Organic-Hybrid Independent Simultaneous Dual-Polarization Modulator: Device Theory and Design," in *Comsol Conference Boston*, Boston, 2017: COMSOL.
- [11] Y. D'Mello *et al.*, "Autocorrelated Differential Algorithm for Real-Time Seismocardiography Analysis," *IEEE Sensors Journal*, vol. 19, no. 13, pp. 5127-5140, 2019, doi: 10.1109/JSEN.2019.2903449.
- [12] Y. D'Mello *et al.*, "Real-Time Cardiac Beat Detection and Heart Rate Monitoring from Combined Seismocardiography and Gyrocardiography," *Sensors*, vol. 19, no. 16, p. 3472, 2019. [Online]. Available: <https://www.mdpi.com/1424-8220/19/16/3472>.
- [13] Y. D'Mello, J. Skoric, L. Moukarzel, S. Hakim, and D. V. Plant, "Wearable Fiber Optic Sensors for Biomechanical Sensing via Joint Angle Detection," in *2019 41st Annual International Conference of the IEEE Engineering in Medicine and Biology Society (EMBC)*, 23-27 July 2019, pp. 32221-32225, doi: 10.1109/EMBC.2019.8857061.
- [14] Y. D'Mello *et al.*, "Identification of the Vibrations Corresponding with Heart Sounds using Vibrational Cardiography," in *42nd Annual International Conference of the IEEE Engineering in Medicine & Biology Society (EMBC)*, 20-24 July 2020 2020, pp. 17-20, doi: 10.1109/EMBC44109.2020.9175323.
- [15] Y. D'Mello, P. Roche, and M. Lortie, "Method and Apparatus for Deriving Biometric Information using Multiple-Axis Seismocardiography," Patent CA2018051006 Patent Appl. CA2018051006, 2018.
- [16] Y. D'Mello, J. Skoric, M. A. Lortie, and D. V. Plant, "Systems, Methods, And Devices For Non-Invasive And Continuous Hemodynamic Measurement," Canada Patent Appl. 63/033,103, 2021.

- [17] D. V. Plant, Y. D’Mello, and J. Skoric, "Non-invasive Physiological Activity Monitoring System (NiPAMS)," vol. \$641,100 CAD, ed. Montreal, Canada: National Science and Engineering Research Council (NSERC), 2019.
- [18] D. V. Plant, Y. D’Mello, J. Skoric, and S. Hakim, "Non-invasive, Wearable Physiological Activity Monitors," vol. \$146,829 CAD, ed. Montreal, Canada: National Science and Engineering Research Council (NSERC), 2019.
- [19] "Glass-like shells of diatoms help turn light into energy in dim conditions," ed. Washington: Optica Publishing Group, 22 November 2022.
- [20] L. Thomson, "New Model Paves the Way Toward Sustainable Optical Devices," in *AZO Optics*, ed: AZO Optics, Nov 24 2022.
- [21] M. Andrews, "Biogenic optical devices for solar energy conversion: glass-like shells of diatoms help turn light into energy in dim conditions," ed: Department of Chemistry, McGill University, 14 December 2022.
- [22] I. Dumé, "Single-celled marine algae light the way for solar energy," in *Biophysics*, ed: Physics World, 31 Jan 2023.
- [23] Optica, "Glass-like shells of diatoms help turn light into energy in dim conditions," in *Phys.org*, ed: Phys.org, NOVEMBER 22, 2022.
- [24] Optica, "Glass-like shells of diatoms help turn light into energy in dim conditions," in *Science Daily*, ed: Science Daily, November 22, 2022.
- [25] J. Skoric, Y. D’Mello, M. Lortie, S. Gagnon, and D. V. Plant, "Effect of Static Respiratory Volume on the Waveform of Cardiac-induced Sternal Vibrations," in *41st Annual International Conference of the IEEE Engineering in Medicine and Biology Society (EMBC)*, 23-27 July 2019, pp. 4917-4921, doi: 10.1109/EMBC.2019.8857505.
- [26] E. Aboulezz *et al.*, "Analyzing Heart Rate Estimation from Vibrational Cardiography Caused with Different Orientations," in *42nd Annual International Conference of the IEEE Engineering in Medicine and Biology Society (EMBC)*, 2020.
- [27] N. Clairmonte *et al.*, "Neural Network-based Classification of Static Lung Volume States using Vibrational Cardiography," in *42nd Annual International Conference of the IEEE Engineering in Medicine and Biology Society (EMBC)*, 2020.

- [28] J. Skoric *et al.*, "Relationship of the Respiration Waveform to a Chest Worn Inertial Sensor," in *42nd Annual International Conference of the IEEE Engineering in Medicine and Biology Society (EMBC)*, 2020.
- [29] J. Skoric *et al.*, "Respiratory Modulation of Sternal Motion in the Context of Seismocardiography," *IEEE Sensors Journal*, vol. 22, no. 13, pp. 13055-13066, 2022, doi: 10.1109/JSEN.2022.3173205.
- [30] P. S. Inc. "Stocate." www.Stocate.com (accessed).
- [31] B. Petroleum, "bp Statistical Review of World Energy," 2022.
- [32] P. Breeze, "Chapter 13 - Solar Power," in *Power Generation Technologies (Third Edition)*, P. Breeze Ed.: Newnes, 2019, pp. 293-321.
- [33] M. H. Bergin, C. Ghoroi, D. Dixit, J. J. Schauer, and D. T. Shindell, "Large Reductions in Solar Energy Production Due to Dust and Particulate Air Pollution," *Environmental Science & Technology Letters*, vol. 4, no. 8, pp. 339-344, 2017/08/08 2017, doi: 10.1021/acs.estlett.7b00197.
- [34] U. Steger *et al.*, *Sustainable development and innovation in the energy sector*. Springer Science & Business Media, 2005.
- [35] F. E. C. R. M. M. D. G. Round, *The Diatoms : biology & morphology of the genera*. Cambridge [England]; New York: Cambridge University Press (in English), 1990.
- [36] J. Nelson, *The Physics of Solar Cells (The Physics of Solar Cells)*. 2003.
- [37] P. Bombelli *et al.*, "Powering a microprocessor by photosynthesis," *Energy & Environmental Science*, 10.1039/D2EE00233G vol. 15, no. 6, pp. 2529-2536, 2022, doi: 10.1039/D2EE00233G.
- [38] P. Moriarty and D. Honnery, "The limits of renewable energy," *AIMS Energy*, vol. 9, no. 4, pp. 812-829, 2021, doi: 10.3934/energy.2021037.
- [39] J. Porzio and C. D. Scown, "Life-Cycle Assessment Considerations for Batteries and Battery Materials," *Advanced Energy Materials*, vol. 11, no. 33, p. 2100771, 2021, doi: <https://doi.org/10.1002/aenm.202100771>.
- [40] L. Chrostowski and M. Hochberg, *Silicon photonics design: from devices to systems*. Cambridge University Press, 2015.
- [41] E. El-Fiky *et al.*, "Ultra-Broadband and Compact Asymmetrical Beam Splitter Enabled by Angled Sub-Wavelength Grating MMI," in *Conference on Lasers and Electro-Optics*, San

- Jose, California, 2018/05/13 2018: Optical Society of America, in OSA Technical Digest (online), p. STh4A.7, doi: 10.1364/CLEO_SI.2018.STh4A.7. [Online]. Available: http://www.osapublishing.org/abstract.cfm?URI=CLEO_SI-2018-STh4A.7
- [42] D. Thomson *et al.*, "Roadmap on silicon photonics," *Journal of Optics*, vol. 18, no. 7, p. 073003, 2016.
- [43] (2016). *Light Technologies – A Strategic Asset*.
- [44] C. Corporation, "Cisco Global Cloud Index: Forecast and Methodology, 2015-2020," 2016.
- [45] L. Chrostowski *et al.*, "Silicon Photonic Circuit Design Using Rapid Prototyping Foundry Process Design Kits," *IEEE Journal of Selected Topics in Quantum Electronics*, pp. 1-1, 2019, doi: 10.1109/JSTQE.2019.2917501.
- [46] R. Soref and B. Bennett, "Electrooptical effects in silicon," *IEEE Journal of Quantum Electronics*, vol. 23, no. 1, pp. 123-129, 1987, doi: 10.1109/JQE.1987.1073206.
- [47] T. G. Brown, "Optical fibers and fiber-optic communications," *FIBER OPTICS HANDBOOK*, 2002.
- [48] A. Yariv and P. Yeh, *Photonics: Optical Electronics in Modern Communications (The Oxford Series in Electrical and Computer Engineering)*. Oxford University Press, Inc., 2006.
- [49] R. Soref and J. Lorenzo, "All-silicon active and passive guided-wave components for $\lambda=1.3$ and $1.6 \mu\text{m}$," *IEEE Journal of Quantum Electronics*, vol. 22, no. 6, pp. 873-879, 1986.
- [50] N. Abadía *et al.*, "Low-Power consumption Franz-Keldysh effect plasmonic modulator," *Optics Express*, vol. 22, no. 9, pp. 11236-11243, 2014/05/05 2014, doi: 10.1364/OE.22.011236.
- [51] S. Pauliac, S. Landis, J. Foucher, J. Thiault, and O. Faynot, *Hybrid lithography process for nano-scale devices*. 2006, pp. 1761-1766.
- [52] "NanoSOI Design Rules." Applied Nanotools Inc. <https://www.appliednt.com/nanosoi/sys/resources/rules/> (accessed 26 March 2019, 2019).
- [53] B. Wu and A. Kumar, "Extreme ultraviolet lithography: A review," *Journal of Vacuum Science & Technology B: Microelectronics and Nanometer Structures Processing, Measurement, and Phenomena*, vol. 25, no. 6, pp. 1743-1761, 2007/11/01 2007, doi: 10.1116/1.2794048.

- [54] H. Chen, X. Luo, and A. W. Poon, "Cavity-enhanced photocurrent generation by 1.55 μm wavelengths linear absorption in a p-i-n diode embedded silicon microring resonator," *Applied Physics Letters*, vol. 95, no. 17, p. 171111, 2009/10/26 2009, doi: 10.1063/1.3257384.
- [55] J. F. Bauters *et al.*, "Planar waveguides with less than 0.1 dB/m propagation loss fabricated with wafer bonding," *Optics Express*, vol. 19, no. 24, pp. 24090-24101, 2011/11/21 2011, doi: 10.1364/OE.19.024090.
- [56] Z. Ruan, L. Shen, S. Zheng, and J. Wang, "Subwavelength grating slot (SWGS) waveguide on silicon platform," *Optics express*, vol. 25, no. 15, pp. 18250-18264, 2017.
- [57] O. Reshef, C. Nacke, J. Upham, and R. W. Boyd, "Waveguide-to-waveguide directional coupling beyond a free space wavelength," in *Conference on Lasers and Electro-Optics*, San Jose, California, 2019/05/05 2019: Optical Society of America, in OSA Technical Digest, p. SF1J.6, doi: 10.1364/CLEO_SI.2019.SF1J.6. [Online]. Available: http://www.osapublishing.org/abstract.cfm?URI=CLEO_SI-2019-SF1J.6
- [58] P. J. Bock *et al.*, "Subwavelength grating periodic structures in silicon-on-insulator: a new type of microphotonic waveguide," *Optics Express*, vol. 18, no. 19, pp. 20251-20262, 2010/09/13 2010, doi: 10.1364/OE.18.020251.
- [59] Y. Wang *et al.*, "Compact single-etched sub-wavelength grating couplers for O-band application," *Optics Express*, vol. 25, no. 24, pp. 30582-30590, 2017.
- [60] R. Halir, P. Cheben, S. Janz, D.-X. Xu, Í. Molina-Fernández, and J. G. Wangüemert-Pérez, "Waveguide grating coupler with subwavelength microstructures," *Optics Letters*, vol. 34, no. 9, pp. 1408-1410, 2009/05/01 2009, doi: 10.1364/OL.34.001408.
- [61] X. Chen and H. K. Tsang, "Nanoholes Grating Couplers for Coupling Between Silicon-on-Insulator Waveguides and Optical Fibers," *IEEE Photonics Journal*, vol. 1, no. 3, pp. 184-190, 2009, doi: 10.1109/JPHOT.2009.2031685.
- [62] M. Papes *et al.*, "Fiber-chip edge coupler with large mode size for silicon photonic wire waveguides," *Optics express*, vol. 24, no. 5, pp. 5026-5038, 2016.
- [63] P. Cheben, D. X. Xu, S. Janz, and A. Densmore, "Subwavelength waveguide grating for mode conversion and light coupling in integrated optics," *Optics Express*, vol. 14, no. 11, pp. 4695-4702, 2006/05/29 2006, doi: 10.1364/OE.14.004695.

- [64] Y. Wang *et al.*, "Compact broadband directional couplers using subwavelength gratings," *IEEE Photonics Journal*, vol. 8, no. 3, pp. 1-8, 2016.
- [65] L. Xu *et al.*, "Polarization beam splitter based on MMI coupler with SWG birefringence engineering on SOI," *IEEE Photon. Technol. Lett.*, vol. 30, no. 4, pp. 403-406, 2018.
- [66] N. Abadía *et al.*, "CMOS-compatible multi-band plasmonic TE-pass polarizer," *Optics Express*, vol. 26, no. 23, pp. 30292-30304, 2018/11/12 2018, doi: 10.1364/OE.26.030292.
- [67] P. Cheben, R. Halir, J. H. Schmid, H. A. Atwater, and D. R. Smith, "Subwavelength integrated photonics," *Nature*, vol. 560, no. 7720, pp. 565-572, 2018/08/01 2018, doi: 10.1038/s41586-018-0421-7.
- [68] D. I. Vulis, O. Reshef, P. Camayd-Muñoz, and E. Mazur, "Manipulating the flow of light using Dirac-cone zero-index metamaterials," *Reports on Progress in Physics*, vol. 82, no. 1, p. 012001, 2018/11/05 2018, doi: 10.1088/1361-6633/aad3e5.
- [69] W. Zhou, Z. Cheng, X. Chen, K. Xu, X. Sun, and H. Tsang, "Subwavelength Engineering in Silicon Photonic Devices," *IEEE Journal of Selected Topics in Quantum Electronics*, vol. 25, no. 3, pp. 1-13, 2019, doi: 10.1109/JSTQE.2019.2899757.
- [70] I. Staude and J. Schilling, "Metamaterial-inspired silicon nanophotonics," *Nature Photonics*, Review Article vol. 11, p. 274, 04/28/online 2017, doi: 10.1038/nphoton.2017.39.
- [71] J. M. Luque-González *et al.*, "Tilted subwavelength gratings: controlling anisotropy in metamaterial nanophotonic waveguides," *Optics Letters*, vol. 43, no. 19, pp. 4691-4694, 2018/10/01 2018, doi: 10.1364/OL.43.004691.
- [72] J. D. Joannopoulos, S. G. Johnson, J. N. Winn, and R. D. Meade, *Photonic Crystals: Molding the Flow of Light*, 2 ed. Princeton University Press, 2008.
- [73] E. C. Regan *et al.*, "Direct imaging of isofrequency contours in photonic structures," *Science Advances*, vol. 2, no. 11, p. e1601591, 2016, doi: 10.1126/sciadv.1601591.
- [74] H. H. Li, "Refractive index of silicon and germanium and its wavelength and temperature derivatives," *Journal of Physical and Chemical Reference Data*, vol. 9, no. 3, pp. 561-658, 1980, doi: 10.1063/1.555624.
- [75] S. John, "Strong localization of photons in certain disordered dielectric superlattices," *Physical Review Letters*, vol. 58, no. 23, pp. 2486-2489, 06/08/ 1987, doi: 10.1103/PhysRevLett.58.2486.

- [76] E. Yablonovitch, "Inhibited Spontaneous Emission in Solid-State Physics and Electronics," *Physical Review Letters*, vol. 58, no. 20, pp. 2059-2062, 05/18/ 1987, doi: 10.1103/PhysRevLett.58.2059.
- [77] P. Yeh, A. Yariv, and C.-S. Hong, "Electromagnetic propagation in periodic stratified media. I. General theory*," *J. Opt. Soc. Am.*, vol. 67, no. 4, pp. 423-438, 1977/04/01 1977, doi: 10.1364/JOSA.67.000423.
- [78] E. D. Palik, *Handbook of optical constants of solids*. Academic press, 1998.
- [79] R. Halir *et al.*, "Waveguide sub-wavelength structures: a review of principles and applications," *Laser & Photonics Reviews*, vol. 9, no. 1, pp. 25-49, 2015.
- [80] S. Berthier and J. Lafait, "Effective medium theory: Mathematical determination of the physical solution for the dielectric constant," *Optics Communications*, vol. 33, no. 3, pp. 303-306, 1980/06/01/ 1980, doi: [https://doi.org/10.1016/0030-4018\(80\)90249-7](https://doi.org/10.1016/0030-4018(80)90249-7).
- [81] S. M. Rytov, "Electromagnetic Properties fo a Finely Stratified Medium," *JETP*, vol. 2, 3, pp. 466-475, 1956.
- [82] M. L. Dakss, L. Kuhn, P. F. Heidrich, and B. A. Scott, "Grating Coupler for Efficient Excitation of Optical Guided Waves in Thin Films," *Applied Physics Letters*, vol. 16, no. 12, pp. 523-525, 1970/06/15 1970, doi: 10.1063/1.1653091.
- [83] S. Yamaguti, J.-i. Inoue, O. Haeberlé, and K. Ohtaka, "Photonic crystals versus diffraction gratings in Smith-Purcell radiation," *Physical Review B*, vol. 66, no. 19, p. 195202, 11/07/ 2002, doi: 10.1103/PhysRevB.66.195202.
- [84] G. A. Swartzlander, "Radiation pressure on a diffractive sailcraft," *J. Opt. Soc. Am. B*, vol. 34, no. 6, pp. C25-C30, 2017/06/01 2017, doi: 10.1364/JOSAB.34.000C25.
- [85] Q. Zhao, J. Zhou, F. Zhang, and D. Lippens, "Mie resonance-based dielectric metamaterials," *Materials Today*, vol. 12, no. 12, pp. 60-69, 2009/12/01/ 2009, doi: [https://doi.org/10.1016/S1369-7021\(09\)70318-9](https://doi.org/10.1016/S1369-7021(09)70318-9).
- [86] N. Yu and F. Capasso, "Flat optics with designer metasurfaces," *Nature Materials*, Review Article vol. 13, p. 139, 01/23/online 2014, doi: 10.1038/nmat3839.
- [87] P. Camayd-Muñoz *et al.*, "Lossless Integrated Dirac-Cone Metamaterials," in *Conference on Lasers and Electro-Optics*, San Jose, California, 2016/06/05 2016: Optical Society of America, in OSA Technical Digest (online), p. JW2A.24, doi:

- 10.1364/CLEO_AT.2016.JW2A.24. [Online]. Available:
http://www.osapublishing.org/abstract.cfm?URI=CLEO_AT-2016-JW2A.24
- [88] D. Xu *et al.*, "Silicon Photonic Integration Platform—Have We Found the Sweet Spot?," *IEEE Journal of Selected Topics in Quantum Electronics*, vol. 20, no. 4, pp. 189-205, 2014, doi: 10.1109/JSTQE.2014.2299634.
- [89] T. Barwicz *et al.*, "Polarization-transparent microphotonic devices in the strong confinement limit," *Nature Photonics*, vol. 1, no. 1, p. 57, 2007.
- [90] M. Streshinsky *et al.*, "A compact bi-wavelength polarization splitting grating coupler fabricated in a 220 nm SOI platform," *Optics Express*, vol. 21, no. 25, pp. 31019-31028, 2013/12/16 2013, doi: 10.1364/OE.21.031019.
- [91] E. Schelew, G. W. Rieger, and J. F. Young, "Characterization of Integrated Planar Photonic Crystal Circuits Fabricated by a CMOS Foundry," *Journal of Lightwave Technology*, vol. 31, no. 2, pp. 239-248, 2013/01/15 2013. [Online]. Available: <http://jlt.osa.org/abstract.cfm?URI=jlt-31-2-239>.
- [92] Y. Ohtera, T. Onuki, Y. Inoue, and S. Kawakami, "Multichannel Photonic Crystal Wavelength Filter Array for Near-Infrared Wavelengths," *Journal of Lightwave Technology*, vol. 25, no. 2, pp. 499-503, 2007/02/01 2007. [Online]. Available: <http://jlt.osa.org/abstract.cfm?URI=jlt-25-2-499>.
- [93] W. Zhou and H. K. Tsang, "Dual-wavelength-band subwavelength grating coupler operating in the near infrared and extended shortwave infrared," *Optics Letters*, vol. 44, no. 15, pp. 3621-3624, 2019/08/01 2019, doi: 10.1364/OL.44.003621.
- [94] Y. Li *et al.*, "On-chip zero-index metamaterials," *Nature Photonics*, vol. 9, no. 11, p. 738, 2015.
- [95] X. Huang, Y. Lai, Z. H. Hang, H. Zheng, and C. T. Chan, "Dirac cones induced by accidental degeneracy in photonic crystals and zero-refractive-index materials," *Nature Materials*, vol. 10, p. 582, 05/29/online 2011, doi: 10.1038/nmat3030
<https://www.nature.com/articles/nmat3030#supplementary-information>.
- [96] D. I. Vulis *et al.*, "Monolithic CMOS-compatible zero-index metamaterials," *Optics Express*, vol. 25, no. 11, pp. 12381-12399, 2017/05/29 2017, doi: 10.1364/OE.25.012381.

- [97] O. Reshef, P. Camayd-Muñoz, D. I. Vulis, Y. Li, M. Lončar, and E. Mazur, "Direct Observation of Phase-Free Propagation in a Silicon Waveguide," *ACS Photonics*, vol. 4, no. 10, pp. 2385-2389, 2017.
- [98] X.-T. He *et al.*, "Realization of Zero-Refractive-Index Lens with Ultralow Spherical Aberration," *ACS Photonics*, vol. 3, no. 12, pp. 2262-2267, 2016/12/21 2016, doi: 10.1021/acsphotonics.6b00714.
- [99] X. Wang, W. Shi, H. Yun, S. Grist, N. A. F. Jaeger, and L. Chrostowski, "Narrow-band waveguide Bragg gratings on SOI wafers with CMOS-compatible fabrication process," *Optics Express*, vol. 20, no. 14, pp. 15547-15558, 2012/07/02 2012, doi: 10.1364/OE.20.015547.
- [100] C. Wang and J. Yao, "Fiber Bragg gratings for microwave photonics subsystems," *Optics Express*, vol. 21, no. 19, pp. 22868-22884, 2013/09/23 2013, doi: 10.1364/OE.21.022868.
- [101] H. Qiu *et al.*, "Silicon band-rejection and band-pass filter based on asymmetric Bragg sidewall gratings in a multimode waveguide," *Optics Letters*, vol. 41, no. 11, pp. 2450-2453, 2016/06/01 2016, doi: 10.1364/OL.41.002450.
- [102] W. Shi *et al.*, "Electrically tunable resonant filters in phase-shifted contra-directional couplers," in *The 9th International Conference on Group IV Photonics (GFP)*, 29-31 Aug. 2012 2012, pp. 78-80, doi: 10.1109/GROUP4.2012.6324092.
- [103] H. Qiu, Y. Su, P. Yu, T. Hu, J. Yang, and X. Jiang, "Compact polarization splitter based on silicon grating-assisted couplers," *Optics Letters*, vol. 40, no. 9, pp. 1885-1887, 2015/05/01 2015, doi: 10.1364/OL.40.001885.
- [104] P. B. Deotare, M. W. McCutcheon, I. W. Frank, M. Khan, and M. Lončar, "High quality factor photonic crystal nanobeam cavities," *Applied Physics Letters*, vol. 94, no. 12, p. 121106, 2009, doi: 10.1063/1.3107263.
- [105] Y. A. Vlasov, M. O'Boyle, H. F. Hamann, and S. J. McNab, "Active control of slow light on a chip with photonic crystal waveguides," *Nature*, vol. 438, no. 7064, pp. 65-69, 2005/11/01 2005, doi: 10.1038/nature04210.
- [106] Z. Huang *et al.*, "Strong Optomechanical Coupling in Nanobeam Cavities based on Hetero Optomechanical Crystals," *Scientific Reports*, Article vol. 5, p. 15964, 11/04/online 2015, doi: 10.1038/srep15964.

- [107] Y. Li *et al.*, "Optomechanical crystal nanobeam cavity with high optomechanical coupling rate," *Journal of Optics*, vol. 17, no. 4, p. 045001, 2015/02/26 2015, doi: 10.1088/2040-8978/17/4/045001.
- [108] B. Qi, P. Yu, Y. Li, X. Jiang, M. Yang, and J. Yang, "Analysis of Electrooptic Modulator With 1-D Slotted Photonic Crystal Nanobeam Cavity," *IEEE Photonics Technology Letters*, vol. 23, no. 14, pp. 992-994, 2011, doi: 10.1109/LPT.2011.2148704.
- [109] J. Hendrickson, R. Soref, J. Sweet, and W. Buchwald, "Ultrasensitive silicon photonic-crystal nanobeam electro-optical modulator: Design and simulation," *Optics Express*, vol. 22, no. 3, pp. 3271-3283, 2014/02/10 2014, doi: 10.1364/OE.22.003271.
- [110] Q. Quan, P. B. Deotare, and M. Loncar, "Photonic crystal nanobeam cavity strongly coupled to the feeding waveguide," *Applied Physics Letters*, vol. 96, no. 20, p. 203102, 2010, doi: 10.1063/1.3429125.
- [111] T. F. Krauss, R. M. D. L. Rue, and S. Brand, "Two-dimensional photonic-bandgap structures operating at near-infrared wavelengths," *Nature*, vol. 383, no. 6602, pp. 699-702, 1996/10/01 1996, doi: 10.1038/383699a0.
- [112] S.-Y. Lin, E. Chow, V. Hietala, P. R. Villeneuve, and J. D. Joannopoulos, "Experimental Demonstration of Guiding and Bending of Electromagnetic Waves in a Photonic Crystal," *Science*, vol. 282, no. 5387, pp. 274-276, 1998, doi: 10.1126/science.282.5387.274.
- [113] P. Cheben *et al.*, "Broadband polarization independent nanophotonic coupler for silicon waveguides with ultra-high efficiency," *Optics Express*, vol. 23, no. 17, pp. 22553-22563, 2015/08/24 2015, doi: 10.1364/OE.23.022553.
- [114] M. Zadka, U. D. Dave, and M. Lipson, "High Tolerance of Metamaterial Waveguides to Fabrication Variations," in *Conference on Lasers and Electro-Optics*, San Jose, California, 2019/05/05 2019: Optical Society of America, in OSA Technical Digest, p. SF1J.7, doi: 10.1364/CLEO_SI.2019.SF1J.7. [Online]. Available: http://www.osapublishing.org/abstract.cfm?URI=CLEO_SI-2019-SF1J.7
- [115] A. Ortega-Moñux *et al.*, "Disorder effects in subwavelength grating metamaterial waveguides," *Optics Express*, vol. 25, no. 11, pp. 12222-12236, 2017/05/29 2017, doi: 10.1364/OE.25.012222.

- [116] V. R. Almeida, Q. Xu, C. A. Barrios, and M. Lipson, "Guiding and confining light in void nanostructure," *Optics Letters*, vol. 29, no. 11, pp. 1209-1211, 2004/06/01 2004, doi: 10.1364/OL.29.001209.
- [117] A. Sánchez-Postigo *et al.*, "Mid-infrared suspended waveguide platform and building blocks," *IET Optoelectronics*, vol. 13, no. 2, pp. 55-61, 2019, doi: 10.1049/iet-opt.2018.5067.
- [118] W. Zhou, Z. Cheng, X. Wu, X. Sun, and H. K. Tsang, "Fully suspended slot waveguide platform," *Journal of Applied Physics*, vol. 123, no. 6, p. 063103, 2018/02/14 2018, doi: 10.1063/1.5017780.
- [119] L. B. Soldano and E. C. Pennings, "Optical multi-mode interference devices based on self-imaging: principles and applications," *Journal of lightwave technology*, vol. 13, no. 4, pp. 615-627, 1995.
- [120] R. Halir *et al.*, "Ultra-broadband nanophotonic beamsplitter using an anisotropic sub-wavelength metamaterial," *Laser & Photonics Reviews*, vol. 10, no. 6, pp. 1039-1046, 2016, doi: 10.1002/lpor.201600213.
- [121] A. H. Bermello, J. M. L. Gonzalez, A. Velasco, A. Ortega-Monux, P. Cheben, and R. Halir, "Design of a broadband polarization splitter based on anisotropy-engineered tilted subwavelength gratings," *IEEE Photonics Journal*, 2019.
- [122] A. Zanzi, A. Brimont, A. Griol, P. Sanchis, and J. Marti, "Compact and low-loss asymmetrical multimode interference splitter for power monitoring applications," *Optics letters*, vol. 41, no. 2, pp. 227-229, 2016.
- [123] Y. Shi, D. Dai, and S. He, "Proposal for an ultracompact polarization-beam splitter based on a photonic-crystal-assisted multimode interference coupler," *IEEE Photonics Technology Letters*, vol. 19, no. 11, pp. 825-827, 2007.
- [124] L. Xu *et al.*, "Compact Broadband Polarization Beam Splitter Based on Multimode Interference Coupler With Internal Photonic Crystal for the SOI Platform," *Journal of Lightwave Technology*, vol. 37, no. 4, pp. 1231-1240, 2019.
- [125] Y. Wang *et al.*, "Ultra-Compact Sub-Wavelength Grating Polarization Splitter-Rotator for Silicon-on-Insulator Platform," *IEEE Photonics Journal*, vol. 8, no. 6, pp. 1-9, 2016, doi: 10.1109/JPHOT.2016.2630849.

- [126] Y. Xu and J. Xiao, "Ultracompact and high efficient silicon-based polarization splitter-rotator using a partially-etched subwavelength grating coupler," *Scientific reports*, vol. 6, p. 27949, 2016.
- [127] D. Zhao, J. Zhang, P. Yao, X. Jiang, and X. Chen, "Photonic crystal Mach-Zehnder interferometer based on self-collimation," *Applied Physics Letters*, vol. 90, no. 23, p. 231114, 2007/06/04 2007, doi: 10.1063/1.2746942.
- [128] K. McGarvey-Lechable and P. Bianucci, "Bloch-Floquet Waves in Optical Ring Resonators," in *Conference on Lasers and Electro-Optics*, San Jose, California, 2019/05/05 2019: Optical Society of America, in OSA Technical Digest, p. SW4J.2, doi: 10.1364/CLEO_SI.2019.SW4J.2. [Online]. Available: http://www.osapublishing.org/abstract.cfm?URI=CLEO_SI-2019-SW4J.2
- [129] M. Soljačić, S. G. Johnson, S. Fan, M. Ibanescu, E. Ippen, and J. D. Joannopoulos, "Photonic-crystal slow-light enhancement of nonlinear phase sensitivity," *J. Opt. Soc. Am. B*, vol. 19, no. 9, pp. 2052-2059, 2002/09/01 2002, doi: 10.1364/JOSAB.19.002052.
- [130] J. Gonzalo Wangüemert-Pérez *et al.*, "Evanescent field waveguide sensing with subwavelength grating structures in silicon-on-insulator," *Optics Letters*, vol. 39, no. 15, pp. 4442-4445, 2014/08/01 2014, doi: 10.1364/OL.39.004442.
- [131] J. Upham, B. Gao, L. O'Faolain, Z. Shi, S. A. Schulz, and R. W. Boyd, "Realization of a flat-band superprism on-chip from parallelogram lattice photonic crystals," *Optics Letters*, vol. 43, no. 20, pp. 4981-4984, 2018/10/15 2018, doi: 10.1364/OL.43.004981.
- [132] J. Moon *et al.*, "Continuous Wave Green Lasing at Room Temperature in Two-Dimensional Photonic Crystal Perovskite Laser," in *Conference on Lasers and Electro-Optics*, San Jose, California, 2019/05/05 2019: Optical Society of America, in OSA Technical Digest, p. SW4N.2, doi: 10.1364/CLEO_SI.2019.SW4N.2. [Online]. Available: http://www.osapublishing.org/abstract.cfm?URI=CLEO_SI-2019-SW4N.2
- [133] B. Jalali, "Making Silicon Lase," *Scientific American*, vol. 296, no. 2, pp. 58-65, Feb 2007. [Online]. Available: <http://www.jstor.org/stable/26069154>.
- [134] P. Tréguer *et al.*, "Influence of diatom diversity on the ocean biological carbon pump," *Nature Geoscience*, vol. 11, no. 1, pp. 27-37, 2018/01/01 2018, doi: 10.1038/s41561-017-0028-x.

- [135] P. Kuczynska, M. Jemiola-Rzeminska, and K. Strzalka, "Photosynthetic pigments in diatoms," *Marine drugs*, vol. 13, no. 9, pp. 5847-5881, 2015.
- [136] T. Fuhrmann, S. Landwehr, M. El Rharbi-Kucki, and M. Sumper, "Diatoms as living photonic crystals," *Applied Physics B*, vol. 78, no. 3-4, pp. 257-260, 2004.
- [137] M. Taniguchi and J. S. Lindsey, "Database of Absorption and Fluorescence Spectra of 300 Common Compounds for use in Photochem CAD," *Photochemistry and photobiology*, vol. 94, no. 2, pp. 290-327, 2018.
- [138] C. Liu, M. Rybin, P. Mao, S. Zhang, and Y. Kivshar, "Disorder-Immune Photonics Based on Mie-Resonant Dielectric Metamaterials," in *Conference on Lasers and Electro-Optics*, San Jose, California, 2019/05/05 2019: Optical Society of America, in OSA Technical Digest, p. FF3B.6, doi: 10.1364/CLEO_QELS.2019.FF3B.6. [Online]. Available: http://www.osapublishing.org/abstract.cfm?URI=CLEO_QELS-2019-FF3B.6
- [139] T. Dbouk, "A review about the engineering design of optimal heat transfer systems using topology optimization," *Applied Thermal Engineering*, vol. 112, pp. 841-854, 2017/02/05/2017, doi: <https://doi.org/10.1016/j.applthermaleng.2016.10.134>.
- [140] J.-H. Zhu, W.-H. Zhang, and L. Xia, "Topology Optimization in Aircraft and Aerospace Structures Design," *Archives of Computational Methods in Engineering*, vol. 23, no. 4, pp. 595-622, 2016/12/01 2016, doi: 10.1007/s11831-015-9151-2.
- [141] J. Lu and J. Vučković, "Nanophotonic computational design," *Optics express*, vol. 21, no. 11, pp. 13351-13367, 2013.
- [142] M. H. Tahersima *et al.*, "Deep Neural Network Inverse Design of Integrated Photonic Power Splitters," *Scientific Reports*, vol. 9, no. 1, p. 1368, 2019/02/04 2019, doi: 10.1038/s41598-018-37952-2.
- [143] B. Shen, P. Wang, R. Polson, and R. Menon, "An integrated-nanophotonics polarization beamsplitter with $2.4 \times 2.4 \mu\text{m}^2$ footprint," *Nature Photonics*, vol. 9, no. 6, p. 378, 2015.
- [144] B. W. Griscom *et al.*, "Natural climate solutions," *Proceedings of the National Academy of Sciences*, vol. 114, no. 44, pp. 11645-11650, 2017, doi: doi:10.1073/pnas.1710465114.
- [145] C. B. Field, M. J. Behrenfeld, J. T. Randerson, and P. Falkowski, "Primary Production of the Biosphere: Integrating Terrestrial and Oceanic Components," *Science*, vol. 281, no. 5374, pp. 237-240, 1998, doi: doi:10.1126/science.281.5374.237.

- [146] C. S. Rousseaux and W. W. Gregg, "Interannual Variation in Phytoplankton Primary Production at A Global Scale," *Remote Sensing*, vol. 6, no. 1, pp. 1-19, 2014. [Online]. Available: <https://www.mdpi.com/2072-4292/6/1/1>.
- [147] J. W. Goessling, S. Yanyan, M. Kühl, and M. Ellegaard, "Frustule Photonics and Light Harvesting Strategies in Diatoms," in *Diatom Morphogenesis*, 2021, pp. 269-300.
- [148] K. Leblanc *et al.*, "Nanoplanktonic diatoms are globally overlooked but play a role in spring blooms and carbon export," *Nature Communications*, vol. 9, no. 1, p. 953, 2018/03/05 2018, doi: 10.1038/s41467-018-03376-9.
- [149] N. Sharma *et al.*, "Diatoms Biotechnology: Various Industrial Applications for a Greener Tomorrow," (in English), *Frontiers in Marine Science*, Review vol. 8, 2021-February-23 2021, doi: 10.3389/fmars.2021.636613.
- [150] J. W. Goessling, W. P. Wardley, and M. Lopez-Garcia, "Highly Reproducible, Bio-Based Slab Photonic Crystals Grown by Diatoms," *Advanced Science*, vol. 7, no. 10, p. 1903726, 2020, doi: <https://doi.org/10.1002/advs.201903726>.
- [151] P. G. Falkowski *et al.*, "The Evolution of Modern Eukaryotic Phytoplankton," *Science*, vol. 305, no. 5682, pp. 354-360, 2004.
- [152] J. Livage and P. J. Lopez, "Biogenic Silica Glasses," in *Encyclopedia of Glass Science, Technology, History, and Culture*, 2021, pp. 955-967.
- [153] E. De Tommasi, J. Gielis, and A. Rogato, "Diatom Frustule Morphogenesis and Function: a Multidisciplinary Survey," *Marine Genomics*, vol. 35, pp. 1-18, 2017/10/01/ 2017, doi: <https://doi.org/10.1016/j.margen.2017.07.001>.
- [154] C. E. Hamm *et al.*, "Architecture and material properties of diatom shells provide effective mechanical protection," *Nature*, vol. 421, no. 6925, pp. 841-843, 2003/02/01 2003, doi: 10.1038/nature01416.
- [155] A. J. Milligan and F. M. M. Morel, "A Proton Buffering Role for Silica in Diatoms," *Science*, vol. 297, no. 5588, pp. 1848-1850, 2002, doi: doi:10.1126/science.1074958.
- [156] S. H. Michelle and G. M. James, "Functional morphology of diatom frustule microstructures: hydrodynamic control of Brownian particle diffusion and advection," *Aquatic Microbial Ecology*, vol. 24, no. 3, pp. 287-295, 2001. [Online]. Available: <https://www.int-res.com/abstracts/ame/v24/n3/p287-295/>.

- [157] W. Wang *et al.*, "Structural basis for blue-green light harvesting and energy dissipation in diatoms," *Science*, vol. 363, no. 6427, p. eaav0365, 2019, doi: 10.1126/science.aav0365.
- [158] J. W. Goessling *et al.*, "Structure-based optics of centric diatom frustules: modulation of the in vivo light field for efficient diatom photosynthesis," *New Phytologist*, vol. 219, no. 1, pp. 122-134, 2018, doi: <https://doi.org/10.1111/nph.15149>.
- [159] X. Chen, C. Wang, E. Baker, and C. Sun, "Numerical and experimental investigation of light trapping effect of nanostructured diatom frustules," *Scientific Reports*, vol. 5, no. 1, p. 11977, 2015/07/09 2015, doi: 10.1038/srep11977.
- [160] E. De Tommasi *et al.*, "Underwater Light Manipulation by the Benthic Diatom *Ctenophora pulchella*: From PAR Efficient Collection to UVR Screening," *Nanomaterials*, vol. 11, no. 11, p. 2855, 2021. [Online]. Available: <https://www.mdpi.com/2079-4991/11/11/2855>.
- [161] J. W. Goessling, S. Frankenbach, L. Ribeiro, J. Serôdio, and M. Kühl, "Modulation of the light field related to valve optical properties of raphid diatoms: implications for niche differentiation in the microphytobenthos," *Marine Ecology Progress Series*, vol. 588, pp. 29-42, 2018. [Online]. Available: <https://www.int-res.com/abstracts/meps/v588/p29-42/>.
- [162] Y. Owari, F. Nakamura, Y. Oaki, H. Tsuda, S. Shimode, and H. Imai, "Ultrastructure of setae of a planktonic diatom, *Chaetoceros coarctatus*," *Scientific Reports*, vol. 12, no. 1, p. 7568, 2022/05/09 2022, doi: 10.1038/s41598-022-11484-2.
- [163] E. De Tommasi, "Light Manipulation by Single Cells: The Case of Diatoms," *Journal of Spectroscopy*, vol. 2016, p. 13, 2016, Art no. 2490128, doi: 10.1155/2016/2490128.
- [164] K. Kieu *et al.*, "Structure-based optical filtering by the silica microshell of the centric marine diatom *Coscinodiscus wailesii*," *Optics Express*, vol. 22, no. 13, pp. 15992-15999, 2014/06/30 2014, doi: 10.1364/OE.22.015992.
- [165] S. Yamanaka *et al.*, "Optical properties of diatom silica frustule with special reference to blue light," *Journal of Applied Physics*, vol. 103, no. 7, p. 074701, 2008, doi: 10.1063/1.2903342.
- [166] S. Bernal, Y. D. Mello, D. Petrescu, M. Andrews, and D. V. Plant, "Optical Response of the Centric Valve in *Cyclotella Quillensis* Diatoms," in *2020 Conference on Lasers and Electro-Optics (CLEO)*, 10-15 May 2020 2020, pp. 1-2.

- [167] L. D. Stefano, I. Rea, I. Rendina, M. D. Stefano, and L. Moretti, "Lensless light focusing with the centric marine diatom *Coscinodiscus walesii*," *Optics Express*, vol. 15, no. 26, pp. 18082-18088, 2007/12/24 2007, doi: 10.1364/OE.15.018082.
- [168] J. Romann, J.-C. Valmalette, M. S. Chauton, G. Tranell, M.-A. Einarsrud, and O. Vadstein, "Wavelength and orientation dependent capture of light by diatom frustule nanostructures," *Scientific Reports*, vol. 5, no. 1, p. 17403, 2015/12/02 2015, doi: 10.1038/srep17403.
- [169] E. De Tommasi *et al.*, "Biologically enabled sub-diffractive focusing," *Optics Express*, vol. 22, no. 22, pp. 27214-27227, 2014/11/03 2014, doi: 10.1364/OE.22.027214.
- [170] M. A. Ferrara *et al.*, "Optical Properties of Diatom Nanostructured Biosilica in *Arachnoidiscus* sp: Micro-Optics from Mother Nature," *PLOS ONE*, vol. 9, no. 7, p. e103750, 2014, doi: 10.1371/journal.pone.0103750.
- [171] E. De Tommasi *et al.*, "Multi-wavelength study of light transmitted through a single marine centric diatom," *Optics Express*, vol. 18, no. 12, pp. 12203-12212, 2010/06/07 2010, doi: 10.1364/OE.18.012203.
- [172] S. G. Johnson, S. Fan, P. R. Villeneuve, J. D. Joannopoulos, and L. A. Kolodziejski, "Guided modes in photonic crystal slabs," *Physical Review B*, vol. 60, no. 8, pp. 5751-5758, 08/15/ 1999, doi: 10.1103/PhysRevB.60.5751.
- [173] L. Cheng, S. Mao, Z. Li, Y. Han, and H. Y. Fu, "Grating Couplers on Silicon Photonics: Design Principles, Emerging Trends and Practical Issues," *Micromachines*, vol. 11, no. 7, p. 666, 2020. [Online]. Available: <https://www.mdpi.com/2072-666X/11/7/666>.
- [174] Y. D'Mello *et al.*, "Integration of Sub-wavelength, Periodic Structures in Silicon-on-Insulator Photonic Device Design," *IET Optoelectronics*, vol. 14, no. 3, pp. 125-135. [Online]. Available: <https://digital-library.theiet.org/content/journals/10.1049/iet-opt.2019.0077>
- [175] P. Lalanne and P. Chavel, "Metalenses at visible wavelengths: past, present, perspectives," *Laser & Photonics Reviews*, vol. 11, no. 3, p. 1600295, 2017, doi: <https://doi.org/10.1002/lpor.201600295>.
- [176] J. Zimmermann, M. Kamp, A. Forchel, and R. März, "Photonic crystal waveguide directional couplers as wavelength selective optical filters," *Optics Communications*, vol. 230, no. 4, pp. 387-392, 2004/02/01/ 2004, doi: <https://doi.org/10.1016/j.optcom.2003.11.026>.

- [177] E. De Tommasi *et al.*, "Frontiers of light manipulation in natural, metallic, and dielectric nanostructures," *La Rivista del Nuovo Cimento*, vol. 44, no. 1, pp. 1-68, 2021/01/01 2021, doi: 10.1007/s40766-021-00015-w.
- [178] G. Cohoon *et al.*, *Analysis of quasi-periodic pore-network structure of centric marine diatom frustules* (SPIE BiOS). SPIE, 2015.
- [179] M. M. Ghobara, M. A. Tiffany, R. Gordon, and L. Reissig, "Diatom Pore Arrays' Periodicities and Symmetries in the Euclidean Plane: Nature Between Perfection and Imperfection," in *Diatom Morphogenesis*, 2021, pp. 117-158.
- [180] S. Yoneda, F. Ito, S. Yamanaka, and H. Usami, "Optical properties of nanoporous silica frustules of a diatom determined using a 10 μm microfiber probe," *Japanese Journal of Applied Physics*, vol. 55, no. 7, p. 072001, 2016/06/08 2016, doi: 10.7567/jjap.55.072001.
- [181] K. Vynck, M. Burrese, F. Riboli, and D. S. Wiersma, "Photon management in two-dimensional disordered media," *Nature Materials*, vol. 11, p. 1017, 10/07/online 2012, doi: 10.1038/nmat3442.
- [182] H. Ding, L. Lalouat, B. Gonzalez-Acevedo, R. Orobtcouk, C. Seassal, and E. Drouard, "Design rules for net absorption enhancement in pseudo-disordered photonic crystal for thin film solar cells," *Optics Express*, vol. 24, no. 6, pp. A650-A666, 2016/03/21 2016, doi: 10.1364/OE.24.00A650.
- [183] R. C. Rumpf, J. J. Pazos, J. L. Digaum, and S. M. Kuebler, "Spatially variant periodic structures in electromagnetics," *Philosophical Transactions of the Royal Society A: Mathematical, Physical and Engineering Sciences*, vol. 373, no. 2049, p. 20140359, 2015.
- [184] A. Oskooi, P. A. Favuzzi, Y. Tanaka, H. Shigeta, Y. Kawakami, and S. Noda, "Partially disordered photonic-crystal thin films for enhanced and robust photovoltaics," *Applied Physics Letters*, vol. 100, no. 18, p. 181110, 2012, doi: 10.1063/1.4711144.
- [185] J. C. Valmalette, J. Romann, A. Røyset, and M. A. Einarsrud, "3D-hyperspectral mapping of light propagation through diatom frustule silica nanostructures," in *2015 Opto-Electronics and Communications Conference (OECC)*, 28 June-2 July 2015 2015, pp. 1-3, doi: 10.1109/OECC.2015.7340196.
- [186] J. Noyes, M. Sumper, and P. Vukusic, "Light manipulation in a marine diatom," *Journal of Materials Research*, vol. 23, no. 12, pp. 3229-3235, 2008/12/01 2008, doi: 10.1557/JMR.2008.0381.

- [187] C. Maibohm, S. M. M. Friis, M. Ellegaard, and K. Rottwitt, "Interference patterns and extinction ratio of the diatom *Coscinodiscus granii*," *Optics Express*, vol. 23, no. 7, pp. 9543-9548, 2015/04/06 2015, doi: 10.1364/OE.23.009543.
- [188] K. B. Dossou, "Large field enhancement obtained by combining Fabry–Perot resonance and Rayleigh anomaly in photonic crystal slabs," *Journal of Optics*, vol. 19, no. 4, p. 045101, 2017/03/21 2017, doi: 10.1088/2040-8986/aa608b.
- [189] J. W. Goessling, Y. Su, C. Maibohm, M. Ellegaard, and M. Köhl, "Differences in the optical properties of valve and girdle band in a centric diatom," *Interface Focus*, vol. 9, no. 1, p. 20180031, 2019, doi: doi:10.1098/rsfs.2018.0031.
- [190] L. R. Prella *et al.*, "Ecophysiological and Cell Biological Traits of Benthic Diatoms From Coastal Wetlands of the Southern Baltic Sea," (in English), *Frontiers in Microbiology*, Original Research vol. 12, 2021-April-12 2021, doi: 10.3389/fmicb.2021.642811.
- [191] M. Florescu, S. Torquato, and P. J. Steinhardt, "Designer disordered materials with large, complete photonic band gaps," *Proceedings of the National Academy of Sciences*, vol. 106, no. 49, pp. 20658-20663, 2009, doi: 10.1073/pnas.0907744106.
- [192] R. Dhama *et al.*, "Extraordinary Effects in Quasi-Periodic Gold Nanocavities: Enhanced Transmission and Polarization Control of Cavity Modes," *ACS Nano*, vol. 12, no. 1, pp. 504-512, 2018/01/23 2018, doi: 10.1021/acsnano.7b07076.
- [193] D. Vobornik and S. Vobornik, "Scanning Near-Field Optical Microscopy," *Bosnian Journal of Basic Medical Sciences*, vol. 8, no. 1, pp. 63-71, 02/20 2008, doi: 10.17305/bjbms.2008.3000.
- [194] B. Hecht *et al.*, "Scanning near-field optical microscopy with aperture probes: Fundamentals and applications," *The Journal of Chemical Physics*, vol. 112, no. 18, pp. 7761-7774, 2000, doi: 10.1063/1.481382.
- [195] M. Hildebrand, "Diatoms, Biomineralization Processes, and Genomics," *Chemical Reviews*, vol. 108, no. 11, pp. 4855-4874, 2008/11/12 2008, doi: 10.1021/cr078253z.
- [196] W. Fu *et al.*, "Intracellular spectral repositioning of light enhances algal photosynthetic efficiency," *Science Advances*, vol. 3, no. 9, p. e1603096, 2017, doi: doi:10.1126/sciadv.1603096.
- [197] B. Schellenberger Costa, A. Jungandreas, T. Jakob, W. Weisheit, M. Mittag, and C. Wilhelm, "Blue light is essential for high light acclimation and photoprotection in the

- diatom *Phaeodactylum tricornutum*," *Journal of Experimental Botany*, vol. 64, no. 2, pp. 483-493, 2012, doi: 10.1093/jxb/ers340.
- [198] J. W. Goessling, P. Cartaxana, and M. Köhl, "Photo-Protection in the Centric Diatom *Coscinodiscus granii* is Not Controlled by Chloroplast High-Light Avoidance Movement," (in English), *Frontiers in Marine Science*, Original Research vol. 2, 2016-January-08 2016, doi: 10.3389/fmars.2015.00115.
- [199] C. Brunet, R. Chandrasekaran, L. Barra, V. Giovagnetti, F. Corato, and A. V. Ruban, "Spectral Radiation Dependent Photoprotective Mechanism in the Diatom *Pseudonitzschia multistriata*," *PLOS ONE*, vol. 9, no. 1, p. e87015, 2014, doi: 10.1371/journal.pone.0087015.
- [200] L. A. Edgar, J. D. Pickett-Heaps, and G. E. Fogg, "The mechanism of diatom locomotion. I. An ultrastructural study of the motility apparatus," *Proceedings of the Royal Society of London. Series B. Biological Sciences*, vol. 218, no. 1212, pp. 331-343, 1983, doi: doi:10.1098/rspb.1983.0042.
- [201] M. Florescu, P. J. Steinhardt, and S. Torquato, "Optical cavities and waveguides in hyperuniform disordered photonic solids," *Physical Review B*, vol. 87, no. 16, p. 165116, 04/10/ 2013, doi: 10.1103/PhysRevB.87.165116.
- [202] K. McGarvey-Lechable and P. Bianucci, "Maximizing slow-light enhancement in one-dimensional photonic crystal ring resonators," *Optics Express*, vol. 22, no. 21, pp. 26032-26041, 2014/10/20 2014, doi: 10.1364/OE.22.026032.
- [203] I. Ricárdez-Vargas, M. D. Iturbe-Castillo, R. Ramos-García, K. Volke-Sepúlveda, and V. Ruíz-Cortés, "Hollow spheres as individual movable micromirrors in optical tweezers," *Optics Express*, vol. 13, no. 3, pp. 968-976, 2005/02/07 2005, doi: 10.1364/OPEX.13.000968.
- [204] M. Soleimani *et al.*, "Modifying the thickness, pore size, and composition of diatom frustule in *Craspedostauros* sp. with Al³⁺ ions," *Scientific Reports*, vol. 10, no. 1, p. 19498, 2020/11/11 2020, doi: 10.1038/s41598-020-76318-5.
- [205] W. Emkey and C. Jack, "Analysis and evaluation of graded-index fiber lenses," *Journal of Lightwave Technology*, vol. 5, no. 9, pp. 1156-1164, 1987, doi: 10.1109/JLT.1987.1075651.

- [206] A. Saha, E. Maria, and M. Z. Baten, "Spectra dependent photonic structure design for energy harvesting by indoor photovoltaic devices," *AIP Advances*, vol. 12, no. 5, p. 055006, 2022, doi: 10.1063/5.0084488.
- [207] E. De Tommasi and A. C. De Luca, "Diatom biosilica in plasmonics: applications in sensing, diagnostics and therapeutics [Invited]," *Biomed. Opt. Express*, vol. 13, no. 5, pp. 3080-3101, 2022/05/01 2022, doi: 10.1364/BOE.457483.
- [208] T. Todd *et al.*, "Iron oxide nanoparticle encapsulated diatoms for magnetic delivery of small molecules to tumors," *Nanoscale*, 10.1039/C3NR05623F vol. 6, no. 4, pp. 2073-2076, 2014, doi: 10.1039/C3NR05623F.
- [209] M. J. Khan, A. Pugazhendhi, B. Schoefs, J. Marchand, A. Rai, and V. Vinayak, "Perovskite-based solar cells fabricated from TiO₂ nanoparticles hybridized with biomaterials from mollusc and diatoms," *Chemosphere*, vol. 291, p. 132692, 2022/03/01/2022, doi: <https://doi.org/10.1016/j.chemosphere.2021.132692>.
- [210] A. Rai *et al.*, "Hydrogen economy and storage by nanoporous microalgae diatom: Special emphasis on designing photobioreactors," *International Journal of Hydrogen Energy*, 2022/02/05/ 2022, doi: <https://doi.org/10.1016/j.ijhydene.2022.01.057>.
- [211] L. McMillon-Brown, "Chapter Eleven - Biomimetic advances in photovoltaics with potential aerospace applications," in *Biomimicry for Aerospace*, V. Shyam, M. Eggermont, and A. F. Hepp Eds.: Elsevier, 2022, pp. 291-329.
- [212] K. Okamoto, *Fundamentals of optical waveguides*. Academic press, 2006.
- [213] G. T. Reed and A. P. Knights, *Silicon photonics: an introduction*. John Wiley & Sons, 2004.
- [214] J. N. Caspers, Y. Wang, L. Chrostowski, and M. Mojahedi, "Active polarization independent coupling to silicon photonics circuit," in *Silicon Photonics and Photonic Integrated Circuits IV*, 2014: International Society for Optics and Photonics.
- [215] E. El-Fiky *et al.*, "200 Gb/s transmission using a dual-polarization O-Band silicon photonic intensity modulator for Stokes vector direct detection applications," *Optics Express*, vol. 25, no. 24, pp. 30336-30348, 2017, doi: 10.1364/OE.25.030336.
- [216] E. Elfiky, A. Samani, D. Patel, and D. Plant, "A high extinction ratio, broadband, and compact polarization beam splitter enabled by cascaded MMIs on silicon-on-insulator," in *Optical Fiber Communication Conference*, 2016: Optical Society of America.

- [217] W. Yang, Y. Xu, Y. Li, X. Wang, and Z. Wang, "A compact and wide-band polarization beam splitter based on wedge-shaped MMI coupler in silicon-on-insulator," in *Optical Fiber Communication Conference*, 2015: Optical Society of America.
- [218] M. Yin, W. Yang, Y. Li, X. Wang, and H. Li, "CMOS-compatible and fabrication-tolerant MMI-based polarization beam splitter," *Optics Communications*, vol. 335, pp. 48-52, 2015.
- [219] W. Bogaerts, M. Fiers, and P. Dumon, "Design challenges in silicon photonics," *IEEE Journal of Selected Topics in Quantum Electronics*, vol. 20, no. 4, pp. 1-8, 2014.
- [220] Y. Jiao, D. Dai, Y. Shi, and S. He, "Shortened polarization beam splitters with two cascaded multimode interference sections," *IEEE Photonics Technology Letters*, vol. 21, no. 20, pp. 1538-1540, 2009.
- [221] D. Dai, "Silicon polarization beam splitter based on an asymmetrical evanescent coupling system with three optical waveguides," *Journal of Lightwave Technology*, vol. 30, no. 20, pp. 3281-3287, 2012.
- [222] C. Liu *et al.*, "Ultrahigh Suppression Broadband Polarization Splitter Based on an Asymmetrical Directional Coupler," *IEEE Photonics Journal*, vol. 9, no. 5, pp. 1-9, 2017.
- [223] X. Sun, M. Alam, J. Aitchison, and M. Mojahedi, "Compact and broadband polarization beam splitter based on a silicon nitride augmented low-index guiding structure," *Optics letters*, vol. 41, no. 1, pp. 163-166, 2016.
- [224] B. Bai, Q. Deng, and Z. Zhou, "Plasmonic-assisted polarization beam splitter based on bent directional coupling," *IEEE Photonics Technol. Lett.*, vol. 29, no. 7, pp. 599-602, 2017.
- [225] Y. Hu, F. Gardes, D. Thomson, G. Mashanovich, and G. Reed, "Interleaved angled MMI CWDM structure on the SOI platform," in *Group IV Photonics (GFP), 2013 IEEE 10th International Conference on*, 2013: IEEE, pp. 21-22.
- [226] H. Li, "Refractive index of silicon and germanium and its wavelength and temperature derivatives," *Journal of Physical and Chemical Reference Data*, vol. 9, no. 3, pp. 561-658, 1980.
- [227] G. Ghosh, "Dispersion-equation coefficients for the refractive index and birefringence of calcite and quartz crystals," *Optics Communications*, vol. 163, no. 1, pp. 95-102, 1999, doi: [https://doi.org/10.1016/S0030-4018\(99\)00091-7](https://doi.org/10.1016/S0030-4018(99)00091-7).
- [228] Y. Wang *et al.*, "Design of broadband subwavelength grating couplers with low back reflection," *Optics letters*, vol. 40, no. 20, pp. 4647-4650, 2015.

- [229] L. Han, S. Liang, H. Zhu, C. Zhang, and W. Wang, "A high extinction ratio polarization beam splitter with MMI couplers on InP substrate," *IEEE Photonics Technology Letters*, vol. 27, no. 7, pp. 782-785, 2015.
- [230] H. Wu, Y. Tan, and D. Dai, "Ultra-broadband high-performance polarizing beam splitter on silicon," *Optics Express*, vol. 25, no. 6, pp. 6069-6075, 2017.
- [231] T. Hu *et al.*, "A compact ultrabroadband polarization beam splitter utilizing a hybrid plasmonic Y-branch," *IEEE Photonics Journal*, vol. 8, no. 4, pp. 1-9, 2016.
- [232] W. Jiang, X. Sun, and B. A. Rahman, "Compact and fabrication-tolerant polarization splitter based on horizontal triple-slot waveguide," *Applied optics*, vol. 56, no. 8, pp. 2119-2126, 2017.
- [233] M.-S. Lai and C.-C. Huang, "Submicron-scale broadband polarization beam splitter using CMOS-compatible materials," *Scientific Reports*, vol. 7, no. 1, p. 4531, 2017.
- [234] D. Jalas *et al.*, "What is — and what is not — an optical isolator," *Nature Photonics*, vol. 7, no. 8, pp. 579-582, 2013/08/01 2013, doi: 10.1038/nphoton.2013.185.
- [235] Z. Yu and S. Fan, "Complete optical isolation created by indirect interband photonic transitions," *Nature Photonics*, vol. 3, no. 2, pp. 91-94, 2009/02/01 2009, doi: 10.1038/nphoton.2008.273.
- [236] H. Tian *et al.*, "Magnetic-free silicon nitride integrated optical isolator," *Nature Photonics*, vol. 15, no. 11, pp. 828-836, 2021/11/01 2021, doi: 10.1038/s41566-021-00882-z.
- [237] D. B. Sohn, O. E. Örsel, and G. Bahl, "Electrically driven optical isolation through phonon-mediated photonic Autler–Townes splitting," *Nature Photonics*, vol. 15, no. 11, pp. 822-827, 2021/11/01 2021, doi: 10.1038/s41566-021-00884-x.
- [238] M.-C. Tien, T. Mizumoto, P. Pintus, H. Kromer, and J. E. Bowers, "Silicon ring isolators with bonded nonreciprocal magneto-optic garnets," *Optics Express*, vol. 19, no. 12, pp. 11740-11745, 2011/06/06 2011, doi: 10.1364/OE.19.011740.
- [239] S. Wang, M. Shah, and J. D. Crow, "Studies of the Use of Gyrotropic and Anisotropic Materials for Mode Conversion in Thin-Film Optical-Waveguide Applications," *Journal of Applied Physics*, vol. 43, no. 4, pp. 1861-1875, 1972, doi: 10.1063/1.1661410.
- [240] S. Yamamoto and T. Makimoto, "Circuit theory for a class of anisotropic and gyrotropic thin-film optical waveguides and design of nonreciprocal devices for integrated optics," *Journal of Applied Physics*, vol. 45, no. 2, pp. 882-888, 1974, doi: 10.1063/1.1663332.

- [241] D. C. Hutchings and B. M. Holmes, "A Waveguide Polarization Toolset Design Based on Mode Beating," *IEEE Photonics Journal*, vol. 3, no. 3, pp. 450-461, 2011, doi: 10.1109/JPHOT.2011.2146765.
- [242] D. C. Hutchings *et al.*, "Quasi-Phase-Matched Faraday Rotation in Semiconductor Waveguides With a Magneto-optic Cladding for Monolithically Integrated Optical Isolators," *IEEE Photonics Journal*, vol. 5, no. 6, pp. 6602512-6602512, 2013, doi: 10.1109/JPHOT.2013.2292339.
- [243] J. Hu, L. Bi, L. C. Kimerling, G. F. Dionne, and C. A. Ross, "Integrated silicon/silicon-germanium magneto-optic isolator," ed: Google Patents, 2010.
- [244] H. Piller and R. F. Potter, "Faraday Rotation Near the Band Edge of Silicon," *Physical Review Letters*, vol. 9, no. 5, pp. 203-205, 09/01/ 1962, doi: 10.1103/PhysRevLett.9.203.
- [245] D. E. M. J. A. T. U. t. H. T. U. t. H. I. f. r. O. u. E. M. Jalas, "Nonreciprocal nanophotonic structures," (in English), 2019. [Online]. Available: <http://nbn-resolving.de/urn:nbn:de:gbv:830-882.056781>.
- [246] D. Jalas, N. Hakemi, M. Cherchi, M. Harjanne, A. Y. Petrov, and M. Eich, "Faraday rotation in silicon waveguides," in *2017 IEEE 14th International Conference on Group IV Photonics (GFP)*, 23-25 Aug. 2017 2017, pp. 141-142, doi: 10.1109/GROUP4.2017.8082236.
- [247] L. Bi *et al.*, "On-chip optical isolation in monolithically integrated non-reciprocal optical resonators," *Nature Photonics*, vol. 5, no. 12, pp. 758-762, 2011/12/01 2011, doi: 10.1038/nphoton.2011.270.
- [248] W. Yan *et al.*, "Waveguide-integrated high-performance magneto-optical isolators and circulators on silicon nitride platforms," *Optica*, vol. 7, no. 11, pp. 1555-1562, 2020/11/20 2020, doi: 10.1364/OPTICA.408458.
- [249] H. Dötsch *et al.*, "Applications of magneto-optical waveguides in integrated optics: review," *J. Opt. Soc. Am. B*, vol. 22, no. 1, pp. 240-253, 2005/01/01 2005, doi: 10.1364/JOSAB.22.000240.
- [250] Y. Shoji, A. Fujie, and T. Mizumoto, "Silicon Waveguide Optical Isolator Operating for TE Mode Input Light," *IEEE Journal of Selected Topics in Quantum Electronics*, vol. 22, no. 6, pp. 264-270, 2016, doi: 10.1109/JSTQE.2016.2574678.

- [251] P. Pintus, D. Huang, P. A. Morton, Y. Shoji, T. Mizumoto, and J. E. Bowers, "Broadband TE Optical Isolators and Circulators in Silicon Photonics Through Ce:YIG Bonding," *Journal of Lightwave Technology*, vol. 37, no. 5, pp. 1463-1473, 2019, doi: 10.1109/JLT.2019.2896650.
- [252] P. Pintus, D. Huang, C. Zhang, Y. Shoji, T. Mizumoto, and J. E. Bowers, "Microring-Based Optical Isolator and Circulator with Integrated Electromagnet for Silicon Photonics," *Journal of Lightwave Technology*, vol. 35, no. 8, pp. 1429-1437, 2017, doi: 10.1109/JLT.2016.2644626.
- [253] D. Huang, P. Pintus, Y. Shoji, P. Morton, T. Mizumoto, and J. E. Bowers, "Integrated broadband Ce:YIG/Si Mach-Zehnder optical isolators with over 100 nm tuning range," *Optics Letters*, vol. 42, no. 23, pp. 4901-4904, 2017/12/01 2017, doi: 10.1364/OL.42.004901.
- [254] D. Huang, P. Pintus, C. Zhang, Y. Shoji, T. Mizumoto, and J. E. Bowers, "Electrically Driven and Thermally Tunable Integrated Optical Isolators for Silicon Photonics," *IEEE Journal of Selected Topics in Quantum Electronics*, vol. 22, no. 6, pp. 271-278, 2016, doi: 10.1109/JSTQE.2016.2588778.
- [255] K. Y. Yang *et al.*, "Inverse-designed non-reciprocal pulse router for chip-based LiDAR," *Nature Photonics*, vol. 14, no. 6, pp. 369-374, 2020/06/01 2020, doi: 10.1038/s41566-020-0606-0.
- [256] B. J. H. Stadler and T. Mizumoto, "Integrated Magneto-Optical Materials and Isolators: A Review," *IEEE Photonics Journal*, vol. 6, no. 1, pp. 1-15, 2014, doi: 10.1109/JPHOT.2013.2293618.
- [257] C. M. Corporation. "Fab: Advanced Micro Foundry (AMF) Silicon Photonics Fabrication Process." <https://www.cmc.ca/WhatWeOffer/Products/CMC-00200-03001.aspx> (accessed 28 May 2019).
- [258] N. D. Cuong, D.-J. Kim, B.-D. Kang, C.-S. Kim, and S.-G. Yoon, "Effect of film thickness on the electrical properties of tantalum nitride thin films deposited on SiO₂/Si substrates for Π -type attenuator applications," *Journal of Vacuum Science & Technology B: Microelectronics and Nanometer Structures Processing, Measurement, and Phenomena*, vol. 24, no. 3, pp. 1398-1401, 2006, doi: 10.1116/1.2201456.

- [259] E. Bozorg-Grayeli *et al.*, "High temperature thermal properties of thin tantalum nitride films," *Applied Physics Letters*, vol. 99, no. 26, p. 261906, 2011, doi: 10.1063/1.3672098.
- [260] P. K. Tien, R. J. Martin, R. Wolfe, R. C. L. Craw, and S. L. Blank, "Switching and modulation of light in magneto-optic waveguides of garnet films," *Applied Physics Letters*, vol. 21, no. 8, pp. 394-396, 1972, doi: 10.1063/1.1654427.
- [261] J. Y. Chin *et al.*, "Nonreciprocal plasmonics enables giant enhancement of thin-film Faraday rotation," *Nature Communications*, vol. 4, no. 1, p. 1599, 2013/03/19 2013, doi: 10.1038/ncomms2609.
- [262] Y. Shoji, T. Mizumoto, H. Yokoi, I.-W. Hsieh, and R. M. O. Jr., "Magneto-optical isolator with silicon waveguides fabricated by direct bonding," *Applied Physics Letters*, vol. 92, no. 7, p. 071117, 2008, doi: 10.1063/1.2884855.
- [263] T. R. Zaman, X. Guo, and R. J. Ram, "Semiconductor Waveguide Isolators," *Journal of Lightwave Technology*, vol. 26, no. 2, pp. 291-301, 2008/01/15 2008. [Online]. Available: <http://jlt.osa.org/abstract.cfm?URI=jlt-26-2-291>.
- [264] W. Zhang, J.-W. Mu, W.-P. Huang, and W. Zhao, "Enhancement of nonreciprocal phase shift by magneto-optical slot waveguide with a compensation wall," *Applied Physics Letters*, vol. 98, no. 17, p. 171109, 2011, doi: 10.1063/1.3584035.
- [265] T. Baehr--Jones, T. Pinguet, Y. Liu, C. Lin, and L. Chrostowski, "IME--OPSIS Design Rule Manual for OI50a Process," 2013.
- [266] A. Pitilakis, D. Chatzidimitriou, T. V. Yioultsis, and E. E. Kriezis, "Asymmetric Si-Slot Coupler With Nonreciprocal Response Based on Graphene Saturable Absorption," *IEEE Journal of Quantum Electronics*, vol. 57, no. 3, pp. 1-10, 2021, doi: 10.1109/JQE.2021.3071247.
- [267] B. O. Seraphin and N. Bottka, "Franz-Keldysh Effect of the Refractive Index in Semiconductors," *Physical Review*, vol. 139, no. 2A, pp. A560-A565, 07/19/ 1965, doi: 10.1103/PhysRev.139.A560.
- [268] D. Patel *et al.*, "Design, analysis, and transmission system performance of a 41 GHz silicon photonic modulator," *Optics Express*, vol. 23, no. 11, pp. 14263-14287, 2015/06/01 2015, doi: 10.1364/OE.23.014263.

- [269] B. Y. Kim, J. N. Blake, H. E. Engan, and H. J. Shaw, "All-fiber acousto-optic frequency shifter," *Optics Letters*, vol. 11, no. 6, pp. 389-391, 1986/06/01 1986, doi: 10.1364/OL.11.000389.
- [270] P. Günter, *Nonlinear optical effects and materials*. Springer, 2012.
- [271] E. L. Wooten *et al.*, "A review of lithium niobate modulators for fiber-optic communications systems," *IEEE Journal of Selected Topics in Quantum Electronics*, vol. 6, no. 1, pp. 69-82, 2000, doi: 10.1109/2944.826874.
- [272] G. Zerbi, *Organic Materials for Photonics*. Oxford: Elsevier, 1993.
- [273] A. Sugita *et al.*, "Second-Order Nonlinear Optical Susceptibilities of Nonelectrically Poled DR1-PMMA Guest-Host Polymers," *The Journal of Physical Chemistry B*, vol. 117, no. 47, pp. 14857-14864, 2013/11/27 2013, doi: 10.1021/jp407892b.
- [274] C. Zhang, L. R. Dalton, M.-C. Oh, H. Zhang, and W. H. Steier, "Low $V\pi$ Electrooptic Modulators from CLD-1: Chromophore Design and Synthesis, Material Processing, and Characterization," *Chemistry of Materials*, vol. 13, no. 9, pp. 3043-3050, 2001/09/01 2001, doi: 10.1021/cm010463j.
- [275] M. N. Sadiku, *Elements of electromagnetics*. Oxford University Press, USA, 2007.
- [276] M. Li *et al.*, "Poling efficiency enhancement of tethered binary nonlinear optical chromophores for achieving an ultrahigh n^3r_{33} figure-of-merit of 2601 pm V⁻¹," *Journal of Materials Chemistry C*, 10.1039/C5TC01049G vol. 3, no. 26, pp. 6737-6744, 2015, doi: 10.1039/C5TC01049G.
- [277] M. Bass *et al.*, *Handbook of Optics*, 3rd ed. New York, USA: McGraw-Hill Professional Publishing, 2009. [Online]. Available: <http://public.ebookcentral.proquest.com/choice/publicfullrecord.aspx?p=4657824>.
- [278] W. R. Hendee, G. S. Ibbott, and E. G. Hendee, *Radiation therapy physics*. John Wiley & Sons, 2013.
- [279] P. W. Hawkes and J. C. Spence, *Springer handbook of microscopy*. Springer, 2019.
- [280] E. J. Jaeschke, S. Khan, J. R. Schneider, and J. B. Hastings, *Synchrotron Light Sources and Free-electron Lasers: Accelerator Physics, Instrumentation and Science Applications*. Springer, 2016.

- [281] B. Barwick, D. J. Flannigan, and A. H. Zewail, "Photon-induced near-field electron microscopy," *Nature*, vol. 462, no. 7275, pp. 902-906, 2009/12/01 2009, doi: 10.1038/nature08662.
- [282] F. J. García de Abajo, A. Asenjo-Garcia, and M. Kociak, "Multiphoton Absorption and Emission by Interaction of Swift Electrons with Evanescent Light Fields," *Nano Letters*, vol. 10, no. 5, pp. 1859-1863, 2010/05/12 2010, doi: 10.1021/nl100613s.
- [283] L. Schächter, *Beam-wave interaction in periodic and quasi-periodic structures*, 2nd ed. Berlin ;: Springer, 2011. [Online]. Available: <http://books.scholarsportal.info/viewdoc.html?id=/ebooks/ebooks2/springer/2011-09-14/1/9783642198489>
<https://doi.org/10.1007/978-3-642-19848-9>
<https://link.springer.com/book/10.1007%2F978-3-642-19848-9>
<http://www.vlebooks.com/vleweb/product/openreader?id=none&isbn=9783642198489>.
- [284] A. Friedman, A. Gover, G. Kurizki, S. Ruschin, and A. Yariv, "Spontaneous and stimulated emission from quasifree electrons," *Reviews of Modern Physics*, vol. 60, no. 2, pp. 471-535, 04/01/ 1988, doi: 10.1103/RevModPhys.60.471.
- [285] A. Mizrahi and L. Schächter, "Optical Bragg accelerators," *Physical Review E*, vol. 70, no. 1, p. 016505, 07/23/ 2004, doi: 10.1103/PhysRevE.70.016505.
- [286] O. Reinhardt and I. Kaminer, "Theory of Shaping Electron Wavepackets with Light," *ACS Photonics*, vol. 7, no. 10, pp. 2859-2870, 2020/10/21 2020, doi: 10.1021/acsp Photonics.0c01133.
- [287] A. Feist, K. E. Echternkamp, J. Schauss, S. V. Yalunin, S. Schäfer, and C. Ropers, "Quantum coherent optical phase modulation in an ultrafast transmission electron microscope," *Nature*, vol. 521, no. 7551, pp. 200-203, 2015/05/01 2015, doi: 10.1038/nature14463.
- [288] J.-W. Henke *et al.*, "Integrated photonics enables continuous-beam electron phase modulation," *Nature*, vol. 600, no. 7890, pp. 653-658, 2021/12/01 2021, doi: 10.1038/s41586-021-04197-5.
- [289] A. Feist *et al.*, "Ultrafast transmission electron microscopy using a laser-driven field emitter: Femtosecond resolution with a high coherence electron beam," *Ultramicroscopy*, vol. 176, pp. 63-73, 2017/05/01/ 2017, doi: <https://doi.org/10.1016/j.ultramic.2016.12.005>.

- [290] R. Dahan *et al.*, "Resonant phase-matching between a light wave and a free-electron wavefunction," *Nature Physics*, vol. 16, no. 11, pp. 1123-1131, 2020/11/01 2020, doi: 10.1038/s41567-020-01042-w.
- [291] Z. Zhao *et al.*, "Design of a tapered slot waveguide dielectric laser accelerator for sub-relativistic electrons," *Optics Express*, vol. 26, no. 18, pp. 22801-22815, 2018/09/03 2018, doi: 10.1364/OE.26.022801.
- [292] N. Rivera and I. Kaminer, "Light–matter interactions with photonic quasiparticles," *Nature Reviews Physics*, vol. 2, no. 10, pp. 538-561, 2020/10/01 2020, doi: 10.1038/s42254-020-0224-2.
- [293] F. J. García de Abajo, "Optical excitations in electron microscopy," *Reviews of Modern Physics*, vol. 82, no. 1, pp. 209-275, 02/03/ 2010, doi: 10.1103/RevModPhys.82.209.
- [294] L. Sun *et al.*, "GV m⁻¹ on-chip particle accelerator driven by few-cycle femtosecond laser pulse," *New Journal of Physics*, vol. 23, no. 6, p. 063031, 2021/06/01 2021, doi: 10.1088/1367-2630/ac03cf.
- [295] K. P. Wootton *et al.*, "Demonstration of acceleration of relativistic electrons at a dielectric microstructure using femtosecond laser pulses," *Optics Letters*, vol. 41, no. 12, pp. 2696-2699, 2016/06/15 2016, doi: 10.1364/OL.41.002696.
- [296] O. Kfir *et al.*, "Controlling free electrons with optical whispering-gallery modes," *Nature*, vol. 582, no. 7810, pp. 46-49, 2020/06/01 2020, doi: 10.1038/s41586-020-2320-y.
- [297] V. Di Giulio, M. Kociak, and F. J. G. de Abajo, "Probing quantum optical excitations with fast electrons," *Optica*, vol. 6, no. 12, pp. 1524-1534, 2019/12/20 2019, doi: 10.1364/OPTICA.6.001524.
- [298] O. Kfir, "Entanglements of Electrons and Cavity Photons in the Strong-Coupling Regime," *Physical Review Letters*, vol. 123, no. 10, p. 103602, 09/06/ 2019, doi: 10.1103/PhysRevLett.123.103602.
- [299] G. Baranes, R. Ruimy, A. Gorlach, and I. Kaminer, "Free electrons can induce entanglement between photons," *npj Quantum Information*, vol. 8, no. 1, p. 32, 2022/03/23 2022, doi: 10.1038/s41534-022-00540-4.
- [300] A. B. Hayun, O. Reinhardt, J. Nemirovsky, A. Karnieli, N. Rivera, and I. Kaminer, "Shaping quantum photonic states using free electrons," *Science Advances*, vol. 7, no. 11, p. eabe4270, 2021, doi: doi:10.1126/sciadv.abe4270.

- [301] R. Dahan *et al.*, "Imprinting the quantum statistics of photons on free electrons," *Science*, vol. 373, no. 6561, p. eabj7128, 2021, doi: doi:10.1126/science.abj7128.
- [302] K. J. Leedle, R. Fabian Pease, R. L. Byer, and J. S. Harris, "Laser acceleration and deflection of 96.3 keV electrons with a silicon dielectric structure," *Optica*, vol. 2, no. 2, pp. 158-161, 2015/02/20 2015, doi: 10.1364/OPTICA.2.000158.
- [303] N. V. Saprà *et al.*, "On-chip integrated laser-driven particle accelerator," *Science*, vol. 367, no. 6473, pp. 79-83, 2020, doi: 10.1126/science.aay5734.
- [304] S. Tan *et al.*, "Silicon nitride waveguide as a power delivery component for on-chip dielectric laser accelerators," *Optics Letters*, vol. 44, no. 2, pp. 335-338, 2019/01/15 2019, doi: 10.1364/OL.44.000335.
- [305] U. Niedermayer, J. Lautenschläger, T. Egenolf, and O. Boine-Frankenheim, "Design of a Scalable Integrated Nanophotonic Electron Accelerator on a Chip," *Physical Review Applied*, vol. 16, no. 2, p. 024022, 08/12/ 2021, doi: 10.1103/PhysRevApplied.16.024022.
- [306] H. Tang *et al.*, "Stable and Scalable Multistage Terahertz-Driven Particle Accelerator," *Physical Review Letters*, vol. 127, no. 7, p. 074801, 08/12/ 2021, doi: 10.1103/PhysRevLett.127.074801.
- [307] H. Deng *et al.*, "Design of racetrack ring resonator based dielectric laser accelerators," *arXiv preprint arXiv:1701.08945*, 2017.
- [308] Y. Adiv *et al.*, "Observation of 2D Cherenkov radiation," p. arXiv:2203.01698. [Online]. Available: <https://ui.adsabs.harvard.edu/abs/2022arXiv220301698A>
- [309] G. Huang, N. J. Engelsen, O. Kfir, C. Ropers, and T. J. Kippenberg, "Coupling ideality of free electrons with photonic integrated waveguides," p. arXiv:2206.08098. [Online]. Available: <https://ui.adsabs.harvard.edu/abs/2022arXiv220608098H>
- [310] N.-N. Feng, R. Sun, L. C. Kimerling, and J. Michel, "Lossless strip-to-slot waveguide transformer," *Optics Letters*, vol. 32, no. 10, pp. 1250-1252, 2007/05/15 2007, doi: 10.1364/OL.32.001250.
- [311] R. Palmer *et al.*, "Low-Loss Silicon Strip-to-Slot Mode Converters," *IEEE Photonics Journal*, vol. 5, no. 1, pp. 2200409-2200409, 2013, doi: 10.1109/JPHOT.2013.2239283.
- [312] K. Soong, R. L. Byer, E. R. Colby, R. J. England, and E. A. Peralta, "Laser damage threshold measurements of optical materials for direct laser accelerators," *AIP Conference Proceedings*, vol. 1507, no. 1, pp. 511-515, 2012, doi: 10.1063/1.4773749.

- [313] K. Soong, R. Byer, C. McGuinness, E. Peralta, E. Colby, and R. England, "Experimental determination of damage threshold characteristics of IR compatible optical materials," in *2011 Particle Accelerator Conference Proceedings*, 2011, vol. 277.
- [314] C. Roques-Carmes, N. Rivera, J. D. Joannopoulos, M. Soljačić, and I. Kaminer, "Nonperturbative Quantum Electrodynamics in the Cherenkov Effect," *Physical Review X*, vol. 8, no. 4, p. 041013, 10/17/ 2018, doi: 10.1103/PhysRevX.8.041013.
- [315] Y. Wang *et al.*, "Focusing sub-wavelength grating couplers with low back reflections for rapid prototyping of silicon photonic circuits," *Optics Express*, vol. 22, no. 17, pp. 20652-20662, 2014/08/25 2014, doi: 10.1364/OE.22.020652.
- [316] B. Cowan, *Optical damage threshold of silicon for ultrafast infrared pulses* (Boulder Damage Symposium XXXIX: Annual Symposium on Optical Materials for High Power Lasers). SPIE, 2007.
- [317] J. Heebner, R. Grover, and T. Ibrahim, *Optical Microresonators: Theory, Fabrication, and Applications*. Springer New York, 2007.
- [318] J. Breuer and P. Hommelhoff, "Laser-Based Acceleration of Nonrelativistic Electrons at a Dielectric Structure," *Physical Review Letters*, vol. 111, no. 13, p. 134803, 09/27/ 2013, doi: 10.1103/PhysRevLett.111.134803.
- [319] E. A. Peralta *et al.*, "Demonstration of electron acceleration in a laser-driven dielectric microstructure," *Nature*, vol. 503, no. 7474, pp. 91-94, 2013/11/01 2013, doi: 10.1038/nature12664.
- [320] E. A. Nanni *et al.*, "Terahertz-driven linear electron acceleration," *Nature Communications*, vol. 6, no. 1, p. 8486, 2015/10/06 2015, doi: 10.1038/ncomms9486.
- [321] M. Kozák *et al.*, "Acceleration of sub-relativistic electrons with an evanescent optical wave at a planar interface," *Optics Express*, vol. 25, no. 16, pp. 19195-19204, 2017/08/07 2017, doi: 10.1364/OE.25.019195.
- [322] J. McNeur *et al.*, "Elements of a dielectric laser accelerator," *Optica*, vol. 5, no. 6, pp. 687-690, 2018/06/20 2018, doi: 10.1364/OPTICA.5.000687.
- [323] R. Ruimy, A. Gorlach, C. Mechel, N. Rivera, and I. Kaminer, "Toward Atomic-Resolution Quantum Measurements with Coherently Shaped Free Electrons," *Physical Review Letters*, vol. 126, no. 23, p. 233403, 06/11/ 2021, doi: 10.1103/PhysRevLett.126.233403.

- [324] A. Gorlach, A. Karnieli, R. Dahan, E. Cohen, A. Pe'er, and I. Kaminer, "Ultrafast non-destructive measurement of the quantum state of light using free electrons," p. arXiv:2012.12069. [Online]. Available: <https://ui.adsabs.harvard.edu/abs/2020arXiv201212069G>
- [325] R. Dahan, G. Baranes, A. Gorlach, R. Ruimy, N. Rivera, and I. Kaminer, "Creation of Optical Cat and GKP States Using Shaped Free Electrons," p. arXiv:2206.08828. [Online]. Available: <https://ui.adsabs.harvard.edu/abs/2022arXiv220608828D>
- [326] A. Gover and A. Yariv, "Free-Electron--Bound-Electron Resonant Interaction," *Physical Review Letters*, vol. 124, no. 6, p. 064801, 02/13/ 2020, doi: 10.1103/PhysRevLett.124.064801.
- [327] Y. Adiv *et al.*, "Observation of the Quantum Nature of Laser-Driven Particle Acceleration," in *2020 Conference on Lasers and Electro-Optics (CLEO)*, 10-15 May 2020 2020, pp. 1-2.
- [328] A. Feist *et al.*, "Cavity-mediated electron-photon pairs," p. arXiv:2202.12821. [Online]. Available: <https://ui.adsabs.harvard.edu/abs/2022arXiv220212821F>
- [329] H. Yu, Y. Peng, Y. Yang, and Z.-Y. Li, "Plasmon-enhanced light–matter interactions and applications," *npj Computational Materials*, vol. 5, no. 1, p. 45, 2019/04/11 2019, doi: 10.1038/s41524-019-0184-1.
- [330] I. Kaminer *et al.*, "Efficient plasmonic emission by the quantum Čerenkov effect from hot carriers in graphene," *Nature communications*, vol. 7, p. ncomms11880, 2016.
- [331] R. Foord, R. Jones, C. J. Oliver, and E. R. Pike, "The Use of Photomultiplier Tubes for Photon Counting," *Applied Optics*, vol. 8, no. 10, pp. 1975-1989, 1969/10/01 1969, doi: 10.1364/AO.8.001975.
- [332] S. Datta, *Electronic transport in mesoscopic systems*. Cambridge university press, 1997.
- [333] E. Bustarret *et al.*, "Superconductivity in doped cubic silicon," *Nature*, vol. 444, no. 7118, p. 465, 2006.
- [334] H. Zhang *et al.*, "Ballistic superconductivity in semiconductor nanowires," *Nature Communications*, Article vol. 8, p. 16025, 07/06/online 2017, doi: 10.1038/ncomms16025 <https://www.nature.com/articles/ncomms16025#supplementary-information>.
- [335] Y. Ding *et al.*, "Effective electro-optical modulation with high extinction ratio by a graphene–silicon microring resonator," *Nano letters*, vol. 15, no. 7, pp. 4393-4400, 2015.

- [336] S. Molesky, Z. Lin, A. Y. Piggott, W. Jin, J. Vucković, and A. W. Rodriguez, "Inverse design in nanophotonics," *Nature Photonics*, vol. 12, no. 11, p. 659, 2018.
- [337] R. Roscher, B. Bohn, M. F. Duarte, and J. Garcke, "Explainable Machine Learning for Scientific Insights and Discoveries," *IEEE Access*, vol. 8, pp. 42200-42216, 2020, doi: 10.1109/ACCESS.2020.2976199.
- [338] P. G. Merli, G. F. Missiroli, and G. Pozzi, "On the statistical aspect of electron interference phenomena," *American Journal of Physics*, vol. 44, no. 3, pp. 306-307, 1976, doi: 10.1119/1.10184.
- [339] R. Eisberg and R. Resnick, "Quantum physics of atoms, molecules, solids, nuclei, and particles," *Quantum Physics of Atoms, Molecules, Solids, Nuclei, and Particles, 2nd Edition*, by Robert Eisberg, Robert Resnick, pp. 864. ISBN 0-471-87373-X. Wiley-VCH, January 1985., p. 864, 1985.
- [340] I. H. Hutchinson, "Principles of plasma diagnostics," *Plasma Physics and Controlled Fusion*, vol. 44, no. 12, p. 2603, 2002.
- [341] E. Wilson, "Fifty years of synchrotrons," in *European Particle Accelerator Conference*, 1996, pp. 135-139.
- [342] M. W. Coffey and J. R. Clem, "Unified theory of effects of vortex pinning and flux creep upon the rf surface impedance of type-II superconductors," *Physical review letters*, vol. 67, no. 3, p. 386, 1991.
- [343] Z. Huang and K.-J. Kim, "Review of x-ray free-electron laser theory," *Physical Review Special Topics-Accelerators and Beams*, vol. 10, no. 3, p. 034801, 2007.
- [344] "Chapter 9," in *Tunable Lasers Handbook*, F. J. Duarte Ed. New York: Academic, 1995.
- [345] Z. V. Vardeny, A. Nahata, and A. Agrawal, "Optics of photonic quasicrystals," *Nature Photonics*, vol. 7, no. 3, pp. 177-187, 2013/03/01 2013, doi: 10.1038/nphoton.2012.343.
- [346] D. S. Wiersma, "Disordered photonics," *Nature Photonics*, Review Article vol. 7, p. 188, 02/27/online 2013, doi: 10.1038/nphoton.2013.29.
- [347] Z.-Y. Li and Z.-Q. Zhang, "Fragility of photonic band gaps in inverse-opal photonic crystals," *Physical Review B*, vol. 62, no. 3, pp. 1516-1519, 07/15/ 2000, doi: 10.1103/PhysRevB.62.1516.

- [348] Y. Tang, Z. Wang, L. Wosinski, U. Westergren, and S. He, "Highly efficient nonuniform grating coupler for silicon-on-insulator nanophotonic circuits," *Optics Letters*, vol. 35, no. 8, pp. 1290-1292, 2010/04/15 2010, doi: 10.1364/OL.35.001290.
- [349] C. Huang, A. Bouhelier, G. C. des Francs, G. Legay, J. C. Weeber, and A. Dereux, "Far-field imaging of the electromagnetic local density of optical states," *Optics Letters*, vol. 33, no. 4, pp. 300-302, 2008/02/15 2008, doi: 10.1364/OL.33.000300.
- [350] C. Chicanne *et al.*, "Imaging the Local Density of States of Optical Corrals," *Physical Review Letters*, vol. 88, no. 9, p. 097402, 02/14/ 2002, doi: 10.1103/PhysRevLett.88.097402.
- [351] C. Girard *et al.*, "Imaging surface photonic states with a circularly polarized tip," *Europhysics Letters (EPL)*, vol. 68, no. 6, pp. 797-803, 2004/12 2004, doi: 10.1209/epl/i2004-10290-6.
- [352] R. Serber, "The Theory of the Faraday Effect in Molecules," *Physical Review*, vol. 41, no. 4, pp. 489-506, 08/15/ 1932, doi: 10.1103/PhysRev.41.489.
- [353] S. Wang, J. D. Crow, and M. Shah, "Thin-Film Optical-Waveguide Mode Converters Using Gyrotropic and Anisotropic Substrates," *Applied Physics Letters*, vol. 19, no. 6, pp. 187-189, 1971, doi: 10.1063/1.1653877.
- [354] D. C. Hutchings, "Prospects for the implementation of magneto-optic elements in optoelectronic integrated circuits: a personal perspective," *Journal of Physics D: Applied Physics*, vol. 36, no. 18, pp. 2222-2229, 2003/09/04 2003, doi: 10.1088/0022-3727/36/18/008.
- [355] E. Tutorials. "Inductor - LR circuits." <https://www.electronics-tutorials.ws/inductor/lr-circuits.html> (accessed 13 July 2020).
- [356] "Beam Optics and Focusing Systems without Space Charge: Sections 3.1 - 3.5," in *Theory and Design of Charged Particle Beams*, 2008, pp. 51-103.
- [357] X. Wang, Z. H. Shen, J. Lu, and X. W. Ni, "Laser-induced damage threshold of silicon in millisecond, nanosecond, and picosecond regimes," *Journal of Applied Physics*, vol. 108, no. 3, p. 033103, 2010, doi: 10.1063/1.3466996.
- [358] I. Aldaya, A. Gil-Molina, J. L. Pita, L. H. Gabrielli, H. L. Fragnito, and P. Dainese, "Nonlinear carrier dynamics in silicon nano-waveguides," *Optica*, vol. 4, no. 10, pp. 1219-1227, 2017/10/20 2017, doi: 10.1364/OPTICA.4.001219.

- [359] A. Gil-Molina, I. Aldaya, J. L. Pita, L. H. Gabrielli, H. L. Fragnito, and P. Dainese, "Optical free-carrier generation in silicon nano-waveguides at 1550 nm," *Applied Physics Letters*, vol. 112, no. 25, p. 251104, 2018, doi: 10.1063/1.5023589.
- [360] D. Negi, L. Jones, J.-C. Idrobo, and J. Ruzs, "Proposal for a three-dimensional magnetic measurement method with nanometer-scale depth resolution," *Physical Review B*, vol. 98, no. 17, p. 174409, 11/06/ 2018, doi: 10.1103/PhysRevB.98.174409.
- [361] S. T. Park, M. Lin, and A. H. Zewail, "Photon-induced near-field electron microscopy (PINEM): theoretical and experimental," *New Journal of Physics*, vol. 12, no. 12, p. 123028, 2010.
- [362] F. J. García de Abajo, B. Barwick, and F. Carbone, "Electron diffraction by plasmon waves," *Physical Review B*, vol. 94, no. 4, p. 041404, 07/11/ 2016, doi: 10.1103/PhysRevB.94.041404.
- [363] S. Nehemia *et al.*, "Observation of the Stimulated Quantum Cherenkov Effect," *arXiv preprint arXiv:1909.00757*, 2019.

Appendix A. Supplementary Information for Chapter 3

A.1. Optical Confinement in Biosilica

The frustule was predominantly made of biosilica. Its refractive index was slightly higher than the surrounding water or inner cytoplasm. Due to this low index contrast and the thinness of the frustule, optical modes were only weakly confined to it. The number of modes and their confinement depended on the thickness, width, and perforation of the frustule as well as the wavelength of the mode. Regions that were perforated with holes had lower effective refractive index [80, 81, 150]. The E-field distributions of some of the lower order modes in the frustule are shown in Figure A.1.

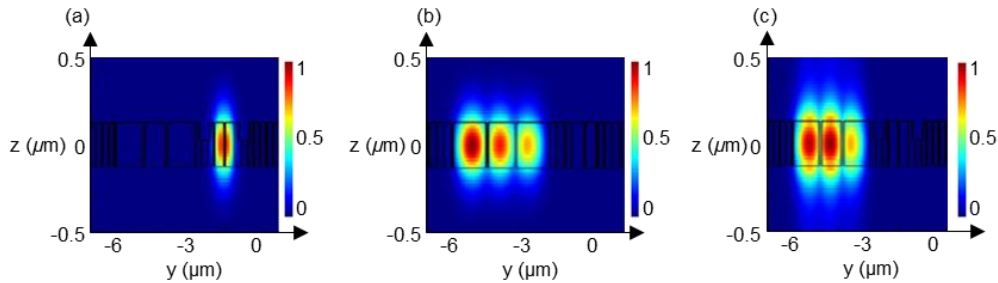


Figure A.1. Mode confinement in the frustule. (a) Fundamental mode inside the valve. (b) Lower order modes inside the girdle. (c) Higher order modes inside the girdle.

Due to weak confinement, the mode field expanded over a larger region such that it penetrated inside the cell. This high overlap facilitated evanescent coupling to the chloroplasts [158, 163] as well as directional coupling to adjacent frustules. Coupling to the chloroplasts was further supported by the marginally higher refractive index of the cytoplasm compared to water, which shifted the field distribution toward the inside of the cell. The location of the chloroplasts inside the cell was found to be variable. Outside the cell, directional coupling with neighboring frustules indicated a mechanism for light to be shared across diatoms in a colony. The weak mode confinement was also found to reduce birefringence resulting in a polarization independent optical response (characterized in Figure A.2(f)), which is beneficial for harvesting unpolarized sunlight.

A.2. Variations in the Photonic Band Structure of the Central Lattice

The central lattice occupied almost the entire exposed surface area of the valve and therefore, the majority of the frustule. This indicated the higher proportion of incident sunlight that it received

in comparison to the other regions of the frustule. The lattice exhibited cylindrical holes from the outside. On the inside, they were covered by 10-nm-thick elliptical protrusions. The knobs were assumed to be artifacts from sputter coating the sample in preparation for scanning electron microscopy (SEM) imaging because otherwise, they would have fatally restricted chemical exchanges between the cell and its environment.

The arrangement of holes in the lattice formed a quasi-periodic photonic crystal (PhC). Different localized regions of the PhC exhibited different symmetries resembling square, triangular, and an intermediate oblique, depending on the angle subtended between the holes. Their corresponding photonic band structures are shown in Figure A.2(a). To quantify the effect of disorder in the PhC, its lattice parameters were varied to produce corresponding variations in the photonic band structure. Using the oblique symmetry as a basis, the dependence of the band structure on variations in angle (or symmetry), refractive index, thickness, spacing, hole diameter, and the polarization of light are shown in Figure A.2. To isolate the effect of a given parameter variation on the overall photonic band structure, only the selected parameter was varied while the others were held constant. The range of the spacing, hole diameter, and thickness parameter variations was two standard deviations from their mean value, that is, 2σ as obtained from the SEM measurements.

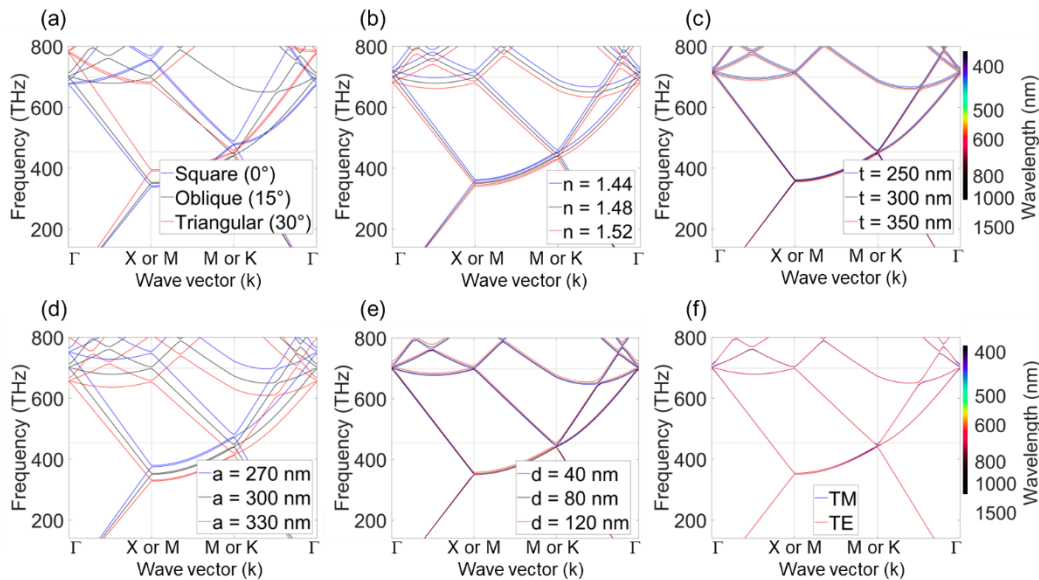


Figure A.2. Dependence of the photonic band diagram on the lattice parameters. Variations in (a) symmetry (corresponding to angle), (b) refractive index, n , (c) thickness, t , (d) spacing, a , (e) diameter, d , and (f) polarization.

For the valve, its guided modes were represented by the bands that were within the light cone of the photonic band structure. Their behavior depended on the localized parameters of the lattice. The strongest variations in the PhC response were due to the lattice symmetry, which could explain the high disorder in the angle between holes despite the longitudinal symmetry of the lattice. This also caused disorder in the spacing between holes. For example, an increase of 20 nm in the spacing proportionally lowered the position of the guided modes by 57 nm toward longer wavelengths. Varying the hole diameter resulted in a similar albeit weaker effect. Diameter variations of up to 100% (or 80 nm) still did not significantly shift the bands. The negligible effect of thickness [181] was attributed to the weak confinement of the modes. Varying the refractive index also had a negligible effect on the response, which justified approximating the biosilica material of the frustule as standard silica. Similarly, the negligible effect of polarization indicated the polarization independence of the optical response. This polarization insensitivity conferred an advantage on the frustule in the context of harvesting sunlight, which is unpolarized.

The central lattice exhibited long-range order despite having no translational symmetry due to the randomized variations of its parameters. This short-range disorder therefore modified the optical response of the PhC without eliminating it [345, 346]. As shown in Figure A.2, any variation of the periodicity of the lattice induced a proportional change in its corresponding photonic band diagram. So, within a localized region where each unit cell contributed to the overall photonic band structure of the lattice, the disorder of the PhC proportionately shifted the bands into neighboring frequencies, ω , and wavevectors, k (or incident angles), corresponding to their (ω, k) position in the band diagram. This resulted in an effective ‘smearing’ of the photonic band structure. The effect is visualized in Figure 3.2, whereby each hole was considered to be a unit cell based on the positions of its neighboring holes, and its corresponding band structure was calculated and plotted. The resulting ensemble average demonstrated an increased likelihood that a mode existed in the PhC to accommodate almost any (ω, k) combination of incident photons.

In this manner, the disorder facilitated random scattering in the lattice. Since the sharpness of peaks in the density of states (DOS) depended on long-range resonant scattering, these peaks got widened and flattened due to the perturbations of the lattice [347]. At each frequency, the DOS was calculated as the sum of all available wavevectors. Since this value depended on the resolution of the simulation, it was normalized within the wavelength range of interest. This broadened the spectrum over which a nonzero (or high) DOS was observed, and therefore increased the range of

conditions for which modes were allowed. Additionally, the band gaps were collapsed due to the low refractive index difference, which caused significant overlap between neighboring modes. This effectively smoothed the overall mode field distribution at a given (ω, k) position. As a result, these hybrid modes better overlapped with incident plane waves and therefore, improved free-space coupling to the lattice. The combined DOS similarly increased retention.

The DPhC analysis showed that the structure was not only tolerant but in fact benefited from variations, which suggests that they might have evolved to enhance light absorption for a range of wavelengths and incident angles.

A.3. Resonances of the PhC

The bands in Figure A.2 indicated the modes of the PhC, that is, the allowed optical states for which the DOS was nonzero [174]. Conversely, empty (ω, k) positions in the diagram were indicative of regions in which there were no states for photons to occupy. For example, in the 550-820 nm wavelength range between the X-M symmetry points, the lowest order mode ran parallel to a higher order mode. Their proximity allowed an overlap of their corresponding DOS and field distribution, which averaged these quantities between both modes within that (ω, k) region. Such a combined mode field distribution offered a better overlap with incident light and therefore improved the coupling efficiency of the lattice. The modes also increased the overall DOS available for retention and waveguiding. Similarly, in the shorter wavelength range, the presence of multiple higher order radiation modes increased the coupling efficiency [136, 348]. However, this did not imply better retention in the frustule due to their position outside the light cone.

Positions in the band diagram where the slope of the band approached zero, implied a reduced group velocity [174]. Such regions typically occurred at band gaps or crossings near symmetry points. A band crossing was composed of at least two bands which crossed each other with a low, and possibly zero, slope. In contrast, a gap was composed of at least two bands near each other but not crossing. The width of the gaps in the central lattice were collapsed due to the low refractive index contrast and small hole diameter. For example, at 430 nm in Figure A.3(a), there was a convergence of multiple modes at the Γ point. The reduced slope and group velocity, combined with the presence of multiple bands, indicated a high DOS in those regions. This effect was amplified by the collapsed gap width, as seen at 900 nm. Here, the DOS was not reduced to zero between the bands, as it was for a typical band gap. On the contrary, these collapsed gaps allowed photon tunneling between the modes and therefore resulted in the DOS reaching a peak at the gap

rather than on either side of it. An analogy in the spatial domain is a directional coupler, in which the separation between two waveguides can be small enough to allow evanescent coupling between them, but when the separation is even smaller, then this results in a slot waveguide in which the intensity is actually higher inside the slot [116]. In this manner, the band gaps and crossings supported a continuously high DOS across the spectrum of photosynthetic active radiation (PAR), which contributed to the resonant behavior of the DPhC, as shown in Figure A.3.

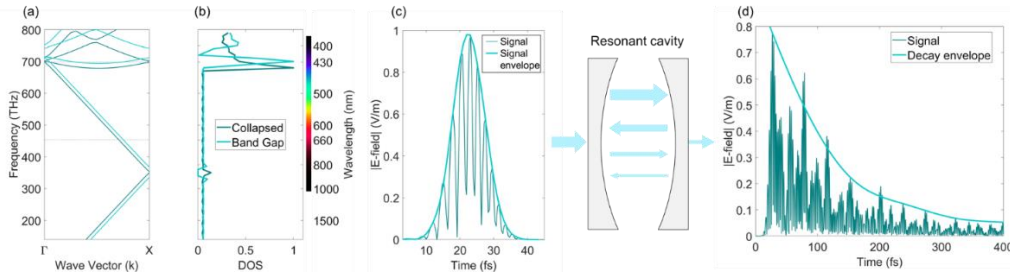


Figure A.3. Effect of resonances on the optical response. (a) Collapsed or open pseudogaps and band crossings with (b) their corresponding DOS. (c,d) Transient response of a resonance (represented by the resonant cavity) showing how (c) an optical pulse undergoes (d) decay due to the retention of light inside the cavity.

The resonances (collapsed pseudogap or band crossing) increased photon lifetimes [7] because photons remained confined or scattered in the frustule for longer durations, as depicted in Figure A.3. Hence, the retention of light by a collapsed pseudogap was more effective than if the gap was widened. Additionally, these resonances enlarged the localized DOS by reducing the group velocity and offering multiple modes for coupling, which increased the coupling efficiency. The increased light retention, light-matter interaction, and coupling efficiency to modes, all directly supported retention in the frustule which could assist the absorption rate of chloroplasts (from evanescent states [72]). In this manner, the resonances in the PhC contributed to the capture, redistribution, and retention of incident PAR.

A.4. Analysis of Scanning, Near-field Optical Microscopy (SNOM) Images

SNOM is a surface selective technique, which can be used to probe diatom frustules due to their transparency and thinness. Evanescent waves were coupled from the aperture to the sample in the near field at a fixed angle, which implied that the interaction for each pixel occurred only at the tip. During scanning, a constant separation between the tip and sample was maintained to ensure constant coupling despite the exponential decay of the wave with increasing separation

distance [194]. Although SNOM is non-destructive, the tip itself damaged the sample in some cases.

In this transmission SNOM configuration, incident light was evanescently coupled into the sample by the apertured probe above it [194]. The amount of light coupled into the sample depended on the focal length of the lens and size of the aperture in the cantilever, both of which had a spectrally dependent optical response. This implied that long wavelengths (near infrared) were limited by the aperture size whereas short wavelengths (near violet) did not reach the aperture due to the correspondingly shorter focal length of the lens. Once coupled to the sample, the transmitted light was detected via an objective lens beneath it. The regions around the valve where light had coupled to, but diffused through, the cover slip provided a baseline intensity. Compared to this background, darker regions in the frustule indicated that light had not been transmitted to the collection optics. In this case, light had either not coupled into the sample due to poor contact (as seen inside the holes) or was redirected away from the point of contact (as seen in the diffraction pattern outside the valve edges). In contrast, the bright points indicated higher transmission through the sample, that is, where light was efficiently coupled to the valve without being diffused or redirected. A collection of these points formed bright lines which were observed along the valve edges as well as laterally across the width of the central lattice. These continuous pathways indicated waveguiding.

The accuracy of the probed optical response was constrained by the measurement technique. For example, the angle at which the aperture was tapered, determined the fidelity of images obtained from surfaces with high curvature. Near the edges of the valve, the field was noticeably darker because the outer edge of the cantilever was physically restricted by its contact with the edge of the valve. As a result, the separation between the tip and the surface could not be maintained, which was confirmed by the blurriness of the AFM image. Similar dark spots were observed between the scaffolds of the raphe. Additionally, the convergence semi-angle of the bottom objective determined the aggregate of all k -vectors which were collected around the Γ symmetry point of the lattice. Hence, SNOM only probed the k -vectors around the Γ symmetry point for a single wavelength. However, note that the tip excited all modes in the lattice even if only the Γ symmetry point was preferred. Hence, light also coupled to modes that existed at other k -vectors. Due to scattering from imperfections in the lattice, residual light from these existing interacting modes would still reach the bottom objective. As a result, the sample was not dark

despite the lack of modes at the Γ point for the SNOM wavelength, but the modes can be expected to appear brighter if probed at the correct angle. To do so, the angle of the detector would need to be adjustable, along with a sweep of the wavelengths within the range of PAR. The lack of mobility in our setup prevented the mapping optical bands in this manner.

Note that SNOM images did not produce a direct measurement of the localized DOS (LDOS) due to cross-coupling between the tip and sample [349]. However, given the experimental conditions and expected topography of the sample, the LDOS was inferred to have some correlation with bright pixels in the image. That is, the partial LDOS can be reconstructed from variations in the transmitted intensity resulting from the interactions between the aperture and the sample [350]. This is the sum of the partial DOS associated with the optical modes in each polarization direction, whereby its electric or magnetic part can be correlated with the near-field measurement [351]. So, the bright spots can be interpreted as the probability of detecting the electric field intensity of photons at that position. The bright points therefore indicated a higher LDOS at the point of contact in comparison to the surrounding regions. Since the LDOS indicated the availability of optical eigenmodes that allowed the existence of photons at a specific location, the bright points in the SNOM image were therefore assumed to map out the optical modes in the frustule. However, the total LDOS was not directly measured due to the vectoral nature of the optical field [351], which required a much larger convergence angles to obtain all k -vectors. Hence generalization was not straightforward. A complete LDOS measurement is only possible if all the modes are excited as well as detected, that is, illumination and detection by a wide solid angle. This was not possible using SNOM, hence, the image was generally interpreted as representing the k -vectors for the given laser wavelength, and possibly around the Γ symmetry point.

A.5. Solar Energy Harvesting Mechanisms of the Frustule

The photosynthetic conversion efficiency of the diatom cell was assumed to match the absorption rate of its chloroplasts. The chloroplasts could receive incident PAR from the frustule via either direct transmission or evanescent coupling. Our results indicate that the frustule contributed to the PAR harvesting mechanisms of capture, redistribution, and retention. Each of these mechanisms was caused by a combination of the localized optical functionalities that were evoked by its architecture. We modeled this process as a photonic circuit, which is represented in Figure A.4(a). An analogous, simplified electrical circuit of this system is shown in Figure A.4(b) and its effect on photosynthesis is depicted in Figure A.4(c).

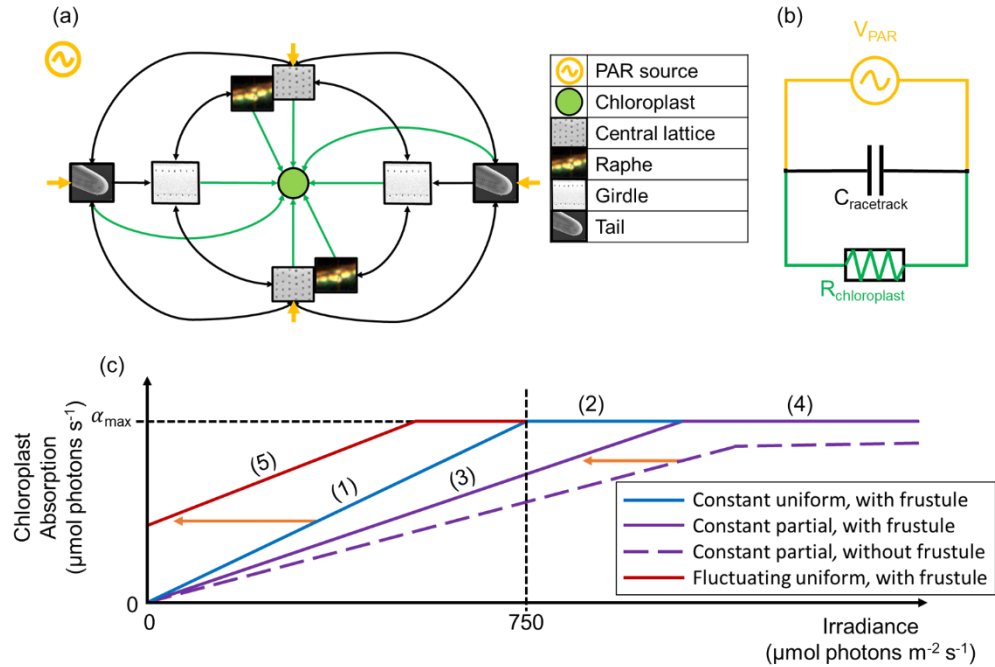


Figure A.4. Model of the optical response of the frustule. (a) Photonic circuit of the frustule showing (yellow arrows) incident PAR, (black arrows) light exchanged between different regions and (green arrows) absorption by the chloroplasts. (b) Electrical equivalent circuit with the chloroplasts, frustule, and PAR represented as a load resistor, capacitor, and variable power supply, respectively. (c) Contribution of the frustule to the absorption by the chloroplasts depending on the amount and distribution of irradiation on the cell. The slope represents the difference in the exposed surface area. The contribution of the frustule is depicted as orange vertical arrows in specific cases. The maximum absorption α_{\max} was reached under an irradiance of $750 \mu\text{mol photons m}^{-2} \text{s}^{-1}$.

The black, inner ring of Figure A.4(a) represents the cross-sectional racetrack formed by the central lattice, raphe, and girdle, which is shown in Figure 3.7(a). It retained photons via circulation with an estimated Q factor of 271 to 822 at the wavelengths of 805 nm to 424.8 nm. For simplicity, this was assumed to be the main cause of retention in the frustule since the contributions from the raphe and DPhC merely amplified this effect. The remaining black arrows in Figure A.4(a) show how the racetrack received light via either butt-coupling from the tails or diffraction from the DPhCs in the central lattice and girdle. The radiation modes of the DPhC allowed light to couple into the racetrack from free-space with a simulated insertion loss (IL) of 4.56 dB at 450 nm [180]. Butt-coupling at the tail resulted in a simulated IL of 1.4 dB with free-space. Note that this is the approximate maximum value since the light source was aligned with the tail to obtain the lowest IL. For light being diffracted into lateral circulation by the central lattice and girdle, it incurred an approximately 7 dB loss [180]. Since these features also maintained lateral circulation by limiting

longitudinal diffusion toward the tails, the loss from diffusion was neglected. The effective index of the racetrack was approximated as 1.38. Its optical loss per roundtrip was therefore calculated as,

$$Loss_{\text{racetrack}} = \frac{2\pi f T_r}{Q} \quad (\text{SA.1})$$

Here, f is the frequency, T_r is the transient time of the ring, and Q is its quality factor. This loss was calculated to be 2.6 dB per roundtrip.

The contribution of the capture, redistribution, and retention mechanisms depended on the initial state and boundary conditions of the system, which are represented in Figure A.4(c). We therefore present the following qualitative analysis of the contribution of the frustule to the absorption of chloroplasts using 5 cases which are based on the amount, location, and consistency of PAR that is incident on the diatom. Note that in all cases, the capture mechanism can be assumed to be always active and is therefore not discussed.

1. Under a constant, low, uniform irradiance (blue, solid, sloping line in Figure A.4(c)), any light in the frustule is immediately absorbed by the chloroplasts, which renders the retention mechanism redundant. Since the irradiance is uniform, the redistribution mechanism is also redundant. Hence, only the capture mechanism is useful to couple ambient light.
2. Under a constant, high, uniform irradiance (blue, solid, horizontal line in Figure A.4(c)), absorption of the chloroplasts is maximized, so excess photons are retained in the frustule. Although retention is activated, it is not used because these photons cannot be absorbed by the chloroplasts while they are already saturated. Similar to case 1, the uniformity of the irradiance renders the redistribution mechanism as redundant.
3. Under a constant, low, partial irradiance (purple, sloping lines in Figure A.4(c)), any captured light gets absorbed. A fraction might be redistributed for absorption by chloroplasts in the remaining regions of the cell, but this is only due to the passive optical behavior of the frustule rather than the presence of excess photons. Similar to case 1, the low irradiance renders the retention mechanism as redundant.
4. Under a constant, high, partial irradiance (purple, horizontal lines in Figure A.4(c)), the illuminated area of the cell absorbs photons at its maximum capacity until the chloroplasts are saturated. Excess photons can be made available to the remaining

chloroplasts via the capture and redistribution mechanisms. This increases photosynthetic conversion in the cell. Similar to case 2, the retention mechanism is activated but not used.

5. Under a fluctuation from high to low, uniform irradiance (red, solid line in Figure A.4(c)), as represented by $t > 0$, the retention mechanism is most useful. Excess photons retained in the frustule are available to the chloroplasts so that photosynthesis can continue despite a drop in irradiance.

The redistribution mechanism was found to be useful when the frustule is partially irradiated. Since it effectively increases the exposed surface area under irradiation, it was represented by an increase in the slope of the corresponding lines in Figure A.4(c). Redistribution across the frustule allowed us to make an analogous assumption that the chloroplasts were distributed throughout the cell. The retention mechanism gets activated when the irradiation exceeds the maximum absorption of the chloroplasts and becomes useful when the irradiation drops below the maximum. Since it provides a smoothing effect during fluctuations in irradiance by releasing stored optical energy during periods of darkness, it was represented by a positive offset of the corresponding lines in Figure A.4(c). The adaptations of chloroplasts to available light were not accounted for in this model.

This retention mechanism was additionally modeled by a capacitor (the frustule) connected in parallel with a resistive load (the chloroplasts) to smoothen spikes or cuts in the power supply (incident irradiance). Similar to a resistor, the maximum absorption rate of chloroplasts, α_{\max} , was assumed to be a constant 3.98×10^{12} photons/s using an irradiance of $750 \mu\text{mol photons m}^{-2} \text{s}^{-1}$ at 440 nm [161]. It was calculated as,

$$\alpha_{\max} = IA\epsilon \quad (\text{SA.2})$$

Here, I is the maximum irradiance, A is the surface area of the frustule, and ϵ is the absorbance coefficient of the chloroplasts approximated as 1 dB [180]. To find the contribution of the frustule to photosynthesis, we calculated the contribution of the racetrack to α . We assumed that all the photons retained in the frustule were available for absorption by the chloroplasts at any time, that is, the retention rate, $Rate_{\text{retained}} = 1 - Rate_{\text{leak}}$, determined the maximum photons per second available for absorption. The leakage or decay rate, $Rate_{\text{leak}}$ was calculated using the total rate of photons/s that coupled into the racetrack due to the initial irradiance and harvesting mechanisms as well as $Loss_{\text{racetrack}}$.

For an irradiance of $550 \mu\text{mol photons m}^{-2} \text{ s}^{-1}$, the $Rate_{\text{retained}}$ that enabled $\alpha \rightarrow \alpha_{\text{max}}$ was calculated as 0.319×10^{12} photons/s. The total contribution to photosynthesis provided by the frustule was then estimated as $Rate_{\text{retained}}/\alpha_{\text{max}}$ because this represented the percentage increase in α due to the retention mechanisms of the frustule. It was found to be 9.83% at a wavelength of 450 nm. Note that this value represents an estimated percentage increase based on the specified conditions and was only calculated for a single wavelength. The accuracy of the calculation can be improved by conducting a full spectral analysis of the frustule within the wavelength range of PAR.

Appendix B. Supplementary Information for Section 5.1

B.1. Polarization Mode Conversion in the Waveguide

A particle of charge q traveling through an electromagnetic field at a velocity \vec{v} experiences a Lorentz force \vec{F} as it interacts with electric and magnetic fields, \vec{E} and \vec{B} , respectively, such that,

$$\vec{F} = q(\vec{E} + \vec{v} \times \vec{B}) \quad (\text{B.1})$$

The force exerted by the magnetic field depends on the direction of propagation of the particle relative to the field lines. In a material, electrons are loosely bound to the nuclei of atoms. Their response to applied forces determines the bulk response of the material. For example, electron oscillations can be induced by an electromagnetic wave propagating through the material. The nature of the oscillations depends on the response of the electrons to the physical properties of the wave. Additionally, if a magnetic field is applied to the material, the electrons would be subjected to the forces in equation (B.1), which would change their response to the electromagnetic wave. In this manner, the optical properties of a material can be modified by the application of a magnetic field.

In the case of linearly polarized light, the Lorentz force manifests as a rotation of its plane of polarization inside a material. Note that linearly polarized light is a superposition of left and right circularly polarized components which add along the plane of polarization and cancel along the transverse plane. Under an applied magnetic field, the difference in velocities between these components rotates the plane of polarization and is known as Faraday rotation. Since the angle of rotation, θ , depends on the direction of the B field lines relative to the propagation direction, the effect is nonreciprocal. It is determined by the direction of propagation of light with respect to the applied B field along an interaction length, l , such that,

$$\theta = VBl \quad (\text{B.2})$$

The Verdet constant, V , is the magneto-optic property of the material that determines the interaction strength. Since the rotation θ is the primary figure of merit for the performance of a Faraday rotator, methods to maximize each of its three parameters were investigated in this work. Figure B.1 illustrates this concept.

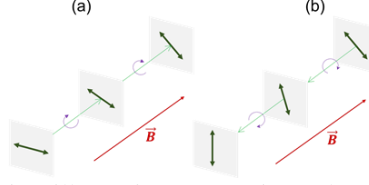


Figure B.1. Schematic of Faraday rotation illustrating non-reciprocal polarization rotation (violet). (a) clockwise rotation of the plane of polarization of light when propagating (green) in the direction of the magnetic field (red) and (b) counter-clockwise rotation when propagating in the opposite direction.

The Verdet constant of a material is determined by its dispersion and scaled by the charge-to-mass ratio of the electrons. It is described by the Becquerel equation [352],

$$V = \frac{q_e}{m_e c_0^2} \cdot \frac{\lambda_0}{2} \cdot \left(\frac{dn_{\text{eff}}}{d\lambda} \right) \quad (\text{B.3})$$

Where q_e and m_e are the charge and mass of an electron (q_e is a negative quantity), c_0 is the speed of light, λ_0 is its vacuum wavelength, and n_{eff} is the effective index of the optical mode. The dispersion $dn_{\text{eff}}/d\lambda$ induced by the material could be modified by its geometry. This parameter was investigated by fabricating different waveguide cross-sections. In a single-mode waveguide, Faraday rotation causes NR PMC [353] between the TE_0 and TM_0 modes. However, the asymmetric cross-section of SiP waveguides results in two different n_{eff} for the two modes, and as such, two different propagation constants, β_{TE_0} and β_{TM_0} . This causes a π phase mismatch at every half-beat length [239],

$$l_{\text{HB}} = \frac{\pi}{|\beta_{\text{TE}_0} - \beta_{\text{TM}_0}|} = \frac{\lambda}{2|n_{\text{eff,TE}_0} - n_{\text{eff,TM}_0}|} \quad (\text{B.4})$$

The phase mismatch reduces the efficiency of PMC by limiting energy transfer between the modes. Essentially, mode beating causes a polarization state evolution which can be tracked using an averaged Stokes vector on the Poincaré sphere [241]. It can be mitigated by periodically reversing the magnetic field to allow quasi-phase matching (QPM) between the modes [242, 354]. The electromagnetic coil in this investigation was designed to produce such a B -field reversal.

B.2. Generation of an Electro-Magnetic Field

The magnetic flux, Φ_B , interacting with the mode is determined by the flux density, B , overlapping with the cross-sectional area, A_{mode} , of the optical mode,

$$\Phi_B = BA_{\text{mode}} \quad (\text{B.5})$$

The rotation of the mode could be determined by the magnetic flux density that overlaps with the Poynting vector at each point in the mode field distribution. In this design, the magnetic field was generated by an electric current, I , in a coil of n windings or turns. The magnetic flux density produced by the coil was,

$$B = \mu_0 \mu_r \frac{nI}{l_{coil}} \quad (\text{B.6})$$

Where μ_r is the relative magnetic permeability of the materials through which the flux is being evaluated and μ_0 is the permeability of free space. Since the length of the coil, l_{coil} , determined the strength of the magnetic field, different coil lengths were designed. The magnetic field in the waveguide was also directly proportional to the current through the coil.

Out of the materials available on-chip, Al and TiN are paramagnetic with susceptibilities of $1.7 \times 10^{-5} \text{ cm}^3/\text{mol}$ and $38 \times 10^{-6} \text{ cm}^3/\text{mol}$, respectively. On the other hand, Si and SiO₂ are diamagnetic with susceptibilities of $-3.9 \times 10^{-6} \text{ cm}^3/\text{mol}$ and $-29.6 \times 10^{-6} \text{ cm}^3/\text{mol}$, respectively. To compensate for the expulsion of the magnetic field by Si and SiO₂, two Al and two TiN layers were deposited co-axially inside the coil to emulate a solenoid core.

B.3. Resistive Heating in the Coil

The resistance of each winding of the coil was a summation of resistances in series formed by the resistance of each layer and the ohmic contacts between them. A larger current would produce a larger current density, J , which generated resistive or Joule heat, Q , from the components of the coil,

$$Q = \rho(T)|J|^2 \quad (\text{B.7})$$

Since the same coil design was used for every device, the evolution of cross-sectional area along the path of electrical current was consistent for a coil length l with an integer number of turns n . Its average resistivity was therefore equivalent to its resistance, R , per unit length of wiring as $R/L = \rho/A$. The electrical resistivity $\rho(T)$ increases with temperature,

$$\rho(T) = \rho_0(1 + \alpha(T - T_0)) \quad (\text{B.8})$$

Where α is the temperature coefficient of resistivity and T_0 is the room temperature at 293.15 K. Resistive heating in the coil was therefore be measured by the relationship between its resistance per unit length and the input current.

B.4. Inductance of the Coil

The maximum operating frequency of the coil was determined by its inductive reactance or impedance,

$$Z_L = r + 2\pi fL \quad (\text{B.9})$$

Where L is its inductance. In this design, R was assumed to be the DC circuit load in a standard RL series circuit. The inductance, L , of the coil was,

$$L = \frac{n\Phi_{B,\text{coil}}}{I} = \mu_0\mu_r \frac{n^2 A_{\text{coil}}}{l} \quad (\text{B.10})$$

The inner width of the coils was $13.7 \mu\text{m}$ or $14.7 \mu\text{m}$, resulting in an A_{coil} of $34.66 \mu\text{m}^2$ or $37.19 \mu\text{m}^2$, respectively. Using equation (B.10), these dimensions resulted in the inductances shown in Table B.1.

Table B.1. Inductance of the six fabricated SiP coils as per design variations.

Gap \ Length	l = 492.9 μm n = 53	l = 744 μm n = 80	l = 1097.4 μm n = 118
g = 0.5 μm	248.2 μH	374.7 μH	552.6 μH
g = 1 μm	266.3 μH	402 μH	593 μH

The response time of the circuit to a change in current could be determined from its time constant [355],

$$\tau = L/R \quad (\text{B.11})$$

Here, R was obtained from the measured resistance per unit length. This resulted in transient times of 196.3 fs and 210.6 fs for coils with a w_{gap} of 0.5 μm and 1 μm , respectively. The response would reach steady state at approximately 5τ , which represented the transient time and indicated its behaviour as a low pass filter. It corresponds to operating frequencies of 2.547 THz and 2.374 THz.

B.5. Characterization of Design Variations

This device design investigated the feasibility of inducing NR PMC via Faraday rotation in the SiP platform. It was based on the operating principle of conventional bulk isolators, in which optical nonreciprocity was induced by rotating the plane of polarized light under an applied magnetic field. As per equation (B.2), the angle of rotation θ was dependent on the magnetic flux density in the direction of propagation B_Y , the Verdet constant of the mode V , and the MO interaction length l_{MO} .

Four variations of waveguides were designed for characterization purposes. The baseline was a Si strip waveguide with a width of 500 nm and height of 220 nm. This base design was modified to produce 15 device variations including a reduced gap of 500 nm between the Si layers, 3 coil lengths (492.9 μm , 744 μm , and 1097.4 μm , which accommodated 53, 80, and 118 windings, respectively), and 4 waveguide types (strip, slot, doped with Boron, or doped with Phosphorus). The slot waveguide consisted of 180 nm wide sidewalls on either side of a 180 nm wide slot. To vary the refractive index, the Si waveguide was also doped with Phosphorus (n-Si) and Boron (p-Si). Overall, fifteen variations were fabricated including four types of waveguides surrounded by two different coil widths spanning three coil lengths of 493 μm , 744 μm , and 1097 μm . The parameter values are listed in Table B.2 for each device.

Table B.2. Parameters of the design variations that were fabricated on-chip.

#	Length (μm)	Separation (μm)	Doping	Slots
1	492.9	1	-	0
2	492.9	0.5	n	0
3	492.9	0.5	p	0
4	492.9	0.5	-	1
5	492.9	0.5	-	0
6	744	1	-	0
7	744	0.5	n	0
8	744	0.5	p	0
9	744	0.5	-	1
10	744	0.5	-	0
11	1097.4	1	-	0
12	1097.4	0.5	n	0
13	1097.4	0.5	p	0
14	1097.4	0.5	-	1
15	1097.4	0.5	-	0

The design layout is shown in Figure B.2 in the form of photographs of the on-chip devices.

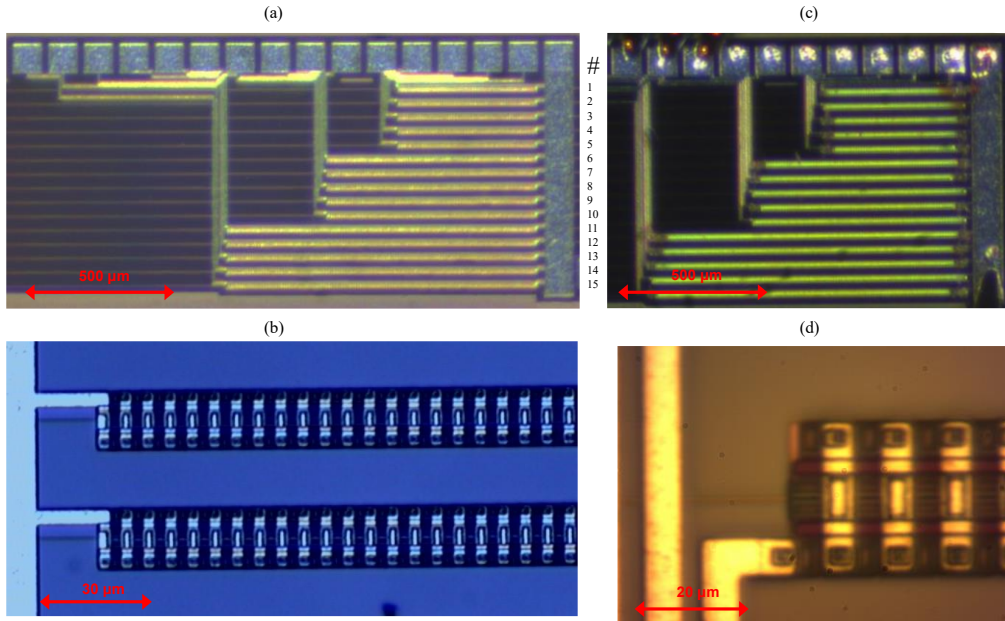


Figure B.2. Top-down photographs of (a) the fabricated SiP chip with 15 variations of the device design as described in Table S2, (b, d) zoom-in of the devices, (c) the coils after breakdown. The different colours are due to the combination of microscope and illumination which was optimized for each image.

The waveguides were extended to the ends of the chip and connected to input/output edge couplers. The edge couplers were 60 μm long and linearly tapered from a width of 500 nm to 180 nm at the edge of the chip. Edge couplers offer a lower polarization sensitivity than vertical couplers, which would allow both TE and TM polarizations to be coupled to the device.

Coils with a 1 μm gap did not have a measurably higher resistance than those with a 0.5 μm gap. This is because the extra width was achieved by elongating the Al strips above the waveguide and their conductivity was higher than the other materials of the coil by orders of magnitude. Note that although the cross-sectional area could be increased without incurring a significantly higher resistance, the inductance (and therefore response time) would be proportionally increased.

A low dopant concentration was chosen to minimize absorption loss. However, such light doping induced only a negligible difference in effective index i.e., $\Delta n_{\text{eff}}/n_{\text{eff}} \rightarrow 0$. As a result, the mode profiles of the p-Si and n-Si waveguides were almost the same as the undoped Si waveguide. Consequently, their Verdet constant was equivalent to the undoped waveguides. Therefore, these two waveguide types were excluded from the remaining analysis. Fundamental TE and TM mode profiles for the strip and slot waveguides are shown in Figure B.3 at a wavelength of 1550 nm. At a wavelength of 1310 nm, mode field distributions were more confined but retained their profile. Doping the waveguides with either P or B did not significantly alter the refractive index of the Si

waveguide and consequently the Verdet constant. As a result, they did not offer a significant performance variation from the base design and were not evaluated further.

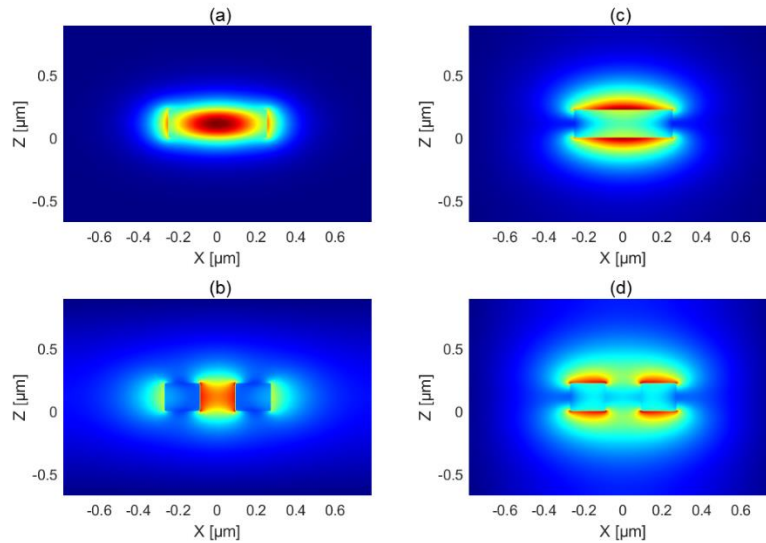


Figure B.3. Distribution of the electric field magnitudes at a wavelength of 1550 nm. TE₀ mode in the (a) strip and (b) slot waveguide, and TM₀ modes in the (c) strip and (d) slot waveguide.

The effective index for each mode across the 1260-1600 nm wavelength range is shown in Figure B.4(a). The right axis shows the corresponding half-beat length between both orthogonal modes for each waveguide type. Chromatic dispersion at a given wavelength was calculated as the slope of the modal effective index. Using this, the Verdet constant of each mode was calculated as shown in Figure B.4(b). The effect of overlap between the evanescent field of the waveguide modes and the lower Al strip was neglected.

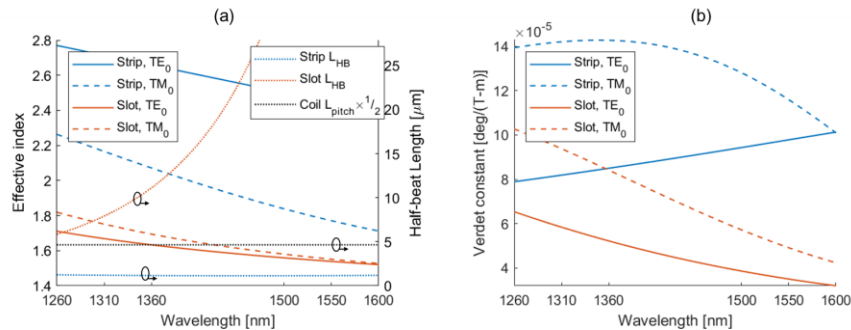


Figure B.4. Characterisation of different modes under study at different wavelengths. (a) Effective index of the TE₀ and TM₀ modes in strip and slot waveguides (solid and dashed lines, left axis) and the half-beat length between the fundamental modes of the slot and strip waveguides (dotted lines, right axis). The half-pitch length of the coil is also shown for reference. (b) Verdet constant for the same two fundamental modes of each waveguide type.

For a strip waveguide, the n_{eff} for the TE_0 mode was higher than that of the TM_0 mode, which corresponded to its larger width in comparison to its height. For a slot waveguide, however, the effective index of the TM_0 mode was higher than TE_0 . This Δn decreased to almost zero at 1600 nm, which produced an asymptotic increase in the corresponding half-beat length, L_{HB} , thereby precluding the need for QPM. At shorter wavelengths, the L_{HB} was almost equal to the pitch of the coil, which would maximize QPM. The effective index difference between the orthogonal waveguide modes resulted a wide range of half-beat lengths. A mismatch between the half-beat length and the coil pitch would reduce PMC efficiency [241]. Perfect phase matching was exhibited for longer wavelengths in the slot waveguide, which indicated the possibility of not requiring mode beating. However, the PMC efficiency might still be reduced by the mismatched coil pitch. In future iterations of the waveguide design, the half-beat length between modes could be matched with the pitch of the coil to ensure QPM for a suitably dispersion engineered [174] waveguide mode.

Although the intensity of the TE mode is indeed stronger inside the Si core layer than the TM mode, note that Faraday rotation did not depend on the intensity of light. Additionally, as per equation (B.3), the interaction depended on the dispersion of the mode (via the Verdet constant) rather than the effective index itself. Although the interaction also depended on the magnetic permeability of the materials, the magnetic permeability of Si and SiO_2 were similar enough that they did not affect the rotation of the TE mode (which was more concentrated in the Si core layer) more than the TM mode. So, the extent of Faraday rotation of the mode depended on its Verdet constant more than its field distribution in the core. Since the Verdet constant of the TE mode was lower than the TM mode, its corresponding Faraday rotation effect was weaker as seen in Table B.3.

Table B.3. Rotation of the polarization state for the evaluated devices. The first column indicates the device number (#) corresponding to Table B.2, which also implies the type of waveguide used. Values are shaded from white to green to reflect the smallest to largest angles of rotation.

Device #	Rotation (pico-degrees)			
	1310 nm		1550 nm	
Mode →	TE_0	TM_0	TE_0	TM_0
1	12.15	21.07	14.48	17.33
4	8.66	13.91	5.2	7.29
5	12.14	21.05	14.47	17.31

6	18.4	31.91	21.94	26.25
9	13.12	21.06	7.87	11.04
10	18.39	31.89	21.92	26.22
11	27.2	47.18	32.43	38.8
14	19.39	31.14	11.64	16.32
15	27.18	47.13	32.4	38.76

The lowest rotation of $5.2 \times 10^{-12} \text{ }^\circ$ was obtained for the TE₀ mode of the slot waveguide at 1550 nm. The interaction was evaluated using the magnetic field strength along the centerline of the waveguide. Accuracy could be improved by integrating the magnetic field at each point in its overlap with the mode field distribution and over all three axes separately.

B.6. Vertical Axis Coils

To reduce the number of layers per winding, vertical-axis coils were also fabricated and tested. These coils employed multiple windings in a single layered spiral before connecting to the next metallization layer, which was also a spiral. The large area and negligible length of these coils resulted in such a high inductance that the response time was on the order of seconds. Since they could only be operated in steady state, they were deemed infeasible for commercial use.

B.7. Additional Methods

B.7.1. Layout Design for Device Fabrication

The chip layout was developed in Mentor Graphics Pyxis and verified in KLayout. The vertical windings of the coil were constructed from a stack of horizontal material layers that were available through the standard chip fabrication process offered by the IME foundry (now AMF). Design parameters were constrained by the fabrication process. The material layers consisted of Si for the waveguides, doped n-Si for electrical wiring in the Si layer, two Al metallization layers for the electrical wiring and solenoid core, TaN for vias between the Si and Al layers, and TiN for an additional solenoid core.

B.7.2. Electrical Measurements of the Coils

All 15 coils were connected to a common ground which was accessed by a single bond pad. This required only one of the electrical probes to be moved to test a new device. For the measurement, each device was probed across its dedicated DC bond pad and the common ground. An ammeter was connected in series with the probing setup to measure the input current through the device. A power supply and oscilloscope were connected across the setup and ammeter. A

voltage difference of up to 145 V was applied across this series connection and measured by the oscilloscope. For each device, the applied voltage was increased in steps of 1 V up to 40 V and beyond 120 V. In the range of 40-120 V, the resistance was more insensitive, which justified a larger step size of 5-10 V. The input voltage was increased until breakdown occurred, which was identified by a spark in the chip and an open circuit with negligible input current as shown in Figure B.2(c).

B.7.3. Simulations

The mode field distributions for each waveguide were simulated in Lumerical Mode. Wavelength-dependent refractive indices were used for the Si core and SiO₂ cladding as obtained from the material database [78]. These points were fitted with a multi-coefficient model using the values ranging from 1200 nm to 1800 nm and a fit tolerance of 0.01.

Resistive heating was simulated using the ‘Electromagnetic Heating’ Multiphysics module in COMSOL Multiphysics, which combined the ‘Electric Currents’ and ‘Heat Transfer in Solids’ modules. The device layout was imported using the ‘ECAD Import’ module and each layer was projected to 3D by specifying its elevation, thickness, and material properties. Two cylindrical Al rods were added to the end terminals of the coil to connect it to the outer surface of the simulation region and send a current through the device.

This electromagnetic coil was simulated using the ‘Magnetic and Electric Fields’ module in COMSOL Multiphysics. All domains associated with the coil were added to the ‘Ampere’s Law and Current Conservation’ node to electrically connect them. The waveguide, cladding, and all four paramagnetic cores were added to the Ampere’s Law node to evaluate the magnetic field through these domains. The input current was swept over a range of 2-14 mA, which generated a magnetic field based on the magnetic permeability, electric permittivity, and conductivity of each material. Due to the low magnetic susceptibilities of Si and SiO₂, the magnetic field distribution was almost continuous across the mode profile within the region in and around the waveguide. Hence, the magnetic flux density in the waveguide was evaluated along a straight line through the center of the waveguide rather than at every point in the cross-section.

The magneto-optic interaction between the electrically generated magnetic field and confined optical modes was calculated in MATLAB. The angle of rotation was determined from equation (B.2) using calculations of V and B_Y . To determine the extent of Faraday rotation induced in the

design, polarization rotation was simulated for a propagation length of 51.5 μm to minimize computation time. These results were then extrapolated to the fabricated device lengths.

Appendix C. Supplementary Information for Chapter 6

C.1. Experimental Setup

The electron beam (eBeam) emitted by the ultrafast transmission electron microscope (UTEM) can be selected within a kinetic energy range of 80 keV to 200 keV, which corresponds to a range of sub-relativistic velocities, v_e , of $0.5c_0$ to $0.7c_0$ respectively, where c_0 is the speed of light in vacuum. The UTEM can be operated in one of the following two modes. The thermionic emission mode delivers a flow of single electrons as random current once the temperature reaches the work function of the material, which is useful to study quantum interactions [288, 290, 308, 323, 325, 328]. For 200 keV electrons in this mode, the emittance is 6 nm-mrad at, implying that the diameter of the spot size, d_e , can be 2-20 nm with a corresponding convergence semi-angle, θ_e , of 3-0.3 mrad, respectively. Alternatively, the photoemission mode [289] delivers electron pulses, which are useful for testing dielectric laser accelerators (DLAs) [302, 303, 306, 318-320, 322]. In this mode, the emittance is 400 nm-mrad at 200 keV, which implies that d_e can be 20-200 nm with a corresponding θ_e of 20-2 mrad, respectively. At a common $d_e = 20$ nm, the thermionic emission mode was selected because its lower emittance allowed for a better overlap between the electron and optical supermode. The dimensions of the eBeam along its trajectory were calculated from these parameters using Rayleigh criterion. We assume a symmetric eBeam profile in the transverse dimension [289] such that the emittance in the X dimension (see Figure 6.1 for reference), $\epsilon_x = \sigma_x \sigma_{ax} = \epsilon_y = \epsilon$ where σ_x and σ_{ax} are the width and convergence angle of the eBeam, respectively. Emittance remains constant for a specific eBeam energy. Within the emittance, the convergence angle and spot size can be modified via the numerical aperture of the magnetic lensing system. To adjust for different eBeam energies, we normalize the emittance [356],

$$\epsilon_n = \beta\gamma\epsilon = \beta\gamma\sigma_x\sigma_{ax} \quad (\text{C.1})$$

Where $\beta = v_e/c_0$ and $\gamma = 1/\sqrt{1-\beta^2}$ is the Lorentz factor. The electron energy (with relativistic correction) is,

$$\epsilon_e = (\gamma - 1)m_e c_0^2 \quad (\text{C.2})$$

Where m_e is the rest mass of the electron. The width of the eBeam is adjusted by the de Broglie wavelength of the electron,

$$\lambda_e = \frac{h_j}{\gamma m_e v_e} \quad (\text{C.3})$$

Where h_j is Planck's constant in Joules. Note that lower electron energies have a larger de Broglie wavelength which enlarges the spot size of the eBeam.

The eBeam undergoes magnetic lensing in order to steer and focus it onto the sample as well as separate the electron energies after the interaction. Since the electrons travel in a helical path, the on-chip device is surrounded by trenches so that the substrate can act a mesa to ensure beam clearance. The protrusion of the mesa must be 50 μm higher than the substrate, which is satisfied by the 675 μm thickness of the Si substrate. Additionally, appropriate clearance is also required beyond the device due to the divergence and the helical trajectory of the eBeam. These constraints limit the maximum effective interaction length, L_{eff} , to 500 μm . After interaction, the electrons would be filtered via a magnetic prism and aperture to measure their energy distribution. The relative arrival time of the electron with respect to the laser pulse, and therefore the location of their interaction, can be determined by the relative delay between the pump and probe pulses.

C.2. Circuit Layout

We design a photonic integrated circuit to be compatible with the constraints of the UTEM. The layout is shown in Figure 6.1. Inside the UTEM, light can be focused onto the chip from a lens with a focal length of 50 mm. This implies that a collimated beam of 5 mm diameter can be focused down to a spot size of 30 μm with a convergence angle of 0.4394° . Incident light is therefore coupled from free-space into the chip by a surface, vertical grating coupler (GC) [315]. We employed only one GC in order to reduce any coupling loss or phase mismatch between the arms of a dual-GC setup [291]. The GC is connected to a 90:10 splitter [41, 122] which routes 90% of the light to the device and uses 10% for feedback. In the 90% arm, light is sent to a mode evolution region (MER) in which the fundamental transverse magnetic (TM_0) mode of the strip waveguide is converted into the desired supermode of the slot waveguide [310, 311]. A waveguide bend ensures the proximity of the MER to the edge of the device. A deep trench is carved into the chip at both ends of the device to act as a mesa and ensure that the diverging eBeam is not obstructed by the underlying BOX layer. The 10% arm of the splitter is connected to a Bragg grating (BG) reflector to provide feedback during the optical alignment of the chip. A secondary GC and BG

are also placed next to the device to enable a coarse alignment. Once the incident angle is coarsely aligned using this secondary GC, the chip could be moved along the Z-axis to couple light into the primary GC and its alignment could be fine tuned based on feedback from the BG in the 10% arm.

As shown in Figure 6.1(a), the input GC produces a TM_0 mode which must then be coupled into the slot waveguide from a single sidewall (to prevent obstruction of the eBeam path), and with a specified electric field distribution. These requirements are addressed by the MER, which we design using supermode analysis [40, 212] for directional couplers and slot waveguides. In this design, a strip waveguide is connected from the 90% arm of the splitter to one of the sidewalls of the slot waveguide whereas the other sidewall was tapered and bent outward. The connected sidewall gradually evolves the effective index of the TM_0 mode in the strip waveguide to become the desired supermode in the slot waveguide. The conversion efficiency to the target supermode is measured as the insertion loss (IL) from the power in the input TM_0 mode to the desired supermode. We assume negligible energy leakage into the other modes which implies that they do not significantly interfere with the desired supermode. So, the phase relationship between the modes is not considered. Since the MER depends on the cross-section of the slot waveguide and its supermode, it must be redesigned for each supermode and waveguide cross-section. In cases where a strip waveguide is used for the interaction, that is, $w_{\text{gap}} = 0$, then the IL can be set as 0 dB since a MER is not necessary. In a future iteration of the design, the IL of the MER can be optimized by also injecting the supermode in the output to maximize the power for both forward and backward propagation. However, note that although the IL of the MER affects the overall interaction strength, it does not affect the coupling strength per photon because this value is normalized to the power of the optical pulse.

For example, an incident beam can be coupled into the GC with an IL of -9 dB [122] and guided through the variable intensity splitter and MER with ILs of -0.45 dB [41] and -10 dB, respectively. The optical pulse parameters in the slot are determined from the material constraints of the slot waveguide in the following section.

C.3. Optical Pulse Parameters

The parameters of the input optical pulse are constrained by the accelerating structure. Under specific conditions, confined photons in the pulse get absorbed by bound electrons in the structure. This photoionization pushes electrons into the conduction band [312, 313]. The conduction electrons get accelerated in the laser field and generate an avalanche from impact ionization [316].

This plasma is heated by the laser pulse, transferring the electron energy to the lattice. If its electron density increases to the point where the plasma frequency matches the laser frequency, then resonance occurs and the material gets damaged by ablation [313]. Although dielectrics can withstand orders of magnitude higher electric fields than metals, their damage threshold still often limits the acceleration gradient, G . It scales as [312], $G \propto \sqrt{F_{th}}$, where F_{th} is the damage threshold fluence of the material. The fluence is given by [316], $F_{th} = \frac{2U_{th}}{\pi w_x w_y}$, where U_{th} is the threshold pulse energy and w_x, w_y are the spot size dimensions. The threshold is further lowered by local field enhancements due to light being confined in the relatively small dimensions of the accelerating structure. For example, a silica grating has a damage threshold fluence of 1.85 J/cm² at 1500 nm, which is 0.53 times that of bulk silica (but still allows for a G of 300 MV/m) [313].

The optical damage threshold of the host material depends on the wavelength and pulse duration of the laser. Since it increases with the laser pulse width [357], we set it at 1 ps for our Si waveguide. The damage threshold of Si for a 1 ps pulse reaches a local maximum within the wavelength range of 1200-1600 nm [312, 313] as compared to 1064 nm [357] or 2000 nm [291] (all of which encompass the one- and two-photon ionization regimes). We therefore select two operating wavelengths of 1310 nm and 1550 nm, which also benefit from the availability of components and laser sources as well as the maturity of fabrication techniques.

For 1 ps pulses at a wavelength of 1550 nm, breakdown occurs around 0.2 J/cm² [316]. In the case of our slot waveguide, the Si core thickness is 220 nm with an average total width $2w_{Si}$ of 500 nm, which occupies a cross-sectional area of 1.1×10^{-9} cm². This allows for a maximum pulse energy of 0.22 nJ corresponding to a peak pulse power of 220 W in the slot. Considering an average loss of -19.4576 dB from the GC, splitter, and MER together (as calculated in the previous section), the energy of the free-space optical pulse that is incident on the chip must be 19.4169 nJ corresponding to 19.4169 kW.

Such a high peak pulse power can induce strong nonlinear effects. In fact, these effects are even caused at lower powers in Si waveguides because the high refractive index of Si increases the confinement [358] and reduces the group velocity [359] of the optical mode, which enhances optical interactions with the Si core. Below 5 mW, intra-bandgap states induce single-photon absorption and as the optical power increases, the 1.12 eV bandgap of Si induces two-photon absorption which dominates beyond 300 mW [359]. Absorption of the optical energy consequently

generates electron–hole pairs, which cause free-carrier dispersion (FCD) and free-carrier absorption (FCA). FCA is further enhanced by the fact that the free-carriers cannot diffuse out of the modal region in the waveguide [359]. It is determined by the effective modal area (calculated from the Poynting vector or the electric field intensity) [359] which corresponds to the surface-to-volume ratio of the waveguide [358]. This nonlinearity enhancement increases the a TPA coefficient to 1.5 cm/GW [359] as compared to 0.4-1.2 cm/GW for bulk structures [358, 359], and the SPA coefficient to 1.9 m⁻¹ [359]. In this case, the recombination rate of the free-carriers limits the rate at which optical pulses can be generated. Carriers are found to have shorter lifetimes of ~800 ps initially, with longer lifetimes up to ~300 ns at later stages, assuming no initial carrier density [358]. In our case, since the IL of the GC already reduces the power by -9 dB when coupling into the chip, followed by a -10 dB loss at the MER, we assume these effects to be negligible in the interaction region. Future analysis could quantify these effects and even exploit FCA and FCD to control light within the Si structure [359].

C.4. Supermodes of the Slot Waveguide

The limits of v_e that are imposed by the UTEM also constrain the range of phase velocities $v_p = \omega/k$ of the supermode and consequently, its effective refractive index, n_{eff} . For example, an eBeam of 80 keV or $0.5c$ requires a n_{eff} of 1.9904 for the supermode. Similarly, an eBeam of 200 keV requires a n_{eff} of 1.4382 which is lower than the index of the buried oxide (BOX) layer. It is therefore unachievable using the standard SOI platform because the mode gets coupled into the BOX layer. The amplitude, E_0 , of the electric field of the supermode, $E_0 \cos(\omega t - kz)$, is obtained from its individual field components as $E_0 = \sqrt{E_X^2 + E_Y^2 + E_Z^2}$. To account for a non-uniform electric field distribution (as opposed to a Gaussian beam profile), we simulate the electric field distribution and obtain its amplitude at each (x, y) point around the waveguide cross-section, $E_0(x, y)$. It is multiplied by the sign of the phase to retain the direction of oscillation of the field,

$$E_{0,Z} = |E_Z| \cdot \text{sgn}(\angle E_Z) \quad (\text{C.4})$$

We then characterize the properties of the three lowest order modes for each variation of the waveguide geometry. These properties are the effective index, n_{eff} , group index, n_g , and the maximum amplitude of the longitudinal electric field component in the center of the gap, $E_{0,Z}(0, y > 0)$. Both n_{eff} and n_g were converted into the corresponding phase and group velocities of the supermode, v_p and v_g , respectively, to compare them directly with the electron velocity, v_e .

We discard the first supermode because its E_z field exhibits an antisymmetric distribution about the Y axis which results in $E_{0,z}(0, y > 0) = 0$ as well as opposite phases on either side, which renders it useless for coupling. Figure C.1 shows the change in v_p , v_g , and $E_{0,z}(0, y > 0)$ for the remaining two supermodes as a result of varying the cross-sectional dimensions of the waveguide, w_{Si} and w_{gap} . The limits of v_e imposed by the UTEM are shown as black, dashed, horizontal lines at $0.5c$ and $0.7c$ in Figure C.1(a,f,k,p).

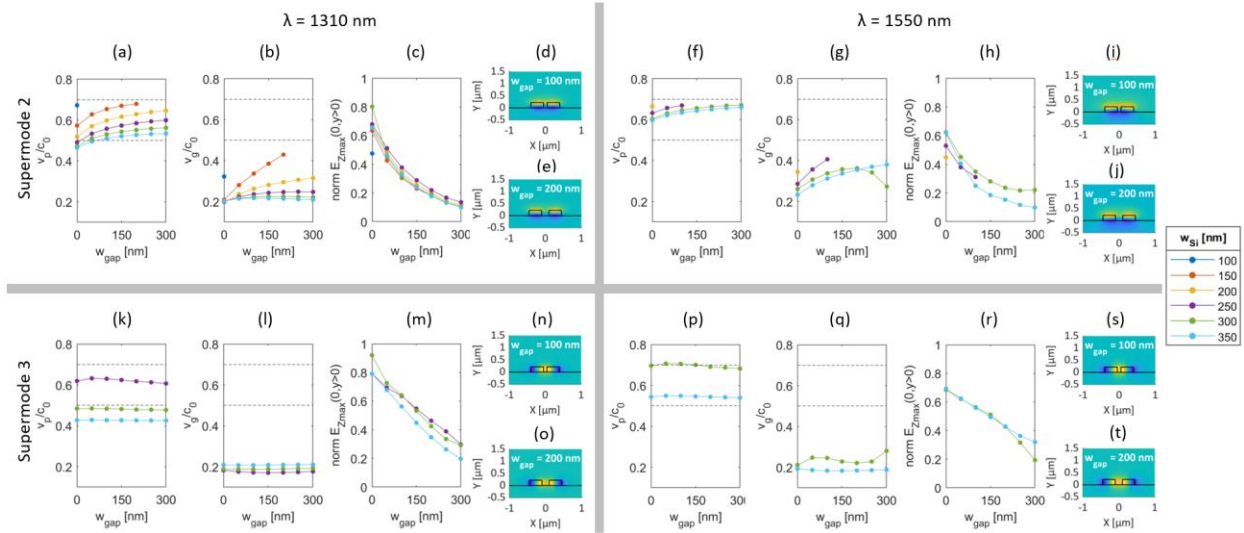


Figure C.1. Supermode characteristics for each variation of the waveguide cross-section. (a)-(j) Variation of supermode 2 properties with slot parameters at wavelengths of (a)-(e) 1310 nm and (f)-(j) 1550 nm. (k)-(t) Variation of supermode 3 properties with slot parameters at wavelengths of (k)-(o) 1310 nm and (p)-(t) 1550 nm. In each set, the first two columns show v_p and v_g along with horizontal, black, dashed lines indicating the limits of v_e . The third column of each set shows the maximum E_z field at the center of the waveguide.

In addition to the upper limit on v_p imposed by the UTEM, the refractive index of the BOX layer also limits the minimum n_{eff} beyond which confinement of the supermodes is weakened. This corresponds to a v_p of $0.6944c$, which is approximately equal to the UTEM limit and therefore not shown. Additionally, we find that just beyond this limit, the supermodes still remain confined over short propagation lengths since majority of the mode field is distributed in either Si or the external vacuum rather than in the BOX layer, that is, due to the vertical asymmetry of the waveguide cross-section. For both supermodes, the positive phase of their E_z field component is above the waveguide due to the lower refractive index of vacuum compared to the underlying BOX layer. The distribution of E_z around the waveguide depends on the cross-sectional dimensions of the slot. Narrower sidewall widths are unable to support supermode 3 especially at

the longer wavelength of 1550 nm. Additionally, longer wavelengths are less confined, which generally decreases $E_{0,z}$ in the gap. This behaviour is evident in the comparison of field distributions between Figure C.1(c) and (h) for supermode 2, and equivalently Figure C.1(m) and (r) for supermode 3. The field amplitude also monotonically decreases as w_{gap} is increased as shown in Figure C.1(c,h,m,r). This is because narrowing w_{gap} squeezes the E_z field between the sidewalls [116]. Although a higher $E_{0,z}$ is beneficial to the interaction, note that a wider w_{gap} accommodates a larger eBeam diameter and therefore a longer interaction length. As the confinement is weakened for a wide w_{gap} and thin w_{Si} , this lowers n_{eff} allowing v_p to reach the upper limit of the system. A higher v_p is more suitable for applications in which the final electron velocity, or kinetic energy, is important.

To obtain the total pulse power, we integrate the Poynting vector over the cross-sectional area of the simulation region since it is a local property of the optical field. This was done by summing the discretized power over the pixels of the simulation region, such that,

$$P = 0.5 \int \text{Re}(P_z) dA = 0.5 \sum_{i=1}^{n_{\text{px}}} P_{z,i} \cdot \Delta a_{\text{px}} \quad (\text{C.5})$$

Where Δa_{px} is the area of each pixel. We evaluate only the P_z component because the other two components are null since the Poynting vector points in the direction of propagation. The simulated, normalized E field was therefore scaled to match the input pulse power by,

$$E_{0,\text{exp}} = \sqrt{\frac{P_{\text{exp}}}{P_{\text{sim}}}} E_{0,\text{sim}} \quad (\text{C.6})$$

C.5. Interaction Length

In a quantum interpretation of the electron, the spatiotemporal distribution of its wavefunction is larger than a classical point particle. Hence, we estimate the duration as 500 fs based on previous measurements in the UTEM (as indicated in the Supplementary Material of [290]). In these calculations, we assume the probability distribution of the electron to be uniform within the spot size of the eBeam since energy can be exchanged at any point in the cross-section. We also approximate the helical trajectory of the eBeam to be straight along L_{eff} . In the X-Y transverse dimension, L_{eff} is limited by the divergence of the eBeam within the slot. For example, since a larger d_e corresponds to a lower θ_e , it allows a longer slot and therefore, longer interaction length,

L_{eff} . The maximum L_{eff} that can be accommodated by the slot is calculated for every combination of eBeam diameter and height,

$$L_{\text{eff}} = \frac{2\sqrt{(\min(h_e, t_{\text{Si}}) - t_{\text{Si}})^2 + \left(\frac{W_{\text{gap}}}{2}\right)^2}}{\tan \theta_e} \quad (\text{C.7})$$

However, maximizing L_{eff} does not necessarily maximize the overall interaction. The interaction could benefit from either a small, focused spot size in a narrow slot width, or a low convergence angle over a longer interaction length, which indicates a trade-off. Along the Z propagation direction, L_{eff} is limited by dephasing as v_e is accelerated beyond v_p . It is also limited by the mismatch with v_g depending on the limited durations of the optical pulse and electron wavefunction, but this limitation is not as severe. This is why L_{eff} is a crucial variable in maximizing the coupling efficiency. In this process, the E_z field distribution overlapping with the electron must also be maximized. As the eBeam converges and diverges through its focal point, the hourglass shape is determined by the convergence angle, width, and depth of focus [360]. To account for these gradually changing conditions along the length of the interaction, we discretize L_{eff} into 10 segments and evaluate coupling using the average cross-sectional area of the eBeam in each segment. The sum of these values determines the overall coupling. Regarding the evolution of the supermode over the interaction region, we assume the pulse profile and peak power to undergo negligible dispersion or modulation throughout propagation [291].

C.6. Coupling Strength

When an optical pulse co-propagates with a free electron, its properties are imprinted onto the wavefunction of the electron by the phase-front of its longitudinal electrical field. Maximum energy transfer occurs when both the photon and electron are traveling in the same direction at the same speed, that is, when v_e is matched to v_p . The electron can then surf the plasma wake-field of the optical wavefront. This stimulated interaction modulates the kinetic energy spectrum of the electron. Adding or removing kinetic energy is equivalent to accelerating or decelerating the electron, respectively. In our case, we assume that the interaction is localized in the near field of the device where diffraction effects are insignificant. We therefore analyze it using PINEM theory [281, 361].

Exciting the charged tip inside the UTEM emits an electron traveling in the +Z direction. Its wavefunction can be written as, $\psi(\mathbf{r}, t) = \phi(\mathbf{r}, t)e^{i(k_0 z - E_0 t/\hbar)}$ with its behaviour described by the reduced Schrödinger equation,

$$\left(v \frac{\partial}{\partial z} - \frac{\partial}{\partial t}\right) \phi = -\frac{q_e v_e}{\hbar \omega} (e^{-i\omega t} E_Z - e^{i\omega t} E_Z^*) \phi \quad (\text{C.8})$$

Here, we replace ∇ by $ik_0 \hat{\mathbf{z}}$, and ignore any wavefunction gradients that do not contribute to the direction of propagation $e^{ik_0 \hat{\mathbf{z}}}$. Hence, in the absence of any interaction, the electric field contributing to the electron energy is $E_Z = 0$ resulting in an incident wavefunction of the form,

$$\phi(\mathbf{r}, t) = \phi_0(\mathbf{r} - v_e t \hat{\mathbf{z}}) \quad (\text{C.9})$$

Which satisfies the reduced Schrödinger equation above and accounts for v_e (or equivalently ε_e as per equation (C.2)). We ignore transverse and mismatched components of the field due to their negligible effect from a co-propagating pulse. During the interaction, the electron wavefunction exchanges quanta of $\hbar\omega$ energy to co-propagating photons. As per the PINEM effect [361], it has an equal probability of absorbing or emitting a photon and therefore gaining or losing energy, which causes it to accelerate or decelerate, respectively. Its spectrum therefore gets redistributed around a periodically spaced set of energies $\varepsilon_0 \pm \ell \hbar\omega$ which modifies equation (C.9) to,

$$\phi(\mathbf{r}, t) = \phi_0(\mathbf{r} - v_e t \hat{\mathbf{z}}) \sum_{\ell} e^{i\ell\omega\left(\frac{z}{v_e} - t\right)} f_{\ell}(\mathbf{r}) \quad (\text{C.10})$$

This represents a Fourier decomposition of the wave function in terms of its energy, which is quantized, or discretized, by the index ℓ . In other words, the main Fourier coefficients f_{ℓ} are spaced from each other by the laser frequency $\hbar\omega$, which allows them to be expressed as a summation instead of an integral. These f_{ℓ} coefficients can be written in terms of Bessel functions as $f_{\ell}(\beta) = e^{i\ell \arg(-\beta)} J_{\ell}(2|\beta|)$ and integrated along the +Z interaction length [362]. The probability of gaining or losing ℓ quanta of photon energy is therefore $P_{\ell} = |J_{\ell}(2|\beta|)|^2$. The coupling strength over the total interaction length $(-\infty, \infty)$ can then be obtained from the probability of absorbing or emitting a photon,

$$\beta(z) = \frac{q_e}{\hbar\omega} \int_{-\infty}^{\infty} E_Z(z) e^{-i\omega \frac{z}{v}} dz \quad (\text{C.11})$$

Note that since ω is in the denominator, this implies that lower frequencies (or equivalently, longer wavelengths) have a higher probability of interaction. However, since they exchange less

$\hbar\omega$ energy with the electron, the resulting coupling strength could still be lower. This could explain why our design produces comparable results at both wavelengths of 1550 nm and 1310 nm alongside previously reported calculations at 2000 nm [291].

After the inelastic interaction with the laser field, the spectral distribution of ε_e can be quantified by the coupling or Rabi parameter [287], g , which represents the transition amplitude between adjacent electron energy states. This coupling constant, g , links the classical acceleration of an electron to the field of the optical mode. If $g \gg 1$, the electron energy width (or bandwidth) scales as $4|g|$ times the optical photon energy [296]. Taking into account the spatial distribution of E_z , the interaction at each spatial co-ordinate (x_0, y_0) overlapping with the spot size of the eBeam can then be written in terms of this dimensionless coupling constant [282, 361, 363],

$$g(x_0, y_0) = \frac{q_e}{\hbar\omega} \int_{-\infty}^{\infty} E_z^{(\omega)}(x_0, y_0, z, t(z)) dz \quad (\text{C.12})$$

The superscript (ω) denotes the frequency dependence of the electric field and $t(z)$ indicates the temporal delay with respect to the electron wavefunction. This integral represents the electron energy gain/loss normalized by the photon energy. It suggests that a maximum of $2|g|$ photons are exchanged during the interaction, which implies both gain and loss resulting in a $2|g|\hbar\omega$ energy spread of the electron spectrum [290].

For optimal coupling, $E_z^{(\omega)}$ must be constant so that the interaction with the electron beam is maintained. In contrast, a DLA configuration would require the phase velocity of E_z to be increased along the interaction length to maximize the energy gain of the electron. The mode field distribution of the electric field $E_z(x, y)$ was obtained from 3D FDTD simulations. The main contribution to the interaction is at the maximal field amplitude near the waveguide surface. At this proximity, the field travels approximately as a phasor so that the expression for E_z can be separated as $E_{0,z}(x_0, y_0)e^{ik_z z}$ and the phase mismatch $(k_z - \omega/v_e)$ can be separated in equation (C.12) as,

$$g(x_0, y_0) = \frac{q_e}{\hbar\omega} \int_{-\infty}^{\infty} E_{0,z}(x_0, y_0) e^{i(k_z - \omega/v_e)z} dz \quad (\text{C.13})$$

Since energy can be exchanged at any (x, y) point in the region of overlap, we average the electric field over this region. Additionally, assuming $v_e = v_p$, the coupling strength along a fixed length simplifies to,

$$g = \frac{q_e}{\hbar\omega} E_{Z,\text{avg}} L_{\text{eff}} \quad (\text{C.14})$$

Note that this is only valid for length scales in which the eBeam spot size does not significantly change. Hence, this simplified form of g must be calculated separately for each discretized segment along L_{eff} depending on the convergence angle of the eBeam, as mentioned in the previous section. Additionally, as in equation (C.10), PINEM theory uses the approximation that the electron velocities remain constant during the interaction. However, when the electrons are accelerated, they no longer match v_p . This implies that L_{eff} is limited by the phase-matching condition, $\frac{1}{v_e} \int (v_e(z) - v_p) dz < \frac{\pi v_p}{\omega}$ where $\frac{\pi v_p}{\omega}$ is the half wavelength of the mode. Note that in this equation, v_e , g , and L_{eff} are inseparable variables and the rigorous electron velocity $v_e(z)$ is not known along its trajectory. Hence, we modify this condition to,

$$\frac{L_{\text{eff}}}{v_{e,\text{avg}}(L_{\text{eff}})} (v_{e,\text{avg}}(L_{\text{eff}}) - v_p) < \frac{\pi v_p}{\omega} \quad (\text{C.15})$$

Here, $v_{e,\text{avg}}(g(L_{\text{eff}})) = \frac{(v_e(z=0) + v_e(z=L_{\text{eff}}))}{2}$ assuming linear acceleration and $\frac{L_{\text{eff}}}{v_{e,\text{avg}}(g(L_{\text{eff}}))}$ is the interaction time. Moreover, since equation (C.14) does not account for the dependence of the pulse envelope, we effectively assume that the optical pulse and electron do not incur significant drift along a particular segment of L_{eff} . The validity of this assumption depends on whether the segment is short enough for the interaction to not be affected by a group velocity mismatch or if the duration of the pulse is long enough for the driving-field amplitude to be relatively constant over the segment. Although the interaction is maximized when both conditions are satisfied, the phase modulation of the electron wavefunction is still expected to be uniform and deterministic for nonideal cases [287, 296]. The energy gained (or lost) by the electron can then be evaluated as [290],

$$\Delta\varepsilon_e = 2g\hbar\omega \quad (\text{C.16})$$

With the acceleration gradient given by,

$$G = \Delta\varepsilon_e/L_{\text{eff}} \quad (\text{C.17})$$

Note that this value is dependent on g , which is dependent on the power (energy and duration) of the optical pulse [288]. In a quantum-optics description [298], we consider PINEM driven by a coherent state $|\alpha\rangle$ with an average number of $|\alpha|^2$ photons. In the classical field of a mode with

total energy per μm , U , the average number of photons is $\langle n \rangle = U/\hbar\omega$. Therefore, we interpret the coupling strength per photon as [298],

$$g_{\text{Qu}} = \frac{g}{\sqrt{n}} = \frac{g}{\alpha} = \frac{q_e}{\alpha\hbar\omega} E_{\text{Z,avg}} L_{\text{eff}}, \quad (\text{C.18})$$

which is a dimensionless parameter [287, 298] representing the proportion of the electron energy gain from one photon in the supermode. The regime of strong coupling is accessed by $g_{\text{Qu}} \geq 1$ [297, 298]. In this manner, g_{Qu} is related to both the output kinetic energy gain of the electron and the input optical energy of the laser pulse, which therefore makes it a suitable indicator of coupling efficiency.

We confirm the validity of our reasoning and assumptions by applying them to the use case presented in this work. Specifically, we use these equations to find the maximum coupling strength per photon or equivalently, the coupling efficiency of the device design. It is done by characterizing the parameter space of the design in the following manner. Each set of slot dimensions, w_{gap} and w_{Si} , host specific supermode profiles with a corresponding effective index, n_{eff} , and phase velocity, v_p . This sets the electron velocity, v_e , which constrains the eBeam emittance, that is, its diameter, d_e , and convergence angle, θ_e . The eBeam height from the BOX layer, h_e , is restricted to less than 500 nm since the interaction strength decayed exponentially with increasing separation [296]. Hence, the maximum L_{eff} is geometrically constrained by w_{gap} , h_e , and d_e . These parameters are used to calculate the coupling constant, g , which is divided by the square root of the number of photons in the pulse, α , [298] to produce the coupling constant per photon, g_{Qu} . In this manner, w_{gap} , w_{Si} , $d_e \leftrightarrow \theta_e$, and h_e are the independent variables in the parameter space; $E_{0,z}$, $v_e = v_p$, L_{eff} , and g are the dependent variables; and g_{Qu} is the figure of merit. We calculate g_{Qu} for both supermodes and both wavelengths over all variations of slot geometry to determine the optimal combination. The characterization of this parameter space is shown in Figure C.2 and Figure C.3.

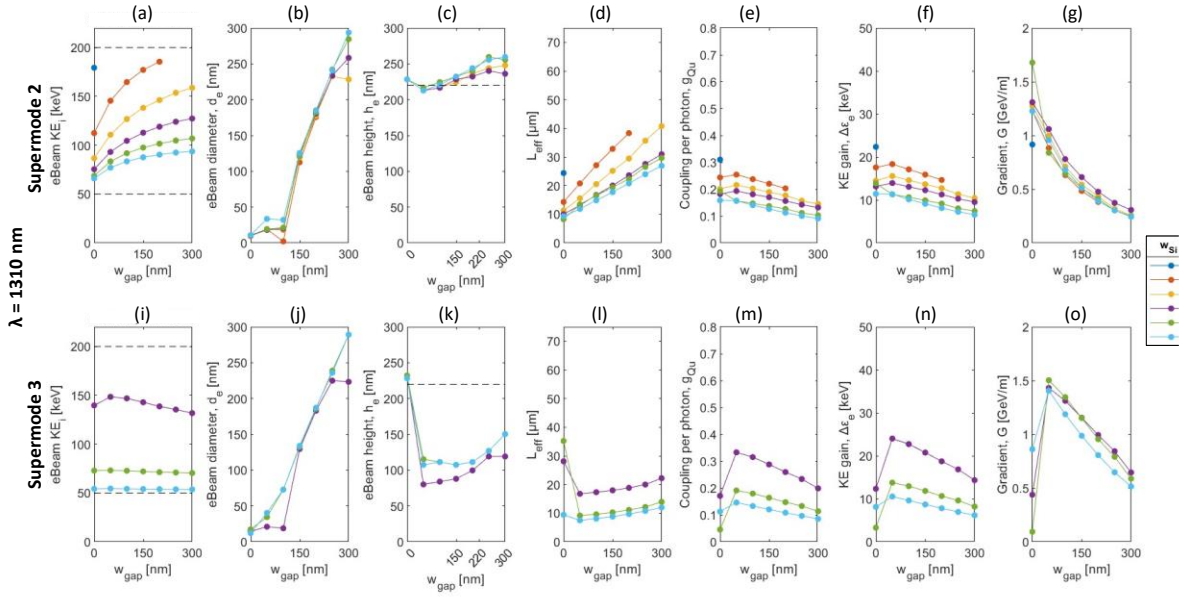


Figure C.2. Coupling results at $\lambda = 1310$ nm for (a-g, top) supermode 2 and (i-o, bottom) supermode 3 hosted by a waveguide with thickness of 220 nm and varying wall and gap widths. Optimal eBeam parameters are shown as (a,i) initial KE, KE_i , (b,j) diameter, d_e , and (c,k) height, h_e . They overlap over (d,l) the effective interaction length, L_{eff} , to maximize (e,m) the coupling per photon, g_{QU} , to produce the calculated (f,n) energy gain, $\Delta\epsilon_e$, and (g,o) acceleration gradient, G .

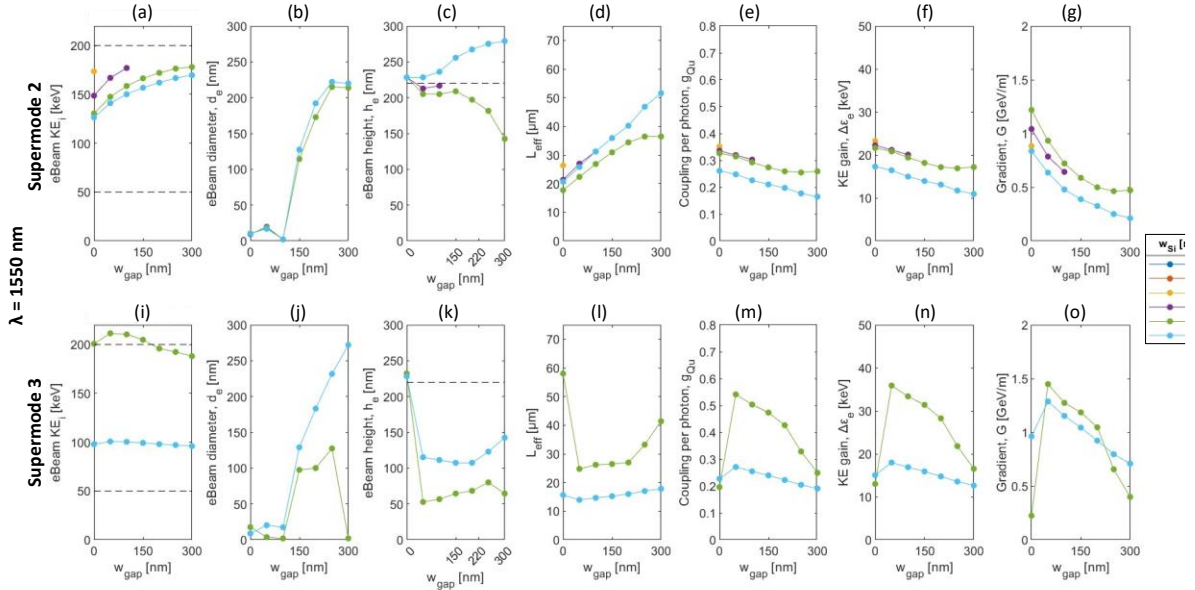


Figure C.3. Coupling results at $\lambda = 1550$ nm for (a-g, top) supermode 2 and (i-o, bottom) supermode 3 hosted by a waveguide with thickness of 220 nm and varying wall and gap widths. Optimal eBeam parameters are shown as (a,i) initial KE, KE_i , (b,j) diameter, d_e , and (c,k) height, h_e . They overlap over (d,l) the effective interaction length, L_{eff} , to maximize (e,m) the coupling per photon, g_{QU} , to produce the calculated (f,n) energy gain, $\Delta\epsilon_e$, and (g,o) acceleration gradient, G .

For a strip waveguide, $w_{\text{gap}} = 0$, which implies that the MER is not needed and therefore a larger amount of optical energy can reach the interaction region, resulting in a higher g although this effect is normalized by g_{Qu} . For cases of a wide w_{gap} , since d_e is determined by v_e , it cannot be increased enough to maximize overlap with the regions where the amplitude of E_z is the highest, such as near the sidewalls. For a narrower w_{gap} , the eBeam is aligned directly above the waveguide whereas for a wider w_{gap} , the optimal h_e is inside the slot. An increase in w_{gap} accommodates an extended L_{eff} since larger eBeam dimensions can fit into a wider gap. It also generally increases v_g towards v_p (as seen in Figure C.1), which improves the temporal overlap. A longer L_{eff} improves the overlap and therefore the coupling strength. The highest E_z amplitudes are found in supermode 3, but this higher order supermode can only be confined if $w_{\text{Si}} > 250 \mu\text{m}$. At a wavelength of 1550 nm, the weaker confinement allows for generally a higher g_{Qu} , especially for supermode 3. However, we must ignore the first 4 results for supermode 3 at 1550 nm, as shown in Figure C.3(i), because their corresponding n_{eff} and v_p are beyond the limits of the BOX and UTEM respectively. Despite this, supermode 3 still achieves the highest g_{Qu} of 0.4266 with a sidewall width of 300 nm and gap width of 200 nm, which induces the largest energy gain of 28.27 keV. This corresponds to an acceleration gradient of 1.05 GeV/m, which is one of the highest, but not the highest gradient achieved in this design scheme. The highest gradient of 1.68 GeV/m is achieved for supermode 2 at 1310 nm hosted by a sidewall width of 300 nm and a gap width of 0 nm as seen in Figure C.2(g) resulting in a g_{Qu} of only 0.1928 corresponding to an energy gain of 13.9 keV. Since both the gradient and gain are important performance metrics for such a device, our results confirm that maximizing g_{Qu} produces the best overall coupling efficiency.

On a chip, the interaction length might need to be shortened due to the space occupied by the waveguide bend and the MER. As a result, we expect a measured $\Delta\varepsilon_e$ to be lower than the calculated value. However, note that before reaching the interaction region, the eBeam must anyway converge over a certain finite length between the surface of the BOX layer and the region above the slot waveguide. Hence, for future designs, this space might be sufficient to fit a compact, dispersion engineered [1] MER without significant loss of coupling strength.

C.7. Methods

The normalized $E_{0,z}$ field was simulated in 2D using Ansys Lumerical Mode. Its calculated properties were then refined using a 3D simulation in Ansys Lumerical FDTD. The MER was also simulated and optimized in 3D using Ansys Lumerical FDTD. The mesh size of the simulation region was set at 8 nm, which determined the resolution of the simulated electric field. This imposed an incremental area dA of $6.4 \times 10^{-17} \text{ m}^2$ over which the E-field was discretized. The simulated E-field was distributed over a specific number of pixels as determined by the resolution of the mesh and was normalized to a maximum amplitude of 1 V/m. These results were exported to MATLAB where the interaction with the electron was calculated and optimized.